The Thesis Committee for Daniel Sanchez Rivera
Certifies that this is the approved version of the following thesis:

Reservoir Simulation and Optimization of CO_2 Huff-and-Puff Operations in the Bakken Shale

APPROVED BY
SUPERVISING COMMITTEE:

Supervisor: ______________________________
Matthew T. Balhoff

Co-Supervisor: ______________________________
Kishore K. Mohanty

Reservoir Simulation and Optimization of
CO_2 Huff-and-Puff Operations in the Bakken Shale

by

Daniel Sanchez Rivera, B.S.P.E.

Thesis

Presented to the Faculty of the Graduate School of
The University of Texas at Austin
in Partial Fulfillment
of the Requirements
for the Degree of

Master of Science in Engineering

The University of Texas at Austin
August 2014

Dedication

Sólo quiero dos cosas en esta vida: ser la mitad del hombre que es mi padre y conocer a una mujer la mitad de hermosa que mi madre. Papá y mamá, Gaytán y Puffy, todo lo que soy y todo lo que tengo es gracias a ustedes. Son mis ejemplos perfectos de amor y dedicación, de sacrificio y constancia. La única manera que tengo de agradecerles su apoyo y cariño es siendo la mejor versión de mí – todos mis logros son suyos. Gracias por enseñarme a decir gracias, perdón, y por favor. Gracias por levantarme cuando he tropezado, por corregirme cuando me he equivocado, y por motivarme cuando se me ha hecho difícil seguir adelante. Gracias por ponerme límites, y gracias por darme toda su confianza. Gracias por enseñarme el significado del esfuerzo y el valor del trabajo. Gracias por darme una hermana tan maravillosa y un segundo padre en mi padrino René. Gracias por rodearme de tíos y primos que me han hecho sentir querido desde que tengo memoria. Gracias por amarme incondicionalmente, y por darles alas a mis sueños. Sin ustedes seguirían siendo sólo eso – sueños. Gracias por darme la vida, y gracias por darme esta vida. Si pudiera pedirle algo más a Dios sería que mis hijos fueran tan afortunados como yo. Esta tesis, y todo lo que hago, es para ustedes. Los amo.

Acknowledgements

First and foremost I would like to thank Dr. Matthew Balhoff. Working for him has been the defining experience of my academic career – it has allowed me to do exciting research, attend graduate school, gain valuable industry experience, and travel to distant places. He has been my professor, supervisor, mentor, and Petrobowl coach, and has challenged and supported me like no other during my almost six years at The University of Texas. My deepest gratitude goes to him.

I would also like to acknowledge my co-supervisor, Dr. Kishore Mohanty, for his exceptional guidance during this project. It has been an honor to work for a man of his caliber, and I am extremely grateful for his patience, insight, and clarity.

My most sincere appreciation goes to the rest of the faculty of the Department of Petroleum and Geosystems Engineering, who have relentlessly pushed the limits of my curiosity and potential. I aspire to be what they all are: the best in the world at what they do. I would also like to express my gratitude to this department's administrative staff for their invaluable help in day-to-day matters, and to the Gas EOR Joint Industry Project for providing the funding for my research.

Finally, I want to thank my friends and colleagues from undergrad and graduate school, especially those in Dr. Balhoff's research group. This has been a fantastic ride, and I couldn't have done it without you. Hook 'em, and God bless.

Abstract

Reservoir Simulation and Optimization of CO_2 Huff-and-Puff Operations in the Bakken Shale

Daniel Sanchez Rivera, MSE
The University of Texas at Austin, 2014

Supervisors: Matthew T. Balhoff and Kishore K. Mohanty

A numerical reservoir model was created to optimize CO_2 Huff-and-Puff operations in the Bakken Shale. Huff-and-Puff is an enhanced oil recovery treatment in which a well alternates between injection, soaking, and production. Injecting CO_2 into the formation and allowing it to “soak” re-pressurizes the reservoir and improves oil mobility, boosting production from the well. A compositional reservoir simulator was used to study the various design components of the Huff-and-Puff process in order to identify the parameters with the largest impact on recovery and understand the reservoir’s response to cyclical CO_2 injection.

It was found that starting Huff-and-Puff too early in the life of the well diminishes its effectiveness, and that shorter soaking periods are preferable over longer waiting times. Huff-and-Puff works best in reservoirs with highly-conductive natural fracture networks, which allow CO_2 to migrate deep into the formation and mix with the reservoir fluids. The discretization of the computational domain has a large impact on the simulation results, with coarser gridding corresponding to larger projected recoveries.

Doubling the number of hydraulic fractures per stage results in considerably greater CO_2 injection requirements without proportionally larger incremental recovery factors. Incremental recovery from CO_2 Huff-and-Puff appears to be insufficient to make the process commercially feasible under current economic conditions. However, re-injecting mixtures of CO_2 and produced hydrocarbon gases was proven to be technically and economically viable, which could significantly improve profit margins of Huff-and-Puff operations.

A substantial portion of this project involved studying alternative numerical methods for modeling hydraulically-fractured reservoir models. A domain decomposition technique known as mortar coupling was used to model the reservoir system as two individually-solved subdomains: fracture and matrix. A mortar-based numerical reservoir simulator was developed and its results compared to a tradition full-domain finite difference model for the Cinco-Ley et al. (1978) finite-conductivity vertical fracture problem. Despite some numerical issues, mortar coupling closely matched Cinco-Ley et al.'s (1978) solution and has potential applications in complex problems where decoupling the fracture-matrix system might be advantageous.

Table of Contents

List of Tables

List of Figures

1. Introduction

Domestic oil and gas production in the United States has experienced an unprecedented surge in recent years. As Figure 1-1 shows, current U.S. daily gas production is the highest in history, and oil production has been steadily increasing since the early 2000s after decades of constant decline (BP Statistical Review of World Energy, 2013). An important reason for this growth is the successful development of unconventional plays. Technological breakthroughs in drilling and stimulation techniques have unlocked the potential of these formations, which were previously considered to be uneconomical. According to Verrastro (2012), shale gas accounted for less than 2% of the domestic output just a decade ago; today it comprises almost a third. In the year 2000, the United States produced about 150,000 barrels of oil per day from tight sands. That number had risen to one million barrels per day in 2011 and is projected to approach three million barrels by 2020 (Verrastro, 2012). According to the United States Energy Information Agency (U.S. EIA), 96% of the 1.8-million-barrel per day growth in production from 2011 to 2013 consisted of light sweet oil from tight formations (U.S. EIA, 2014).

Economic production rates in unconventional plays are achieved through horizontal drilling and multi-stage hydraulic fracturing. However, recovery factors in shale plays remain modest even after stimulation. Increasing output from these formations relies on enhanced oil recovery methods, like chemical and gas flooding. According to Hoffman (2012), gas injection projects account for 300,000 barrels of oil per day in the United States. One of these gas flooding techniques, called CO_2 Huff-and-Puff, is a cyclical process in which a well alternates between injection and production.

Injecting CO_2 into the formation re-pressurizes the reservoir and improves oil mobility, boosting production from the well.

The Bakken Shale, which extends across Montana, South Dakota, and North Dakota, is perhaps the most important shale play in the continental United States, and could benefit immensely from the wide-scale application of tertiary recovery methods like CO_2 Huff-and-Puff. According to the U.S. Geological Survey (USGS), there are 7.38 billion barrels of oil and 6.72 trillion SCF of gas in place in the Bakken Petroleum System (U.S. Geological Survey, 2013). Because of the massive volume of hydrocarbons in place, there are great incentives to improve recovery factors in the Bakken.

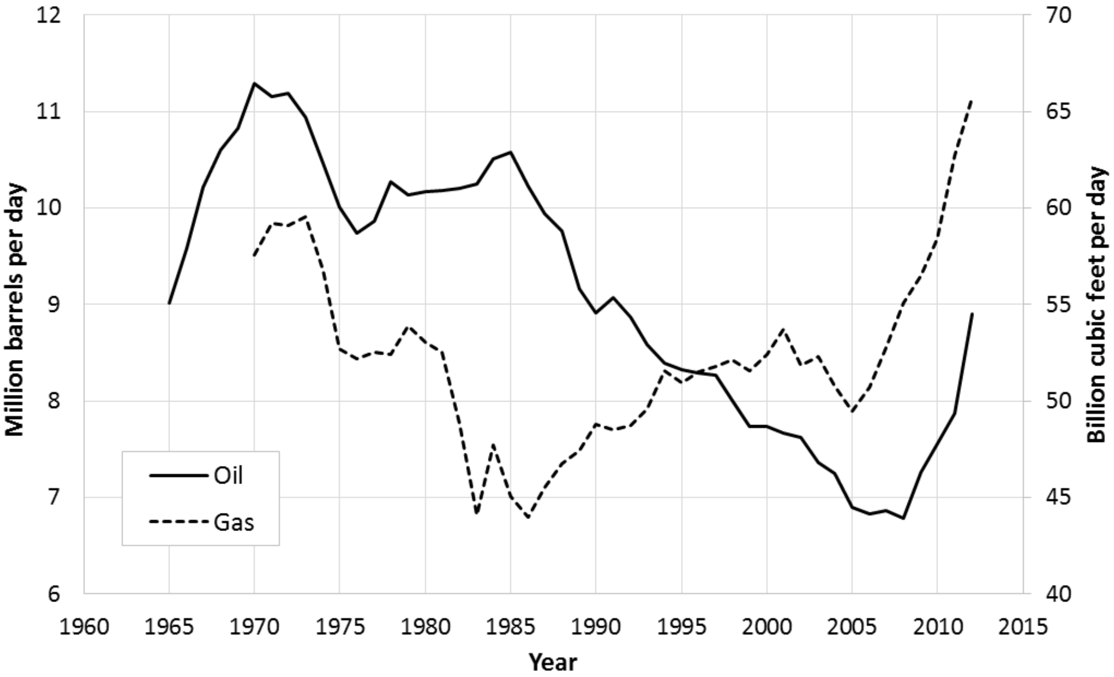

Figure 1-1. United States daily oil and gas production (BP Statistical Review of World Energy, 2013)

The goal of this study is to determine the optimum method of maximizing incremental recovery in the Bakken by CO_2 Huff-and-Puff. This involves using numerical reservoir simulation to study several design parameters of the Huff-and-Puff process. Special attention is paid to identifying opportunities to maximize the efficiency of Huff-and-Puff in addition to its effectiveness. Because of the complexity of simulating multi-phase, multi-component systems, additional research is presented on alternative methods of modeling hydraulically-fractured reservoirs. The method explored in this project is known as mortar coupling, a numerical technique that involves decomposing a complex system into two or more subdomains that are solved independently of each other and then coupled together by imposing continuity at their shared interface. The purpose of the mortar coupling research is to determine its applicability to hydraulically-fractured reservoir models, in which the fracture and the matrix are two distinctly different regions.

The rest of this Introduction (Chapter 1) provides background on the Bakken Petroleum System and the Huff-and-Puff process. It also describes previous studies on CO_2 Huff-and-Puff in oil shales and provides a list of objectives. Chapter 2 describes in length the approach taken to develop the fluid and reservoir models for the Huff-and-Puff simulations. The simulation results are presented and discussed in Chapter 3, and Chapter 4 explains the mortar coupling method and compares it to traditional full-domain finite difference modeling. Finally, Chapter 5 lists this study's conclusion and its recommendations for future work.

1.1. BACKGROUND

This section contains information about the geologic and geographic setting of the Bakken Petroleum System. It explains the importance of finding viable enhanced oil recovery alternatives in the Bakken, and gives an overview of the CO_2 Huff-and-Puff process.

1.1.1. The Bakken Formation

The Bakken Formation was deposited in the Williston Basin approximately 360 million years ago during the late Devonian/ early Mississippian age. The Williston Basin is a large intracratonic depression along the southwestern edge of the Canadian Shield, occupying an area of 300,000 mi^2 across parts of North Dakota, South Dakota, Montana, and the Canadian provinces of Manitoba and Saskatchewan. The distribution of oil and gas follows major geologic structures such as the Nesson, Little Knife, Billings and Antelope anticlines (Pollastro et al., 2010). According to Pollastro et al. (2010), "dynamic modifications of these structures at all scales" are responsible for the modern-day petrophysical and depositional characteristics of the Bakken. The Bakken is sandwiched between the Lower Mississippian Lodgepole Limestone and the Upper Devonian Three Forks Formation, and together they comprise the Bakken Petroleum System (Pollastro et al., 2010). A map of the Williston Basin Province and the Bakken Petroleum System are shown in Figure 1-2 (U.S. Geological Survey, 2013).

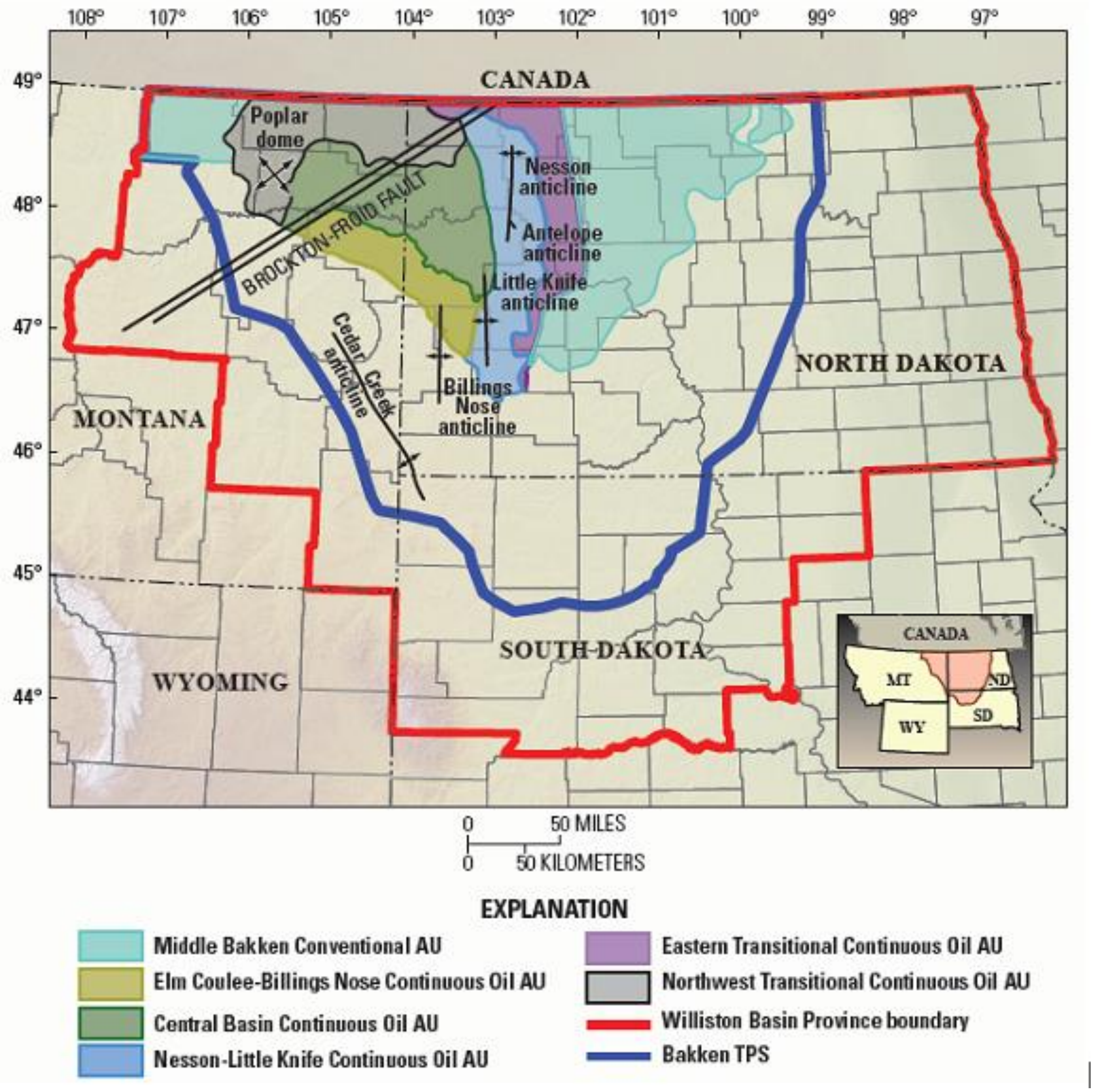

Figure 1-2. Map of the Williston Basin Province, Bakken Total Petroleum System, and the Bakken Formation Assessment Units (U.S. Geological Survey, 2013)

The Bakken Formation consists of three members: upper, middle, and lower. The upper layer consists of dark, kerogen-rich organic shale, while the lower member is made up of brownish, argillaceous siltstone. They both contain large volumes of thermally-mature organic matter (up to 35% by weight) and serve as source rocks for the Bakken

Petroleum System. The main Bakken reservoir is located in the middle layer, a silty dolostone with permeabilities between 0.01 and 0.04 md and porosities ranging between 3 and 9% (Sonnenberg and Pramudito, 2009). According to the U.S. Geological Survey (2013), the Middle Bakken varies in thickness across the Williston Basin, reaching its thickest point (90 ft) along the eastern edge of the Nesson anticline.

Oil was first produced in the Bakken in 1953 when the Antelope Field was discovered. The first horizontal well was drilled in 1987; prior to that, the formation produced 19 million barrels from 194 vertical wells (Breit et al., 1992). A 1995 report by the USGS estimated that the technically-recoverable oil reserves in the Bakken were approximately 151 million barrels (Zargari and Mohaghegh, 2010). This estimate increased to 3.65 billion barrels by 2008 (Pollastro et al., 2010), largely due to the advent of multistage hydraulic fracturing and the application of new drilling, stimulation, and enhanced oil recovery techniques. The discoveries of the Elm Coulee Field in 2000 and the Parshall Field in 2006 greatly increased the rate of exploration, drilling, and production in the area (Pollastro et al., 2010). Since the 2008 assessment by the USGS, more than 4,000 wells have been drilled and over 450 million barrels of oil have been produced from the Bakken/Three Forks system. Oil production from the Bakken has allowed North Dakota to surpass Alaska as the second-largest oil producing state in the U.S. (Nicas, 2012). The most recent report by the USGS estimates that there are 7.38 billion barrels of oil and 6.72 trillion SCF of gas in place in the Bakken and Three Forks Formations (U.S. Geological Survey, 2013).

1.1.2. Motivation for Enhanced Oil Recovery in the Bakken

Despite the enormous volumes of oil and gas in place, the Bakken Shale suffers from low production rates and small recovery factors because of its ultralow permeability[1]. According to the North Dakota Department of Mineral Resources, in March 2014 the average daily oil production in the state – 90% of which comes from the Bakken, according to the U.S. EIA (2012) – was 977,000 barrels from 10,457 producing wells. This means that the average Bakken well produces approximately 95 barrels of oil per day, paling in comparison to deep-water Gulf of Mexico wells that can reach daily oil rates of thousands of barrels. Even though production rates in the Bakken are high in the first few months following hydraulic fracturing, they eventually go into a quick and steep decline. According to Adekunle and Hoffman (2014) the average Bakken well experiences a 75% decline in oil rate within the first two years due to depletion of the natural reservoir drive (Figure 1-3).

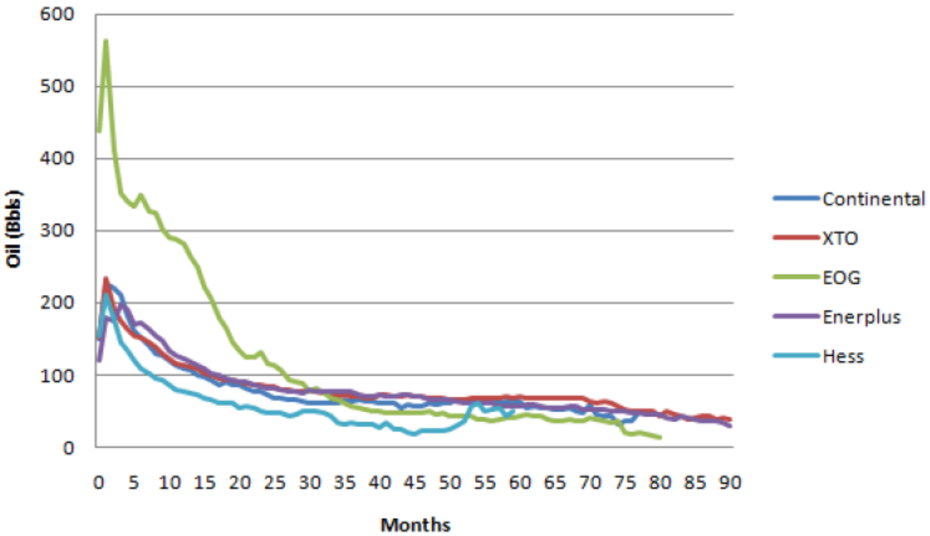

Figure 1-3. Production trends of different operators in the Bakken (Adekunle and Hoffman, 2014)

---

[1] Between 0.01 and 0.04 mD according to Sonnenberg and Pramudito (2009). Please refer to Table 2-7 for a list of values given in other studies.

In addition to low production rates, modest recovery factors are observed in wells produced exclusively through primary depletion. According to Shoaib and Hoffman (2009), only 5 to 10% of the original oil in place is recovered during primary production; Kurtoglu et al. (2013) estimate the recovery factor to be between 3 and 12%. According to Clark (2009), there is a wide range of values, from 1 to 19%. He identified a weak bi-modal distribution with peaks at 6 and 15%, with a mean value of 8.8% and a standard deviation of 4.7%. Regardless of the exact number, there is tremendous potential for improvement. Because of the massive volume of hydrocarbons in place, even modest enhancements in recovery would translate into millions of additional barrels of oil.

1.1.3. Secondary and Enhanced Oil Recovery Options in the Bakken

Waterflooding is the most common secondary recovery method in traditional reservoirs, but it is not a viable option in unconventional plays like the Bakken. Water exhibits poor injectivity into shales because of the matrix's ultralow permeability and high capillary pressures. Middle Bakken rocks are typically oil-wet or mixed-wet, which makes it difficult for aqueous phases to penetrate into the matrix and displace the oil (Shuler et al., 2011). Furthermore, waterflooding may reduce the sweep efficiency by initiating undesired fractures, and cause clay swelling that could further reduce the permeability of the formation (Yu et al., 2014).

Gas flooding has been extensively studied as an alternative to waterflooding in unconventional plays, and CO_2 in particular has been identified as a suitable injectant. CO_2 exists as a supercritical fluid at pressures above 1,070 psi and temperatures higher than 31°C, both of which are well within operating conditions. In this state, CO_2 is 10 to 25% as viscous as water and 70% as dense, facilitating its dispersion into the matrix

(Chen et al., 2013). Furthermore, it becomes first or multi-contact miscible with the oil if the pressure is high enough, allowing it to mix with the reservoir fluids and improve their mobility. According to Adekunle and Hoffman (2014), CO_2 develops miscibility with the Bakken oil at pressures between 3,000 and 3,400 psi, which is lower than other gases and can easily be reached during injection. A study by Song and Yang (2013) concluded that recovery performance in tight rocks is “significantly enhanced” by cyclical CO_2 injection over traditional waterflooding. According to Gamadi et al. (2013), some of the benefits of CO_2 injection include reduction of oil viscosity and interfacial tension, oil swelling, reservoir re-pressurization, relative permeability improvements, and wettability alteration.

1.1.4. Huff-and-Puff

The extremely low permeability of the Bakken raises important questions regarding the most effective flooding technique. Traditional well-to-well flooding might not be ideal in tight reservoirs because of the long propagation time of the injected fluid into the formation. Therefore, it might be advantageous to consider a cyclic “Huff-and-Puff” approach in which the same well alternates between injection and production.

Unlike traditional well-to-well continuous flooding, Huff-and-Puff is done in cycles. Every cycle consist of three periods: injection, soaking, and production. The first Huff-and-Puff cycle is preceded by a primary depletion period during which the well is allowed to naturally produce by reservoir drive alone. During every cycle, CO_2 (or another gas) is first injected into the reservoir at high pressure. This is followed by a soaking (or waiting) period, during which the well is shut in to allow for the CO_2 to diffuse into the formation, mix with the reservoir fluids, and re-pressurize the reservoir.

The soaking period must be long enough to allow thermodynamic equilibrium to occur. CO_2 dissolves into the oil, swelling its volume and reducing its viscosity and interfacial tension (Liu et al., 2005). Finally, the well is opened again to production, allowing the reservoir fluids to expand and flow into the wellbore. This injection-soaking-production cycle is repeated several times over the life of the well.

Some of the earliest CO_2 Huff-and-Puff projects were conducted by Texaco in the 1960s in California and Louisiana. Early candidates for treatment were conventional vertical wells with low oil production and reservoir pressures close to or exceeding the minimum miscibility pressure (Palmer et al., 1986). Huff-and-Puff has been successfully applied in conventional fields such as the Jiangsu Field in China (Liu et al., 2005) and the Jake Field in Sudan (Tang et al., 2011), as well as heavy oil deposits like the Chinese L-Block reservoir of Tuha Basin (Wenlong et al., 2008). There are currently no reports in the literature regarding Huff-and-Puff implementation in the Bakken, and blind-testing in the field would be impractical and wildly uneconomical. Therefore, a reservoir simulation approach is the most efficient way to determine the optimum combination of production parameters that would maximize the profitable recovery of hydrocarbons in the Bakken.

1.2. LITERATURE REVIEW

Gamadi et al. (2013) conducted an experimental study to measure the potential for enhanced oil recovery in oil shales through cyclical gas injection. They used unfractured shale core plugs from the Barnett, Eagleford, and Marcos formations saturated with mineral oil, and injected nitrogen to analyze the effects of injection time, injection pressure, soaking time, and number of cycles on recovery. The range of injection pressures covered both miscible and immiscible conditions, and the experiments were designed to mimic a typical Huff-and-Puff injection-soaking-production cycle. Gamadi et al. (2013) found that greater recovery factors are achieved when the injection pressure is large enough to develop miscibility. Their experiments showed that longer soaking times offer no additional production benefits when miscibility is not developed, but that extended soaking periods positively affect the recovery factor when miscible conditions are present. However, even under miscible conditions, they identified a point after which oil recovery stops increasing with soaking time, meaning that the length of the shut-in period must be optimized. Gamadi et al. (2013) also found that incremental oil recovery is significant after the first few cycles but stabilizes in subsequent injection runs. Furthermore, the number of cycles after which oil recovery stops increasing is affected by the injection pressure. These findings show that there is an optimum number of cycles that must be determined on a case-by-case basis and which, under real operating conditions, will be determined by technical and economic considerations.

Gamadi et al.'s (2013) results are significant because they show the need to optimize key design parameters of the Huff-and-Puff process. It is important to expand on their research and determine the applicability of their findings (obtained with nitrogen) to CO_2 injection. Furthermore, while the same trends are observed across core plugs from different plays, the authors note that cyclical gas injection proved more effective in some shale types than in others[2]. This shows the need to expand Gamadi et al.'s (2013) study into the Bakken, because the effectiveness of Huff-and-Puff varies from play to play.

Song and Yang (2013) combined numerical simulation with experimental methods to evaluate the performance of several enhanced oil recovery methods in tight shale formations. Their study considered immiscible, near-miscible, and miscible CO_2 Huff-and-Puff, as well as traditional waterflooding, and used actual Bakken core plugs and fluid samples to gather experimental measurements. Numerical models of core plugs were created in a compositional reservoir simulator (CMG GEM) and calibrated using the pressure and production profiles measured from the experimental core floods. The numerical models were used to determine the impact of injection pressure and soaking time on oil recovery by CO_2 Huff-and-Puff. Song and Yang (2013) found that CO_2 flooding, regardless of the miscibility conditions, vastly outperforms traditional waterflooding in tight shales. They observed that miscible and near-miscible injection leads to larger recoveries than immiscible Huff-and-Puff, and noted that further increasing the injection pressure above the minimum miscibility pressure yields marginal additional recovery. Song and Yang (2013) had similar results as Gamadi et al. (2013) in terms of the correlation between oil recovery and soaking time. Song and Yang (2013) found that the recovery factor increases with soaking time up to a certain point, after which incremental recovery remains almost constant regardless of the length of the shut-in period. According to Song and Yang (2013), after a certain time no more CO_2 is able to dissolve into the oil, minimizing the benefits of extended soaking periods. The existence of this point of diminishing returns for the soaking time, as evidenced by Song and Yang (2013) and Gamadi et al. (2013), indicates the need to optimize this and other

---

[2] The Eagleford shale sample showed consistently higher recovery factors than the Barnett or Marcos shales.

production variables and to extrapolate these findings from the core-scale to field-scale Huff-and-Puff operations.

Wang et al. (2010) conducted a field-scale study assessing the viability of different gas injection strategies in the Bakken. They used a numerical reservoir simulator to determine the effect on recovery of the injection type, gas composition, and reservoir heterogeneity. Their study considered a 13-well field and used history-matching to tune their reservoir model. Two types of injection were considered: a continuous scheme in which nine wells served as producers and four wells as injectors for the length of the simulation, and a cyclic scheme in which the four injection wells were divided into two groups that alternated between injection and production. Wang et al. (2010) found that continuous CO_2 injection is more effective than cyclic schemes, while not necessarily more efficient. While continuous CO_2 injection showed “fairly higher” recovery factors, it also required a “relatively greater injected amount of solvent” than cyclic CO_2 injection (Wang et al., 2010). Wang et al. (2010) compared pure CO_2, CO_2-enriched produced gas (60% mol CO_2, 40% CH_4) and CO_2-enriched flue gas (60% CO_2, 40% N_2) and determined that the cumulative oil recovery of CO_2-enriched produced gas is “relatively higher” than that of pure CO_2, while CO_2-enriched flue gas provides “only slightly lower” cumulative recovery. They concluded that CO_2-enriched gas (both produced and flue) is a “good choice” when the supply of CO_2 supply is limited (Wang et al., 2010). Finally, they introduced heterogeneity in the permeability field of their reservoir model, and observed that it had limited effects on the cumulative recovery and pressure distribution.

Wang et al.’s (2010) finding that continuous CO_2 injection is more effective but not necessarily more efficient than cyclic injection is significant. While continuous injection yields greater recovery factors it also has much larger CO_2 requirements. In theory, it makes sense for more oil to be produced if more CO_2 is injected. However, Wang et al. (2010) did not make a comparison of oil recovered per volume of CO_2 injected, so continuous CO_2 injection could actually make less economic sense despite yielding larger recovery factors. Furthermore, Wang et al.'s (2010) cyclic injection scheme was not ideal. Only four wells were set up as Huff-and-Puff wells, while the remaining nine produced for the duration of the simulation. A more direct comparison would have been for all thirteen wells to alternate between injection and production. It is also safe to assume that optimum lengths for the injection, soaking, and production periods were not used (because that was outside the scope of their research), so continuous injection was not compared against the best possible cyclic injection scenario.

Hoffman (2012) also used a numerical reservoir simulator to study the performance of various injectants in the Elm Coulee Field of the Bakken Shale. The purpose was to determine if re-injecting a mixture of CO_2 and separator gases is a technically-viable alternative in cases where CO_2 is not available (or cost-prohibitive) on location. He considered three cases: immiscible hydrocarbon gas flooding, miscible hydrocarbon gas flooding, and miscible CO_2 injection. For the miscible and immiscible hydrocarbon cases, he set the composition of the injection gas equal to the produced gas composition. Hoffman (2012) found that miscible gas flooding outperforms immiscible injection, as it reduces the residual oil saturation and improves the mobility of the oil in addition to providing pressure support. Furthermore, he determined that miscible hydrocarbon injection performs as well as pure CO_2 flooding, leading him to conclude that "significant oil can be recovered regardless of the type of gas injected," and to describe hydrocarbon gas as a "viable alternative" when CO_2 is unavailable (Hoffman, 2012). These findings are very similar to Wang et al.'s (2010), who concluded that CO_2-enriched gas is "a good choice" for field applications of gas flooding.

While Hoffman's (2012) study provides extremely valuable insight into the viability of separator gas as an injectant, there are some key differences with this study. The main difference is that he considered a traditional injector-producer scheme instead of a Huff-and-Puff approach. Hoffman (2012) considered continuous gas flooding for a period of 20 years, while Huff-and-Puff is, by definition, a cyclical process. Furthermore, his study was done at the field scale, on a two-mile by two-mile sector, while this project's domain comprises one hydraulic fracture on a single well. For these reasons, it is necessary to determine if Hoffman's (2012) findings can be extended to a different domain and injection scheme.

Chen et al. (2013) used UT-COMP, a compositional reservoir simulator, to study the effect of reservoir heterogeneity in Huff-and-Puff operations. Unlike Wang et al. (2010), they concluded that the effectiveness of CO_2 Huff-and-Puff is significantly affected by the permeability field. They observed that the impact of CO_2 is maximized if the permeability structure is able to contain CO_2 in the near-fracture region instead of allowing it to diffuse deep into the formation. Chen et al. (2013) determined that while recovery is linearly correlated to the heterogeneity of the permeability field, it is insensitive to its correlation length. They also studied some operational parameters and found that, for a fixed length of time, shorter waiting periods are preferable over longer soaking times because they lead to more injection cycles and increased recovery. However, they also observed that shorter soaking periods reduce the efficiency of CO_2 (recovery per mole injected) because they do not allow for complete mixing of the injected gas with the reservoir fluids.

The main difference between this study and Chen et al.'s (2013) is that while they focused on reservoir properties such as the heterogeneity and correlation length of the permeability field, which cannot be altered, this project deals primarily with treatment design parameters under the operator's control. Furthermore, Chen et al. (2013) encountered numerical stability issues which prevented them from running their simulations under actual Bakken operating conditions. This project uses CMG GEM instead of UT-COMP, which improves numerical stability and allows for more realistic operating conditions to be simulated. Finally, this study had access to Chen et al.'s (2013) fluid model and it was determined that their fluid characterization had room for improvement. This project improves upon Chen et al.'s (2013) fluid characterization, resulting in a fluid model that more closely resembles the PVT behavior of Bakken oil.

Yu et al. (2014) used CMG GEM to run a sensitivity analysis on the effect of reservoir properties, fluid properties, fracture characteristics, and operational parameters on the recovery factor. Properties for their reservoir model were obtained by history-matching historical production and pressure data from a hydraulically-fractured well in the Middle Bakken. Yu et al. (2014) found that incremental recovery of oil is most sensitive to the CO_2 injection rate, followed by the length of the injection period, the number of cycles injected, and the diffusivity of CO_2 in the oil phase. The impact of other parameters (fracture conductivity, soaking time, matrix permeability and fracture half-length) was found to be much smaller. Yu et al. (2014) also concluded that wells in which two fractures are created per stage show higher incremental recoveries after Huff-and-Puff than those with one, three, or four clusters per stage.

Yu et al.'s (2014) study can be expanded by better understanding the effect of Huff-and-Puff at the reservoir level. While their sensitivity analysis did a terrific job of identifying the most impactful Huff-and-Puff design variables, they did not explore the physical reasons behind their observations. For instance, while Yu et al. (2014) concluded that the length of the soaking period has a small effect on incremental recovery, they did not offer an explanation for this observation. Their objective was not to optimize the Huff-and-Puff process, but to determine which variables affect it the most. Yu et al.'s (2014) work is a great starting point for this project, because their findings provide valuable insight into which design parameters should be studied most extensively.

1.3. OBJECTIVE

The objective of this study is to optimize the CO_2 Huff-and-Puff process in order to maximize the profitable recovery of hydrocarbons. A numerical reservoir model has been created to study several components of the Huff-and-Puff design, such as:

1) The length of the primary depletion period.

2) The length of the injection period.

3) The length of the soaking period.

4) The number of cycles.

5) The production pressure.

6) The injection rate.

7) The composition of the injection gas.

It is also important to understand the role of thermodynamic mechanisms (molecular diffusion) and reservoir characteristics (permeability of the matrix and natural fractures) in the Huff-and-Puff process. This study will use quantitative results to reach qualitative conclusions about the reservoir's response to cyclical CO_2 injection, which will help guide the design of Huff-and-Puff treatments. Because the objective of any oil and gas venture is to generate value, special attention has been paid to maximizing efficiency in addition to raw production. A positive balance must be struck between the incremental revenue generated by Huff-and-Puff and the costs associated with it (namely CO_2 acquisition and pressurization). Therefore, the goal of this study is not only to identify the design criteria with the largest impact on recovery, but also the best strategy for maximizing profits.

Because of the complexity of multi-phase compositional reservoir simulation, part of this research is focused on studying alternative numerical methods of solving hydraulically-fractured reservoir models. One of these methods, known as mortar coupling, allows complex systems to be decomposed into two or more individually-solved subdomains that are mathematically coupled together. This is particularly applicable to stimulated reservoir models because the fracture and the matrix are two distinctly different regions in terms of permeability (relative and absolute), pressure transient behavior, and fluid dynamics. A mortar-based numerical reservoir simulator has been developed and its results compared to a tradition full-domain finite difference model for the Cinco-Ley et al. (1978) finite-conductivity vertical fracture problem.

2. Modeling Approach

The reservoir model built for this study was composed of two parts: a fluid characterization and a computational domain. This chapter describes the modeling approach taken to construct both of these components.

2.1. FLUID CHARACTERIZATION

An accurate fluid characterization is a vital component of any reservoir model. PVT and composition data for a Bakken fluid sample were obtained and a fluid model was generated using CMG WinProp. The sample was taken at a depth of 9,500 ft., and a pressure and temperature of 6,840 psi and 241°F. This section describes the pseudocomponent lumping, generation of the pseudocritical properties, and tuning of the model to match the experimental properties of the fluid sample.

2.1.1. Pseudocomponent Lumping

The first step of the fluid characterization was lumping the thousands of components of the reservoir fluid into pseudocomponents. Pedersen et al. (2007) define lumping as "deciding what carbon number fractions to lump (group) into the same pseudocomponents, and averaging the critical temperature (T_c), critical pressure (P_c), and acentric factor (ω) of the individual carbon number fractions into one T_c, P_c, and ω representative for the whole lumped pseudocomponent." Following the classification of Pedersen et al. (2007), three types of components were considered: defined components, C_{7+} fractions, and a plus fraction. Defined components are pure components whose properties have been experimentally measured. In petroleum fluids, these are N_2, CO_2, H_2S, C_1, C_2, C_3, nC_4, iC_4, nC_5, iC_5, and C_6 (which is typically considered to be nC_6). C_{7+}

fractions are groupings of hydrocarbons with similar boiling points; they typically contain paraffinic, naphthenic, and aromatic compounds. For instance, a C_9 fraction might contain n-nonane (an n-paraffin), 1,2-dimethylcyclohexane (a naphthene) and ethyl benzene (an aromatic). Finally, the plus fraction consists of the heavy components that cannot be grouped into individual C_{7+} fractions (Pedersen et al., 2007). The fluid report used for the characterization considered C_7-C_{29} fractions in addition to the defined components, and a C_{30+} plus fraction with a molecular weight of 545 g/mol and a density of 0.93 g/cc.

Liu et al. (2005) recommend lumping the fluid into five to eight pseudocomponents based on their volatility. For this project, the lumping followed the approach taken by Chen et al. (2013), in which the sample was characterized using seven pseudocomponents. The fluid sample contained no H_2S and a small mole percent of N_2 (1.72%), which was deemed negligible and divided equally among the remaining 33 components. While CO_2 was also present in trace amounts (0.43% by mole), it was included in the fluid model as an individual component because it would be injected during the simulations. Methane (C_1) was the most abundant component in the sample (37.7%), and also characterized individually. It was decided not to combine defined components with C_{7+} fractions, so C_2-C_6 were lumped into two pseudocomponents and C_7-C_{30+} were grouped into three. The lumping followed the recommended weight-based grouping by Pedersen et al. (2007), in which the weight percent of a component (WT_i) is given by Eq. 2-1 and the pseudocomponents contain approximately the same weight amount (ΣWT_i). Table 2-1 shows the grouping of the fluid's components based on the described criteria. In this section, and the rest of this report, the distinction between defined components (CO_2, N_2, C_1…) and pseudocomponents (CO2, C1, C23…) is made through the use of subscripts.

$$
\begin{aligned}
&WT_i = \frac{z_i M_i}{\sum_{i=1}^{i=n} z_i M_i}, \\
&where: \\
&z_i = mol\ \%\, of\ component\, i \\
&M_i = molecular\ weight\, of\ component\, i
\end{aligned}
\qquad (2\text{-}1)
$$

Table 2-1 – Weight-based lumping of pseudocomponents

Pseudocomponent	**Components**	**Mol % (*z*)**	**Weight % (*WT*)**
CO2	CO_2	0.48	0.28
C1	C_1	37.75	8.18
C23	C_2-C_3	24.27	11.53
C46	C_4-C_6	11.11	10.36
C7P1	C_7-C_{12}	15.06	24.45
C7P2	C_{13}-C_{21}	7.32	22.04
C7P3	C_{22+}	4.01	23.15

2.1.2. Pseudocritical Properties

Compositional reservoir simulators such as CMG GEM that perform phase equilibrium calculations using cubic equations of state require the critical pressure, critical temperature, and acentric factor of each component in the mixture (Pedersen et al., 2007). Values of T_c, P_c, and ω for defined components (CO_2 and C_1-C_6) have been measured experimentally and are widely available in the literature. The critical properties of the C_{7+} fractions can be estimated as functions of density (ρ) and molecular weight (M) from correlations (Eq. 2-2 through 2-4), with different c, d, e, and f coefficients for the Peng-Robinson (PR) and Soave-Redlich-Kwong (SRK) equations of state (Appendix I, Pedersen et al., 2007).

$$T_c = c_1\rho + c_2 \ln M + c_3 M + \frac{c_4}{M} \tag{2-2}$$

$$\ln P_c = d_1 + d_2\rho^{d_5} + \frac{d_3}{M} + \frac{d_4}{M^2} \tag{2-3}$$

$$e_1 + e_2 M + e_3\rho + e_4 M^2 = f_1 + f_2\omega - f_3\omega^2 \tag{2-4}$$

The fluid report used for the characterization did not contain density or molecular weight information for the C_{7+} fractions, so assumptions were required in this regard. In Chapter 5 of *Phase Behavior of Petroleum Reservoir Fluids*, Pedersen et al. (2007) present a fluid characterization for a North Sea condensate and provide density and molecular weight data for C_7 through C_{80}. Pedersen et al.'s (2007) data was used in this project to calculate the critical properties of the C_{7+} fractions for both the PR and SRK equations of state. This approach was taken as a first approximation, knowing that the fluid model still needed to be fine-tuned to match the experimental measurements of the fluid sample. The molecular weight of the C_{30+} fraction was known, so its critical properties were estimated by developing correlations of T_c, P_c, and ω as functions of M (Figures 2-1 through 2-3).

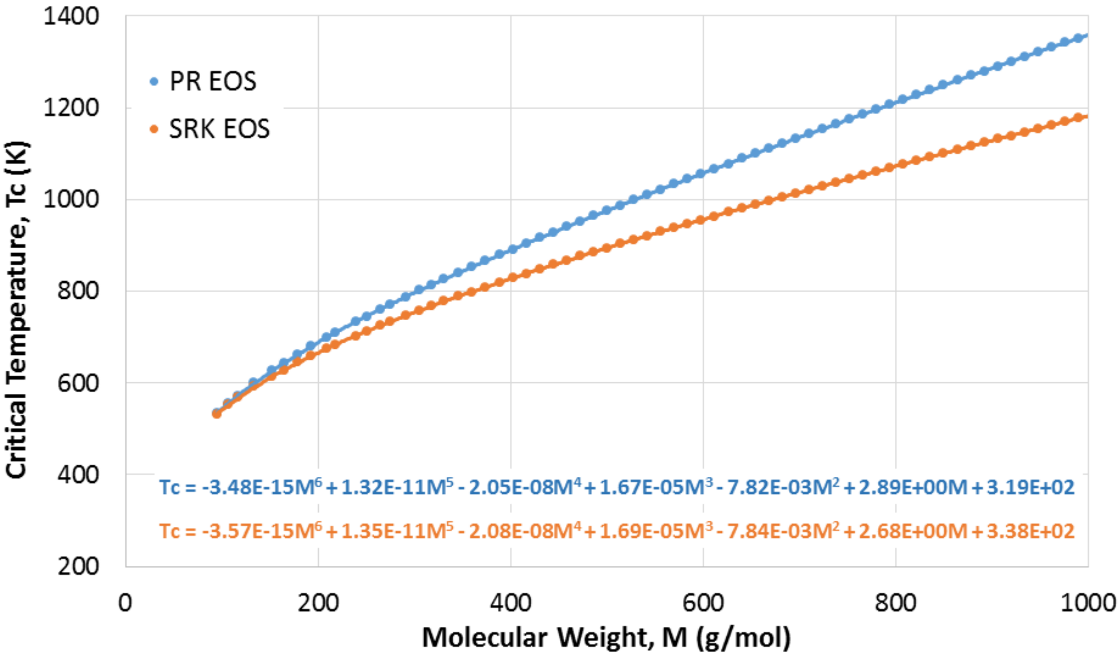

Figure 2-1. Critical temperature vs. molecular weight

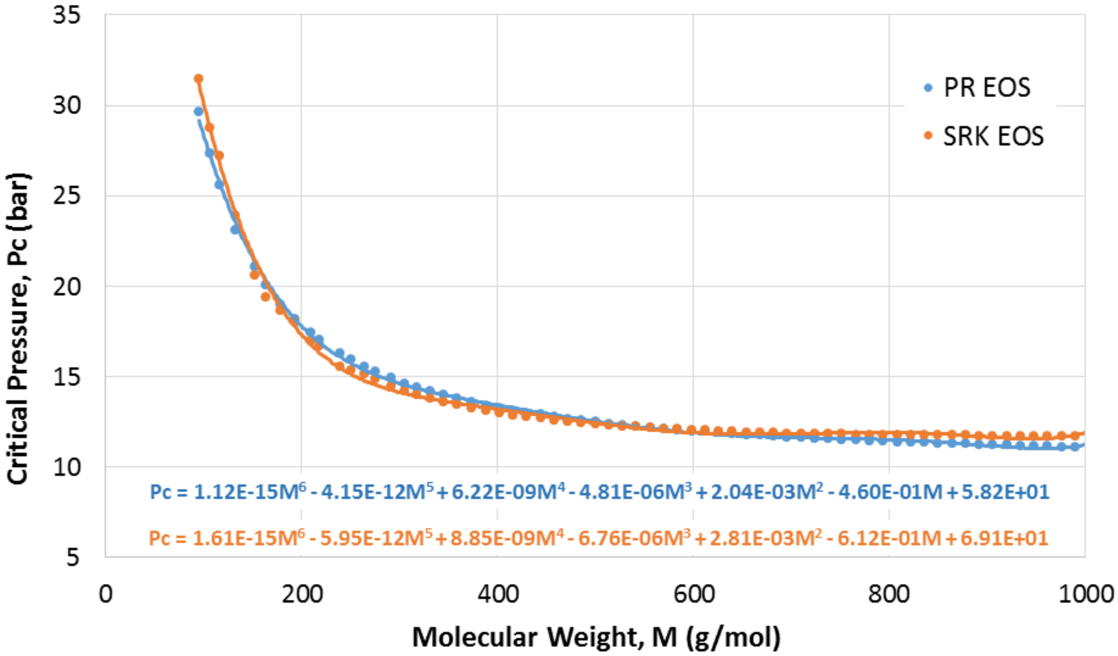

Figure 2-2. Critical pressure vs. molecular weight

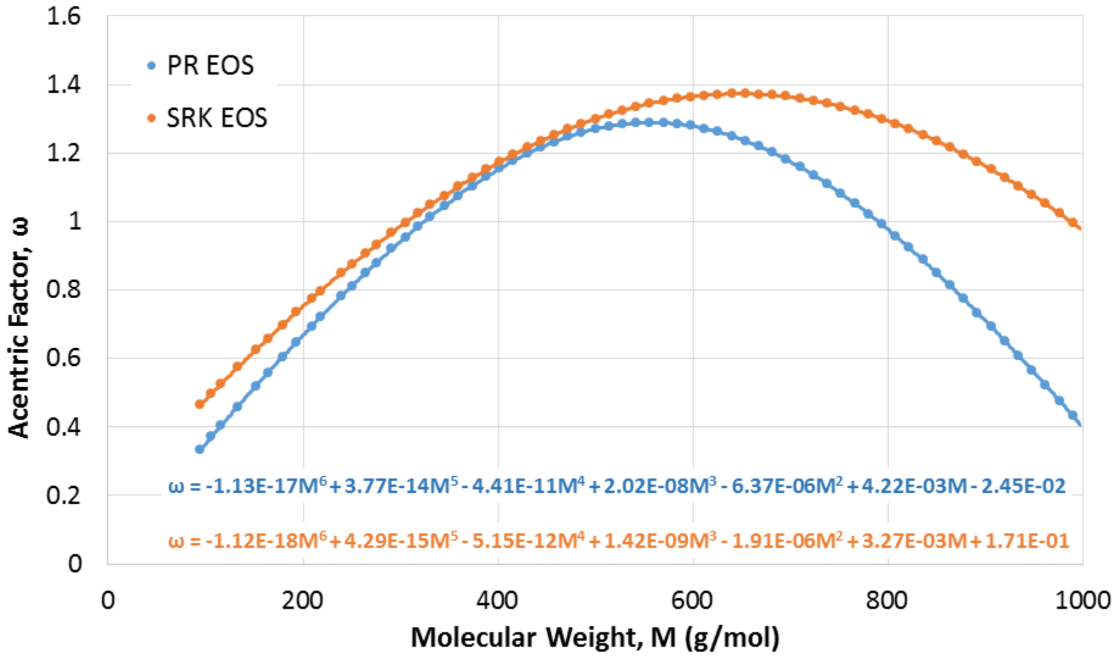

Figure 2-3. Acentric factor vs. molecular weight

The critical properties of the seven pseudocomponents were found as the weight mean averages of T_c, P_c, and ω of the individual components, as described by Pedersen et al. (2007). Eq. 2-5 shows the formula for calculating the pseudocritical pressure of pseudocomponent k, which contains C-fractions m to n; the pseudocritical temperature and acentric factor are calculated in a similar fashion (Pedersen et al., 2007). Table 2-2 shows the complete fluid characterization before tuning.

$$P_{ck} = \frac{\sum_{i=m}^{n} z_i M_i P_{ci}}{\sum_{i=m}^{n} z_i M_i} \tag{2-5}$$

Table 2-2 – Fluid characterization before tuning

Pseudo-component	***M* (g/mol)**	***P_c* (atm)**		***T_c* (K)**		***ω***	
		PR	**SRK**	**PR**	**SRK**	**PR**	**SRK**
CO2	44.01	72.8	72.8	577.4	577.4	0.225	0.225
C1	16.04	45.4	45.4	463.8	463.8	0.008	0.008
C23	35.17	45.3	45.3	334.8	334.8	0.123	0.123
C46	69.03	33.6	33.6	461.2	461.2	0.238	0.238
C7P1	120.20	24.6	28.8	583.9	550.0	0.431	0.495
C7P2	222.91	16.7	18.1	720.3	659.5	0.748	0.740
C7P3	427.33	12.9	12.8	931.9	850.9	1.173	1.195

As Table 2-2 shows, only C7P1, C7P2, and C7P3 show any differences in pseudocritical properties between the PR and SRK equations of state. This was one of the objectives of the lumping scheme: to separate defined components, whose critical properties have been experimentally measured, from C_{7+} fractions that rely on correlations. Grouping the components in this fashion allowed for parameters with the highest degree of uncertainty to be isolated and targeted for fine-tuning.

2.1.3. Model Tuning

The objective of tuning the model was to match the PVT properties of the fluid characterization to the experimental measurements of the fluid sample. The report used to develop the fluid characterization did not contain PVT measurements over a range of pressures and temperatures, only at initial reservoir conditions. Therefore, only five experimental measurements were used as constraints (or targets) when optimizing the fluid model; these can be seen in Table 2-3. The Peng-Robinson equation of state was used in CMG WinProp for all simulations.

Table 2-3 – Constraints for fluid model optimization

Property	Value
Oil density*	39.56 lb/ft^3
Oil FVF*	1.71 bbl/stb
Oil viscosity*	0.246 cP
Oil compressibility*	14.55×10^{-6} psi^{-1}
Bubble point (241°F)	2,872 psi
*At initial reservoir conditions, 6840 psi and 241°F	

Without any tuning, the model closely matched the oil compressibility, density, and formation volume factor at initial reservoir conditions, but grossly underestimated the viscosity and overestimated the bubble point. The first simulation run was done without volume shift corrections and with the default WinProp exponent for calculating hydrocarbon-hydrocarbon (HC-HC) binary interaction coefficient (*PVC3* = 1.2). Table 2-4 shows the summary of results for the initial, non-optimized simulation run.

Table 2-4 – Comparison of PVT behavior between fluid sample and initial model

	Sample	Model	Error (%)
Bubble point (psi)	2,872	3,351	16.66
Oil viscosity (cp)	0.246	0.149	-39.51
Oil density (lb$_m$/ft^3)	39.6	39.3	-0.85
Oil FVF (rb/stb)	1.71	1.72	0.30
Oil compressibility (psi^{-1})	14.55×10^{-4}	14.68×10^{-4}	1.24

The tuning was performed by WinProp's "regression" tool. According to WinProp's User's Guide, the software uses Agarwal's regression procedure to tune the equation of state's parameters to match experimental measurements. Once the optimization parameters are selected, the procedure orders them in order of sensitivity and performs regressions on a small subset of parameters at a time. Once a parameter is tested across its specified range of values, or it no longer contributes to improving the match, WinProp moves on to the next parameter on the list (CMG, 2012b). For the optimization of this study's fluid model, the following properties were selected as regression parameters:

1) Critical pressure
2) Critical temperature
3) Acentric factor
4) Molecular weight
5) Omega A (EOS parameter)
6) Omega B (EOS parameter)
7) Critical volume for viscosity
8) Exponent for calculating HC-HC binary interaction coefficients

With the exception of the exponent for calculating the binary interaction coefficients (*PVC3*), all of the listed parameters were optimized only for C7P1, C7P2, and C7P3. As previously mentioned, unlike CO2, C1, C23, and C46, which only contained defined components, the heavier pseudocomponents carried the most uncertainty due to the lack of density and molecular weight data. Setting the constraints listed on Table 2-3 as targets, WinProp was able to generate an almost perfect match to the fluid sample. Table 2-5 shows the final fluid characterization, and Table 2-6 shows the parameters that were tweaked by the program's regression tool:

Table 2-5 – Comparison of PVT behavior between fluid sample and optimized model

	Sample	**Model**	**Error (%)**
Bubble point (psi)	2,872	2,872	0.00
Oil viscosity (cp)	0.246	0.246	0.00
Oil density (lb_m/ft^3)	39.6	39.4	-0.47
Oil FVF (rb/stb)	1.71	1.71	0.09
Oil compressibility (psi^{-1})	14.55×10^{-4}	14.55×10^{-4}	0.00

Table 2-6 – List of parameter changes for optimized model

Parameter	**Component**	**Initial Value**	**Final Value**	**Change (%)**
Tc (K)	C7P3	931.9	915.9	-1.71
Omega B	C7P1	0.0778	0.0779	0.13
Critical volume for viscosity	C7P1	0.4954	0.5878	18.65
Critical volume for viscosity	C7P2	0.8051	0.9575	18.93
HC-HC BIC exponent	N/A	1.2	0.46	-61.51

2.1.4. Minimum Miscibility Pressure

Hoffman (2012) and Gamadi et al. (2013) described the benefits of achieving miscibility during gas injection operations. Hoffman (2012) found that miscible gas flooding outperforms immiscible injection by reducing the residual oil saturation and improving the mobility of oil. There are two types of developed miscibility: first contact and multi-contact. First-contact miscibility (FCM) is developed when the two fluids mix completely upon contact, while multi-contact miscibility (MCM) occurs when some time is needed for the fluids to mix into a single phase. For a specific temperature and composition, multi-contact miscibility is developed at a lower pressure than first-contact miscibility (Adekunle and Hoffman, 2014). The pressure at which miscibility is first developed is known as the minimum miscibility pressure (MMP). The lowest pressure at which two fluids are miscible by first contact is known as the first contact minimum miscibility pressure, or FCMMP (Pedersen et al., 2007).

Because of the benefits of achieving miscibility between the CO_2 and reservoir fluids, knowing the minimum miscibility pressure is a key design consideration. One of the most widely-used methods for determining the MMP is the slim tube test, in which gas is injected into an oil-saturated tube with the purpose of displacing the oil. Recovery is measured at several injection pressures, and the minimum miscibility pressure is the lowest pressure at which at least 90% of the oil is recovered (Pedersen et al., 2007).

A series of slim tube tests were simulated in CMG GEM in order to determine the minimum miscibility pressure of CO_2 and the reservoir fluid. A 200-block 1D reservoir model was created and saturated entirely with oil. The model had a pore volume of 20,000 ft^3: it was 1,000 ft. long (200 blocks × 5 ft.), 10 ft. wide, 10 ft. thick, and had a porosity of 20%. A constant rate injection well was placed in the first grid block and a constant bottomhole pressure production well was placed in the last (Figure 2-4). Permeability was set to 10,000 mD. Oil recovery was measured at 1.2 PV injected, so the simulation was run for 1,000 days at a constant injection rate of 24 res. ft^3/day. The bottomhole pressure of the producing well was set equal to the initial tube pressure, and this pressure was changed for different simulation runs.

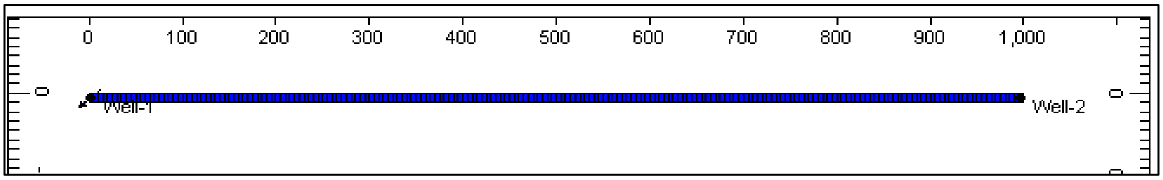

Figure 2-4. Slim tube test model

According to Wu and Batycky (1990), the commonly-accepted definition of the MMP (multi-contact miscibility) is the slim tube test pressure at which 90% of the oil is recovered after 1.2 PV of solvent injection. Meanwhile, first contact miscibility is characterized by total (or nearly total) oil recovery at 1.2 PV injected. Figure 2-5 is a plot of the percentage of oil recovered at 1.2 PV of CO_2 injected versus the test pressure. As Figure 2-5 shows, multi-contact miscibility (90% recovery) occurs at about 2,400 psi.

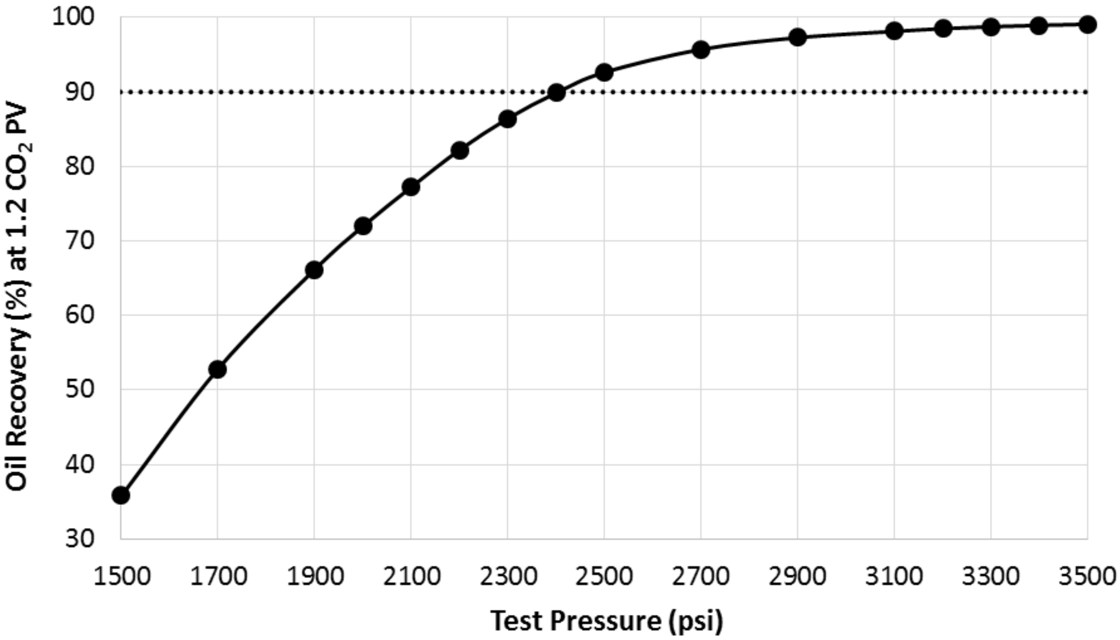

Figure 2-5. Oil recovery at 1.2 PV CO_2 injection vs. slim tube test pressure

The slim tube results showed that first contact miscibility (>98% recovery) is first developed at around 3,100 psi. This estimate was confirmed by looking at the oil saturation profile of the slim tubes. As Figure 2-6 shows, at 3,200 psi there is a sharp displacement front at the oil-CO_2 interface, meaning that oil and CO_2 are moving together as a single phase. On the other hand, at 3,100 psi and below the existence of a saturation gradient is indicative of MCM displacement. Hoffman (2012) and Adekunle and

Hoffman (2014) found that the minimum miscibility pressure of Bakken oil is between 3,100 and 3,400 psi. Our study suggests that while first contact miscibility indeed occurs within that pressure range, multi-contact miscibility might develop at lower pressures (2,250-2,500 psi).

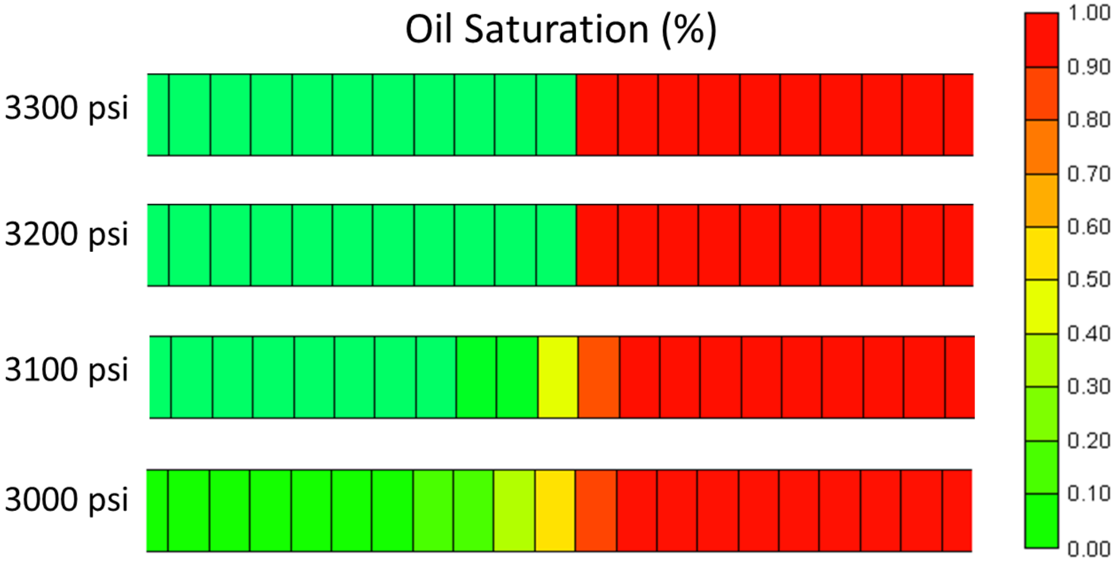

Figure 2-6. Oil saturation in slim tube tests

2.2. COMPUTATIONAL DOMAIN

Previous studies have examined the Huff-and-Puff process over a wide range of scales. Gamadi et al. (2013) and Song and Yang (2013) did experimental research on core plugs, while Wang et al. (2010) and Hoffman (2012) used numerical reservoir simulation to study gas injection at the field level. These field-scale studies used a stimulated reservoir model (SRV) with logarithmic grid refinement (LGR) approach to model hydraulic fractures. Wang et al. (2010) assigned a permeability of 100 mD to the grid blocks around the wellbore, while Hoffman (2012) represented hydraulic fractures as "zones of increased permeability in the grid." This study's domain is a single-stage scale, akin to the research by Chen et al. (2013). This choice of domain allows for fluid behavior in the near-fracture region to be captured in much more detail, while still allowing for real operating conditions to be simulated (which cannot be done at the core-scale). Furthermore, because of well and flow geometry, findings can be extrapolated to a larger scale.

Figure 2-7 shows this study's computational domain. The domain is centered at one wing of a transverse hydraulic fracture on a horizontal well. In this section, width refers to the *x*-direction, parallel to the wellbore, while length refers to the *y*-direction, parallel to the hydraulic fracture. In the *x*-direction, the domain runs along the wellbore from the halfway point to the fracture ahead to the halfway point to the fracture behind. The well is assumed to be a 5,000-ft lateral fractured in 15 single-cluster stages, so the domain's width is 320 ft. In the *y*-direction, the domain runs to the halfway point to an adjacent well 2,000 feet away, so it has a length of 1,000 ft. According to the USGS (2013) the Middle Bakken varies in thickness across the Williston Basin, so a thickness (*z*-direction) of 10 ft. was used mirroring the work of Chen et al. (2013). The computational domain was modeled as a 25×40×1 Cartesian grid. Increasing the number of grid blocks to 50×80×1 had negligible effects on the simulation results but resulted in much longer computation times. However, using a coarser mesh (reducing the number of grid blocks) had a significant impact on the projected recovery factors – this is discussed at length in Section 3.9. Two horizontal wells (one for injection and the other for production) were placed along the topmost set of grid blocks and perforated across the entire width of the domain. This perforation scheme resembles an open-hole completion style (as opposed to cemented Plug-and-Perf), which is widely used by operators in the Bakken (Appleton and Rivenbark, 2013).

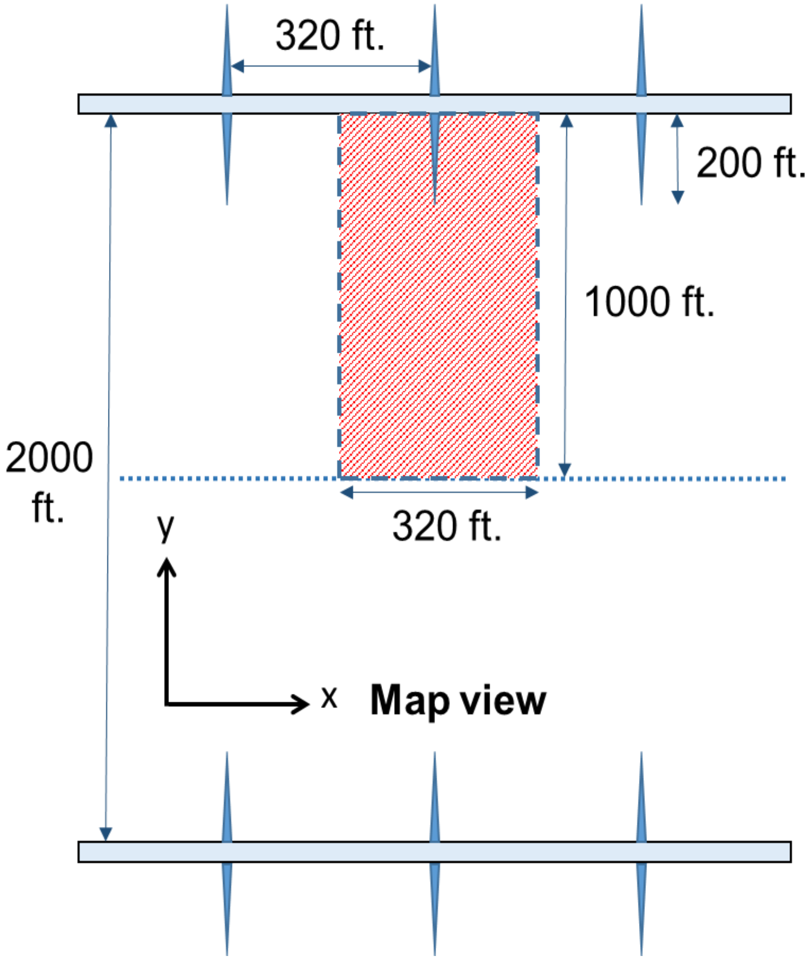

Figure 2-7. Computational domain

2.2.1. Hydraulic Fracture Modeling

The hydraulic fracture is the main pathway through which reservoir fluids are produced and CO_2 is injected into the formation. Therefore, it was of paramount importance to develop a computational domain that accurately modeled fluid behavior around the fracture. This study used the same fracture properties as Chen et al. (2013), who assumed a fracture width of 0.005 ft. and a fracture permeability of 10,000 mD. While a different fracture half-length was used, the fracture conductivity was identical to the value obtained by Yu et al. (2013) through history matching of Bakken wells. This study assumed a 200-ft. fracture with a permeability of 10,000 mD, resulting in a fracture conductivity of 50 mD-ft.

Chen et al. (2013) modeled the hydraulic fracture explicitly, as a .005-ft.-thick set of grid blocks with a 10-Darcy permeability. They used a single-porosity permeability model, in which fractures are "represented explicitly as single planar planes" (Li et al., 2011). Chen et al. (2013) encountered numerical errors because of the huge permeability contrast between the fracture and the matrix, limiting the operational conditions they could impose. For example, their study was unable to simulate injection pressures above 3,500 psi, and they had to gradually reduce the bottomhole pressure during primary depletion in order to reach the target production pressure of 1,000 psi.

Initially, the computational domain was built similarly to Chen et al.'s (2013) "explicit fracture" single-porosity model, and numerical instability was suppressed by adjusting CMG GEM's numerical parameters. The first time step size after well change (*DTWELL*) and the minimum time step size (*DTMIN*) were set to 1×10^{-10} days, and the maximum number of linear solver iterations (*ITERMAX*) was increased from 80 to 160. However, reaching the target production pressure during primary depletion still required gradual reduction of the well's bottomhole pressure, and large injection gradients caused failures in convergence in the simulation. Additionally, because individual time steps had to be repeated several times until convergence was reached, simulation run times were impractical. Adding more complex phenomena, like molecular diffusion and dispersion, caused the simulations to crash immediately.

CMG GEM's *Hydraulically-Fractured Wells Wizard* was used as an alternative to explicit fracture modeling. This tool models a 2-ft wide "pseudo-fracture" and adjusts other fracture parameters to match the dimensionless fracture conductivity of the actual fracture. It vastly increases the numerical stability of the simulation by reducing the permeability contrast between the fracture and the matrix. It also performs local grid refinement close to the "pseudo" or "equivalent" fracture, where fine gridding is required to accurately capture fluid behavior (CMG, 2012a). Eq. 2-6 through 2-8 show the derivation behind the pseudo-fracture permeability calculation. The condition imposed is that the flow rate into the equivalent fracture must be equal to the flow rate into the original fracture. Therefore, a fracture with a permeability of 10,000 mD and a width of 0.005 ft. is modeled as (and assumed to be equal to) a 2-ft. wide fracture with a permeability of 25 mD.

$$Q_{original} = Q_{new} \tag{2-6}$$

$$\frac{k_f w_f h}{\mu}\frac{\partial P}{\partial x} = \frac{k_{eff} w_{eff} h}{\mu}\frac{\partial P}{\partial x} \Rightarrow k_f w_f = k_{eff} w_{eff} \tag{2-7}$$

$$k_{eff} = \frac{k_f w_f}{w_{eff}} \tag{2-8}$$

Initially, the domain was divided into 25 uniform blocks in the *x*-direction, and the pseudo-fracture was modeled in the middle block (Figure 2-8). The *Hydraulically-Fractured Wells Wizard* was used to add local refinement in the *x* and *y* directions around the fracture, where high resolution is needed. While the pseudo-fracture approach greatly reduced numerical instability, it did not eliminate it completely. Although crashes were much more infrequent than with the explicit fracture model, they still occurred sporadically. Numerical stability problems were especially likely to occur when diffusion and dispersion were included in the model, and reaching the target production pressure during primary depletion still required gradual reduction of the well's bottomhole pressure. However, stable runs were achieved with a pressure reduction period of only 22 simulation days, as opposed to the 100 days needed in Chen et al.'s (2013) model.

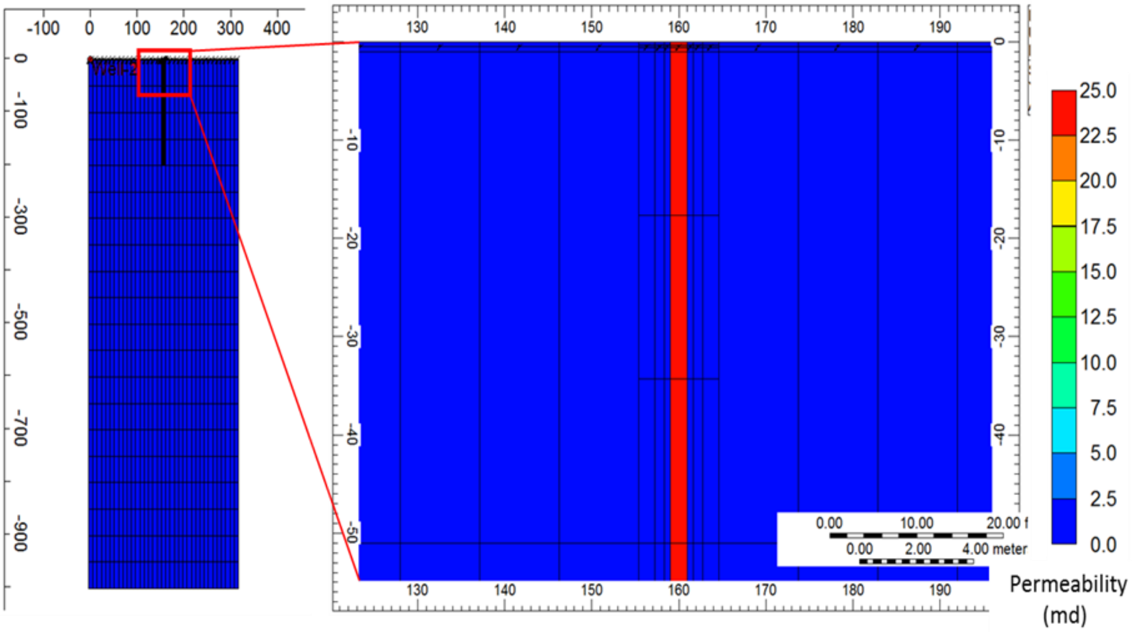

Figure 2-8. Pseudo-fracture modeling

Numerical instability increased when too much local refinement was applied around the fracture. Over-discretizing the domain caused numerical stability issues when a grid block experienced large changes in pressure and/or composition from one timestep to the next. However, as Section 3.9 will discuss, under-discretizing significantly affected the accuracy of the model and the simulation results. The decision was made to bypass the *Hydraulically-Fractured Wells Wizard* entirely and to manually design a pseudo-fracture model that would maximize resolution close to the fracture while minimizing numerical instability. A locally-refined gridding scheme was devised around a 2-ft.-wide fracture. In the x-direction, the grid blocks became wider as they got farther away from the fracture, where less resolution is needed. In the y-direction, the blocks had the same length up the fracture half-length ($0 < y < 200$ ft.), and became progressively longer as they approached the boundary ($200 < y < 1{,}000$ ft.). The permeability of the 2-ft.-wide pseudo-fracture was calculated by Eq. 2-8 assuming a fracture permeability of 10,000 mD. As Figure 2-9 shows, the pseudo-fracture approach proved to be an excellent approximation of fluid flow into the actual fracture, with the added benefits of increased numerical stability and simulation run time. Effective porosity was not calculated because, as Figure 2-10 shows, fracture porosity has a negligible effect on recovery. Therefore, the original fracture porosity of 43% was assigned to the pseudo-fracture. Additional research on numerical methods to solve hydraulically-fractured reservoir models is presented in Chapter 4.

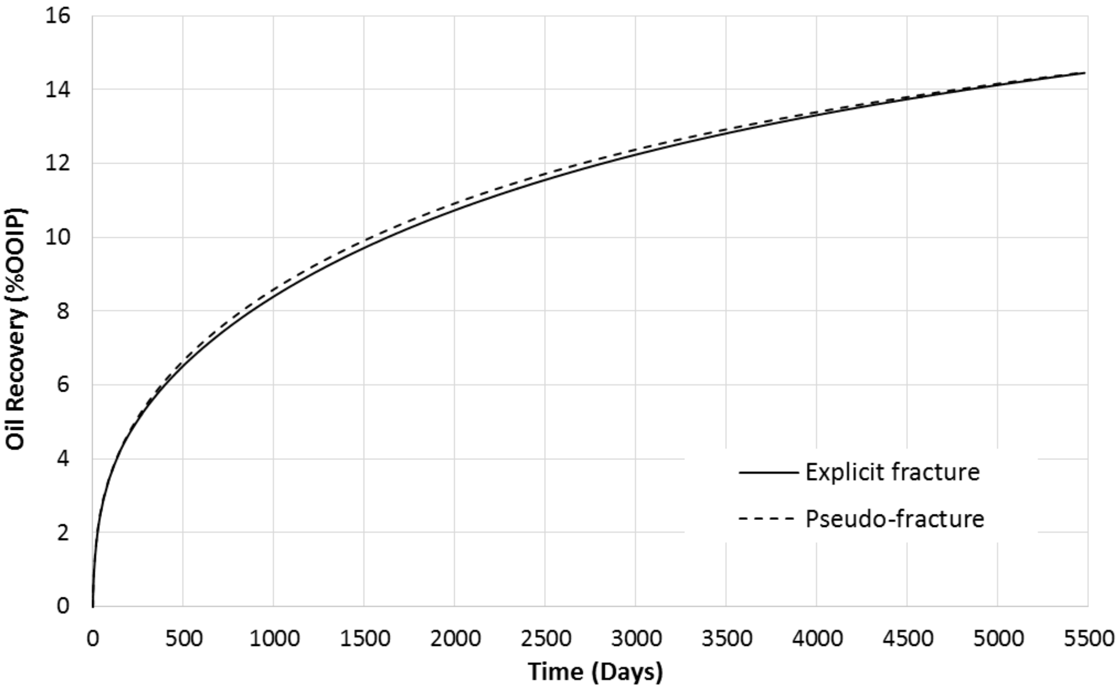

Figure 2-9. Comparison of pseudo and explicit fractures

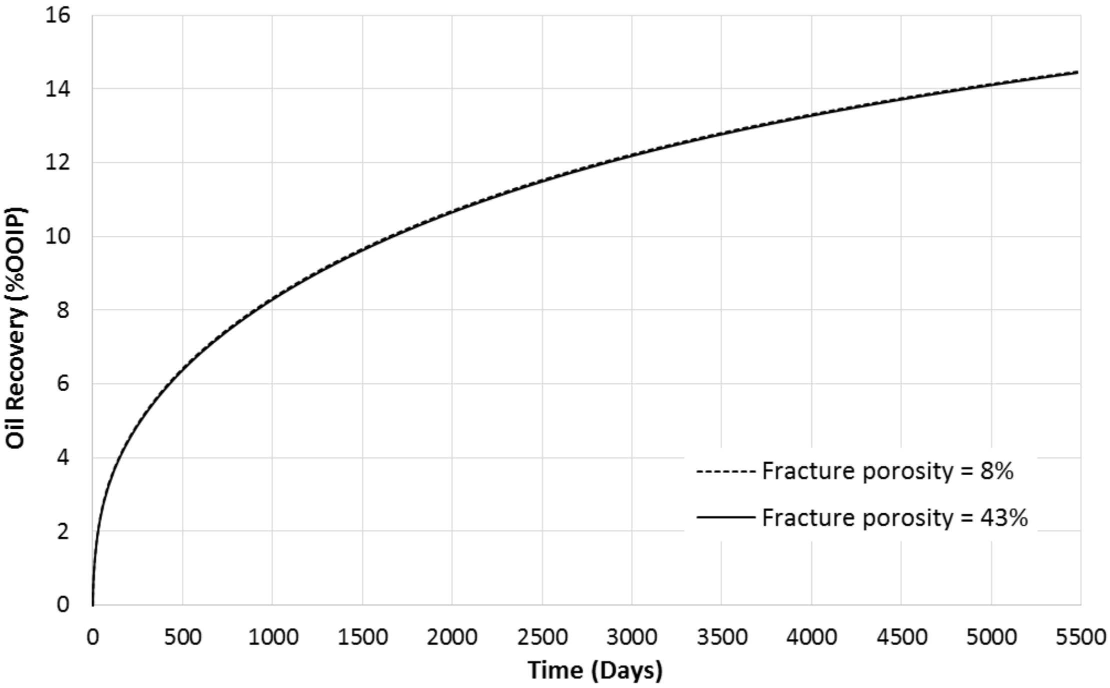

Figure 2-10. Effect of fracture porosity on oil recovery

2.2.2. Reservoir Permeability

The permeability of the Middle Bakken is largely consistent across different studies. As Table 2-7 shows, matrix permeability is usually assumed to be in the 10 μD (0.01 mD) range. A permeability of 0.01 mD was assigned to the matrix, in the lower end of the range given by Sonnenberg and Pramudito (2009). However, Kurtoglu and Kazemi (2012) note that permeability from core measurements is on the order of 10^{-4} mD, one hundred times lower. Therefore, they conclude that field measurements of ~0.01 mD must include the contribution of natural fractures. According to Sonnenberg and Pramudito (2009), natural fractures caused by structural tectonics and regional stress are important conduits for hydrocarbons in the Bakken. Kurtoglu and Kazemi (2012) describe the presence of interconnected micro-fractures as “the main contributing factor to flow to the well.” The dual-porosity nature of the reservoir was incorporated into the single-porosity model by including five 2-ft. wide “natural” fractures connected perpendicularly to the main hydraulic fracture; a permeability of 1 mD was assigned to these grid blocks. Figure 2-11 shows the gridding scheme and permeability field close to the fracture. The full reservoir grid can be found in Appendix II.

Table 2-7 – Middle Bakken permeability from different studies

Study	Permeability (mD)
Clark (2009)	0.05
Shoaib and Hoffman (2009)	0.015
Sonnenberg and Pramudito (2009)	0.01 - 0.04
Wang et al. (2010)	0.04
Chen at al. (2013)	0.01
Yu et al. (2014)	0.005

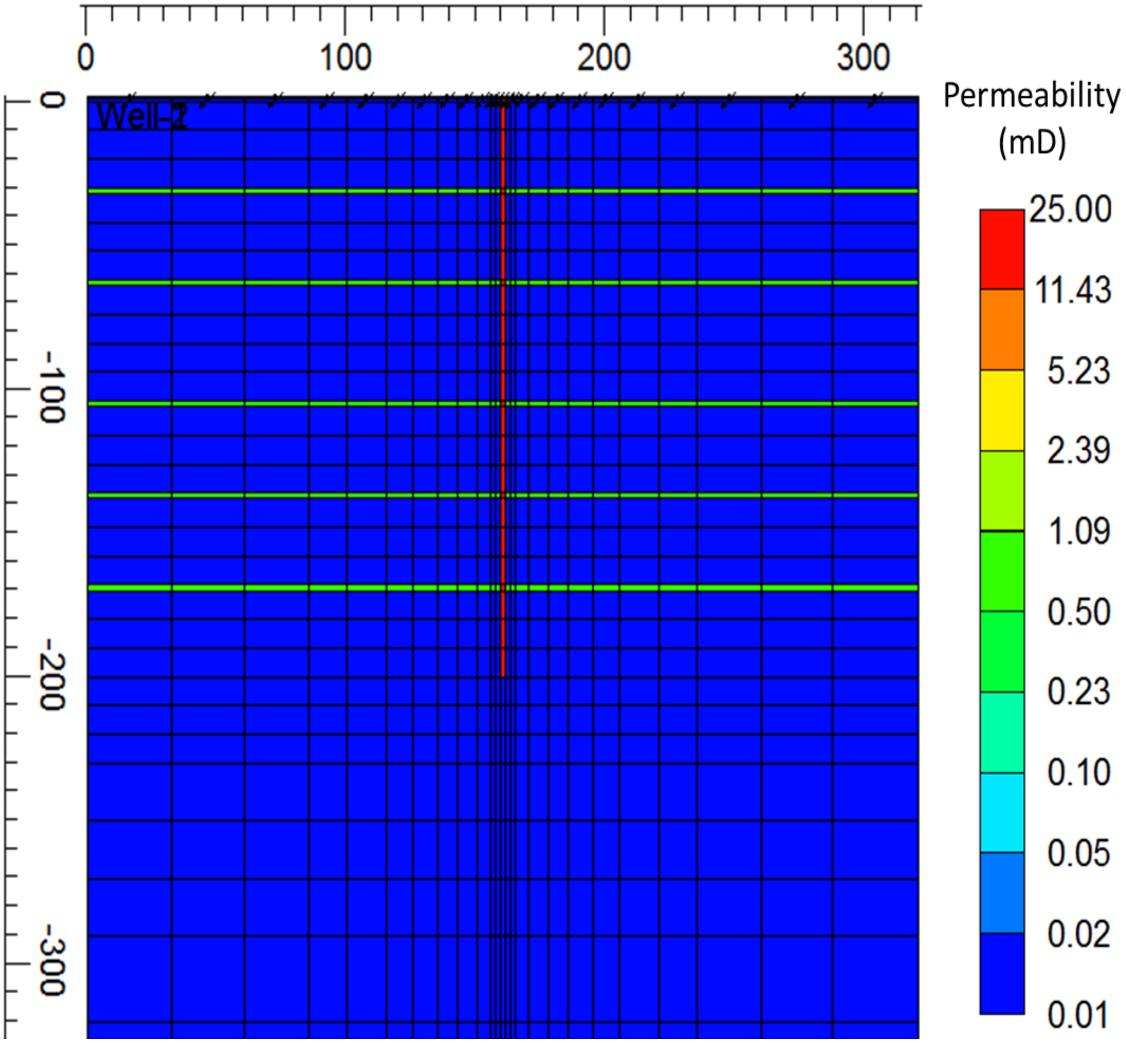

Figure 2-11. Gridding and permeability field close to the fracture

2.2.3. Relative Permeability

The oil-water and liquid-gas relative permeability curves were sources of significant uncertainty in this study. Relative permeability in ultra-tight oil reservoirs is extremely hard to measure and has a significant impact on recovery projections by numerical reservoir simulators (Yu et al., 2014). Previous studies of CO_2 injection in the Bakken have estimated relative permeability by different approaches. Yu et al. (2014) obtained their relative permeability curves by history-matching Bakken production data, and found the rock to be slightly water-wet. Wang et al. (2010) calculated their permeability values based on a correlation for water-wet dolomites. Shoaib and Hoffman (2009) included their relative permeability data in their paper, but did not mention its origin, while Chen et al. (2013) made an assumption in this regard. The oil-water and gas-liquid relative permeability curves for these studies are shown in Figures 2-12 and 2-13.

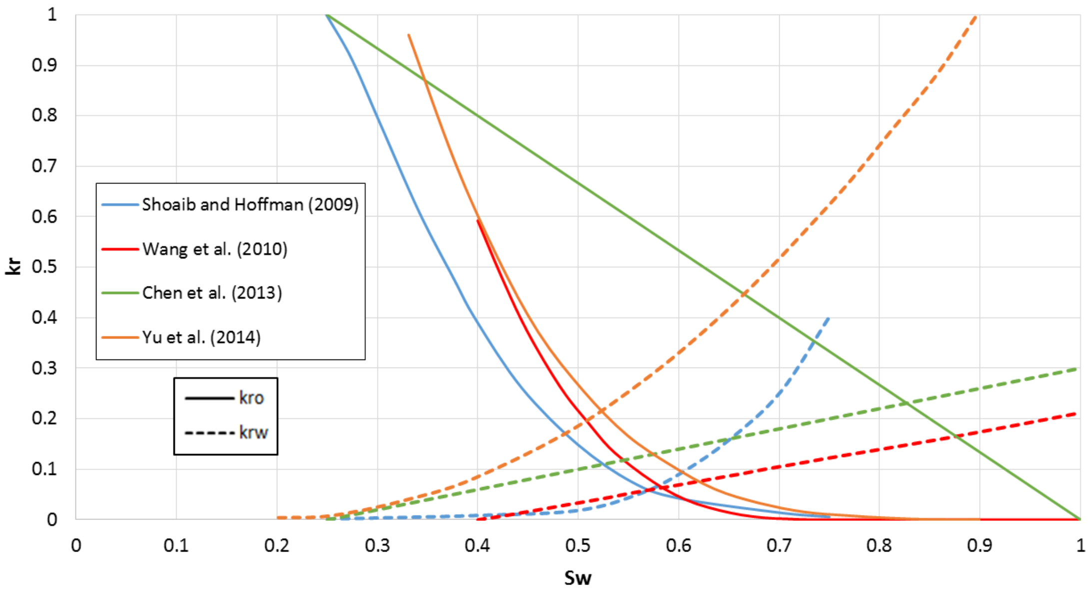

Figure 2-12. Oil-water relative permeability curves for different studies

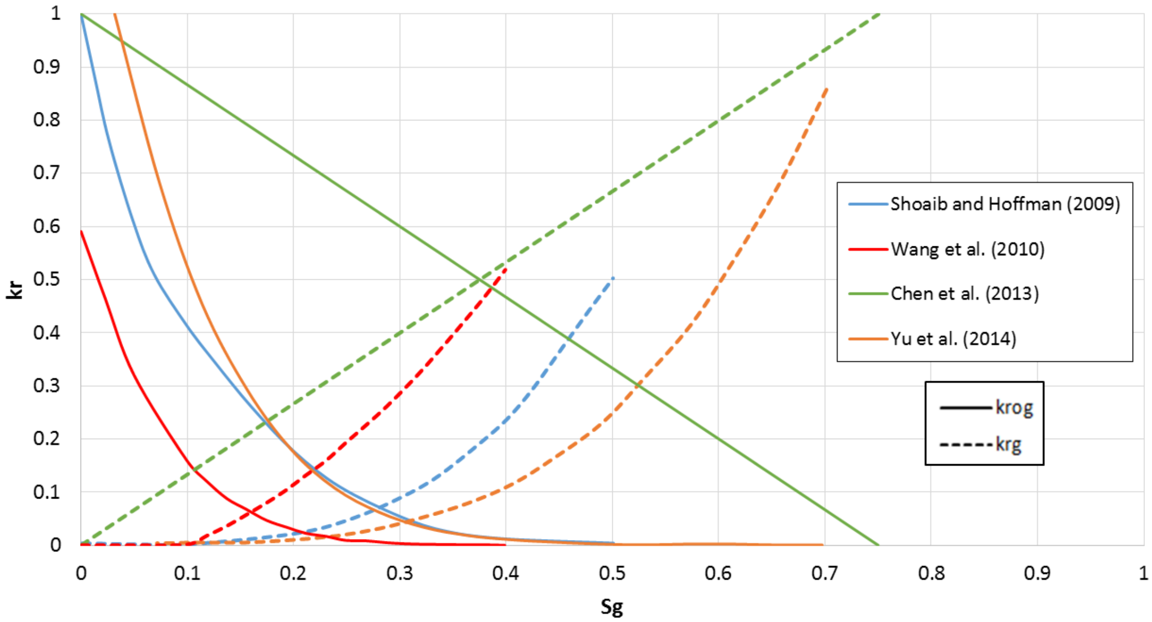

Figure 2-13. Gas-liquid relative permeability curves for different studies

According to Wang et al. (2012), Bakken shale cores are typically oil-wet or intermediate-wet. Shuler et al. (2011) characterize the Middle Bakken as oil-wet or mixed-wet with high oil saturations (between 75% and 90%). These wettability conditions are most closely represented by Yu et al.'s (2014) curves. Furthermore, their values were deemed to be the most reliable because they were obtained by history-matching production and pressure data. For this study, Yu et al.'s (2014) data was fit to Corey-Brooks models (Eq. 2-9 through 2-11) and tweaked slightly to facilitate its input into CMG GEM. Eq. 2-9 through 2-11 can be adapted to fit gas-liquid relative permeability data.

$$k_{rw} = k_{rw}^{o} S^{n} \tag{2-9}$$

$$k_{ro} = k_{ro}^{o} (1-S)^{m} \tag{2-10}$$

Where k_{ro}^{o} and k_{rw}^{o} are the endpoint oil and water relative permeabilities, and

$$S = \frac{S_w - S_{wr}}{1 - S_{or} - S_{wr}} \tag{2-11}$$

It should be noted that in Yu et al.'s (2014) data the residual water saturation is not equal to the critical water saturation. The endpoint oil relative permeability is not at the residual water saturation (S_{wr}) of 0.20, but at the critical saturation (S_{wcrit}) of 0.325. Therefore, the normalized water saturation (S) for the oil relative permeability curve was calculated with respect to S_{wcrit} instead of S_{wr}. Water saturations between S_{wr} and S_{wcrit} were assumed to have relative permeability values of 1 for oil and 0 for water. Table 2-8 shows the Corey-Brooks constants used in this study.

Table 2-8 – Corey-Brooks constants for relative permeability curves

Oil-Water Relative Permeability (as a function of S_{w})	
Residual water saturation, S_{wr}	0.2
Critical water saturation, S_{wcrit}	0.325
Residual oil saturation, S_{or}	0.1
Endpoint water relative permeability k_{rw}^{o}	1
Endpoint oil relative permeability, k_{ro}^{o}	1
Exponent for calculating k_{rw}, n	2
Exponent for calculating k_{ro}, m	3.5
Gas-Liquid Relative Permeability (as a function of S_{l})	
Residual gas saturation, S_{gr}	0.03
Critical gas saturation, S_{gcrit}	0.07
Endpoint gas relative permeability, $k_{\text{rog}}^{\text{o}}$	1
Endpoint liquid relative permeability, k_{rg}^{o}	0.85
Exponent for calculating k_{rog}, n	5.75
Exponent for calculating k_{rg}, m	3.15

Two relative permeability zones were considered: matrix and fracture. The matrix was assigned the relative permeability properties discussed thus far. The proppant in the fracture was assumed to have much more favorable flow conditions, so it was assigned linear relative permeability curves with the same endpoints and residual saturations as the matrix, but with Corey-Brookes exponents (*m* and *n*) of 1. Figures 2-14 and 2-15 show this study's relative permeability curves. While the importance of capillary pressure due to the low permeability of the matrix is acknowledged, capillary forces were not incorporated into the model due to lack of core data. To the best of our knowledge, none of the studies cited in this work have included capillary pressure in their reservoir models.

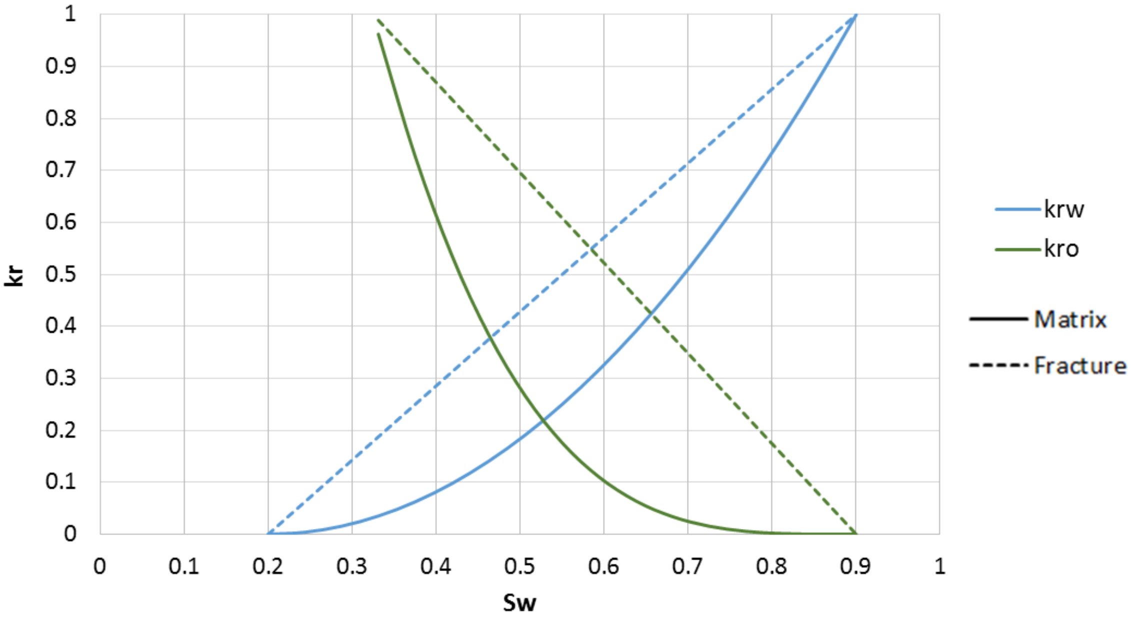

Figure 2-14. Oil-water relative permeability curves

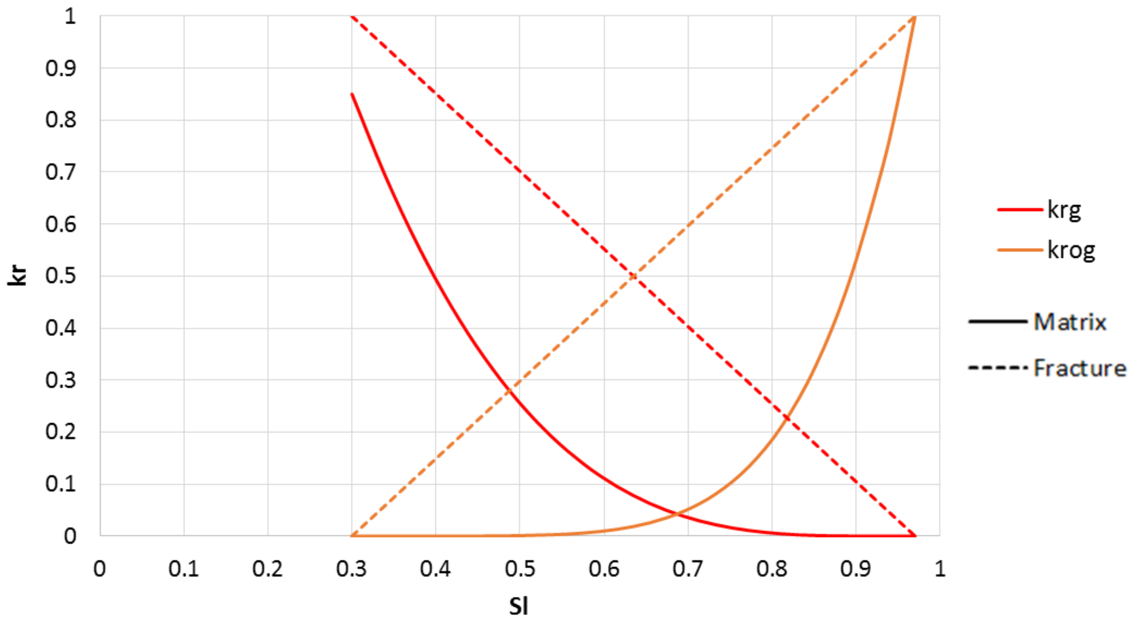

Figure 2-15. Gas-liquid relative permeability curves

2.2.4. Domain Properties

Properties for the reservoir model were obtained from the literature and compared with similar studies. A porosity value of 8% was used, which is consistent with studies from Shoaib and Hoffman (2009), Wang et al. (2010) and Chen et al. (2013) (7.5%, 7.5% and 8%, respectively). As previously discussed, the hydraulic fracture was assumed to have a permeability of 10,000 mD (modeled as 25 mD), and the natural fractures were assigned a 1-mD permeability. A permeability of 0.01 mD was used for the matrix. According to Clark (2009), the matrix is at irreducible water saturation, so an initial water saturation of 20% was assumed; this is consistent with values used by Clark (2009) and Yu et al. (2014) (25% and 21%, respectively). Because of the variable thickness of the Bakken, a nominal value of 10 ft. was used. Results in this study are presented in terms of the percentage of the model's OOIP (original oil in place) that was recovered, so the actual thickness of the reservoir is not important. Even if actual volumes in stock tank barrels were to be used, flow geometry allows the domain to be extrapolated in order to accommodate thicker parts of the Bakken and any number of fractures and wells. For example, if the oil rate were 1 stb/day at the domain scale, it would be 60 stb/day for a 15-fracture well in a 20-ft.-thick part of the Bakken.[3] An isotropic dispersivity of 0.033 ft. (1 cm) was used, and the molecular diffusion coefficients are listed in Table 2-9. These molecular diffusion coefficients are the same used by Chen et al. (2013). Finally, a constant bottomhole injection pressure of 7,000 psi and a constant bottomhole producing pressure of 1,000 psi were assumed unless otherwise stated. Table 2-10 shows the full list of domain properties.

Table 2-9 – Molecular diffusion coefficients (Chen et al., 2013)

cm^2/s	**Oil**	**Gas**	**Water**
CO2	1.08×10^{-5}	1.08×10^{-3}	0
C1	1.61×10^{-5}	1.61×10^{-3}	0
C23	1.08×10^{-5}	1.08×10^{-3}	0
C46	7.53×10^{-6}	7.53×10^{-4}	0
C7P1	6.45×10^{-6}	6.45×10^{-4}	0
C7P2	4.30×10^{-6}	4.30×10^{-4}	0
C7P3	3.23×10^{-6}	3.23×10^{-4}	0

---

[3] 1 stb/day × 2 x_f × 2x width × 15 fractures

Table 2-10 – Domain properties

Property	**Value**	**Unit**
Fracture width	.005	ft
Modeled fracture width	2	ft
Matrix Permeability	.01	md
Fracture permeability	10,000	md
Fracture modeled permeability	25	md
Matrix porosity	8	%
Fracture porosity	43	%
Initial water saturation	20	%
Initial reservoir pressure	6,840	psi
Production pressure	1,000	psi
Injection pressure	7,000	psi
Reservoir temperature	241	deg F
Reservoir depth	9,500	ft
Formation compressibility	1×10^{-6}	psi^{-1}
Pore volume	259,686 46,064	ft^3 bbl
HCPV	207,749	ft^3
OOIP	22,368	stb
OGIP	28,556	Mscf
OWIP	9,440	stb

3. Huff-and-Puff Results and Discussion

This section presents and discusses the Huff-and-Puff simulation results. It begins with a graphical description of the Huff-and-Puff process, and the selection of a "base case" against which all simulations are evaluated. The discussion includes an in-depth analysis of several design parameters: the length of the primary depletion period, the length of the injection and soaking periods, the number of cycles, and the composition of the injection gas. An analysis of the role of molecular diffusion, matrix permeability, natural fracture conductivity and domain discretization is also presented, as well as a comparison between one and two-fracture configurations.

3.1. THE HUFF-AND-PUFF PROCESS

As previously discussed, Huff-and-Puff is a cyclical process in which an injection-soaking-production sequence is repeated over the life of the well. The following figures illustrate the Huff-and-Puff process for a 3-cycle treatment, in which every cycle consists of 30 days of injection, 30 days of soaking, and 200 days of production. All figures are zoomed in around the near-fracture region ($0 > x > 320$ ft., and $0 > y > 380$ ft.). A primary depletion period, shown in Figure 3-1, precedes the first Huff-and-Puff cycle. At first, the reservoir is at its initial pressure of 6,840 psi. After 500 days of primary depletion, pressure in the near-fracture and near-wellbore region has dropped close to the bottomhole production pressure of 1,000 psi. At that point, CO_2 is injected into the formation for 30 days at a constant bottomhole pressure of 7,000 psi. As Figure 3-2 shows, the near-fracture region is re-pressurized, with the natural fractures serving as conduits for the CO_2 to move deep into the formation. The injection pressure is large enough for first contact miscibility to occur, so CO_2 and the reservoir fluids mix into a single phase upon contact.

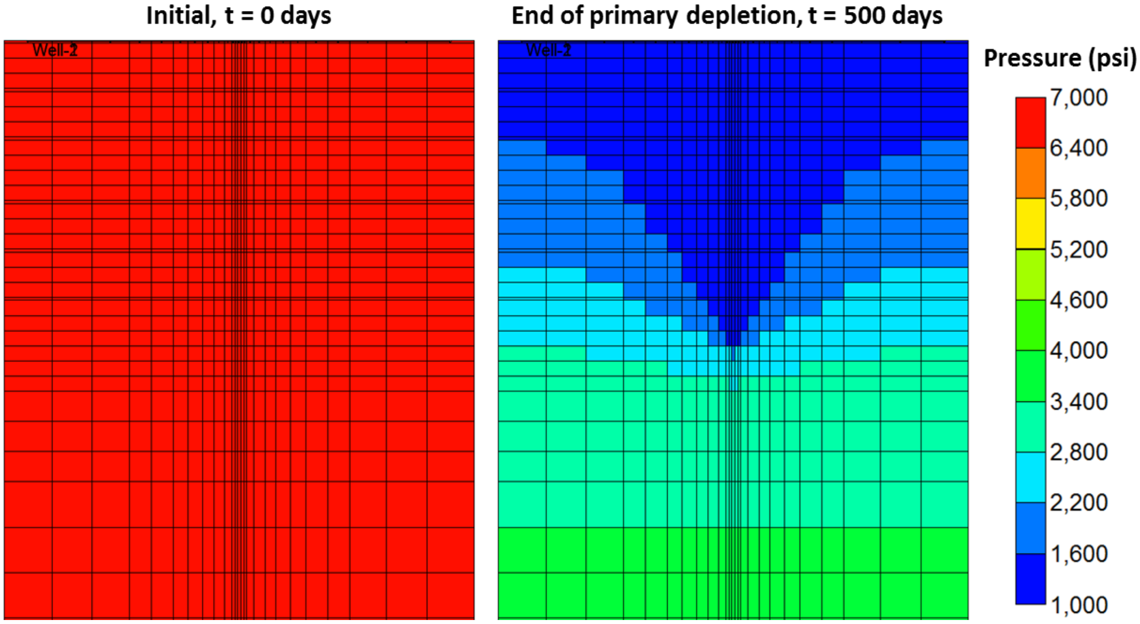

Figure 3-1. Reservoir pressure during primary depletion

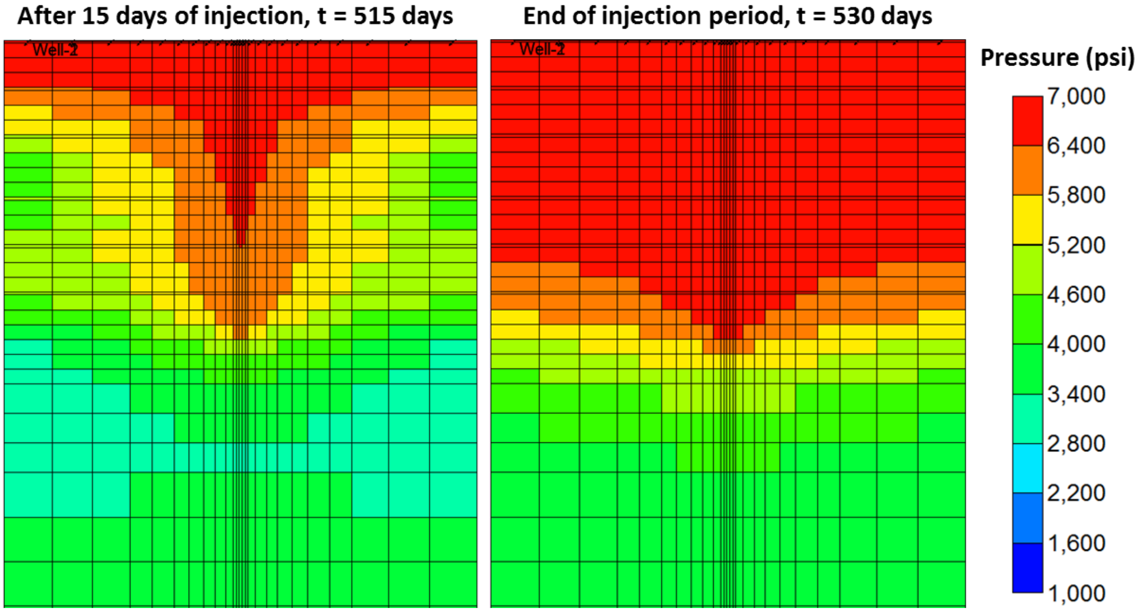

Figure 3-2. Reservoir pressure during injection period

The injection period is followed by a 30-day soaking period, shown in Figure 3-3. The purpose of the soaking (or waiting) period is to allow for CO_2 to diffuse into the formation and mix with the reservoir fluids. Figure 3-3 shows the pressure diffusion during the waiting period, while Figure 3-4 shows the diffusion of CO_2 into the formation.

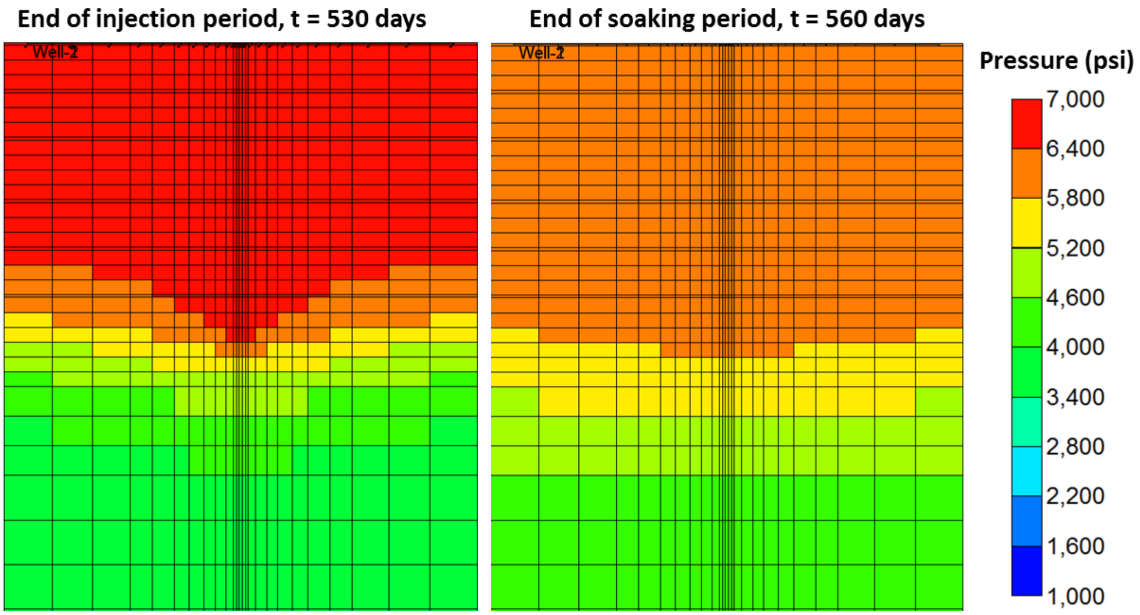

Figure 3-3. Reservoir pressure during soaking period

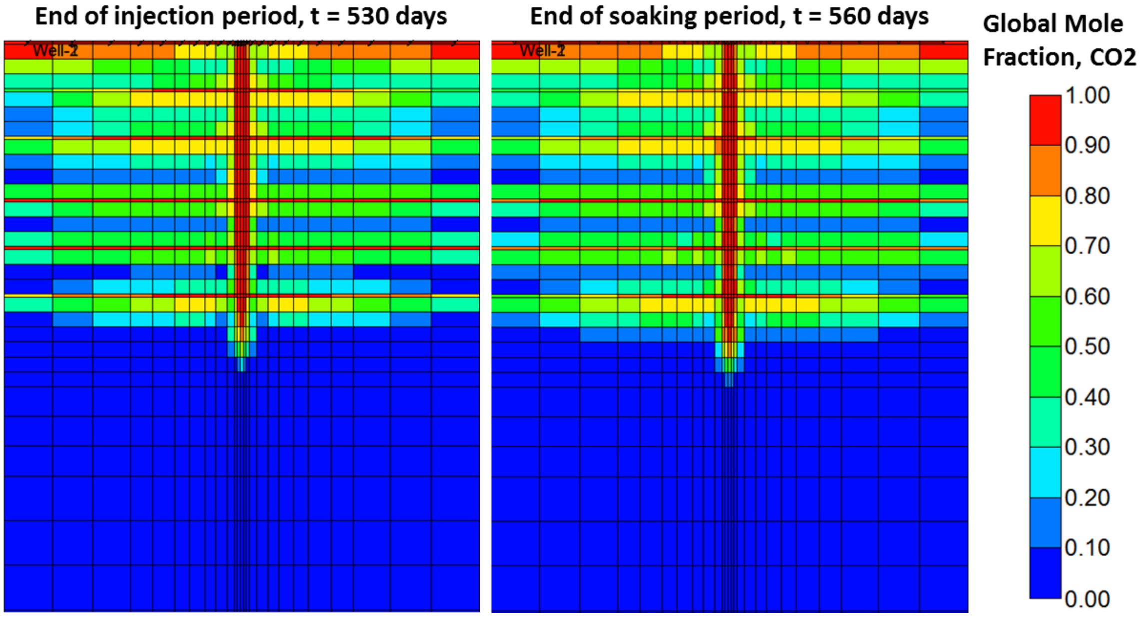

Figure 3-4. CO_2 global mole fraction during soaking period

Finally, the well is opened again to production (Figure 3-6). The re-pressurization of the reservoir (Figures 3-2 and 3-3) and the reduction in oil viscosity as a result of mixing with the CO_2 (Figure 3-5) enhance the oil rate during the production period. Average reservoir pressure increases from 4,200 to 5,300 psi following the injection and soaking periods, and there is an evident reduction in oil viscosity in the near-fracture region. After 200 days of production, CO_2 is once again injected into the formation and the process is repeated several times over the life of the well.

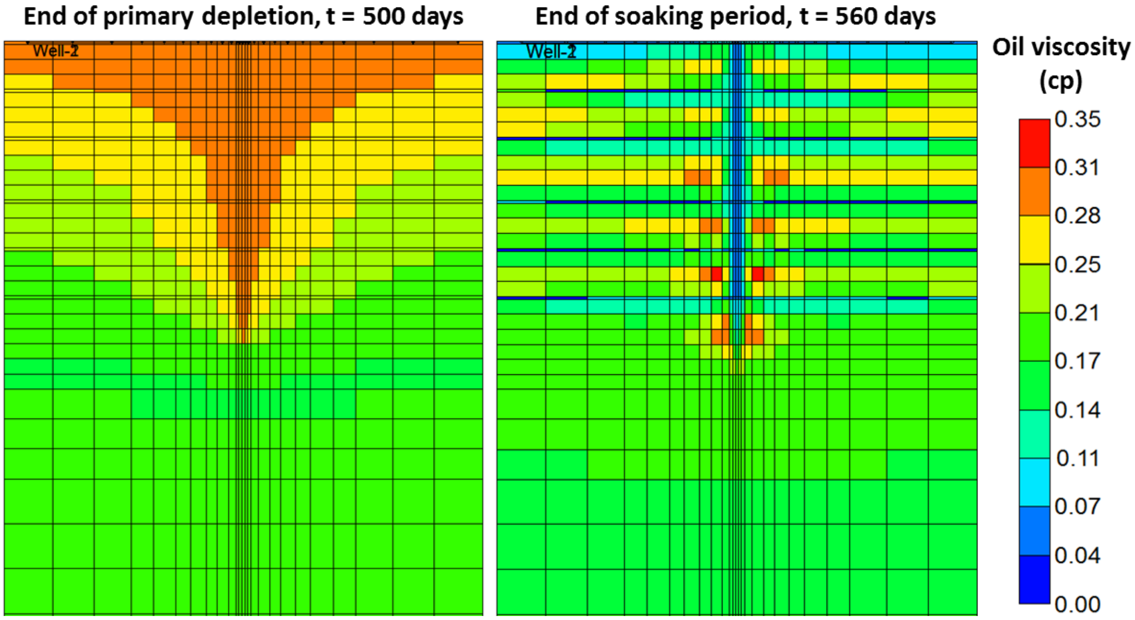

Figure 3-5. Oil viscosity after CO_2 injection

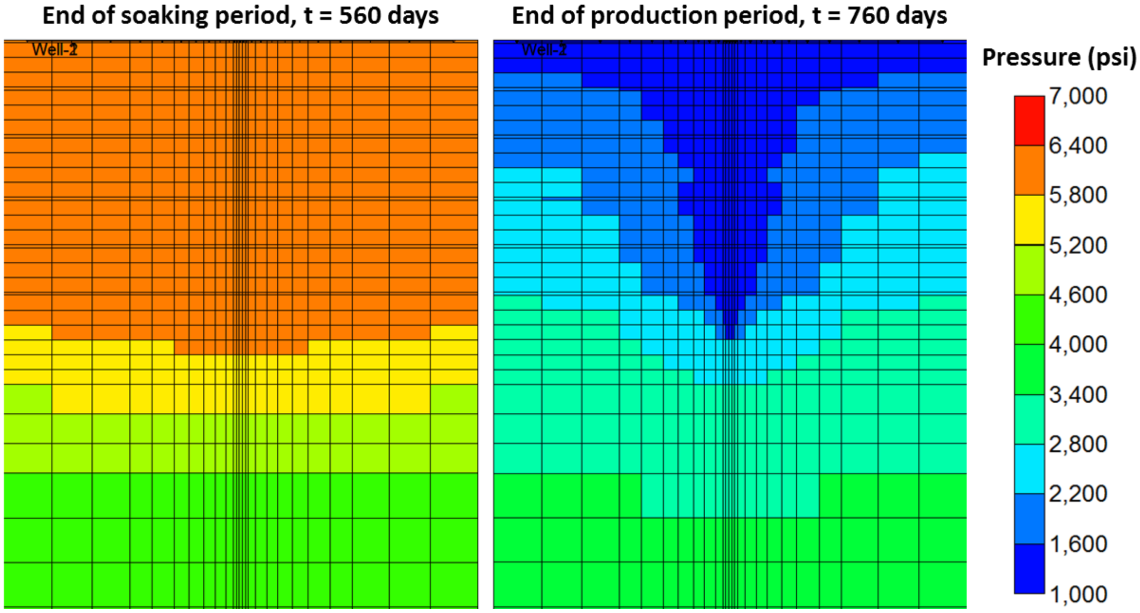

Figure 3-6. Reservoir pressure during production period

3.2. BASE CASE

The objective of CO_2 Huff-and-Puff, or any enhanced oil recovery method, is to recovery additional oil beyond what is produced by primary depletion. Therefore, a baseline must be established to assess the effectiveness of the Huff-and-Puff process. This "base case" consists of primary production for a period of 15 years, without injection of any kind, at a constant bottomhole pressure of 1,000 psi. The 15-year period was chosen by trial and error based on a study by Clark (2009), who found that roughly 75% of total production in Bakken wells occurs above the bubble point. As Figure 3-7 shows, if recovery after 15 years is assumed to be the ultimate recovery, cumulative production is 77% of the EUR when the average reservoir pressure reaches the bubble point (2,872 psi). Figure 3-8 shows the cumulative recovery and oil rate for the base case after 15 years (~5,500 days). The model exhibits the characteristic behavior of a fractured reservoir whose pressure drops below the bubble point: a high initial oil rate followed by a steady decline. The high initial oil rate is due to linear flow inside the natural fractures, and the decline begins as reservoir pressure falls below the bubble points and gas starts coming out of solution (Tran et al., 2011).

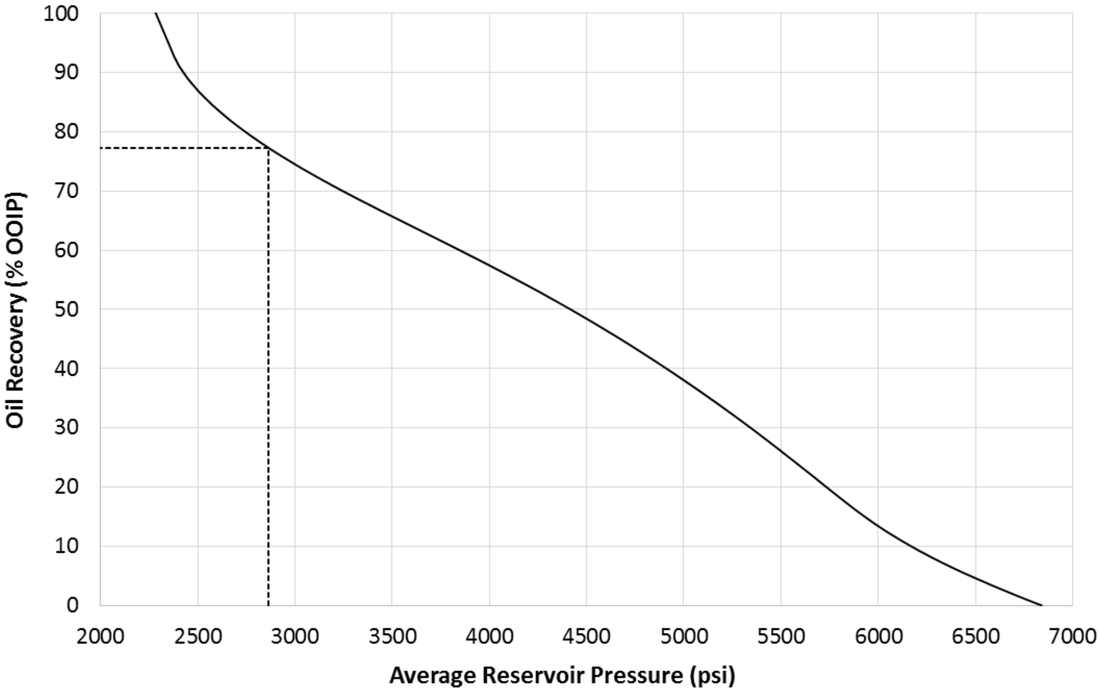

Figure 3-7. Average reservoir pressure vs. % EUR

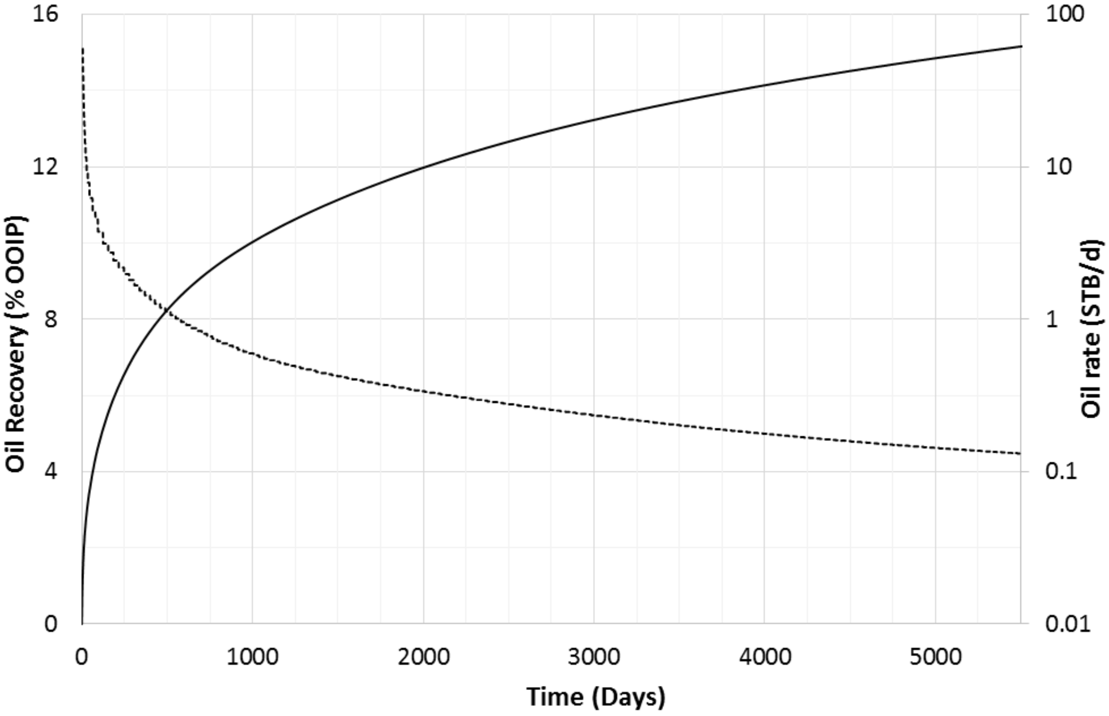

Figure 3-8. Base case: ultimate recovery and oil rate

As Figure 3-8 shows, the recovery factor is 15.1% after 15 years. This recovery factor might be considered slightly high by some estimations, but in practice it depends largely on economic considerations. Kurtoglu et al. (2013) estimated the recovery factor of Bakken wells to be between 3 and 12%, while Clark (2009) identified a weak bi-modal distribution with peaks at 6 and 15%. It is worth remembering that the ~0.01 mD matrix permeability usually found from well-testing (and which is used in this study) accounts for the presence of natural fractures, as described by Kurtoglu and Kazemi (2012). Unlike other studies, which have been done at the field scale using a stimulated reservoir volume (SRV) approach, natural fractures were modeled explicitly in order to understand fluid behavior in the near-fracture region. As explained in the *Computational Domain* section (Section 2.2), a single porosity model was used and natural fractures were modeled as thin high-permeability grid blocks connected perpendicularly to the main hydraulic fracture. It is possible that the permeability of the matrix and natural fractures may have been slightly overestimated, although a 15.1% recovery factor is still reasonable. A better estimate could have been obtained by performing history-matching of production and pressure data, but the model serves the ultimate objective of this study: to obtain a qualitative understanding of the Huff-and-Puff process through quantitative simulation results. The effect of matrix and natural-fracture permeability on primary and incremental recovery will be discussed later in this chapter.

3.3. PRODUCTION PRESSURE

The bottomhole production pressure is an extremely important variable of the recovery process. It determines the pressure drawdown at the wellbore and the pressure profile in the reservoir, which significantly affect the drive mechanism, relative permeability, and miscibility conditions. Two cases were considered: one in which the reservoir was kept above its bubble point and another in which it was allowed to dip below the saturation pressure. Case 1 involved producing at 3,000 psi, higher than the fluid's saturation pressure of 2,872 psi (at 241°F), while Case 2 produced at 1,000 psi, as originally considered in the base case. Both simulations were run for 30 years without any CO_2 injection. Figures 3-9 and 3-10 show the oil rate and recovery versus time for both cases.

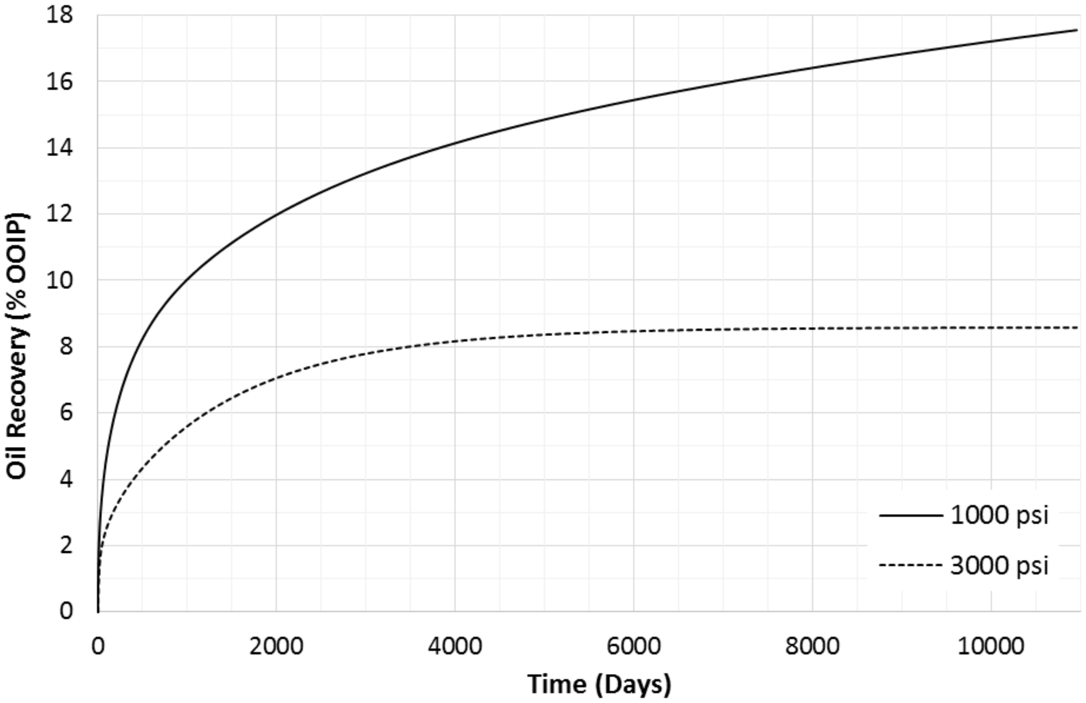

Figure 3-9. Primary recovery at different production pressures

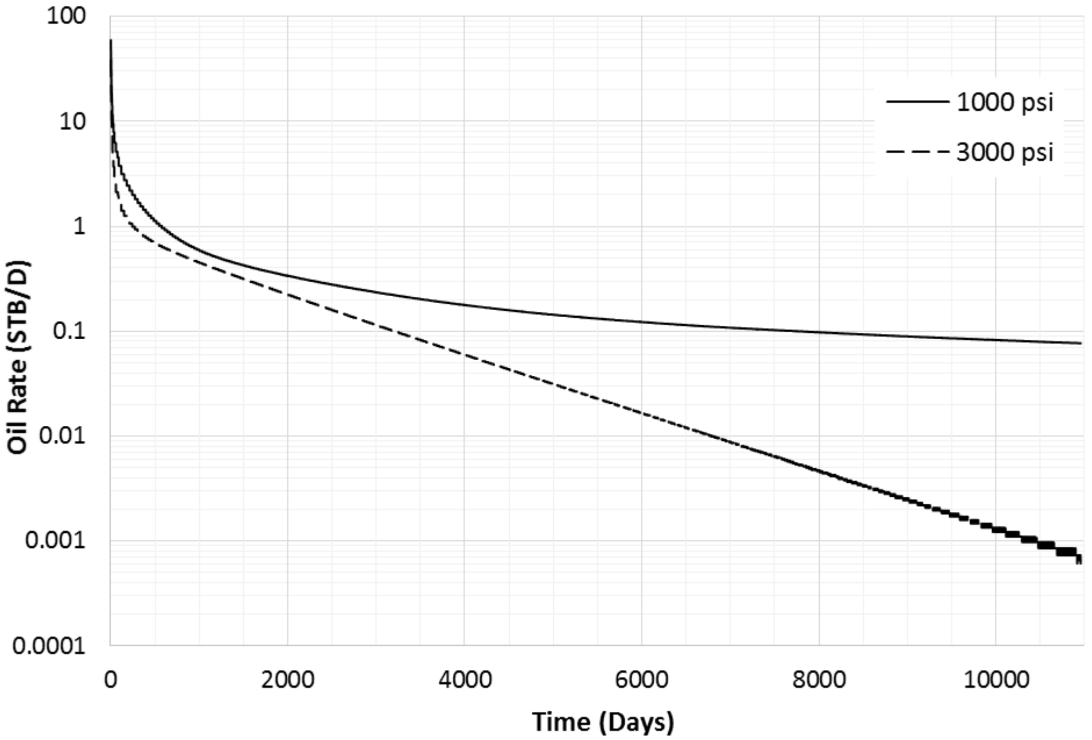

Figure 3-10. Oil rate at different production pressures

As Figure 3-9 shows, the case in which the bottomhole production pressure was set to 1,000 psi vastly outperformed the 3,000 psi case. The 1,000 psi case had an ultimate recovery of 17.6% after 30 years, vs. 8.6% of the reservoir produced at 3,000 psi. The exponential decline trend for the 3,000 psi case (straight line on a semilog plot, Figure 3-10) is indicative of single phase flow. Gas does not come out of solution, and oil is produced exclusively by oil expansion drive (Tran et al., 2011). The oil rate drops almost to zero as the oil in the near-fracture region is drained and reservoir pressure is depleted. While producing the reservoir above the bubble point has advantages in terms of relative permeability effects, there are significant benefits from producing at a lower pressure. The larger drawdown and evolved gas drive appear to compensate for the reduction in oil relative permeability. As Figure 3-10 shows, there is pressure support from the gas as it evolves from solution, driving oil production through the life of the reservoir. Furthermore, gas production is also boosted from 8.5 to 26.5% of the OGIP after 30 years.

An interesting question involves the effectiveness of Huff-and-Puff as both a single and multi-phase process. Keeping the production pressure above the MMP means that CO_2 will mix with the reservoir fluids and flow together as a single phase. As discussed in Section 2.1.4, the first-contact miscibility pressure for the fluid is roughly 3,100 psi, while multi-contact miscibility is developed at around 2,400 psi. Three cases were run at different production pressures: 1,000, 2,900, and 3,500 psi. 2,900 psi was chosen because it lies between the first-contact and multi-contact miscibility pressures and is above the bubble-point (2,872 psi), while 3,500 psi is high enough for first-contact miscibility to occur. In every instance, three Huff-and-Puff cycles were simulated, each of them consisting of 30 days of injection, 10 days of soaking, and 200 days of production. Two sets of simulations were run: one in which the production pressure was maintained constant throughout the life of the well (Figure 3-11), and another in which the well was produced at 1,000 psi during the primary depletion period and the bottomhole pressure was adjusted after the first injection period (Figure 3-12).

As Figures 3-11 and 3-12 show, even though miscibility conditions are not present while producing at 1,000 psi, the lowest production pressure (1,000 psi) vastly outperforms the 2,900 and 3,500 psi cases in both sets of simulations. Imposing a larger drawdown and developing a robust gas drive seem to outweigh the benefits of developing miscibility and having oil and CO_2 flow as a single phase.

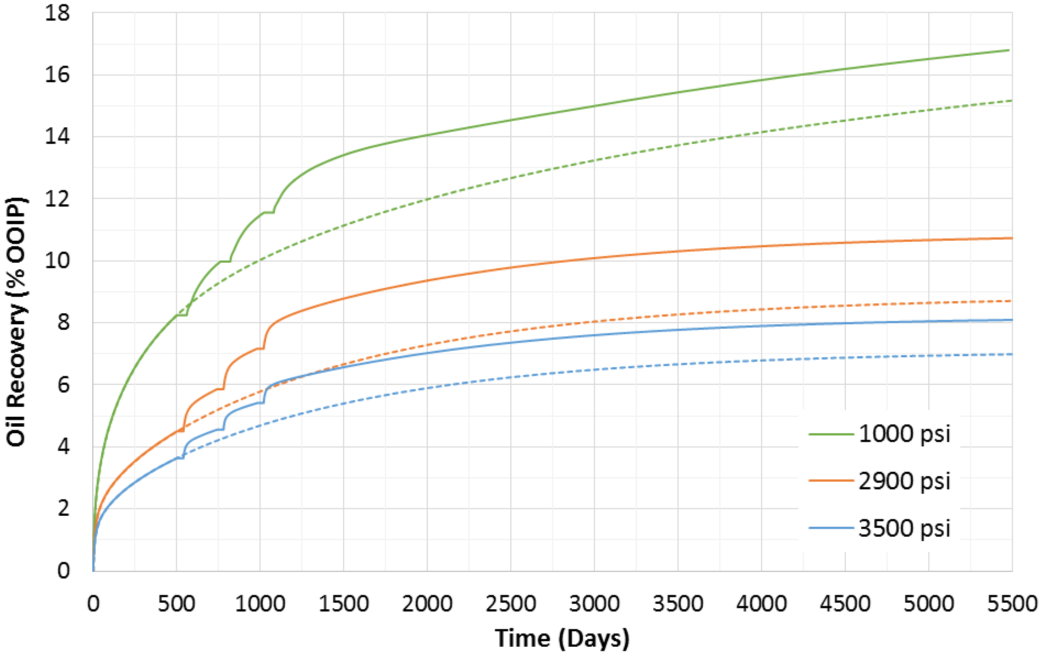

Figure 3-11. Incremental recovery at different production pressures

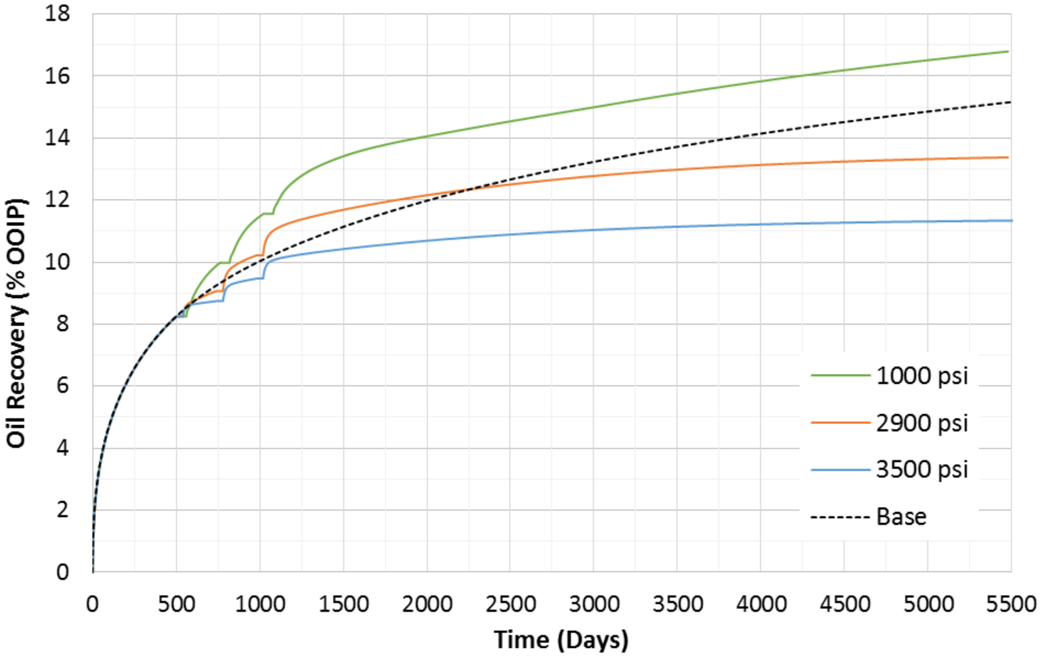

Figure 3-12. Incremental recovery at different production pressures, 1000 psi primary production pressure

3.4. LENGTH OF THE PRIMARY DEPLETION PERIOD

The ideal time in the life of a well to start Huff-and-Puff operations is an important question that remains largely unanswered. The optimal length of the primary depletion period, during which the well is allowed to naturally produce prior to the first Huff-and-Puff cycle, has not been explored by previous studies. Wang et al. (2010) began CO_2 injection from the very beginning of their simulations, Chen et al. (2013) did so after 200 days, and Yu et al. (2014) assumed a primary depletion period of five years. No reasons were given for these choices and the authors did not vary the starting time of the treatment to study its impact on recovery, so it is likely that these were simply judgment calls by the researchers.

A single-cycle Huff-and-Puff treatment was simulated for different starting times. The cycle consisted of 30 days of injection and 20 days of soaking. As previously discussed, the base case (primary depletion through the length of the simulation) shows a recovery of 15.1% of the OOIP after 5,500 days. As Figure 3-13 shows, the length of the primary depletion period has a noticeable effect on the incremental recovery of oil. The case in which Huff-and-Puff was started after 500 days had an incremental recovery of 0.9% of the original oil in place over the base case. While this might seem like a modest boost in production, it is important to remember that it is the result of a single Huff-and-Puff cycle (actual treatments consist of multiple cycles) and 0.9% of the OOIP would translate into thousands of additional barrels of produced oil[4]. Meanwhile, the case in which injection was started after 200 days produced 15.7% of the OOIP after 5,500 days, an incremental recovery of only 0.6%. Beginning the Huff-and-Puff treatment after only 30 days showed no benefits over natural depletion, and even had a negative impact on recovery early in the life of the well.

---

[4] 0.90% of OOIP = 12,880 stb. for a 15-fracture, 5,000-ft lateral in a 20-ft.-thick zone.

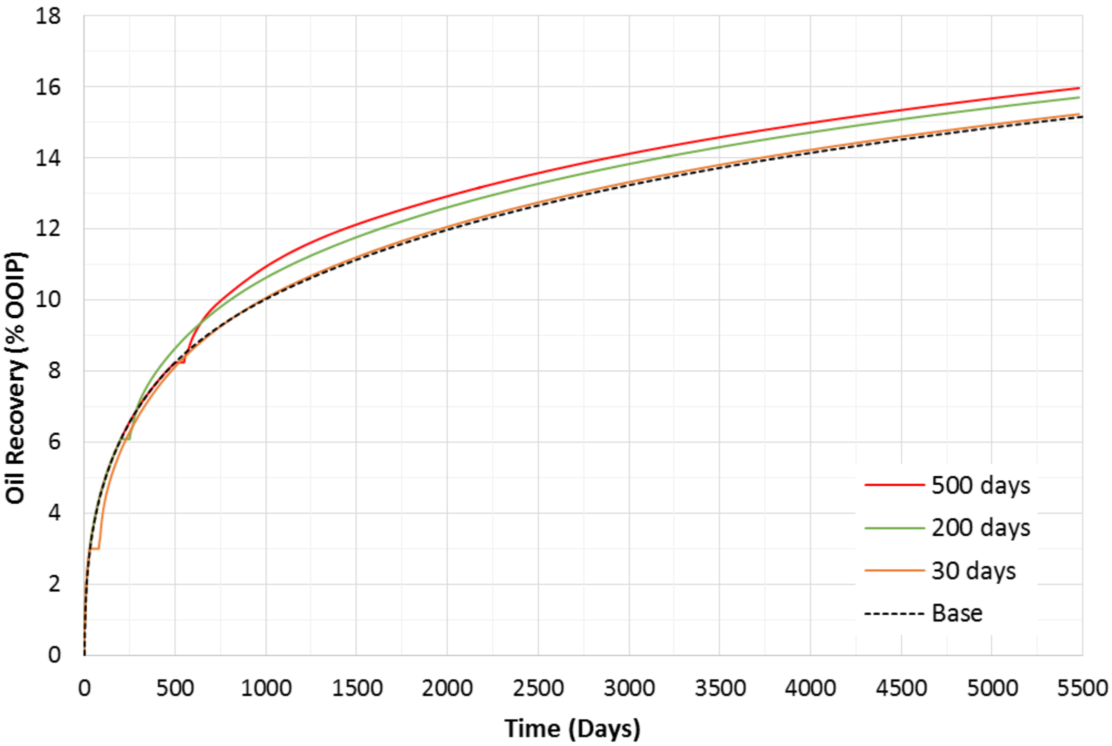

Figure 3-13. Recovery for different lengths of primary depletion period (30, 200, and 500 days)

The trend observed in Figure 3-13 indicates that delaying the start of Huff-and-Puff is beneficial to production. However, as Figure 3-14 shows, there is a point after which this is no longer the case. An additional case was run starting injection after 1,000 days of primary production. The incremental recovery was exactly the same as the case with the 500-day natural depletion period (0.9% of the OOIP). However, its net present value (NPV) would actually be lower because of the lower cumulative production (and therefore, discounted cash-flow) between days 500 and 1,000. Therefore, CO_2 injection must begin no later than the time at which the length of the primary depletion period stops affecting incremental recovery in order to maximize production without impacting the net present value. By trial and error, it was determined that the latest starting time at which recovery is affected is approximately 350 days. While reliable guidelines for identifying the optimum starting time could not be established, the main conclusion from these results is that starting the Huff-and-Puff treatment too early is detrimental to recovery, while starting it too late is only disadvantageous from a net present value standpoint.

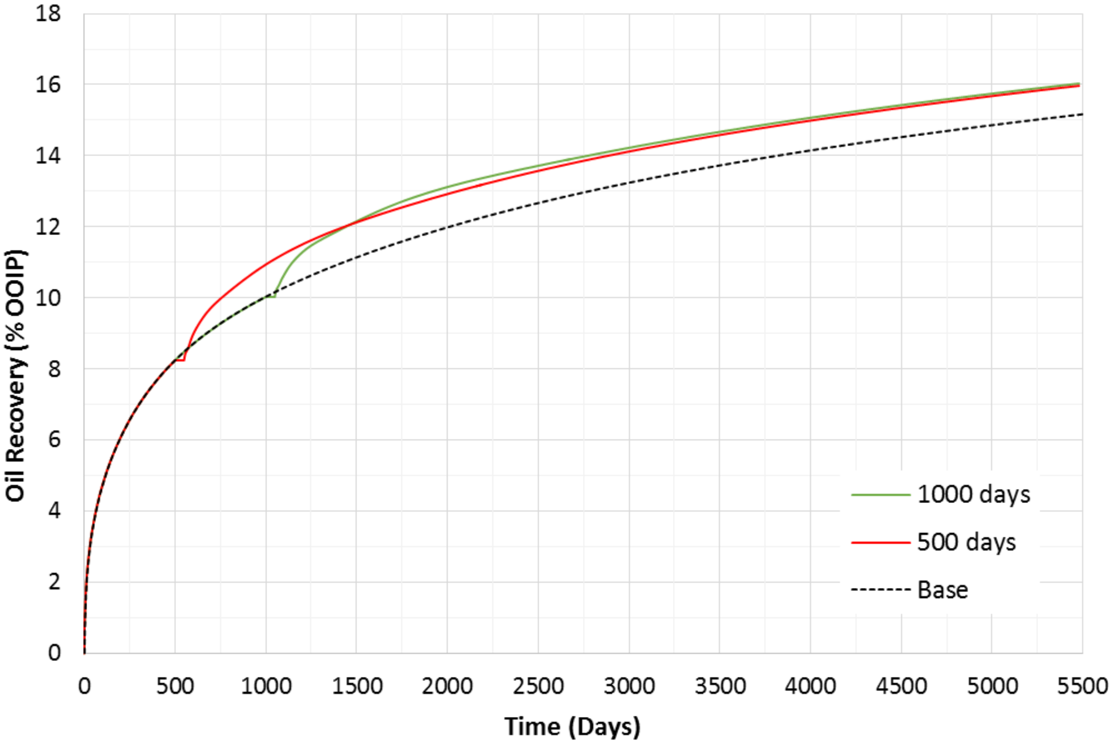

Figure 3-14. Recovery for 500 and 1000 days of primary depletion

3.5. LENGTH OF THE INJECTION PERIOD

The length of the injection period is a key component of the Huff-and-Puff process. In a sensitivity analysis of eight design criteria, Yu et al. (2014) found that the CO_2 injection rate and injection time have the largest impact on incremental oil recovery. The injection time is directly related to the volume of CO_2 injected and the degree to which Huff-and-Puff induces changes in reservoir pressure and fluid properties. A series of cases were run simulating a 3-cycle Huff-and-Puff treatment. The length of the injection period was varied from case to case, while the soaking and production periods were kept constant at 10 and 200 days, respectively. The first cycle began after 500 days of primary production, and a constant injection pressure of 7,000 psi was used. Figure 3-15 shows the results for these simulations.

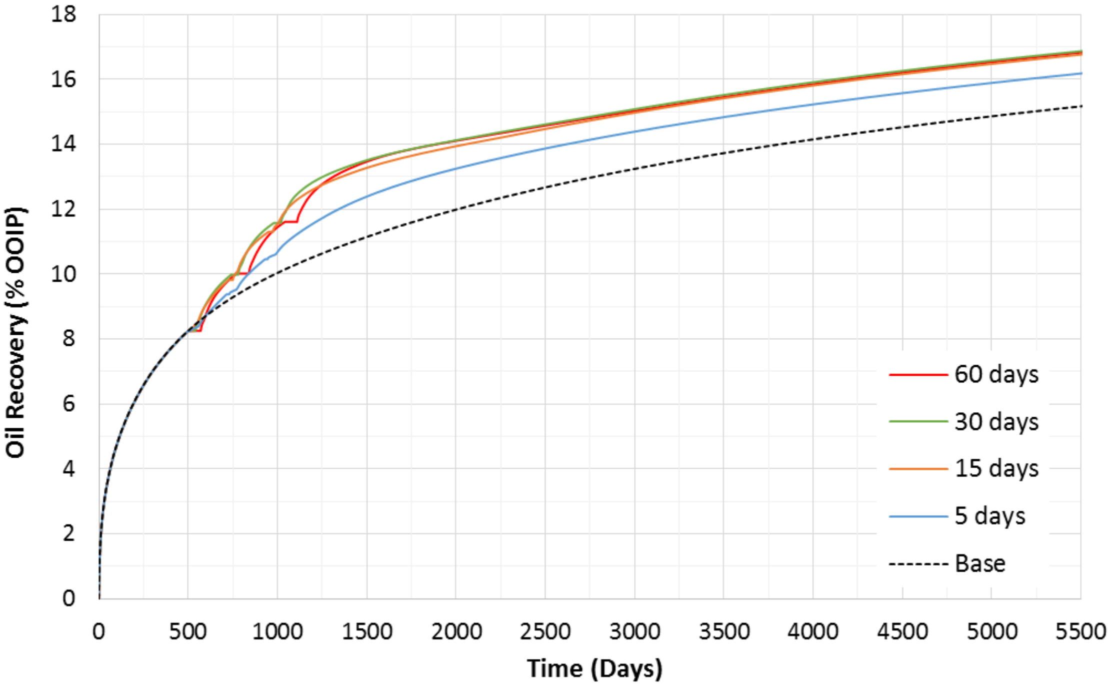

Figure 3-15. Oil recovery for different lengths of injection period, constant injection pressure

As Figure 3-15 shows, there is a marked increase in incremental recovery between 5 and 15 days of injection time. However, there are nearly no benefits from increasing the injection period from 15 to 30 or 60 days. The reason for this behavior is the pressurization of the near-wellbore region, which reduces the injection drawdown between the well and the reservoir. As reservoir pressure increases, the gas injection rate at a constant bottomhole pressure decreases. As Table 3-1 shows, there is a non-linear relationship between the injection time and the volume of gas injected. Increasing the injection time by a factor of three, from 5 to 15 days, does not triple the volume of CO_2 injected (it only yields a 62% increment). Moreover, doubling the injection time from 30 to 60 days represents only a 7% difference in CO_2 consumption. There appears to be a semi-linear relationship between the volume of CO_2 injected and the incremental recovery of oil for short injection periods. A 61% increase in the volume of gas injected (from 9,400 to 15,100 Mcf) yields roughly a 55% boost in incremental recovery (1.1 to 1.7% of the OOIP). However, doubling the volume of CO_2 injected (from 9,400 to 18,800 Mcf) does not double the incremental recovery of oil, but merely increases it by 64%. While there is a strong positive correlation between the volume of gas injected and the incremental recovery of oil, this correlation deviates from linear as pressure in the near-fracture region approaches the bottomhole pressure of the injection well.

Table 3-1 – Incremental recovery and volume of gas injected vs. injection time, constant injection pressure

Injection time (Days)	**Gas injected (Mcf)**	**Recovery after 15 years (% OOIP)**	**Incremental Recovery (% OOIP)**
Base	N/A	15.1	N/A
5	9,360	16.2	1.1
15	15,100	16.8	1.7
30	17,500	16.9	1.8
60	18,800	16.9	1.8

To further explore the relationship between injection volume and recovery a series of constant rate cases were run. Once again, a three-cycle Huff-and-Puff treatment starting after 500 days of primary depletion was simulated. The lengths of the soaking and production periods were kept constant at 10 and 200 days, respectively, and the injection time was varied from case to case. A constant injection rate of 500 Mcf/day was imposed, obtaining the results shown in Figure 3-16.

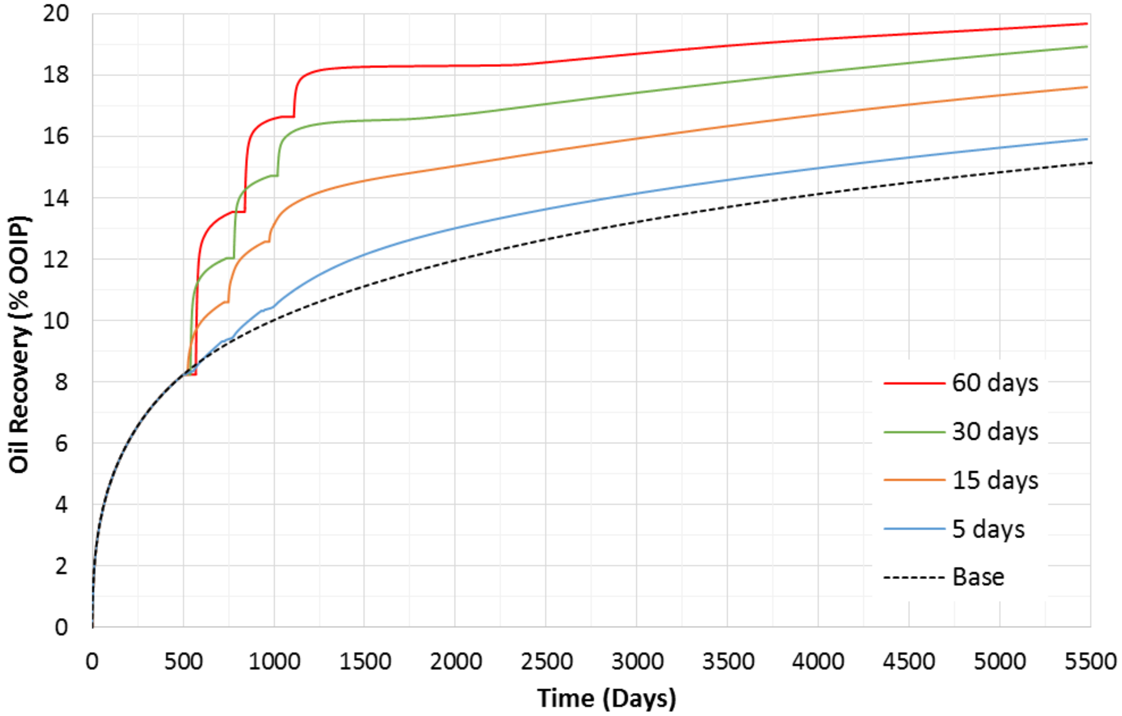

Figure 3-16. Oil recovery for different lengths of injection period, constant injection rate

As Table 3-2 shows, a similar relationship between injected volume and recovery as in the constant pressure case can be observed. Initially, a 300% increase in the injection volume (7,500 to 22,500 Mcf) yields a three-fold boost in incremental recovery (0.8 to 2.5%). However, doubling the volume from 22,500 to 45,000 Mcf only increases it by 52%, and quadrupling it to 90,000 Mcf only yields an 84% increment (from 2.5 to 4.6%).

Table 3-2 – Incremental recovery and volume of gas injected vs. injection time, constant injection rate

Injection time (Days)	**Gas injected (Mcf)**	**Recovery after 15 years (%OOIP)**	**Incremental Recovery (%OOIP)**	**Peak BHP (psi)**
Base	N/A	15.1	N/A	N/A
5	7,500	15.9	0.8	7,400
15	22,500	17.6	2.5	16,600
30	45,000	18.9	3.8	57,500
60	90,000	19.7	4.6	145,000

An important aspect to consider is that pumping large volumes of CO_2 into the reservoir at a constant rate might not be feasible from an operational standpoint. As Table 3-2 shows, injecting those volumes of gas results in extremely unrealistic bottomhole pressures. An additional test was run in order to compare constant rate to constant pressure injection under realistic operating conditions. Injecting CO_2 for three 15-day injection cycles at 7,000 psi required 15,100 Mcf of gas. The same volume of gas was pumped over three 50-day cycles at a constant injection rate of 101 Mcf per day. The rest of the Huff-and-Puff parameters were maintained the same: 500 days of primary depletion, 10 days of soaking, and 200 days of production. A 7,000-psi maximum bottomhole pressure constraint was imposed during the injection period. As Figure 3-17 shows, the recovery factor for both cases was very similar. The constant pressure case recovered 16.8% of the OOIP, compared to 16.6% by constant rate injection. Even though the same volume of CO_2 was injected into the formation in both instances, doing so faster, at a high constant bottomhole pressure appears to be slightly better for recovery.

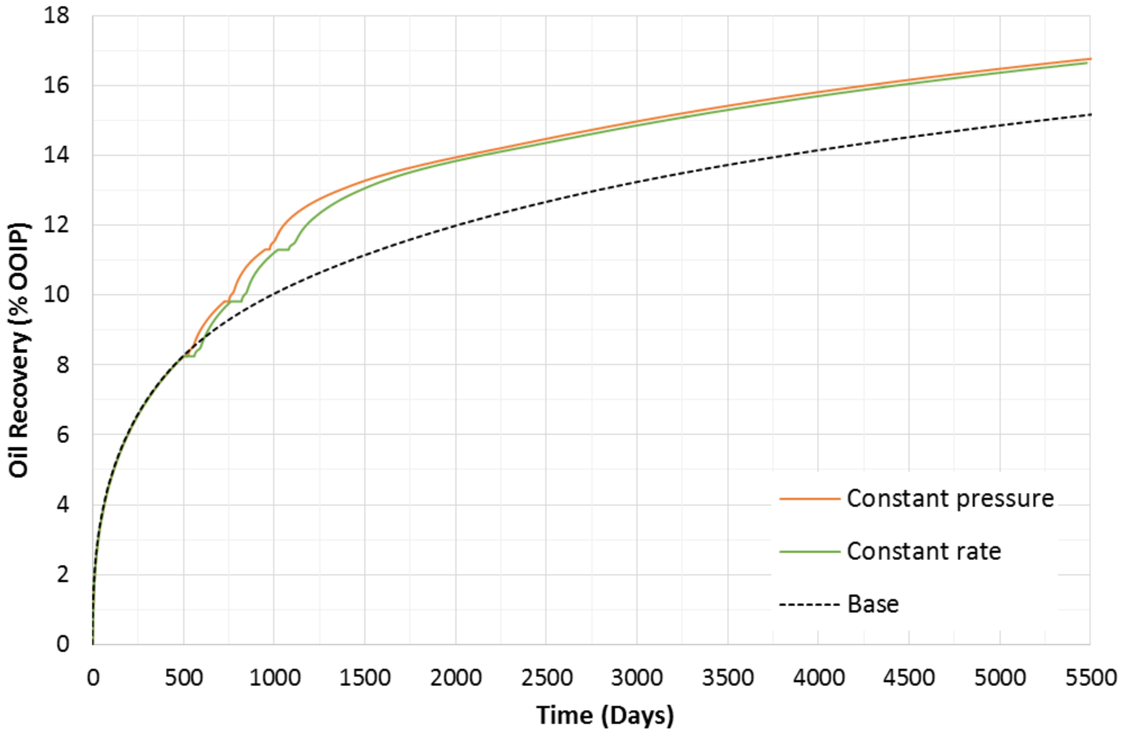

Figure 3-17. Oil recovery for constant pressure and constant rate injection

As discussed thus far, incremental oil recovery is strongly dependent on the volume of CO_2 injected, but reservoir pressure limits the volume of CO_2 that can be injected into the formation. Therefore, the optimum injection time should be dictated by the time it takes to pressurize the near-fracture region. Figure 3-18 shows a sector of the reservoir labeled as the *near-fracture region*, which is shaded in pink. The average pressure in the near-fracture region during a 60-day injection period (following 500 days of primary depletion) is shown in Figure 3-19.

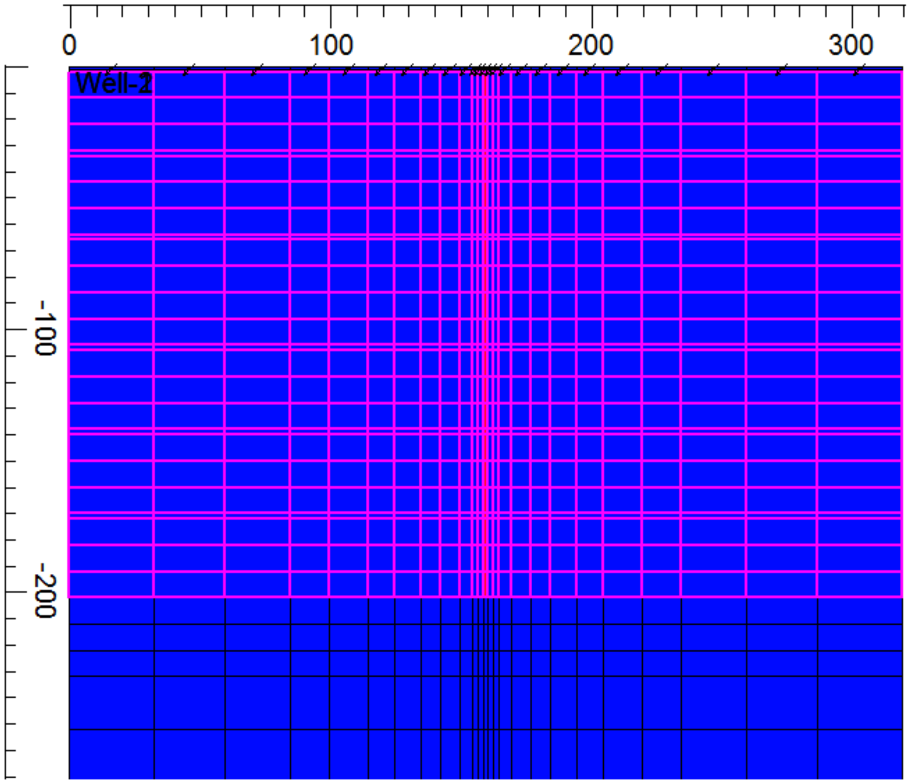

Figure 3-18. Near-fracture region (shaded in pink)

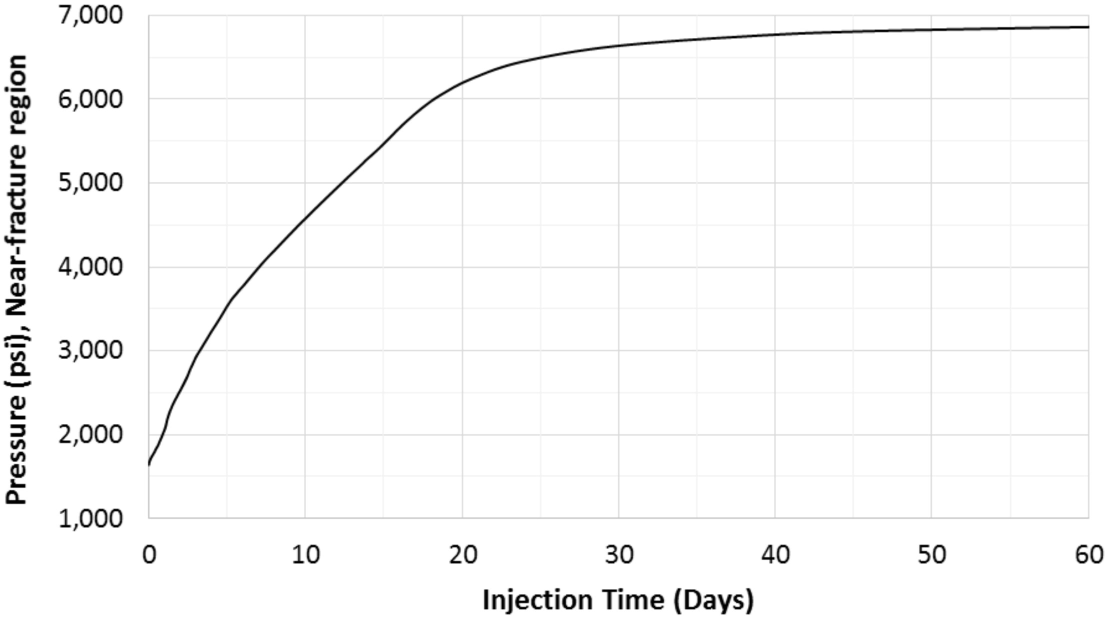

Figure 3-19. Pressure of near-fracture region during injection period

As Figure 3-19 shows, most of the pressurization occurs in the first 20 days of injection. The average pressure in the near-fracture region rises from 1,640 to 6,250 psi after 20 days, and during the next 40 days it only increases an additional 610 psi (to 6,860 psi). The behavior in Figure 3-19 explains why there are nearly no benefits in recovery from increasing the injection time from 30 to 60 days. During that time, the difference in the average pressure of the near-fracture region (where the oil is contacted and from where it is produced) is only 220 psi (6,860 vs 6,640 psi). The marginal increase in recovery generated by an additional 30 days of injection (Table 3-1) simply does not offset the ancillary gas-acquisition and pressurization costs and the lost production time. Therefore, the optimal injection time must be calibrated in terms of the surface gas rate and estimated reservoir pressure. For example, wells in parts of the Bakken with highly-conductive networks of natural fractures would require shorter injection times than those in less permeable zones. Figure 3-20 shows the pressurization of the near-fracture region during injection for a reservoir model in which the permeability of the natural fractures is 0.1 mD instead of 1 mD. As Figure 3-20 shows, the average pressure in the near-fracture region plateaus after 20 days when the natural fractures have a permeability of 1 mD, and it stabilizes after roughly 40 days in the 0.1-mD case. From Figures 3-15 and 3-19, we can see that incremental recovery plateaus after 15 to 20 days of injection, when pressure in the near-fracture region is roughly 6,000 psi. If we assume that 6,000 psi is the "critical" average pressure in the near-fracture region, it can be determined from Figure 3-20 that the optimal injection time for the 0.1 mD case is approximately 40 days. The influence of natural fractures on injection (and production) is discussed in detail in Section 3.8.

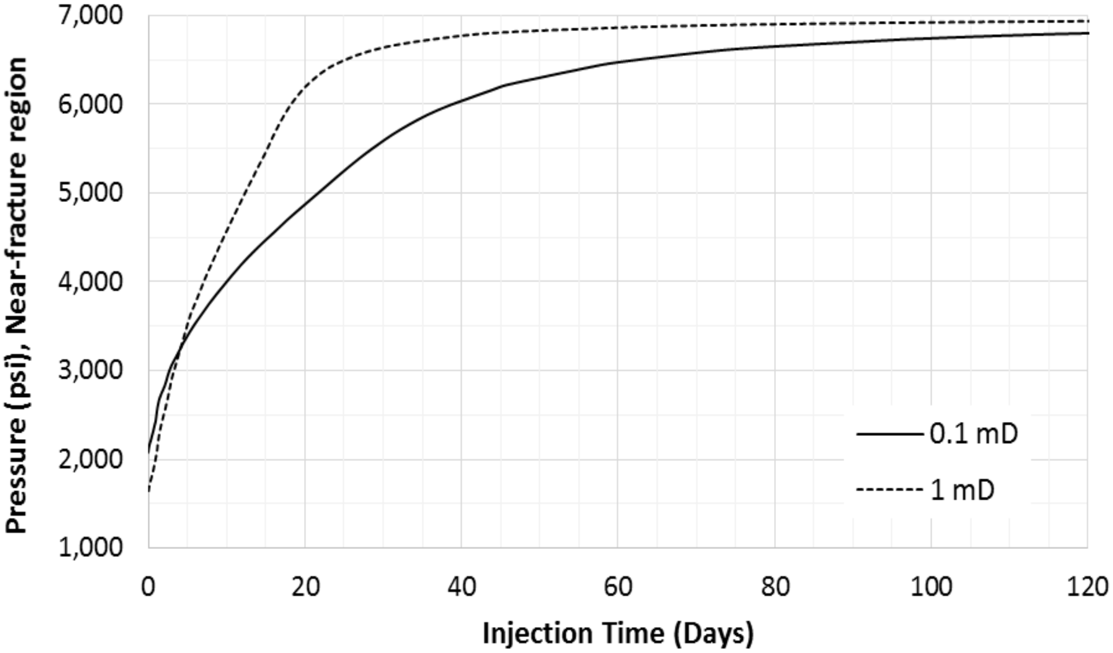

Figure 3-20. Pressure in near-fracture region during injection period for different natural fracture permeabilities

3.6. LENGTH OF THE SOAKING PERIOD AND EFFECT OF MOLECULAR DIFFUSION

The ideal length of the soaking period has been explored by previous studies. Yu et al. (2014) concluded that CO_2 soaking time has a small impact on incremental recovery, although longer waiting times (6 month vs. 3 months) are beneficial to production. Meanwhile, Chen et al. (2013) found that shorter soaking times result in higher recoveries but consume more CO_2. Figure 3-21 shows a series of simulations using different soaking periods: 1, 30, and 100 days. In all cases, three cycles were simulated. Each cycle consisted of 30 days of injection and 200 days of production, and the first cycle occurred after 500 days. As Figure 3-21 shows, this study's findings are in line with those by Chen et al. (2013). The case with the shortest waiting time (1 day) had the largest incremental recovery (1.8% of the OOIP) after 15 years, while the simulation with the longest soaking period (100 days) had the smallest (1.6% of the OOIP). Meanwhile, the intermediate case recovered an additional 1.7% of the OOIP. These results indicate that longer soaking periods have no benefits over shorter waiting times, and are actually detrimental to production. Furthermore, as Table 3-3 shows, longer waiting times proved to be *less* efficient: the 100-day case had the smallest recovery of all three cases, but injected practically the same volume of CO_2. These findings are significant, and call into question the need for any type of soaking period during Huff-and-Puff operations in the Bakken.

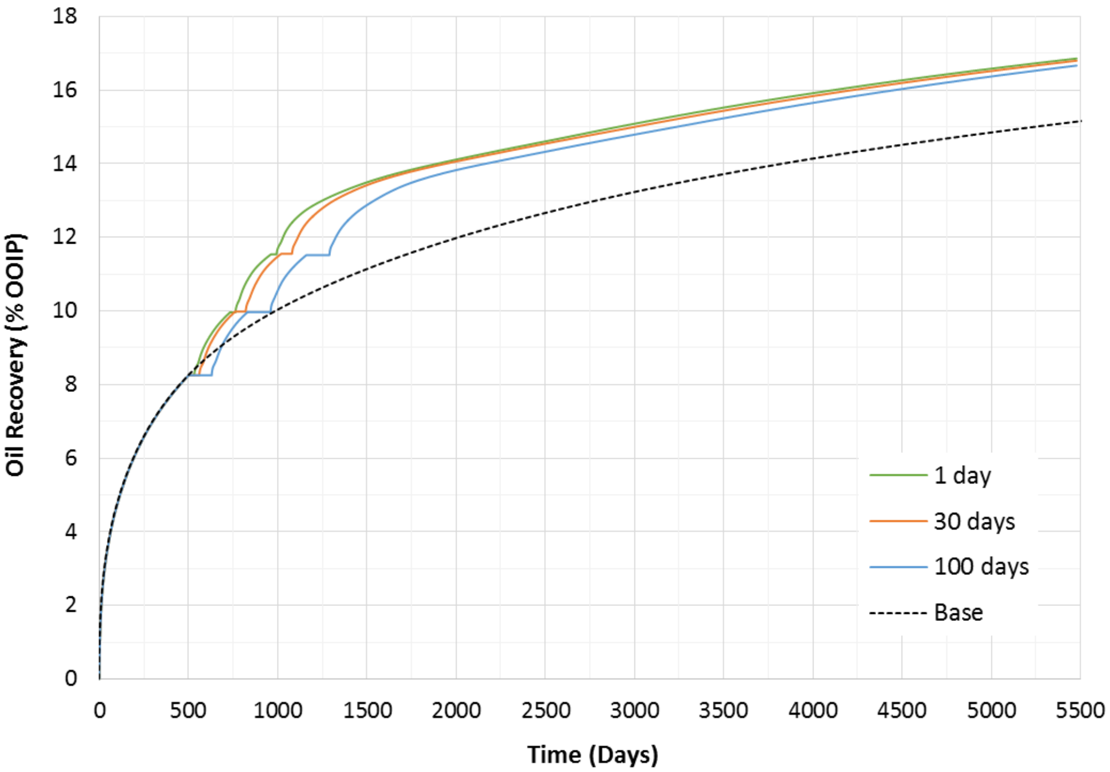

Figure 3-21. Recovery for different soaking times

Table 3-3 – Efficiency for different soaking times

Soaking time (days)	**Oil recovered (stb)**	**CO_2 injected (Mcf)**	**Efficiency (stb/Mcf)**
1	3,770	1,753	2.15
30	3,757	1,753	2.14
100	3,727	1,750	2.13

Molecular diffusion plays an important role during the soaking period because diffusion is the only mechanism through which CO_2 can move into the formation while the well is shut in. As Figure 3-4 in Section 3.1 shows, however, CO_2 diffusion after 30 days of soaking does not appear to be significant. The global mole distribution of CO_2 at the beginning of the waiting period is almost identical as at the end. Diffusion is a microscopic process modeled macroscopically in CMG GEM, which complicates capturing it accurately. Experimentally-obtained values of diffusion might not work at the field scale. According to CMG GEM's User's Guide (2012a), molecular diffusion coefficients should be regarded as "adjustable parameters" that need to be tuned to give acceptable results. Yu et al. (2014) found that Huff-and-Puff processes are highly sensitive to the magnitude of the molecular diffusion coefficients. In their study, increasing molecular diffusion by a factor of 100 affected incremental recovery by nearly 50%. In order to evaluate the sensitivity of the model to molecular diffusion four cases were run:

1) No molecular diffusion

2) Molecular diffusion coefficients calculated by CMG GEM using the Sigmund Correlation

3) Molecular diffusion coefficients from Chen et al. (2013) (Table 2-9 in Section 2.2.4, the standard input in this study)

4) Molecular diffusion coefficients from Chen et al. (2013) increased by a factor of 10

In all cases, diffusion into the aqueous phase was assumed to be zero. A three-cycle treatment was simulated: 30 days of injection, 30 days of soaking, 200 days of production, and 500 days of primary depletion.

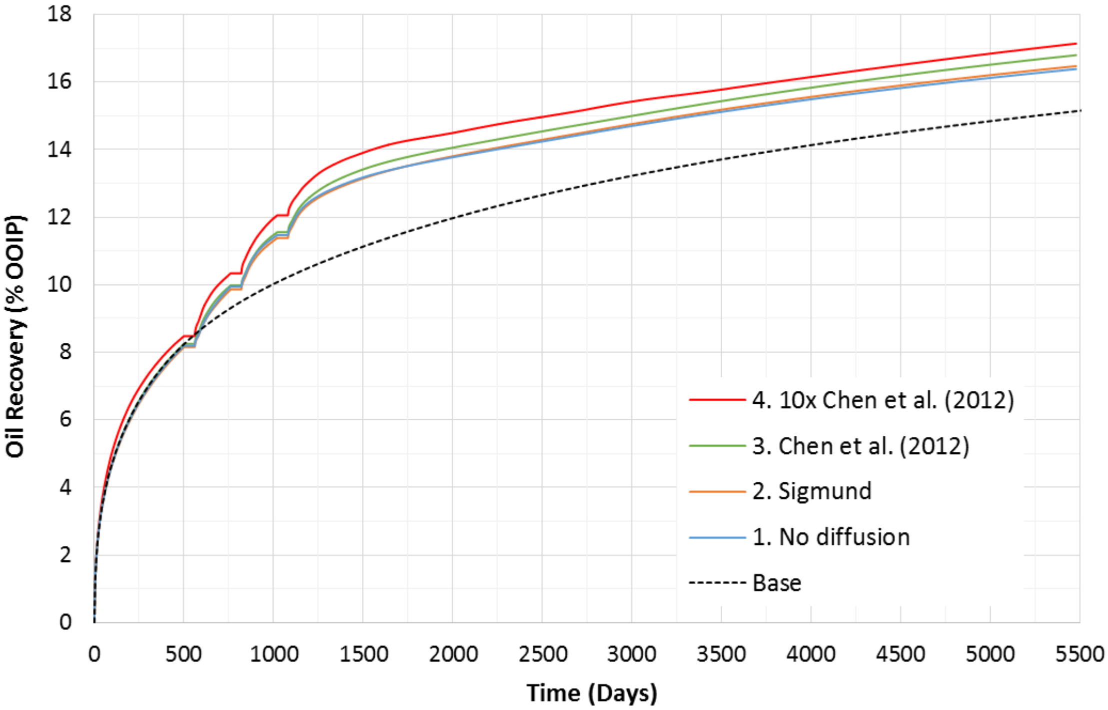

Figure 3-22. Effect of molecular diffusion on recovery

As Figure 3-22 shows, the magnitude of the molecular diffusion coefficients significantly affects the projected recovery. Case # 4, in which the standard diffusion coefficients were increased by a factor of 10, had the largest incremental recovery (2.1% of the OOIP). Meanwhile, including no molecular diffusion reduced incremental recovery from 1.7% to 1.3%. Molecular diffusion coefficients calculated by the Sigmund correlation had a marginal effect on Case #1's (no diffusion) recovery, boosting it from 16.4 to 16.5% of the OOIP. It is difficult to know whether molecular diffusion is better modeled by Chen et al.'s (2013) coefficients or those obtained by the Sigmund correlation, but either data set could serve as a basis for fine-tuning.

Having established that molecular diffusion has a considerable impact on the model, a series of cases was run to determine if using larger diffusion coefficients would change the conclusion that shorter soaking periods are better for recovery. Using the coefficients from Case # 4, the same three 3-cycle treatments as in Figure 3-21 were run: 1, 30, and 100 days of soaking, with 30 days of injection and 200 days of production. As Figure 3-23 shows, a 1-day soaking time yielded a recovery factor of 17.2%, while the case with the 100-day soaking period recovered 16.9% of the OOIP. The larger molecular diffusion coefficients changed the recovery factors but not the overall conclusion that longer soaking periods have a negative impact on recovery.

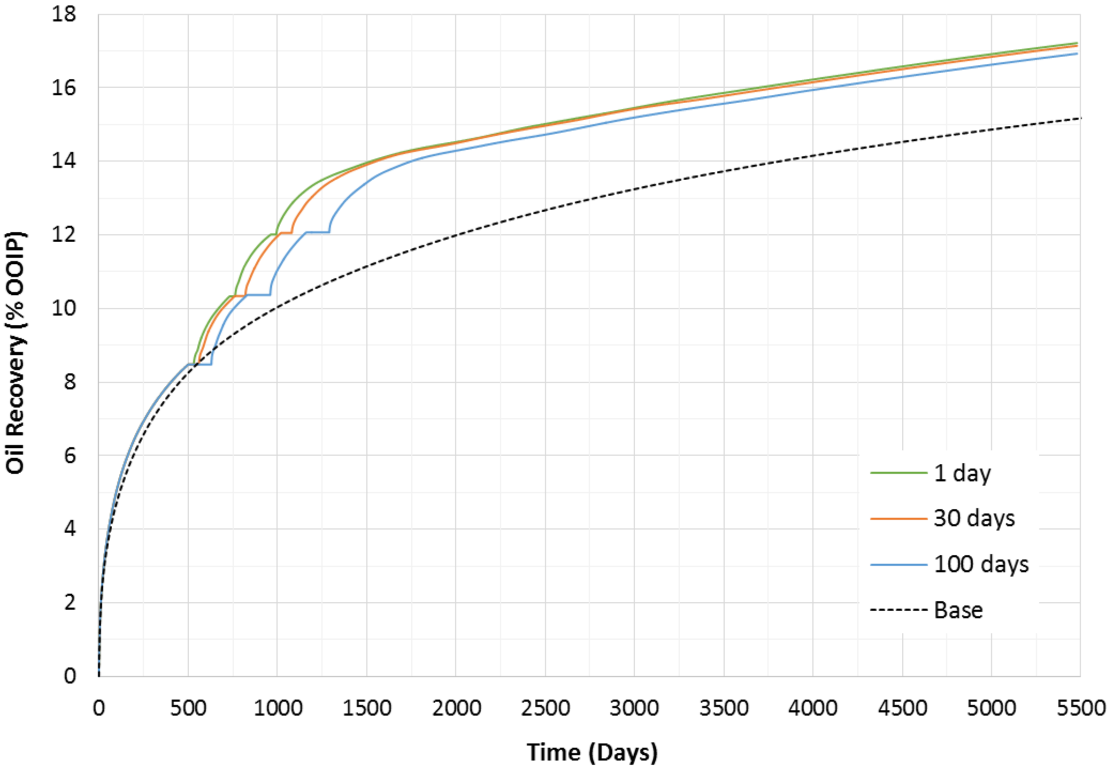

Figure 3-23. Recovery for different soaking times with larger molecular diffusion coefficients (10x)

3.7. NUMBER OF CYCLES

By its very nature, Huff-and-Puff is a multi-cyclical process driven by the positive effects of CO_2 injection on reservoir pressure and fluid properties. Yu et al (2014) found the recovery factor to be closely correlated to the number of Huff-and-Puff cycles: increasing the number of cycles from two to three boosted incremental recovery from 6.1 to 9.1%, while a single cycle yielded only 3.4%. In other words, there was an almost linear correlation between the number of cycles and the incremental recovery factor. It is important to understand if this correlation extends to later cycles, and to determine if and why the effectiveness of Huff-and-Puff diminishes over the life of the well. In order to address these questions an eight-cycle treatment was simulated. The treatment began after 500 days of primary recovery, and each cycle consisted of 15 days of injection, 1 day of soaking, and 184 days of production. Figure 3-24 shows the cumulative production for this case, which had an incremental recovery of 2.7% of the OOIP over the base case after 15 years. Figure 3-25 shows the oil rate, which is significantly boosted after every injection period. The “spikes” in the oil rate translate into “humps” in the cumulative recovery curve, and a new cycle is started once production falls back to the “base”, pre-injection rate.

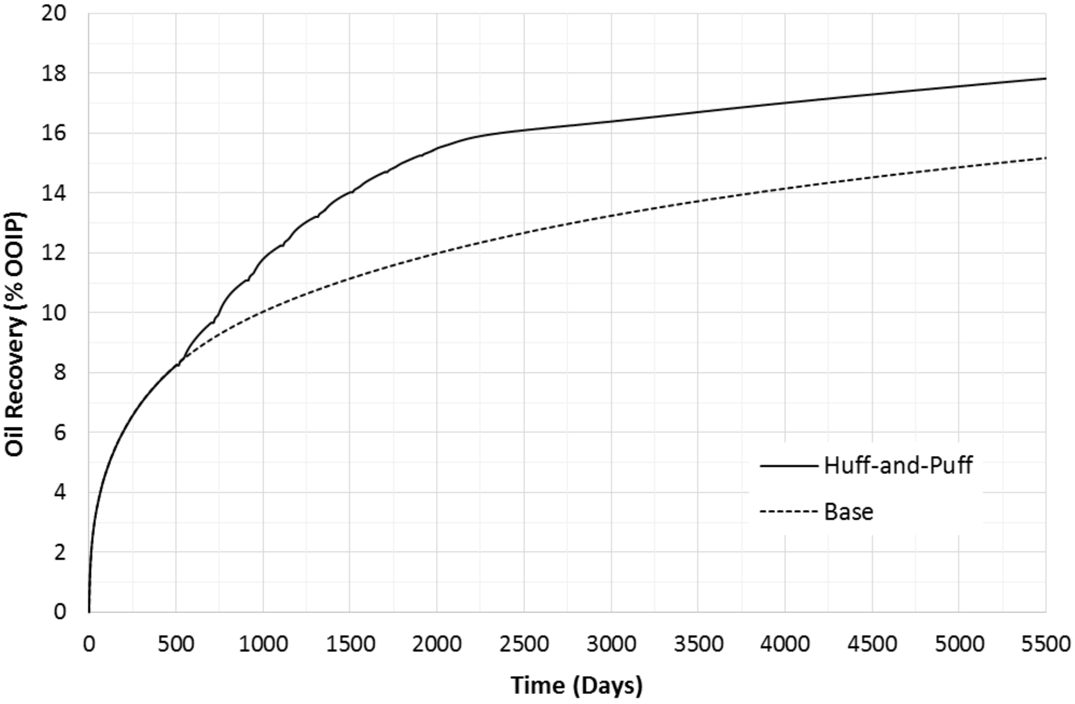

Figure 3-24. Oil recovery for eight-cycle case

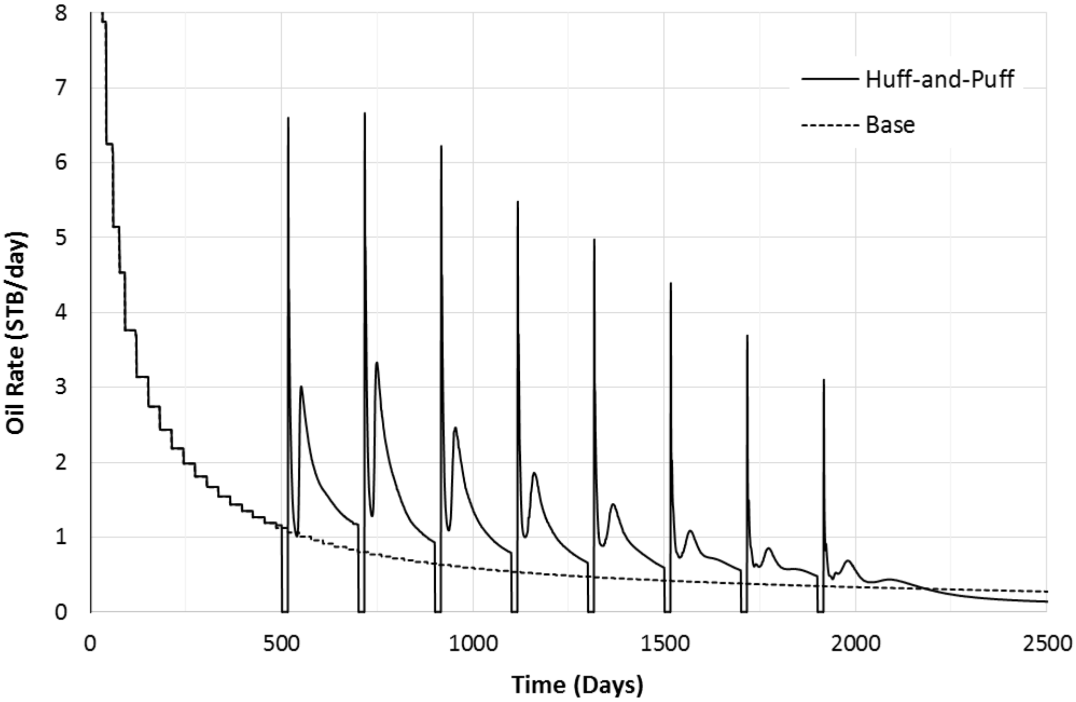

Figure 3-25. Oil rate for eight-cycle case

Additional cases were run in order to establish a correlation between the number of cycles and incremental recovery. As Table 3-4 shows, the relationship between the number of cycles and the incremental recovery factor is decidedly non-linear. The first cycle is by far the most effective, increasing recovery from 15.1 to 15.9% of the OOIP. A second cycle adds only an addition 0.39% of the OOIP, and a third one 0.36%. By the time an eight cycle is conducted, its effectiveness is only one-eighth of the first. While more cycles yield additional incremental recovery, their impact on production is progressively diminished. This agrees with findings by Chen et al. (2013), who observed that "the incremental recovery in a cycle decreases as the cycle number increases, because of the depletion of oil in the reservoir."

Table 3-4 – Incremental recovery for different number of cycles

Number of cycles	**Oil recovery (%OOIP)**	**Incremental recovery (%OOIP)**	**Incremental recovery over previous cycle (%OOIP)**
Base	15.1	N/A	N/A
1	15.9	0.85	0.85
2	16.3	1.24	0.39
3	16.7	1.60	0.36
4	17.0	1.92	0.32
5	17.3	2.21	0.29
6	17.5	2.45	0.24
7	17.7	2.61	0.16
8	17.8	2.72	0.11

The reduction in effectiveness of Huff-and-Puff cycles can be plainly observed in Figure 3-25, as the "spikes" in the oil rate become progressively smaller and smaller. The reason for this is oil depletion in the near-fracture and near-wellbore region, as shown in Figure 3-26. As oil saturation close to the fracture decreases, the effectiveness of the injected CO_2 is reduced because it comes into contact with less oil. Furthermore, if CO_2 is injected at a constant pressure, more gas is pumped into the reservoir in later cycles than in early ones. Reservoir pressure is lower late in the life of the reservoir, resulting in larger injection drawdowns. As Table 3-5 shows, the average reservoir pressure drops from 4,174 to 3,061 psi between the first and eighth cycles, resulting in a 37% increase in CO_2 consumption (from 4,900 to 6,700 Mcf).

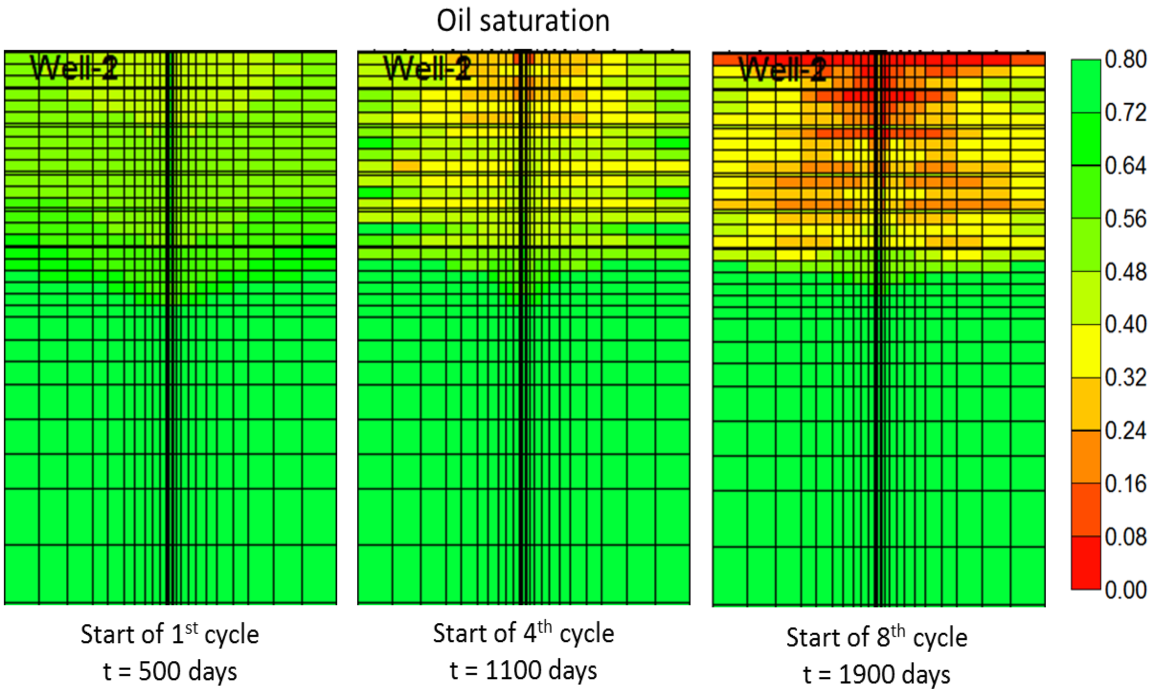

Figure 3-26. Oil saturation over time

Table 3-5 – Average reservoir pressure and CO_2 injected per cycle

Cycle	Average reservoir pressure (psi)	Cumulative CO_2 injected (Mcf)	CO_2 injected per cycle (Mcf)
1	4,170	4,920	4,920
2	3,970	9,730	4,810
3	3,760	14,900	5,220
4	3,580	20,600	5,620
5	3,430	26,500	5,960
6	3,290	32,800	6,260
7	3,170	39,300	6,520
8	3,060	46,100	6,740

As Tables 3-4 and 3-5 show, the effectiveness and efficiency of Huff-and-Puff is greatly diminished in later cycles: not only does the treatment yield smaller incremental recoveries, but it consumes more CO_2. Therefore, identifying the optimal number of cycles is largely an economic matter that depends on each case's specific conditions. Table 3-6 shows a simple economic analysis comparing the upside of performing the first Huff-and-Puff cycle versus the seventh (Figure 3-27). The price of oil was assumed to be \$90/stb, and the cost of CO_2 \$2/Mcf. Pressurization costs were not included, but neither was incremental revenue from gas production. Again, these numbers are just from one wing of one hydraulic fracture in a 10-ft thick pay-zone. As Table 3-6 shows, the first Huff-and-Puff cycle is profitable, with incremental oil revenue (on a pre-tax basis) being roughly twice the cost of CO_2. However, by the seventh cycle, the incremental oil revenue no longer offsets the associated CO_2 cost. While the ideal number of cycles will vary from well to well, it is important to consider the diminishing effectiveness and efficiency of Huff-and-Puff when designing multi-cycle treatments.

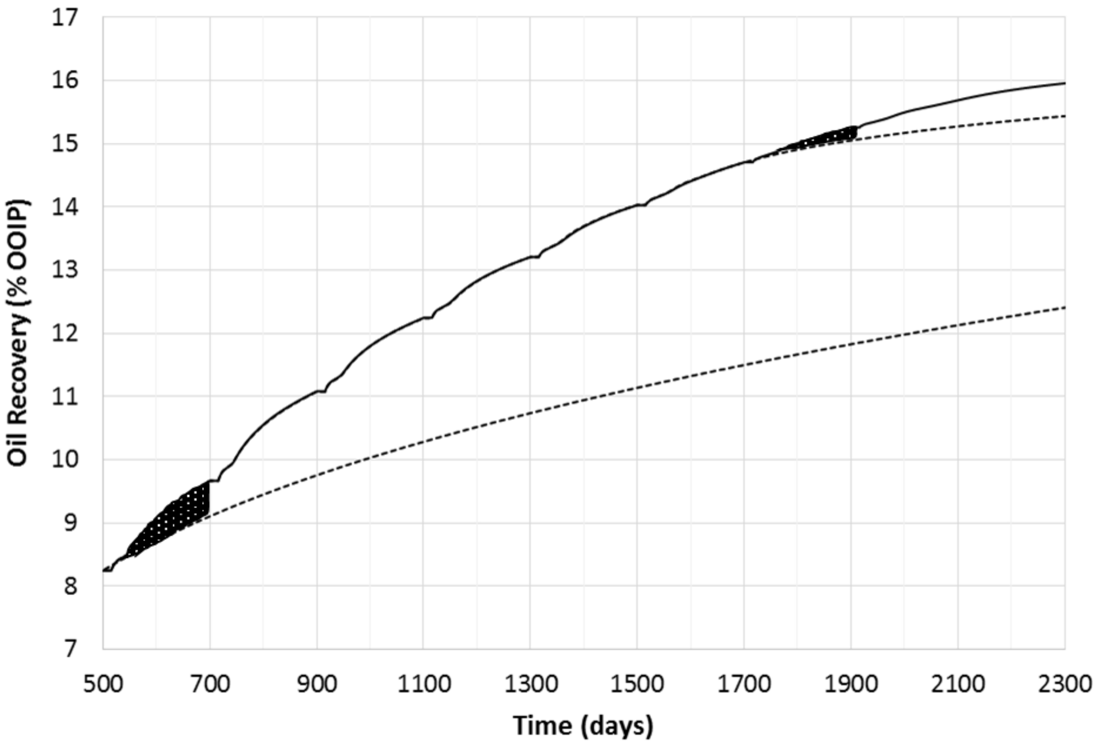

Figure 3-27. Incremental recovery, first vs. seventh cycle

Table 3-6 – Oil revenue vs. gas cost comparison, first vs. seventh cycle

	1st cycle		**7th cycle**	
	Without cycle	**With cycle**	**Without cycle**	**With cycle**
Cumulative oil recovered (stb)	3,390	3,570	3,930	3,960
Cumulative gas injected (Mcf)	0	4,920	32,750	39,250
Incremental oil revenue	$16,050		$3,210	
Incremental gas cost	$9,840		$12,990	
Difference	$6,200		-$9,780	

Table 3-7 is an extension of Table 3-6. It shows the estimated incremental oil revenue and CO_2 cost of performing additional cycles. Once again, the price of oil was assumed to be \$90/stb, and the cost of CO_2 \$2/Mcf; all numbers are at the single-stage scale. Pressurization costs and incremental revenue from gas production were not included, and CO_2 recycling was not considered. Incremental gas revenue was not included because, as Sections 3.8 and 3.11 will show, a significant percentage of the produced gas consists of previously-injected CO_2 (which has a significantly lower BTU content than natural gas). As Table 3-7 shows, only the first Huff-and-Puff cycle is profitable. In all subsequent cycles, the cost of CO_2 exceeds the incremental revenue from oil production. These results indicate that current economic conditions might not be favorable for multi-cycle Huff-and-Puff treatments. If Huff-and-Puff is to be widely implemented, cost-cutting measures must be found to increase revenue margins. One of these measures, involving the re-injection of CO_2-enriched produced gas, is discussed in Section 3.11.

Table 3-7 – Economics for different number of cycles

Cycle Number	**Cumulative oil recovery (stb)**	**Cumulative CO_2 injected (Mcf)**	**Cycle incremental oil revenue (\$ USD)**	**Cycle incremental CO_2 cost (\$USD)**	**Cycle Profit (before taxes and OPEX, \$USD)**
Base	3,390	0	N/A	N/A	N/A
1	3,570	4,920	16,050	9,840	6,210
2	3,650	9,730	7,790	9,620	-1,830
3	3,740	14,900	7,300	10,340	-3,040
4	3,810	20,600	6,480	11,400	-4,920
5	3,870	26,500	5,850	11,800	-5,950
6	3,930	32,800	4,790	12,600	-7,820
7	3,960	39,300	3,210	13,000	-9,780
8	3,990	46,100	2,250	13,600	-11,350

3.8. PERMEABILITY OF THE MATRIX AND NATURAL FRACTURES

The influence of matrix permeability on the effectiveness of CO_2 Huff-and-Puff was studied by Yu et al. (2014), who found that it has a marginal effect on incremental oil recovery. A 60% increase in matrix permeability (from 5 to 8 μD) only increased the incremental recovery factor from 6.1 to 6.4%, while a 60% decrease (from 5 to 2 μD) had an almost negligible impact. In order to test this, three cases were run assuming three different matrix permeabilities: 5, 10, and 50 μD. Three cycles were simulated for every case, each consisting of 50 days of injection, one day of soaking, and 200 days of production. In order to account for the possible differences in the volume of gas injected at constant pressure, a constant injection rate of 60 Mcf/day was used. As Table 3-8 shows, recovery is not significantly affected by matrix permeability in the range studied by Yu et al. (.001 to 0.01 mD), which is consistent with their results. However, at higher permeabilities there appear to be other mechanisms in play, which affect the way in which CO_2 is transported through the reservoir and interacts with the reservoir fluids.

Table 3-8 – Incremental recovery for different matrix permeabilities

	Recovery (%OOIP)		
Matrix permeability (mD)	**Base**	**Huff and Puff**	**Incremental**
0.005	13.3	14.5	1.3
0.01	15.1	16.2	1.1
0.05	20.5	20.3	-0.2

The conductivity of natural fractures is potentially more important to the Huff-and-Puff process than the permeability of the matrix. Chen et al. (2013) observed that the effectiveness of Huff-and-Puff "depends significantly on the permeability structure." According the their study, Huff-and-Puff is less effective when CO_2 migrates deep into the formation because it is unable to sufficiently increase pressure in the near-fracture region and transport oil back to the well. They concluded that Huff-and-Puff works best with permeability structures that prevent CO_2 from escaping the injection point, and suggested sealing the microscopic natural fractures near the well in order to isolate the injection region (Chen et al., 2013).

As discussed in the Section 2.2.2, thin high-permeability "fractures" were incorporated into the model in order to reproduce natural fluid pathways into the reservoir (Figure 2-10 in Section 2.2.2). The permeability of these "natural fractures" was varied in order to get a qualitative analysis of the impact of natural conduits on enhanced oil recovery by CO_2 Huff-and-Puff. First, the reservoir was allowed to naturally deplete for a period of 15 years, as shown in Figure 3-28. Four cases were considered: the originally-assumed natural fracture permeability (1 mD), a case in which the permeability of the natural fractures was set equal to the permeability of the matrix (0.01 mD), an in-between value (0.1 mD), and a highly-conductive value (10 mD). As Figure 3-28 shows, there is a noticeable difference in primary recovery between the cases with the least and most conductive natural fractures. The 10-mD case recovered 15.9% of the OOIP after 15 years, while the 0.01-mD case only recovered 14.4%. This result is expected and in line with Kurtoglu and Kazemi's (2012) description of natural fractures and fissures as "the main contributing factor to flow to the well."

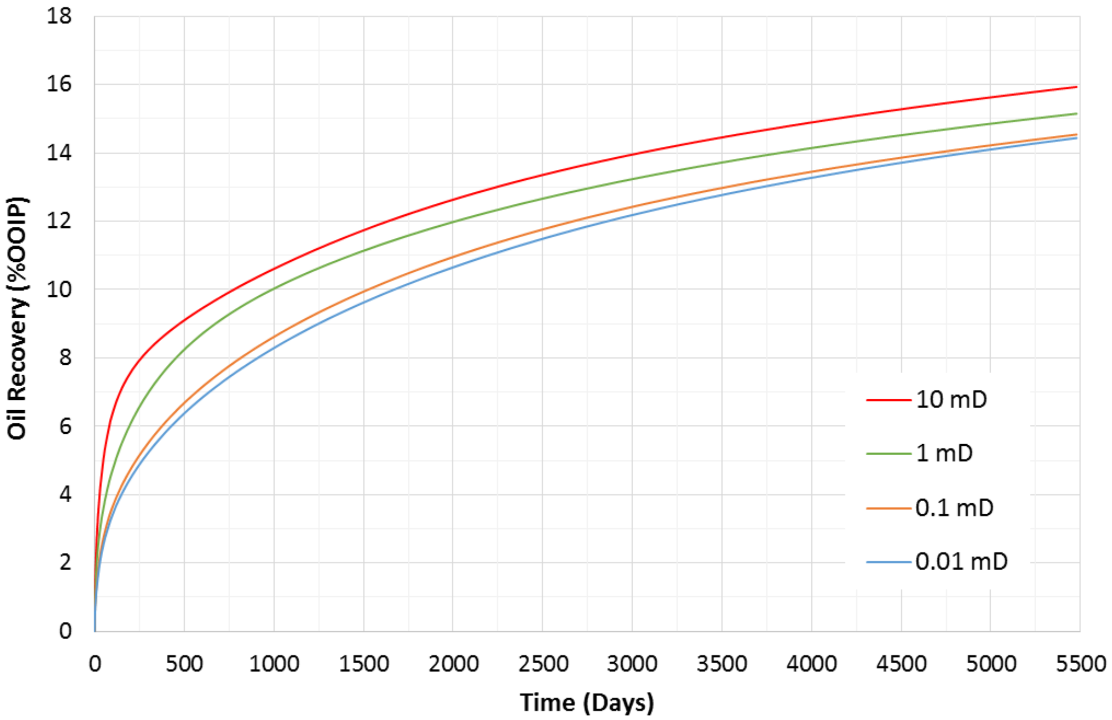

Figure 3-28. Primary recovery for different natural fracture permeabilities

The most important aspect of natural fractures in this study is their impact on the Huff-and-Process. In addition to providing conduits for oil to reach the well during the production period, natural fractures serve as pathways for CO_2 to reach deep into the formation and contact larger volumes of reservoir fluids. The same three-cycle Huff-and-Puff treatment was simulated for the four cases described above. Each cycle consisted of 15 days of constant pressure injection, 1 days of soaking, and 184 days of production. As Table 3-9 shows, there is a very clear correlation between higher natural-fracture permeability and larger incremental oil recovery. The 10-mD case recovered an additional 2.8% of the OOIP, while the case in which the natural-fracture permeability was set equal to the permeability of the matrix (0.01 mD) actually recovered less oil when treated with Huff-and-Puff than by primary depletion. For a very similar case (uniform 0.01 mD matrix permeability), Chen et al. (2013) also found that Huff-and-Puff recovery was lower than the base case, due to the oil rates in the production period being insufficient to offset the losses in recovery during injection and soaking.

Table 3-9 – Incremental recovery and gas injection volume for different natural-fracture permeabilities, constant injection pressure

$K_{\text{Nat frac}}$ (mD)	**Base recovery (% OOIP)**	**Huff-and-Puff recovery (% OOIP)**	**Incremental recovery (% OOIP)**	**Volume of CO_2 injected (Mcf)**
10	15.9	18.7	2.8	23,000
1	15.1	16.7	1.6	15,000
0.1	14.5	14.4	-0.1	8,750
0.01	14.4	14.2	-0.2	7,500

An important detail in Table 3-9 is that the 10-mD case had the largest incremental recovery, but also injected the most CO_2. This is due to the fact that the high-permeability natural fractures deplete the formation faster, creating larger injection drawdowns between the reservoir and the well. In order to avoid differences in the injection volume (which, as shown in Section 3.5, has a direct effect on incremental recovery) an additional set of cases was run. The same cumulative gas volume (9,000 Mcf) was injected into the reservoir at a constant injection rate of 60 Mcf/day and a 7,000 psi injection pressure constraint. Once again, three cycles were simulated: 50 days of injection, 1 day of soaking, and 200 days of production. The results of these simulations can be seen in Table 3-10, and the results for both sets of simulations (constant injection pressure and constant injection rate) can be seen in Figures 3-29 and 3-30.

Table 3-10 – Incremental recovery and gas injection volume for different natural fracture permeabilities, constant injection rate

K $_{\text{Nat frac}}$ (mD)	**Base recovery (% OOIP)**	**Huff-and-Puff recovery (% OOIP)**	**Incremental recovery (% OOIP)**	**Volume of CO_2 injected (Mcf)**
10	15.9	16.7	0.8	9,000
1	15.1	16.2	1.1	9,000
0.1	14.5	14.5	0.0	9,000
0.01	14.4	14.2	-0.2	9,000

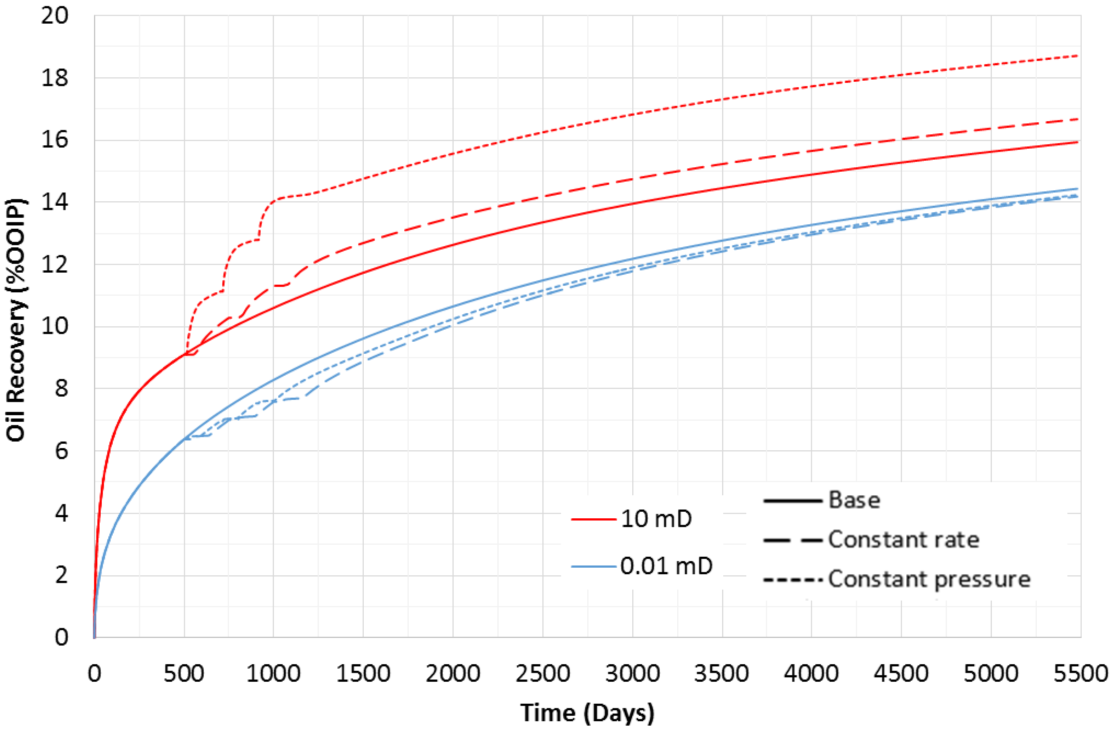

Figure 3-29. Oil recovery for different natural fracture permeabilities (0.01 and 10 mD)

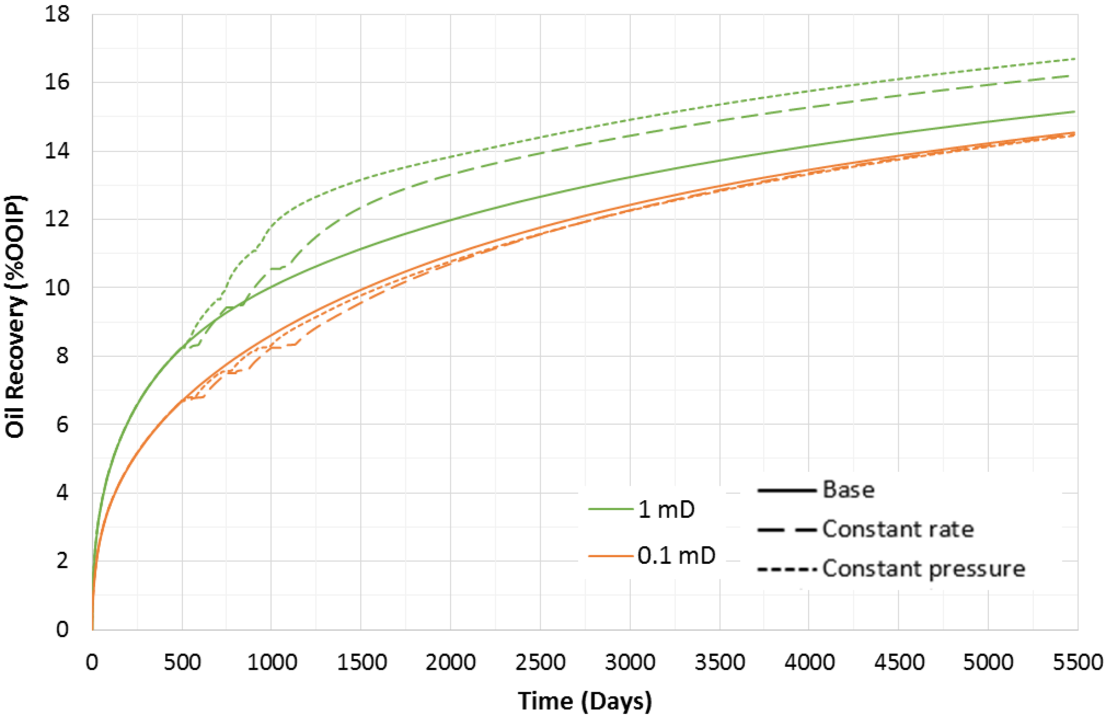

Figure 3-30. Oil recovery for different natural fracture permeabilities (0.1 and 1 mD)

As Table 3-10 shows, the 1-mD case actually outperformed the 10-mD model, perhaps because the volume of gas injected was too small for the 10-mD case. Most significantly, the case with the least-conductive fractures once again responded negatively to Huff-and-Puff stimulation. In order to understand why Huff-and-Puff performs so poorly in the absence of natural conduits, a comparison was made between the 1-mD and 0.01-mD cases. These two cases were chosen because one of them is the "standard" (every simulation until this point has assumed a 1-mD natural fracture permeability) and the other is equivalent to having no natural fractures at all (the matrix permeability is 0.01 mD).

The first property examined was the oil rate for these two cases at a constant injection rate. As Figure 3-31 shows, in both instances there is a similar sequence of events following every injection/soaking period: 1) a brief spike immediately following the re-opening of the well to production, 2) a dramatic slump during which the oil rate drops to almost zero, 3) a second surge, during which oil rate is boosted as a result of CO_2 injection, and 4) a gradual decline due to depletion.

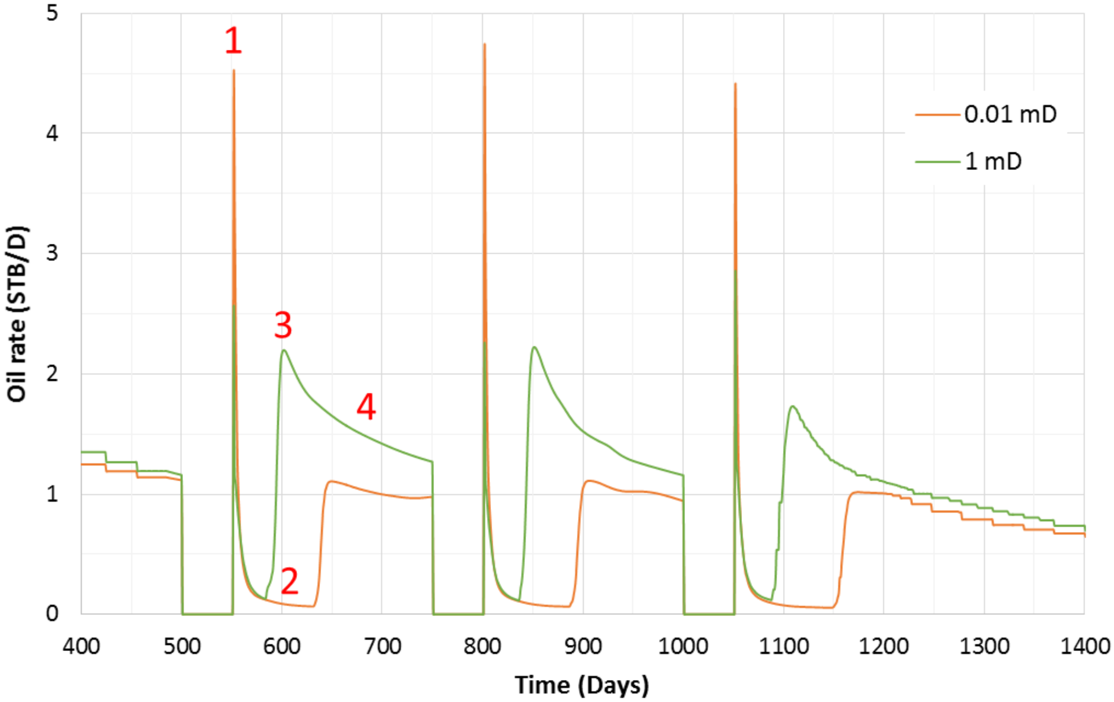

Figure 3-31. Oil rates for different natural fracture permeabilities

From Figure 3-31, two differences are evident between the low-conductivity and high-conductivity cases. First, the length of the “slump” period (labeled *2* in Figure 3-31), during which the oil rate falls to almost zero, is much longer in the 0.01-mD case. Second, the second spike (labeled *3*), which drives incremental recovery, is much larger in the 1-mD case. In fact, the 0.01-mD case seems to merely return to the pre-injection oil rate instead of displaying any kind of stimulation. Figure 3-32 shows the global mole fraction of CO_2 at the end of the first injection period. Since a constant injection rate was imposed, both cases have the same volume of CO_2 in the reservoir at this time. As Figure

3-32 shows, CO_2 in the 0.01-mD case is contained around the near-fracture region. Meanwhile, the high-conductivity fractures in the 1-mD case allow for the same volume of CO_2 to spread deep into the formation. The “slump” period shown in Figure 3-31, during which the oil flow nearly stops, is the result of relative permeability effects during the early part of the production period. During the injection and soaking periods the reservoir is above the saturation and minimum miscibility pressures, with the oil and CO_2 existing as a single liquid phase. Once the well is put back into production at a bottomhole pressure of 1,000 psi, some of the CO_2 and hydrocarbon gases come out of solution, reducing the liquid relative permeability. If CO_2 is fully contained around the fracture and wellbore, as in the 0.01-mD case, it effectively blocks the oil from reaching the well. However, if CO_2 is diffused evenly through the formation, the CO_2 that comes out of solution is quickly produced and followed by reduced-viscosity oil. The “blockage” takes longer to clear in the 0.01-mD case because the CO_2 is concentrated in the near-fracture and near-wellbore region, resulting in a longer period during which the oil rate is practically zero.

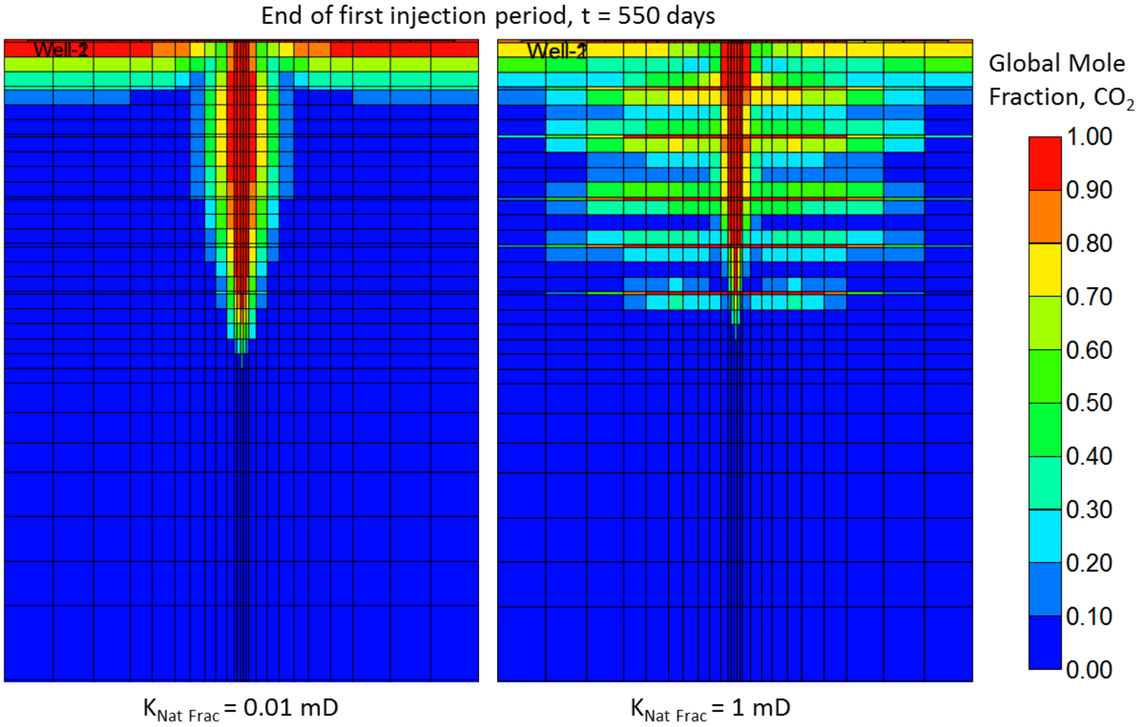

Figure 3-32. Global CO_2 mole fraction for different natural fracture permeabilities

The second effect of having no natural pathways in the reservoir is the reduced size of the oil rate spike following the production of undissolved CO_2. If CO_2 is restricted to the near-fracture region it only mixes with a limited volume of oil. A concentrated accumulation of CO_2 not only limits the area of the reservoir that experiences viscosity reduction as a result of mixing, but also increases the volume of CO_2 that is produced back. As Figure 3-33 shows, almost 85% (by mass) of the CO_2 is produced back during the first production period in the 0.01-mD case, compared to 63% in the 1-mD model. The degree of oil-CO_2 mixing can be seen in Figure 3-34, which shows the oil mole fraction of CO_2 100 days into the first production period. High-conductivity pathways allow CO_2 to mix with large volumes of reservoir fluids instead of saturating the near-fracture oil. Widespread mixing causes more CO_2 to stay in the oil phase instead of coming out of solution, resulting in shorter blockage periods and larger boosts to production.

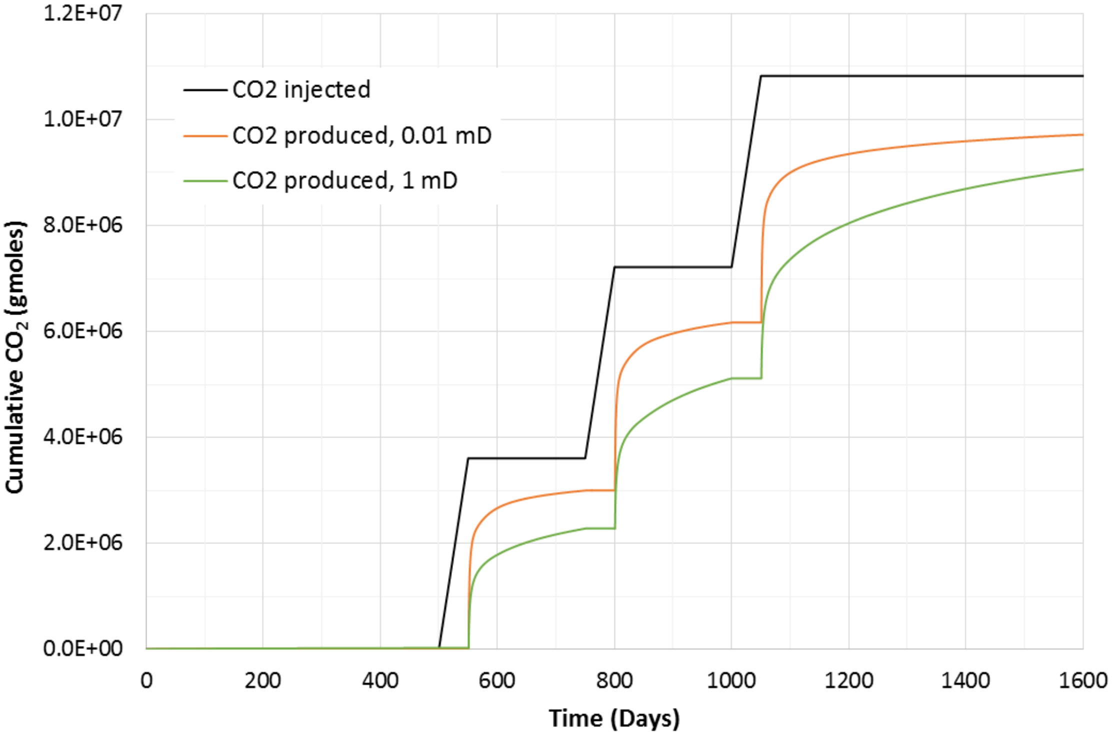

Figure 3-33. CO_2 injected and produced for different natural fracture permeabilities

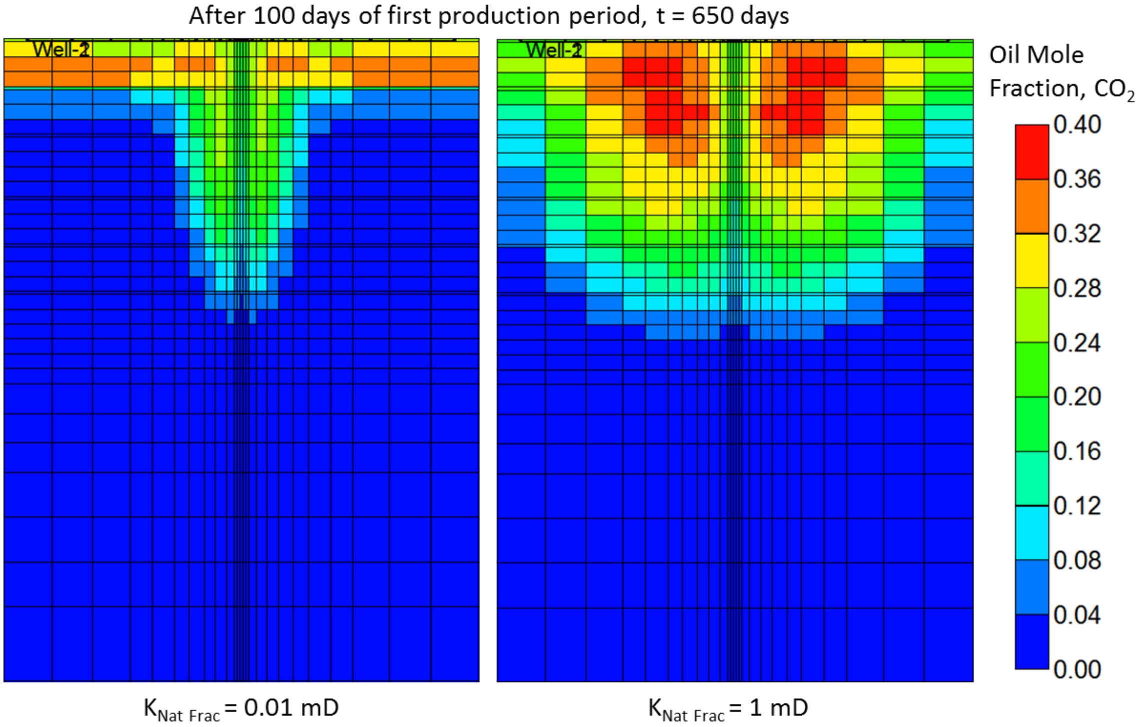

Figure 3-34. Oil mole fraction of CO_2 for different natural fracture permeabilities

From these results, it is evident that natural high-conductivity pathways are critical to the effectiveness of CO_2 Huff-and-Puff. This is contrary to the findings by Chen et al. (2013), who concluded that CO_2 accumulation around the fracture was better for recovery than deep CO_2 migration into the reservoir. Our results indicate that Huff-and-Puff could be especially useful in brittle portions of the Bakken where complex networks of natural fracture are likely to be present.

3.9. DISCRETIZATION OF THE COMPUTATIONAL DOMAIN

In order to put this project's simulation results in context it is important to compare its projected incremental recovery factors to those in previous Huff-and-Puff studies. Under realistic operating conditions, the expected incremental recovery determined by this study is between 1 and 2% of the OOIP after 15 years. These results are modest when compared to Yu et al. (2014), whose model predicted gains in recovery of up to 9.4% after 30 years. While Yu et al.'s (2014) computational domain was similar to this study's (a single 340×1320×40 ft. stage in a hydraulically-fractured horizontal well), their sensitivity analysis considered a two-fracture configuration. In a head-to-head comparison, a two-fracture cluster had a considerably larger incremental recovery factor than a single-fracture scheme for the same Huff-and-Puff treatment (6.1% vs. 3.8%) (Yu et al., 2014). Significantly, Chen et al. (2013) obtained smaller incremental recoveries than this study (less than 1%) while also modeling a single-fracture configuration. However, their fracture half-length was 50 ft. instead of 200 ft., which could account for the lower production. Furthermore, they were only able to simulate injection pressures of 3,500 psi due to numerical stability issues. Figure 3-35 shows a comparison of the three studies' computational domains. As previously mentioned, Yu et al.'s (2014) domain is 340×1320×40 ft., while Chen et al.'s (2013) and this study's is 320×1000×10 ft.

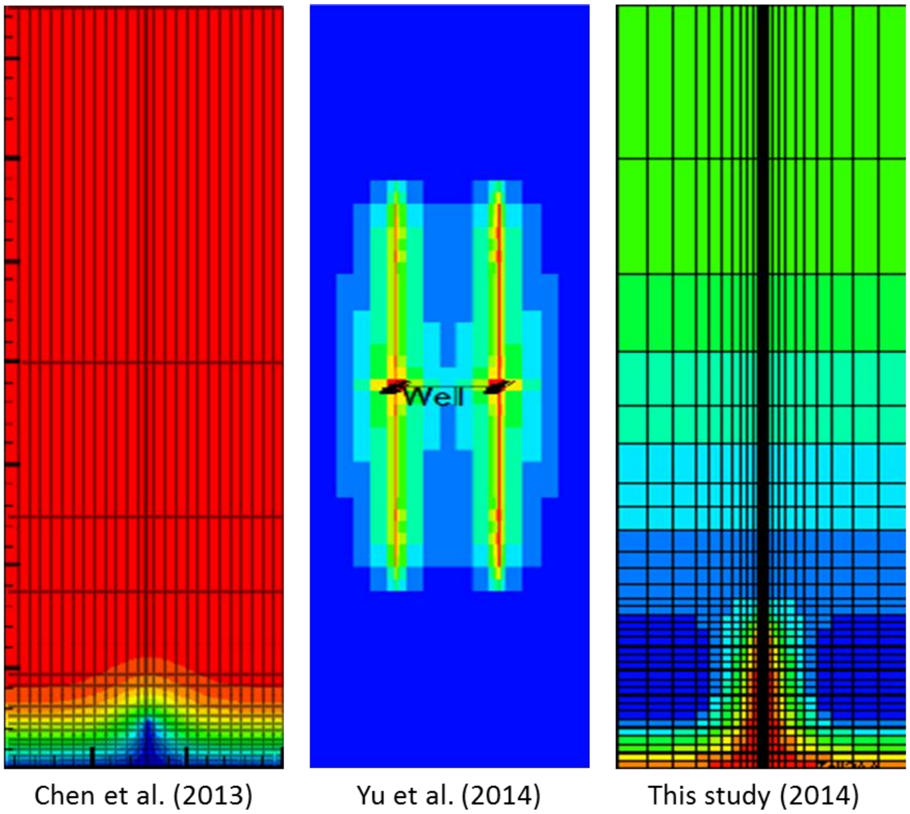

Chen et al. (2013) Yu et al. (2014) This study (2014)

Figure 3-35. Comparison of computational domains (Chen et al., 2013; Yu et al., 2014)

While trying to account for the differences in projected incremental recovery, it was found that the degree of discretization of the domain has a significant impact on the simulation results. The same Huff-and-Puff treatment (3 cycles, 15 days of injection, 1 day of soaking, 184 days of production) was simulated for three versions of the same model. Model A consisted of this project's standard computational domain, which is described at length in Section 2.2. Model B consisted of the same number of grid blocks as Model A (25 in the *x*-direction, 40 in the *y*-direction, 1 in the *z*-direction), but with uniform gridding in the *x* and *y* directions instead of extensive local refinement around the fracture. The fracture was modeled using CMG GEM's *Hydraulically-Fractured Wells Wizard* in the middle block, which calculated the effective width and permeability of the fracture using Eq. 2-8 in Section 2.2.1 and automatically applied local grid refinement. The rest of the reservoir and fluid properties (matrix permeability, relative permeability curves, porosity, initial pressure, initial water saturation, and fluid characterization) were the same as in Model A. Finally, Model C was a coarser version of Model B, with 25 uniform-sized blocks in the *y*-direction and only 20 in the *x*-direction. To account for the lack of natural fractures in Models B and C, the permeability of the natural fractures in Model A was set equal to the matrix permeability (0.01 mD). Figure 3-37 (at the end of this section) shows the discretization of Models A, B, and C, and their pressure profile at the end of the natural depletion period.

As Table 3-11 and Figure 3-36 show, the discretization of the domain has a significant impact on both primary and incremental recovery. A coarser mesh results in more optimistic recovery estimates, and dramatically affects the projected effectiveness of the Huff-and-Puff treatment. Injecting CO_2 into a formation without natural fractures was shown in Section 3.8 to be counterproductive, because containing the injection gas in the near-fracture region results in relative-permeability problems during the production period and minimizes the oil-CO_2 mixing area. These results were obtained with Model A, which has the most resolution around the well and fracture. Repeating the simulation with Models B and C yielded significantly different results: instead of a negative 0.2% incremental recovery factor, Model B had an incremental recovery of *positive* 0.1% and Model C produced an additional 0.5% of the OOIP over the base case.

Table 3-11 – Oil recovery for different domain discretization models

Model	Degree of refinement	Recovery (% OOIP)		
		Base	Huff-and-Puff	Incremental
A	High	14.4	14.2	-0.2
B	Medium	15.1	15.2	0.1
C	Low	15.3	15.8	0.5

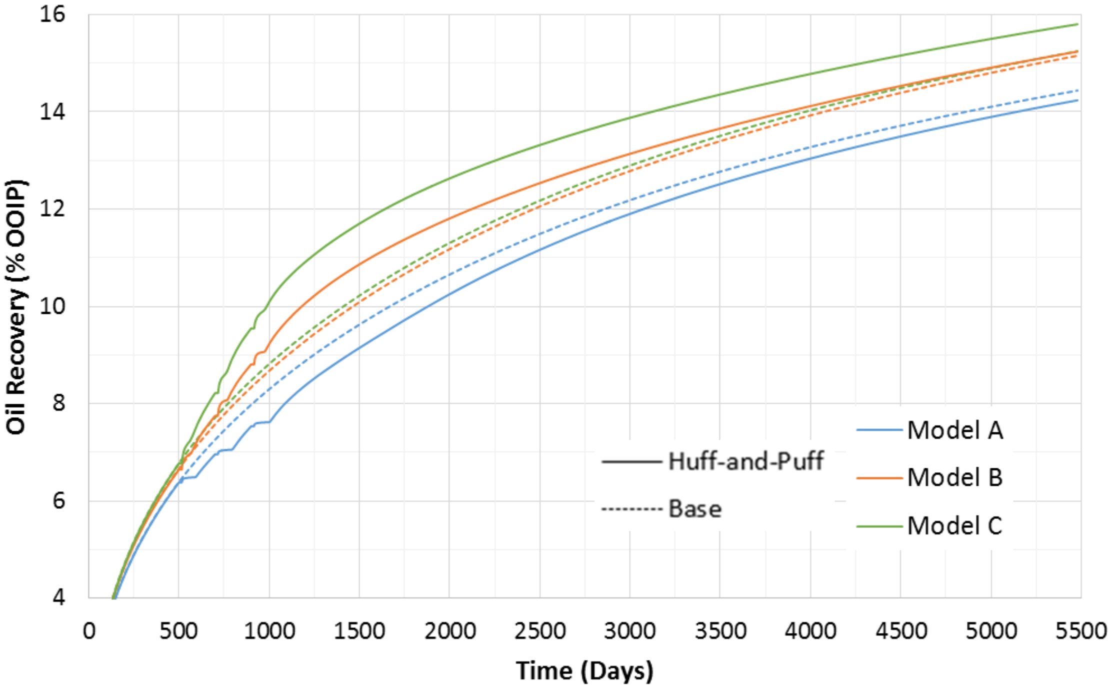

Figure 3-36. Oil recovery for different domain discretization models

The reason for this difference in results can be seen in Figures 3-37 and 3-38. Using a coarser mesh involves having larger grid blocks and a significant loss of resolution. As discussed in Section 3.3, producing below the bubble point has substantial benefits in terms of reservoir drive and pressure support. However, it also magnifies the relative permeability effects in the near-fracture region due to the presence of evolved gas. Even small accumulations of gas around the fracture can significantly affect the flow rate of oil due to the harmonic-mean nature of the "effective" phase permeability for linear flow (Eq. 3-1). Coarser discretization of the domain causes the properties of blocks in the near-fracture/wellbore region to be combined into an average, failing to capture the reservoir conditions in enough detail to accurately model primary and incremental recovery. The determining factor is not the number of grid blocks (Models A and B are both 25×40×1 domains) as much as the degree of refinement around the wellbore and fracture. Table 3-12 shows the properties of a block in roughly the same location (highlighted in Figure 3-37) in order to illustrate the loss of resolution with increasingly coarser grids.

$$k_{eff} = \frac{L}{\sum \frac{L_i}{k_i \, k_{ri}}} \tag{3-1}$$

Table 3-12 – Comparison of block properties for different discretization models, 30 days into first production period

Model	**Degree of refinement**	**Pressure (psi)**	**Gas saturation**	**Oil relative permeability**
A	High	1130	0.424	0.006
B	Medium	1690	0.373	0.017
C	Low	1950	0.326	0.036

As Table 3-12 shows, a lower degree of refinement results in more favorable conditions to production (higher pressure and oil relative permeability, and lower gas saturation). As Figure 3-35 (above) shows, both Chen et al. (2013) and this study employed a finely-meshed gridding scheme with LGR around the fracture, which would explain why comparably low incremental recoveries were projected. While the discretization of Yu et al.'s (2014) domain is unknown, the higher recovery factors estimated by their reservoir model could be due, at least in part, to a coarser gridding scheme.

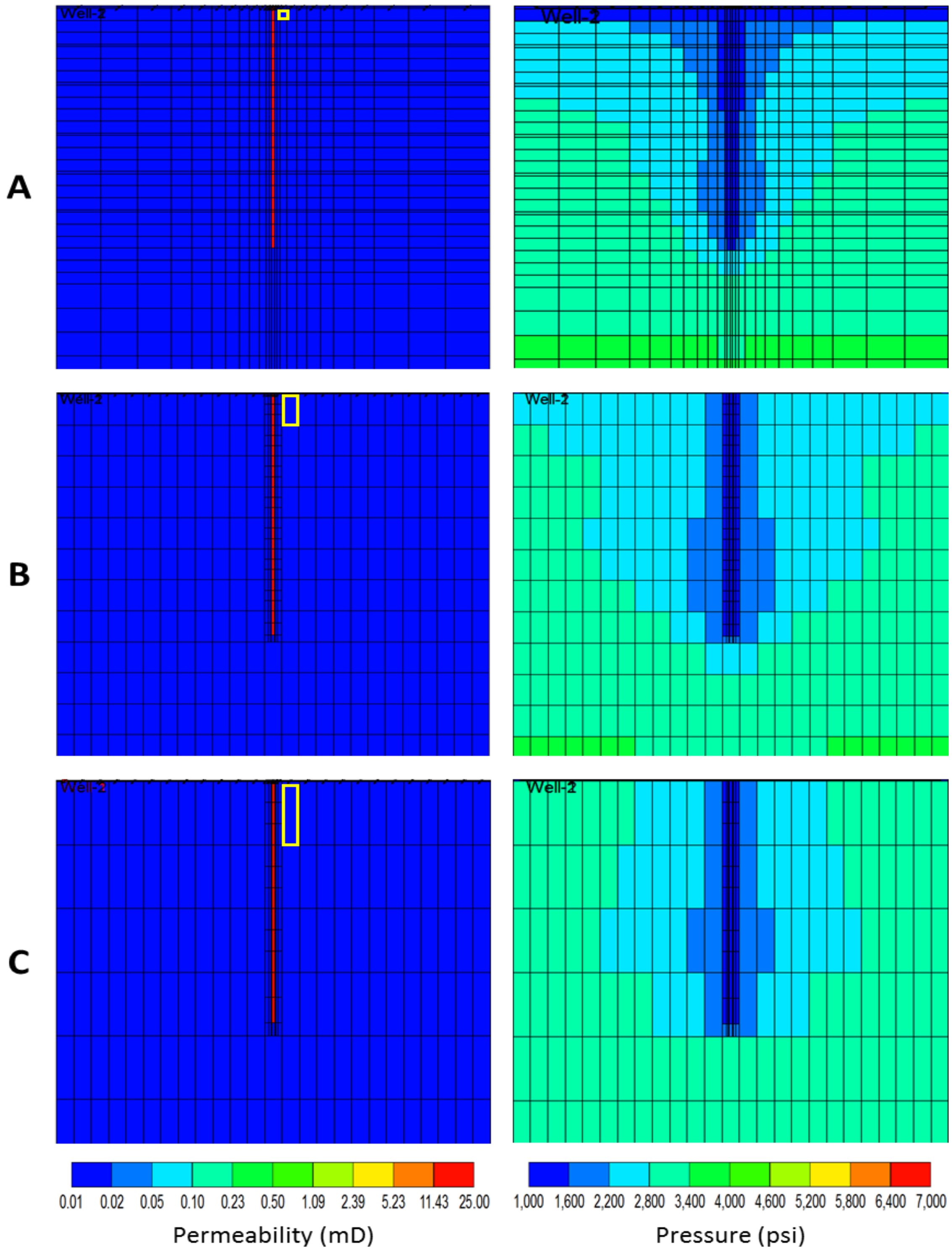

Figure 3-37. Permeability and pressure distributions for different discretization models with highlighted block for Table 3-11 comparison, 30 days into first production period

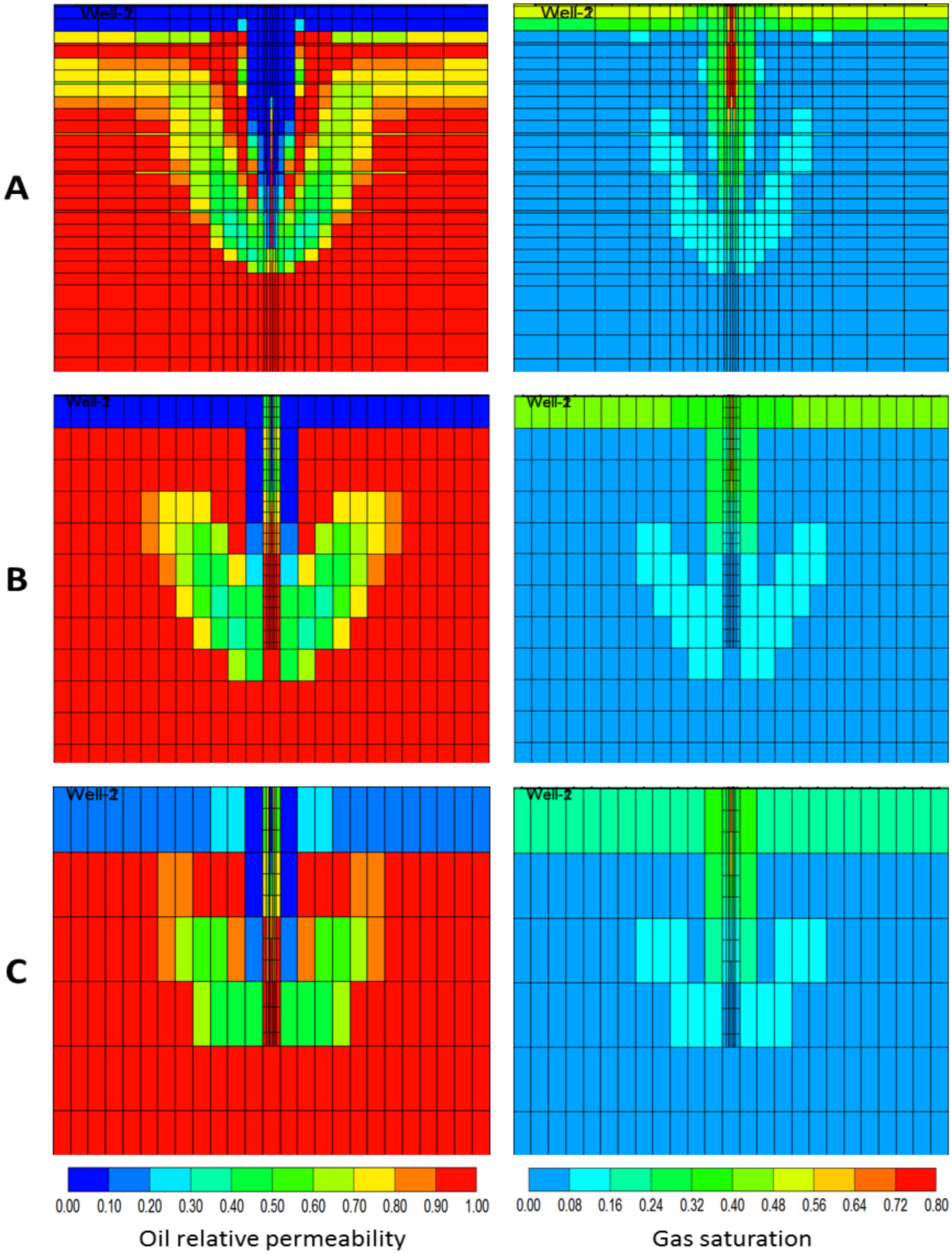

Figure 3-38. Oil relative permeability and gas saturation distributions for different discretization models, 30 days into first production period

3.10. PERFORMANCE OF A TWO-FRACTURE CONFIGURATION

The low recovery factors projected by this study were motivation for exploring additional solutions for increasing the effectiveness CO_2 Huff-and-Puff. One of these alternatives involved changing the number of fractures in the domain to model a multi-cluster stimulation stage. Yu et al. (2014) found that two-fracture configurations show higher incremental recoveries after Huff-and-Puff than those with one, three, or four-fracture schemes (Figure 3-39). They concluded that having two fractures per stage maximizes reservoir exposure to CO_2 while minimizing inter-fracture interference.

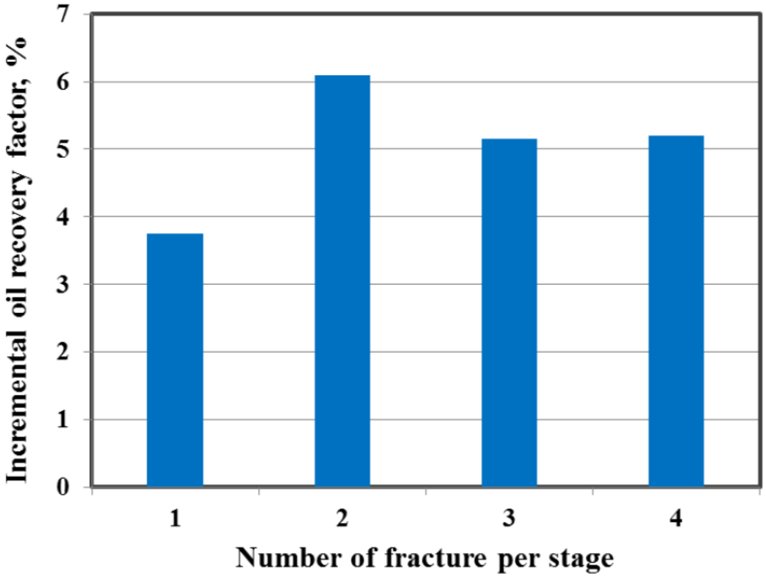

Figure 3-39. Comparison of incremental oil recovery factor for different number of fractures per stage (Yu et al., 2014)

A two-fracture model was created in order to determine the impact of multi-cluster stages on the effectiveness of CO_2 Huff-and-Puff. The same dimensions for the computational domain were used as for the single-fracture model (320 × 1000 × 10 ft.), but the domain was discretized into twice as many grid blocks in the *x*-direction (the model was 50×40×1 instead of 25×40×1). The fractures were located 80 ft. from the edges of the domain and 160 ft. away from each other. They were modeled as 2-ft.-thick pseudo-fractures following the procedure in Section 2.2.1. Figure 3-40 shows the near-fracture discretization and permeability field of the two-fracture model. The full computational domain can be found in Appendix III.

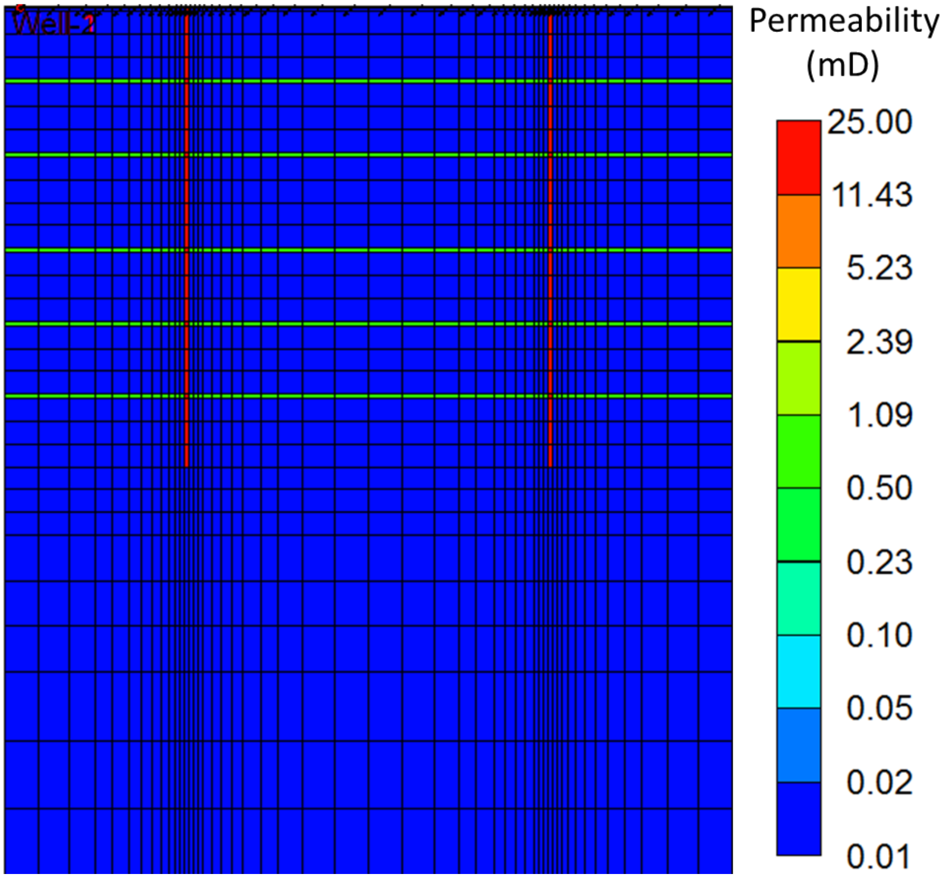

Figure 3-40. Permeability field for two-fracture model

A Huff-and-Puff treatment was simulated for one to eight cycles, as well as for a 15-year primary production base case. The Huff-and-Puff treatment was the same as in the case discussed in Section 3.7: 500 days of primary recovery, 15 days of injection, 1 day of soaking, and 184 days of production. As Table 3-13 shows, the two-fracture configuration recovered a larger percentage of the OOIP by primary production than the single-fracture case (16 vs. 15.1%). However, Huff-and-Puff did not prove to be significantly more effective. The incremental recovery after the first cycle was almost the same for both cases (0.85 and 0.80%), and the two models had an identical 2.7% incremental recovery factor after 8 cycles. As Figure 3-41a shows, Yu et al.'s (2014) conclusion that two-fracture configurations have larger recovery factors than single-fracture schemes is true for up to eight Huff-and-Puff cycles. However, after the fourth cycle, Huff-and-Puff appears to be more effective in single-fracture configurations in terms of the incremental recovery over the previous cycle (Fig 3-41b). A quick economic analysis of the two-fracture model (Table 3-14) shows that, despite having greater recovery factors, a dual-cluster configuration is not necessarily more profitable due to the larger CO_2 requirements. As with the single-fracture model, only the first cycle generates enough incremental revenue to offset the associated cost of CO_2.

Table 3-13 – Incremental recovery for different number of cycles

Number of cycles	Oil recovery (%OOIP)	Incremental recovery (%OOIP)	Incremental recovery over previous cycle (%OOIP)
Base	16.0	N/A	N/A
1	16.8	0.80	0.80
2	17.3	1.39	0.58
3	17.9	1.92	0.54
4	18.2	2.24	0.31
5	18.4	2.46	0.22
6	18.6	2.59	0.13
7	18.6	2.68	0.09
8	18.7	2.73	0.04

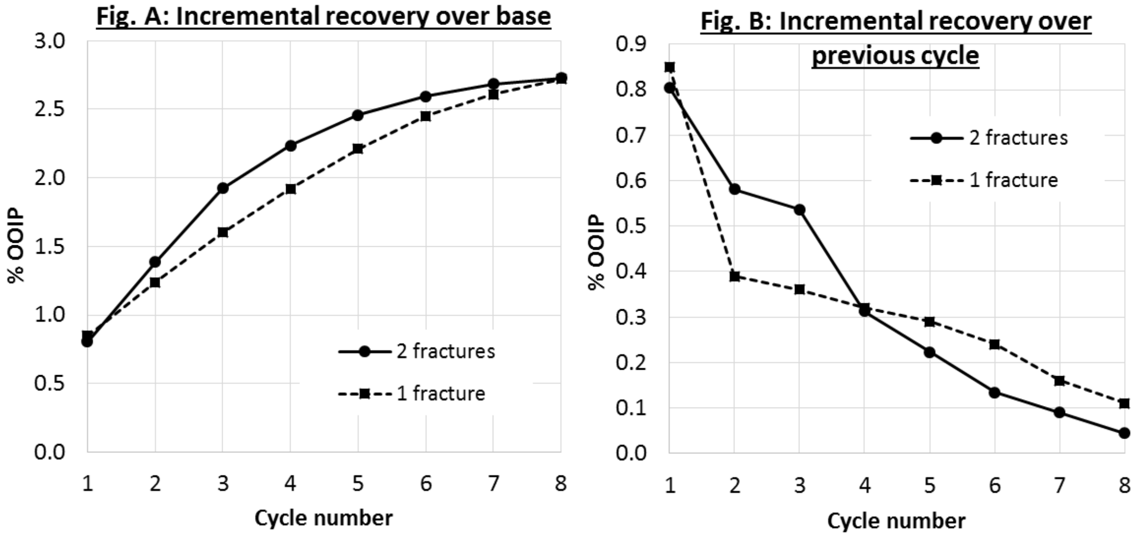

Figure 3-41. Incremental recovery comparison between one and two-fracture models

Table 3-14 – Economics for different number of cycles, two-fracture model

Cycle Number	**Cumulative oil recovery (stb)**	**Cumulative CO_2 injected (Mcf)**	**Cycle incremental oil revenue ($ USD)**	**Cycle incremental CO_2 cost ($USD)**	**Cycle Profit (before taxes and OPEX, $USD)**
Base	3,570	0	0	0	0
1	3,750	6,360	16,200	12,720	3,480
2	3,880	12,600	11,700	12,480	-780
3	4,000	19,800	10,800	14,400	-3,600
4	4,070	27,200	6,300	14,800	-8,500
5	4,120	35,600	4,500	16,800	-12,300
6	4,150	44,600	2,700	18,000	-15,300
7	4,170	54,200	1,800	19,200	-17,400
8	4,180	64,800	900	21,200	-20,300

Significantly, the two-fracture scheme is less efficient than the single-fracture configuration in terms of volume of gas injected per barrel of oil recovered. As Table 3-15 and Figure 3-42 show, CO_2 requirements in the two-fracture model are considerably greater without resulting in proportionally larger incremental recovery factors. The efficiency aspect has often been neglected by previous studies, but it is a crucial factor to consider when analyzing the potential wide-scale implementation of CO_2 Huff-and-Puff in the Bakken Shale.

Table 3-15 – Efficiency comparison between one and two-fracture models

	1 fracture			**2 fractures**		
Cycle number	**Incremental oil (stb)**	**CO_2 injected (Mcf)**	**Efficiency (Mcf/stb)**	**Incremental oil (stb)**	**CO_2 injected (Mcf)**	**Efficiency (Mcf/stb)**
1	180	4,920	27	180	6,360	35
2	80	4,810	60	130	6,240	48
3	90	5,170	57	120	7,200	60
4	70	5,700	81	70	7,400	106
5	60	5,900	98	50	8,400	168
6	60	6,300	105	30	9,000	300
7	30	6,500	217	20	9,600	480
8	30	6,800	227	10	10,600	1,060

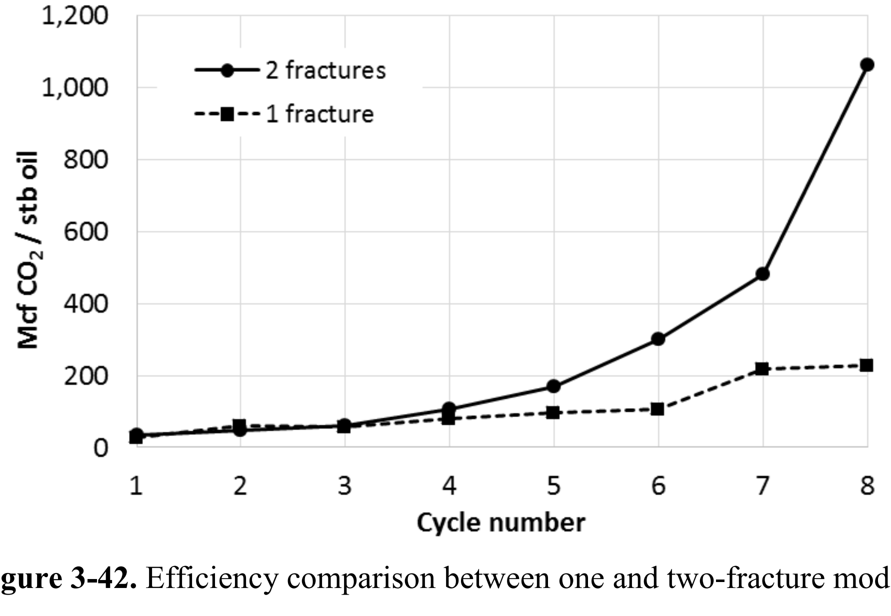

Figure 3-42. Efficiency comparison between one and two-fracture models

3.11. COMPOSITION OF THE INJECTION GAS

Every case discussed so far has considered an injection gas consisting of 100% CO_2. An extremely interesting question involves the viability of other gas mixtures as injectants in cases where the supply of CO_2 is limited or injecting other gases makes more economic sense. Under the right economic conditions, re-injecting produced CO_2-hydrocarbon gas mixtures could significantly reduce CO_2 acquisition costs and make the Huff-and-Puff process more commercially attractive.

Hoffman (2012) studied the injection of hydrocarbon gases as an alternative to CO_2, citing concerns about CO_2 availability in the Bakken. He concluded that "miscible hydrocarbon injection performs as well as miscible CO_2" (Hoffman, 2012) and was thus a solid option when CO_2 is unavailable on location. Hoffman (2012) also observed that recovery factors increase significantly regardless of the type of gas injected (miscible hydrocarbon, immiscible hydrocarbon, or pure CO_2). He ran a simple economic forecast for a traditional well-to-well gas flooding model, and concluded that "injecting hydrocarbon gases has potential from both a technical and economic standpoint" (Hoffman, 2012). Wang et al. (2010) had similar results as Hoffman (2012). They found that CO_2-enriched produced gas (60-40 mol% CO_2-CH_4) and CO_2-enriched flue gas (60-40 mol% CO_2-N_2) display "high oil recovery performance" and would be an efficient choice for gas-flooding projects in the Bakken.

Two cases were run, each consisting of a 4-cycle Huff-and-Puff treatment (20 days of injection, 10 day of soaking, 200 days of production, 7,000 psi constant injection pressure). In one case, CO_2 was injected in every cycle. In the other, pure CO_2 was injected in the first cycle and the composition of the injection gas was adjusted to match the composition of the separator gas in subsequent cycles (Table 3-16). As Figure 3-43 shows, the separator gas case slightly outperformed pure CO_2 injection. Injecting 100 mol% CO_2 recovered 17.2% of the OOIP after four cycles, while the CO_2-hydrocarbon mixture recovered 17.5%. This is in line with the results by Wang et al. (2010) and Hoffman (2012), and supports the observation that mixtures of CO_2 and hydrocarbon gases are extremely viable alternatives to pure CO_2 injection.

Table 3-16 – Composition of injection gas

	Mol %			
Component	***1st cycle***	***2nd cycle***	***3rd cycle***	***4th cycle***
CO2	100	50.5	45.6	43.2
CH4	0	28.0	31.1	32.6
C23	0	16.1	17.7	18.4
C46	0	5.1	5.4	5.4
C7P1	0	0	0	0
C7P2	0	0	0	0
C7P3	0	0	0	0

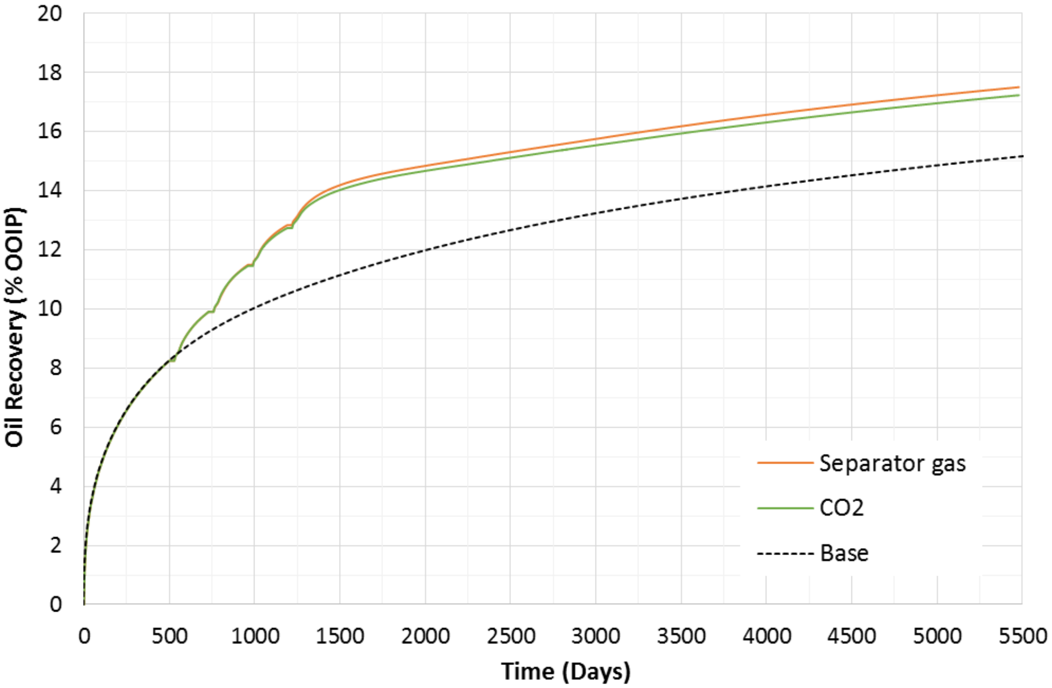

Figure 3-43. Oil recovery for different injection gas compositions

The simple economic analyses presented in Sections 3.7 and 3.10 did not include incremental gas revenue because, as shown in Figure 3-33 (Section 3.8) and Table 3-16, a significant mole percentage of the produced gas consists of previously-injected CO_2. The analyses assumed no CO_2 recycling, either, and considered the cost of 100% "fresh" CO_2 in every cycle. Figure 3-44 compares the gas injected per cycle to the gas produced from the previous cycle for the case in Table 3-16. As Figure 3-43 shows, the gas produced in a Huff-and-Puff cycle is almost enough to fulfill the gas injection requirements of the next cycle. Although 100 mol% CO_2 is injected in the first cycle, CO_2 consumption would be significantly smaller in subsequent cycles.

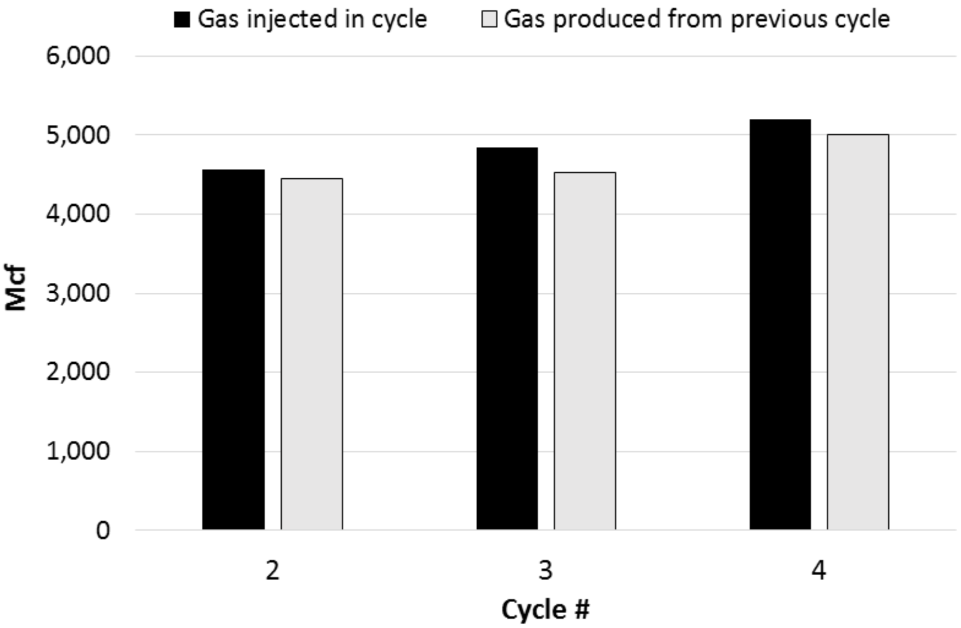

Figure 3-44. Gas injected in cycle vs. gas produced in previous cycle

Re-running the economic analysis of the single-fracture configuration for different numbers of Huff-and-Puff cycles (Table 3-7) assuming a 90% gas reutilization rate (90% of the gas injected in a cycle is produced gas from the previous cycle) significantly changes the economic outlook (Table 3-17). As Table 3-17 shows, the reduction of CO_2 acquisition costs has a dramatic impact on the per-cycle profitability. Please notice that the first cycle does not change from Table 3-7 because 100% CO_2 is being injected. Table 3-18 shows the numbers in Table 3-17 extrapolated from the single-stage, single-wing 10-ft.-thick computational domain to a 15-stage well in a 40-ft.-thick part of the Bakken. To obtain Table 3-18 from 3-17 a multiplier of 120 was applied: 2 x_f × 15 stages × 4x the domain thickness. Table 3-18 gives an idea of the available margins for operating expenses and gas pressurization costs if gas recycling is implemented. The results in this section indicate that produced gas reinjection is technically effective and economically efficient, and could significantly improve the commercial viability of Huff-and-Puff.

Table 3-17 – Economics for different number of cycles, 90% gas reutilization rate

Number of cycles	**Cumulative oil recovery (stb)**	**Cumulative CO_2 injected (Mcf)**	**Oil revenue per cycle ($ USD)**	**CO_2 cost per cycle ($USD)**	**Profit per cycle (before taxes and OPEX, $USD)**
Base	3,390	0	N/A	N/A	N/A
1	3,570	4,920	16,050	9,840	6,210
2	3,650	5,401	7,790	962	6,830
3	3,740	5,918	7,300	1,030	6,270
4	3,810	6,488	6,480	1,140	5,340
5	3,870	7,078	5,850	1,180	4,670
6	3,930	7,708	4,790	1,260	3,530
7	3,960	8,358	3,210	1,300	1,910
8	3,990	9,038	2,250	1,360	890

Table 3-18 – Economics for different number of cycles, 90% gas reutilization rate, 15-stage well in 40-ft.-thick part of the Bakken

Number of cycles	**Cumulative oil recovery (stb)**	**Cumulative CO_2 injected (Mcf)**	**Oil revenue per cycle ($ USD)**	**CO_2 cost per cycle ($USD)**	**Profit per cycle (before taxes and OPEX, $USD)**
Base	406,800	0	N/A	N/A	N/A
1	428,400	590,400	1,926,000	1,181,000	745,200
2	438,000	648,100	934,800	115,400	819,400
3	448,800	710,200	876,000	124,100	751,900
4	457,200	778,600	777,600	136,800	640,800
5	464,400	849,400	702,000	141,600	560,400
6	471,600	925,000	574,800	151,200	423,600
7	475,200	1,003,000	385,200	156,000	229,200
8	478,800	1,085,000	270,000	163,200	106,800

4. Mortar Coupling Modeling of Fracture-Matrix Systems

The reservoir model created for this study (Chapter 2) is a multi-phase, multi-component, and multi-dimensional system that solves complex mass and energy balances to describe fluid behavior in the subsurface. Huff-and-Puff, in particular, is an extremely complicated process to simulate: the constant alternation between injection and production subjects to the reservoir to sudden changes in pressure, composition, and saturation. Numerical errors occur when these variations are too dramatic from one timestep to the next, causing failures in convergence in the simulation. These errors are especially likely to occur in the fracture and near-fracture region of the domain, where the grid-blocks have small volumes (due to local refining, which is needed for accuracy as shown in Section 3.9) and experience large influxes of mass during injection and production.

As explained in the *Computational Domain* section of this study (Section 2.2), over-discretization introduces numerical instability by increasing the likelihood of extreme pressure and composition variations in a given block. Furthermore, the large difference in permeability between the fracture and the matrix creates transmissibility contrasts that may result in ill-conditioned systems. The permeability contrast between the proppant and the silty Middle Bakken matrix is of 6 orders of magnitude (10^4 to 10^{-2} mD), and it is even larger in tighter shale formations like the Barnett. Reducing this contrast is one of the reasons for modeling the pseudo-fracture described in Section 2.2.1. A 2-ft. wide, 25-mD fracture behaves as a 0.005-ft., 10,000-mD fracture, but it has two significant advantages: 1) it can withstand larger influxes/outfluxes of mass in a given timestep because of its larger volume (mitigating extreme variations in pressure and composition), and 2) it reduces the permeability contrast between the fracture and the matrix from 6 to 3 orders of magnitude.

As discussed in Section 2.2.1, the pseudo-fracture is an excellent approximation of the actual hydraulic fracture. However, it is not perfect, as it slightly underestimates cumulative recovery for parts of the simulation. An important part of this study involves exploring alternative techniques for modeling hydraulically-fractured reservoirs. One of these numerical methods, called mortar coupling, solves two or more domains separately and then couples them together by imposing continuity at their shared boundary (called the interface). This is particularly applicable to stimulated reservoir models because the fracture and the matrix are two distinctly different regions in terms of permeability (relative and absolute), pressure transient behavior, and fluid dynamics. A detailed description of mortar coupling is included in Section 4.2.3. In order to determine the viability of this method in hydraulically-fractured reservoirs models, a very simple problem was considered: the Cinco-Ley et al. (1978) semi-analytical solution for single-phase flow into a vertical finite-conductivity fracture, which is described in Section 4.1.

4.1. CINCO-LEY ET AL.'S (1978) FINITE-CONDUCTIVITY FRACTURE MODEL

Cinco-Ley et al. (1978) developed a semi-analytical model to describe "the transient behavior of a well with a finite-conductivity vertical fracture in an infinite-slab reservoir." They considered two flow regions, the reservoir and the fracture, and made the following assumptions:

1. The reservoir is an isotropic, homogeneous, horizontal slab bound vertically by impermeable strata.

2. The reservoir has constant thickness (h), permeability (k), and porosity (φ).

3. The reservoir contains a slightly-compressible fluid of constant viscosity (μ) and compressibility (c).

4. Production occurs through a vertical hydraulically-fractured well.

5. The hydraulic fracture is fully-penetrating, has finite conductivity, and has constant dimensions and properties: fracture half-length (x_f), width (w), permeability (k_f), and porosity (φ_f).

The fracture flow model (Figure 4-1) considers flow into the fracture at a rate $q(x,t)$ per unit length. Flow across the edge is considered negligible because the fracture's width is considerably smaller than its length. Flow is assumed to be linear in the fracture, and production is driven by a constant flux plane at the wellbore axis ($x = 0$ in Figure 4-1). Unsteady-state flow in the fracture is described by Eq. 4-1, subject to the initial condition in Eq. 4-2 and the boundary conditions in Eq. 4-3 and 4-4. Eq. 4-2 states that at $t = 0$ the pressure in the fracture is equal to the initial pressure p_i. Meanwhile, Eq. 4-3 describes the constant flux plane at the wellbore axis, and Eq. 4-4 imposes a no-flow boundary through the fracture edge (Cinco-Ley et al., 1978).

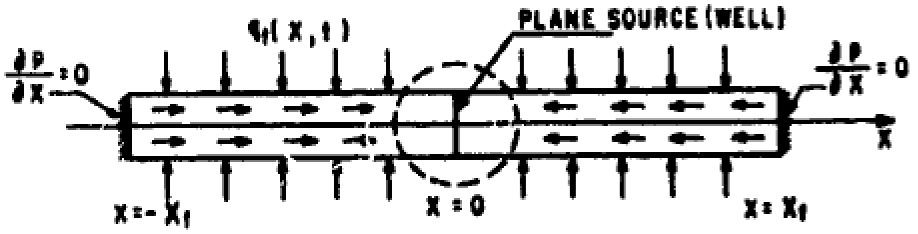

Figure 4-1. Fracture flow model for Cinco-Ley semi-analytical solution (Cinco-Ley et al., 1978)

$$\frac{\partial^2 p_f}{dx^2} + \frac{\mu}{k_f}\frac{q_f(\mathrm{x},\mathrm{t})}{wh} = \frac{\phi_f \mu c_{ft}}{k_f}\frac{\partial p_f}{\partial t} \tag{4-1}$$

$$p_f(x,\mathrm{t}=0) = p_\mathrm{i},\ 0 \le x \le x_f \tag{4-2}$$

$$\left.\frac{\partial p_f}{\partial x}\right|_{x=0} = -\frac{q_w \mu}{2wk_f h} \tag{4-3}$$

$$\left.\frac{\partial p_f}{\partial x}\right|_{x=x_f} = 0 \tag{4-4}$$

In Eq. 4-1, q_f *(x,t)* is "a source term that represents the fluid flow from the reservoir to the fracture" (Cinco-Ley et al., 1978). The dimensionless flux into the fracture is given by Eq. 4-5, where $q_\mathrm{f}(x',\tau)$ is the rate per unit length at which fluid enters the fracture at location *x'* and time τ, and q_w is the total flow rate into the well. The dimensionless pressure drop, where *B* is the formation volume factor of the fluid, is given in Eq. 4-6, and the dimensionless time t_D is shown in Eq. 4-7 (Cinco-Ley et al., 1978).

$$q_{fD}(x',\tau) = \frac{2q_f(x',\tau)}{q_w}x_f \tag{4-5}$$

$$p_{fD}(xD,tD) = \frac{kh[\mathrm{p_i} - \mathrm{p(x,t)}]}{141.2\,q_w B\,\mu} \tag{4-6}$$

$$t_D = \frac{0.000264\,kt}{\phi \mu c_t x_f^2} \tag{4-7}$$

The reservoir flow model is defined by Eq. 4-8, which describes the transient pressure behavior in the reservoir in terms of the dimensionless pressure drop. Eq. 4-9 gives the dimensionless pressure drop at any point (x_D, y_D) in the reservoir at time t_D (Cinco-Ley et al., 1978). The reservoir flow model is shown in Figure 4-2.

$$p_D(x_D, y_D, t_D) = \frac{kh[\mathrm{p_i} - \mathrm{p(x, y, t)}]}{141.2 q_w B \mu} \tag{4-8}$$

$$p_D(\mathrm{x_D}, \mathrm{y_D}, \mathrm{t_D}) = \frac{1}{4}\int_0^{t_D}\int_{-1}^{1} q_D(x', \tau) \frac{\exp\left[-\frac{(x_D - x')^2 + y_D^2}{4(t_D - \tau)}\right]}{(t_D - \tau)} dx' d\tau \text{, where} \tag{4-9}$$

$$q_D(x', \tau) = \frac{2q(x', \tau)}{q_w} x_f \text{, and} \tag{4-10}$$

$$x_D = \frac{x}{x_f}\ ;\ y_D = \frac{y}{x_f} \tag{4-11; 4-12}$$

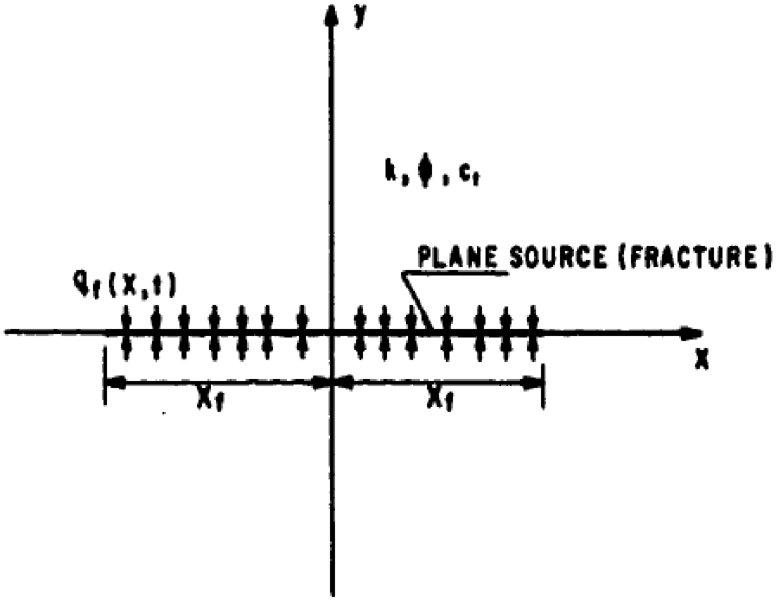

Figure 4-2. Reservoir flow model for Cinco-Ley semi-analytical solution (Cinco-Ley et al., 1978)

Cinco-Ley et al. (1978) coupled the fracture and the reservoir by imposing continuity between the two flow regions. They established the condition that the dimensionless pressure drop and flux density in the fracture (p_{fD} and q_{fD}) must be equal to their counterparts in the reservoir (p_{D} and q_{D}):

$$p_{fD}(x_D,t_D) = p_D(x_D, y_D = 0, t_D)\text{, and} \tag{4-13}$$

$$q_{fD}(x_D,t_D) = q_D(x_D,t_D) \tag{4-14}$$

Combining the two flow regions with the continuity conditions yields Eq. 4-15, which can be solved "by discretization in time and space so that the fracture is divided into 2*N* equal segments and time is divided into *K* intervals" (Cinco-Ley et al., 1978). Eq. 4-15 is solved for each $q_{\mathrm{D}\,i,j}$, the flux density of fracture segment *i* in time interval *j*. The full solution to Eq. 4-15 can be found in Cinco-Ley et al. (1978). C_{fDf} (Eq. 4-16) is the dimensionless fracture storage capacity, and n_{fD} (Eq. 4-17) is the dimensionless hydraulic fracture diffusivity.

$$\begin{aligned}&\frac{1}{C_{fDf}}\left\{\begin{array}{l} t_D + \dfrac{2}{\pi^2 n_{fD}}\displaystyle\sum_{n=1}^{\infty}\frac{1}{n^2}\cos(n\pi x_D)\cdot\left\{1-e^{-n_{fD}n^2\pi^2 t_D}\right\} \\ -\displaystyle\int_0^{t_D}\int_{-1}^{1} q_D(x',\tau)\left\{\frac{1}{2}+\sum_{n=1}^{\infty}\cos \mathrm{n}\,\pi\,(x_D-x')\,e^{-n_{fD}n^2\pi^2(t_D-\tau)}\right\}dx'd\tau \end{array}\right\} \\ &= \frac{1}{4}\int_0^{t_D} q_D(x',\tau)\frac{e^{-\frac{(x_D-x')^2}{4(t_D-\tau)}}}{(t_D-\tau)}dx'd\tau\end{aligned} \tag{4-15}$$

$$C_{fDf} = \frac{w\phi_f c_{ft}}{\pi x_f \phi c_t}\text{, and} \tag{4-16}$$

$$n_{fD} = \frac{k_f \phi c_t}{k \phi_f c_{ft}} \tag{4-17}$$

Cinco-Ley et al. (1978) used their solution to determine the flux distribution and dimensionless pressure drop along the fracture for several values of C_{fDf} and n_{fD}. They simulated cases for values between 2×10^{-6} to 1×10^{-3} for C_{fDf} and 1×10^{3} to 1×10^{8} for n_{fD}, which were based on published hydraulic fracture data. They observed that solutions could be correlated by a single parameter that combined the dimensionless storage capacity (C_{fDf}) and hydraulic diffusivity (n_{fD}). This parameter, called the dimensionless fracture conductivity (C_{D}), is shown in Eq. 4-18. As Eq. 4-18 shows, this correlation parameter does not depend on the porosity or compressibility of the formation.

$$C_{fDf}\, n_{fD} = C_D = \frac{k_f w}{\pi k x_f} \tag{4-18}$$

Cinco-Ley at al. (1978) compared their solution for a highly-conductive fracture ($C_{\mathrm{fDf}} = 1\times10^{-3}$, $n_{\mathrm{fD}} = 1\times10^{7}$, $C_{\mathrm{D}} = 1\times10^{4}$) to Gringarten et al.'s (1974) infinite conductivity solution (Figure 4-3). They found the solutions differed by less than 1% for "small" values of t_{D} and less than 0.025% for other values (Cinco-Ley et al., 1978). Figure 4-3 shows the dimensionless flux from the formation into the fracture (q_{fD}, Eq. 4-5) at different dimensionless times. It is a representation the flow distribution along the fracture length, from wellbore ($x_{\mathrm{D}} = 0$) to fracture tip ($x_{\mathrm{D}} = 1$). For example, at $t_{\mathrm{D}} = 1\times10^{-5}$ there is a uniform flow distribution along the fracture, as opposed to $t_{\mathrm{D}} = 2\times10^{-1}$ when most of the fluid is flowing into the fracture at the tip.

As Figure 4-3 shows, at early dimensionless times ($t_{\mathrm{D}} = 1\times10^{-5}$) the total area under the flux density curve is smaller than 1, meaning that the flow rate into the fracture is less than the total flow rate into the well (q_{w}). The storage capacity of the fracture accounts for the remaining fraction of q_{w}, as opposed to intermediate and late times during which well flow is driven exclusively by "the expansion of the system outside the fracture” (Cinco-Ley et al., 1978). In these cases ($t_D \geq 1\times10^{-4}$), the area under each flux distribution curve is equal to unity, as shown in Figure 4-3.

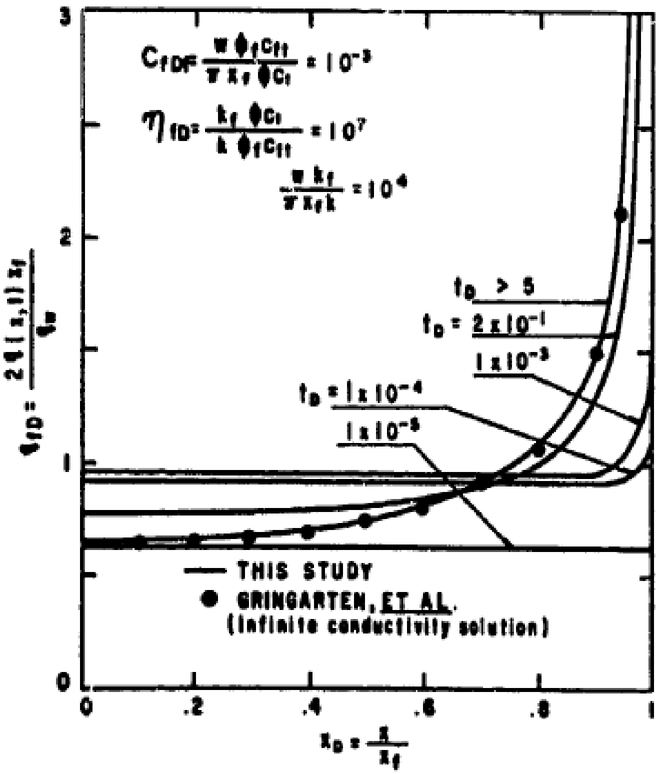

Figure 4-3. Flux distribution at various times along a highly-conductive vertical fracture (Cinco-Ley et al., 1978)

Cinco-Ley et al. (1978) studied the effect of C_D on the flux distribution when flow becomes stabilized at large values of t_D ($t_D \geq 5$). They found that for highly-conductive fractures ($C_D \geq 300$) flux density is highest at the fracture tip (Figure 4-4). Meanwhile, as fracture conductivity decreases, flux density becomes larger close to the wellbore. As Figure 4-4 shows, in a low conductivity fracture (C_D = 0.2) the flow distribution is noticeably slanted towards the first third of the fracture. According to Cinco-Ley et al. (1978), this is evidence that high-conductivity fractures are desirable in order to overcome flow restrictions in the near-wellbore region.

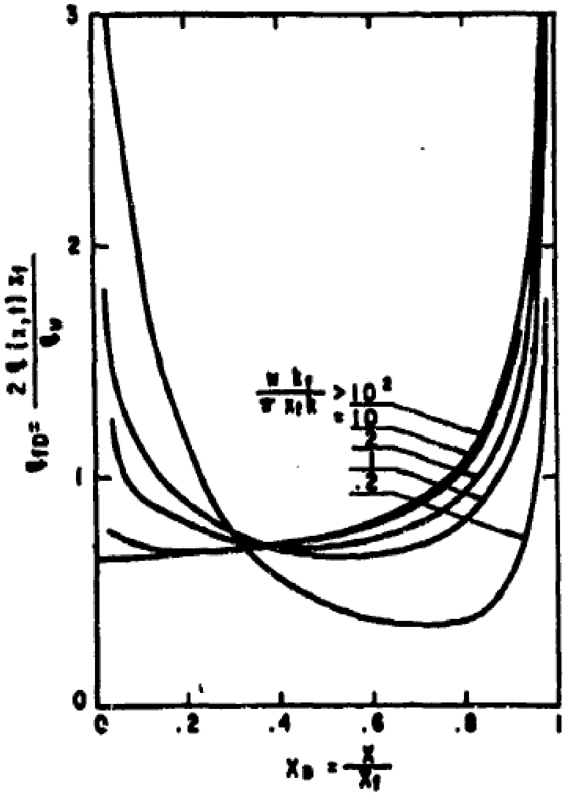

Figure 4-4. Stabilized flux distribution for different fracture conductivities (Cinco-Ley et al., 1978)

In terms of the stabilized ($t_D \geq 5$) pressure distribution in the fracture, Cinco-Ley et al. (1978) found that the pressure drop along the fracture is almost negligible for high-conductivity fractures. The pressure drop is defined as "the difference between the pressure at any point on the fracture and the pressure at the tip of the fracture" (Cinco-Ley et al., 1978). The pressure drop increases as the fracture conductivity decreases, and as the fracture permeability approaches the formation permeability the pressure distribution in the fracture becomes equal to the pressure profile for radial flow (Cinco-Ley et al., 1978). Figure 4-5 shows the stabilized dimensionless pressure drop distribution along a finite conductivity fracture for several values of C_D.

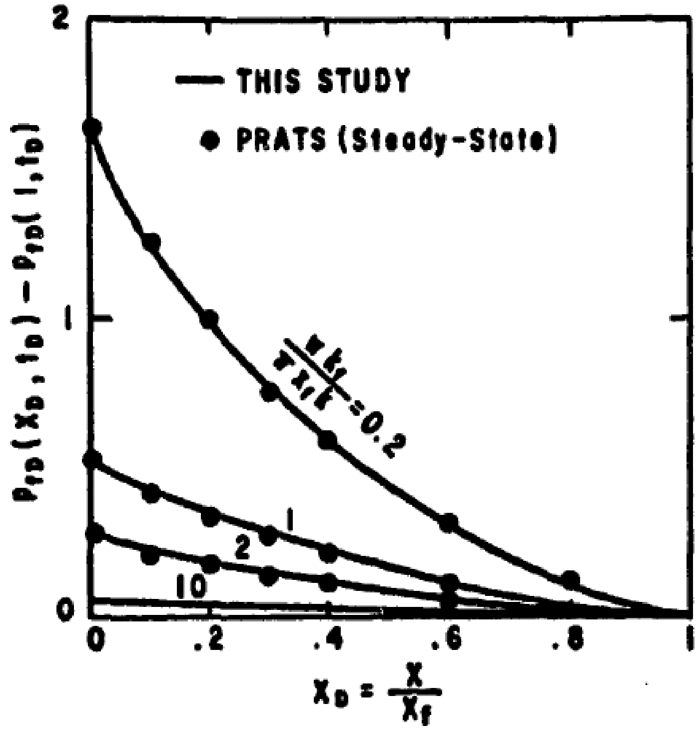

Figure 4-5. Dimensionless pressure drop distribution along a finite-conductivity fracture ($t_D \geq 5$) (Cinco-Ley et al., 1978)

4.2. NUMERICAL APPROACHES

This section presents the three numerical approaches taken to model the transient behavior of a finite-conductivity vertical fracture: replicating the Cinco-Ley et al. (1978) semi-analytical solution, developing a finite difference numerical reservoir simulator, and creating a mortar-based numerical simulator applying domain decomposition techniques.

4.2.1. Semi-Analytical Solution

Cinco-Ley et al.'s (1978) semi-analytical solution was coded into a Matlab program. The goal was to validate the program by replicating the figures from Cinco-Ley et al.'s (1978) paper, and use it to obtain the flux and pressure distributions for any value of the dimensionless storage and diffusivity parameters (C_{fDf} and n_{fD}). Figures 4-6, 4-7, and 4-8 show the semi-analytical solution from the Matlab program overlaid on top of Cinco-Ley et al.'s (1978) original plots (Figures 5, 6, and 7 in their paper). Cinco-Ley et al. (1978) divided the fracture into 20 equal segments for their simulations, and used 10 intervals per log cycle of dimensionless time, so the same discretization and time-stepping schemes were used in this study. As Figure 4-6, 4-7, and 4-8 show, there is excellent agreement between the Cinco-Ley et al. (1978) plots and the output from the Matlab program. The stabilized flux distributions (Figure 4-7) are almost perfectly reproduced, and the agreement is especially good in terms of the dimensionless pressure drop along the fracture (Figure 4-8). There are slight discrepancies in Figures 4-6 and 4-7 towards the fracture tip, but for the most part the results from the Matlab program are accurate reproductions of Cinco-Ley et al.'s (1978) semi-analytical solution for transient behavior in a finite-conductivity fracture.

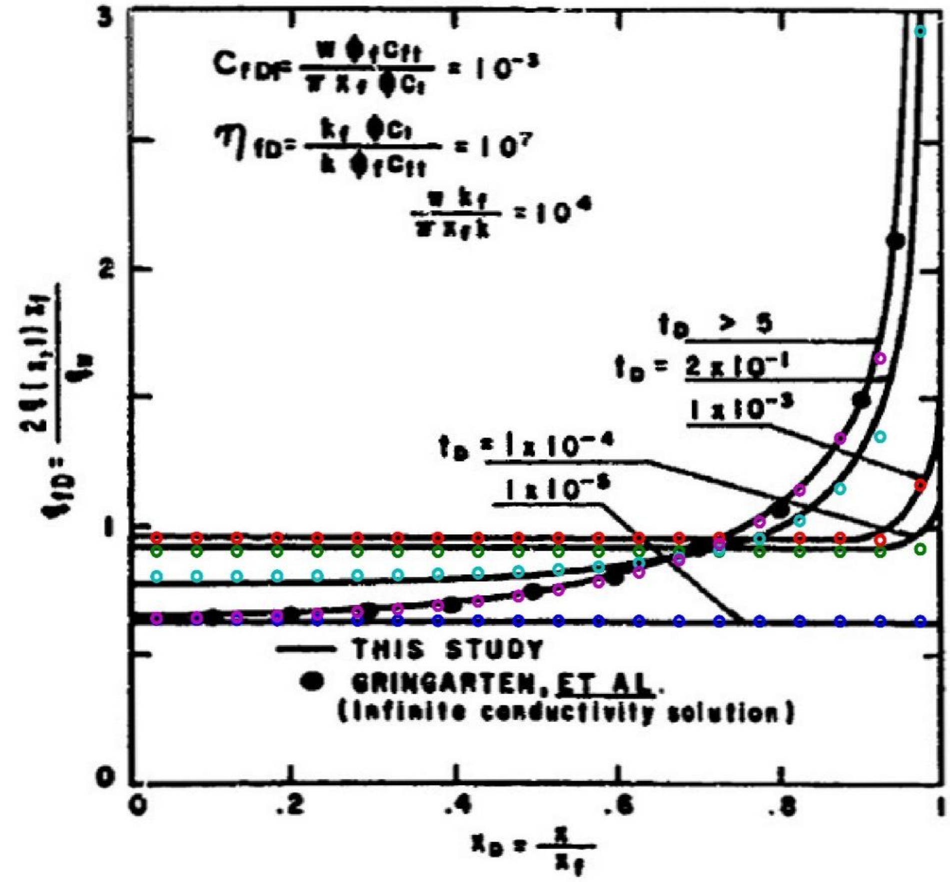

Figure 4-6. Comparison of Cinco-Ley et al. (1978) Figure 5 with Matlab program of their semi-analytical solution

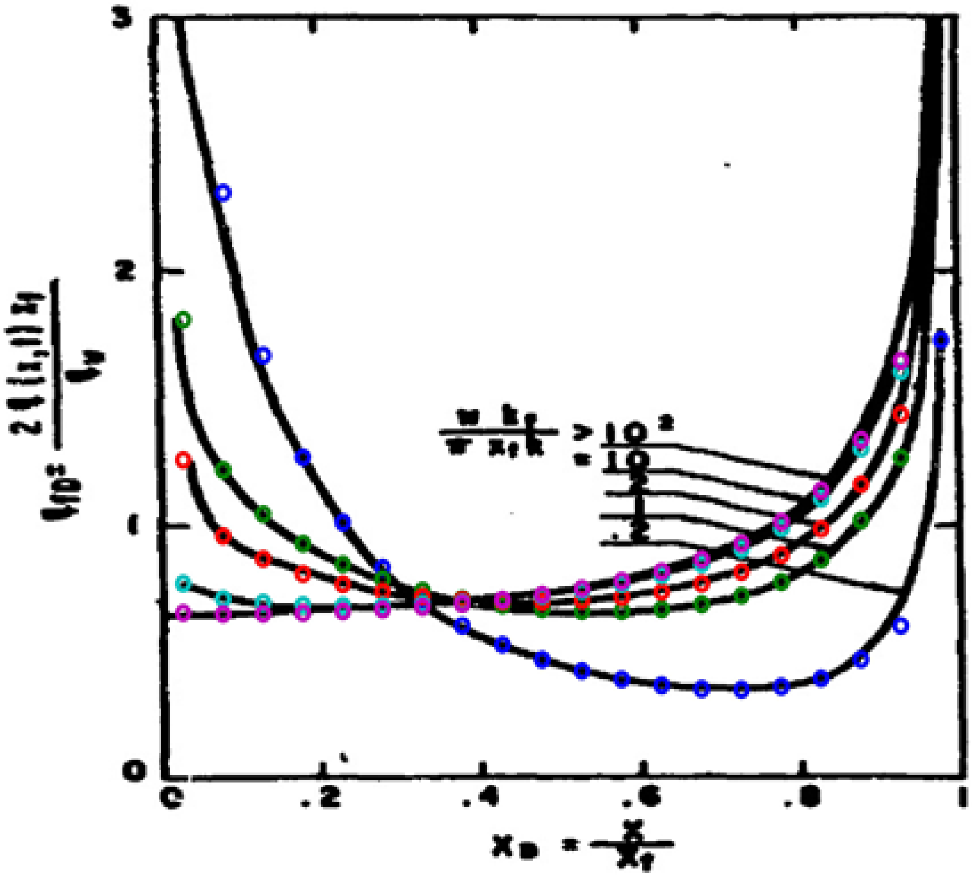

Figure 4-7. Comparison of Cinco-Ley et al. (1978) Figure 6 with Matlab program of their semi-analytical solution

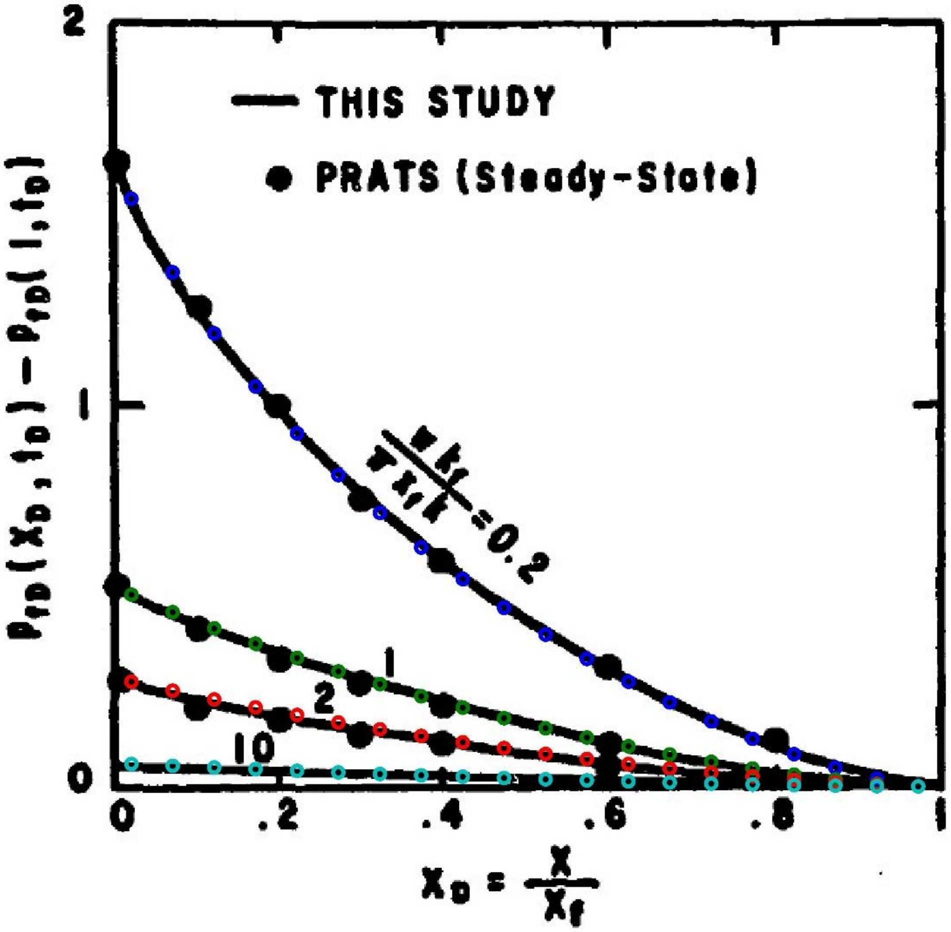

Figure 4-8. Comparison of Cinco-Ley et al. (1978) Figure 7 with Matlab program of their semi-analytical solution

Two variables of Cinco-Ley et al.'s (1978) semi-analytical solution were studied in order to try to improve the results from the Matlab program. The first involved the number of segments into which the fracture is discretized. Figure 4-9 shows a comparison between two cases trying to replicate Figure 5 in Cinco-Ley et al.'s (1978) original paper ($C_{fDf} = 1\times10^{-3}$, $n_{fD} = 1\times10^{7}$, $C_D = 1\times10^{4}$). 20 fracture segments were used in one and 50 in the other; 10 intervals per log cycle were used in both instances. As Figure 4-9 shows, the degree of accuracy is very similar regardless of the number of fracture segments; the

$t_D = 2\times10^{-1}$ curve is slightly off in both cases, and there are slight discrepancies around the fracture tip between the Matlab output and Cinco-Ley et al.'s (1978) plot.

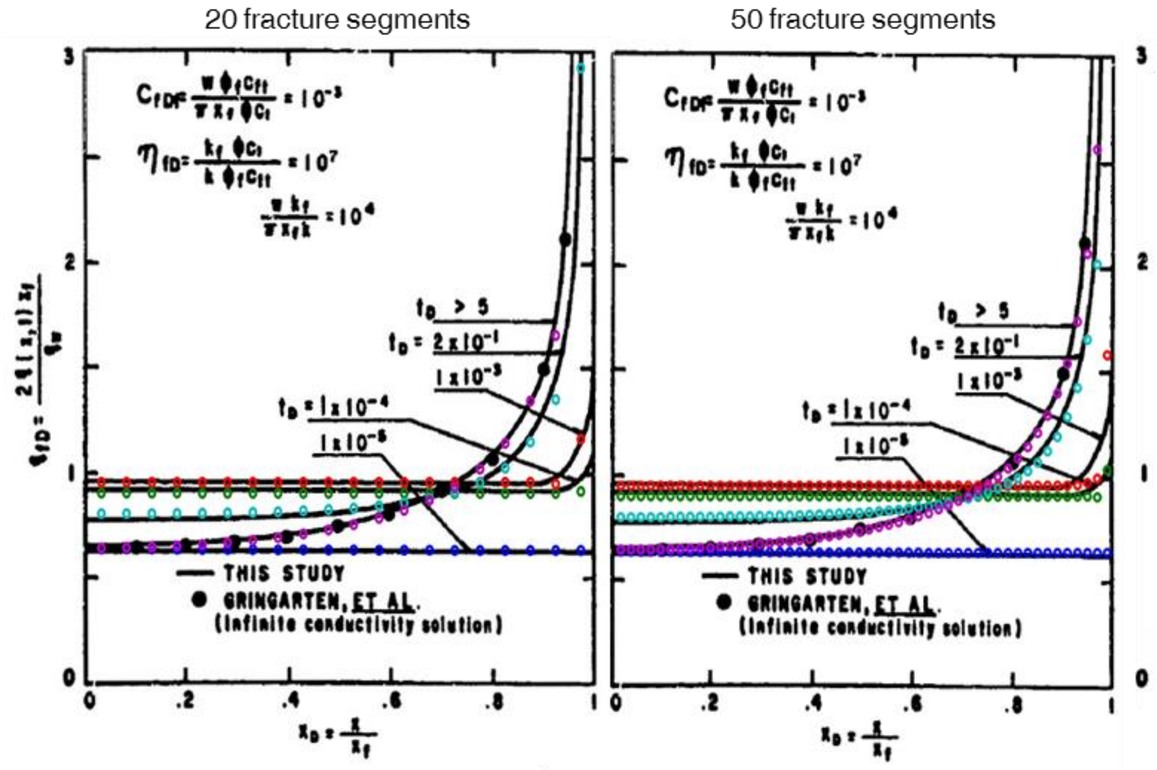
20 fracture segments

50 fracture segments

Figure 4-9. Comparison of Cinco-Ley et al.'s (1978) solution for different number of fracture segments

The second variable studied was the number of intervals per log cycle. Three cases were considered: 6, 10, and 20 intervals. In all cases, 20 fracture segments were used. Once again, Figure 5 from Cinco-Ley et al.'s (1978) paper was used as the basis for comparison. Figure 4-10 shows the 6 and 10-interval cases, while Figure 4-11 shows 10 and 20 intervals per log cycle. As Figures 4-10 and 4-11 show, there is no discernible difference between the three sets of results. Taking smaller dimensionless timesteps does not appear to have any advantages in terms of improved accuracy, while significantly impacting the total computation time.

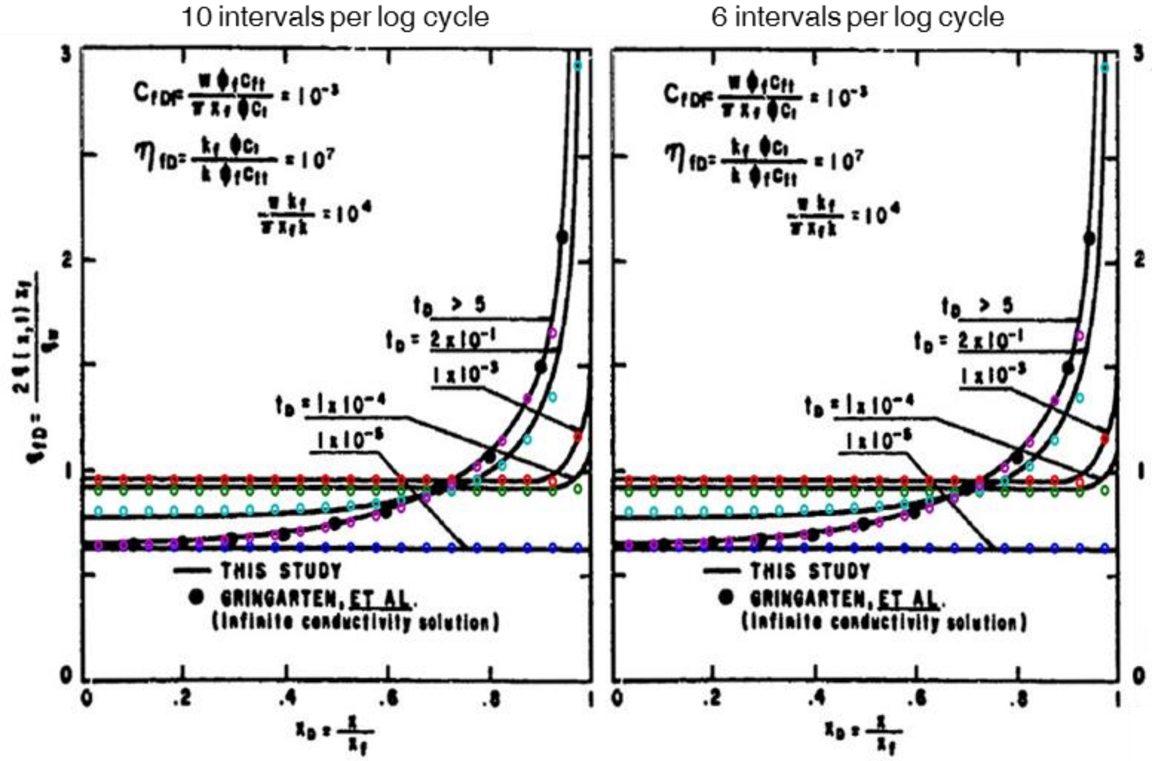

10 intervals per log cycle

6 intervals per log cycle

Figure 4-10. Comparison of Cinco-Ley et al.'s (1978) solution for different number of intervals per log cycle (6 vs. 10)

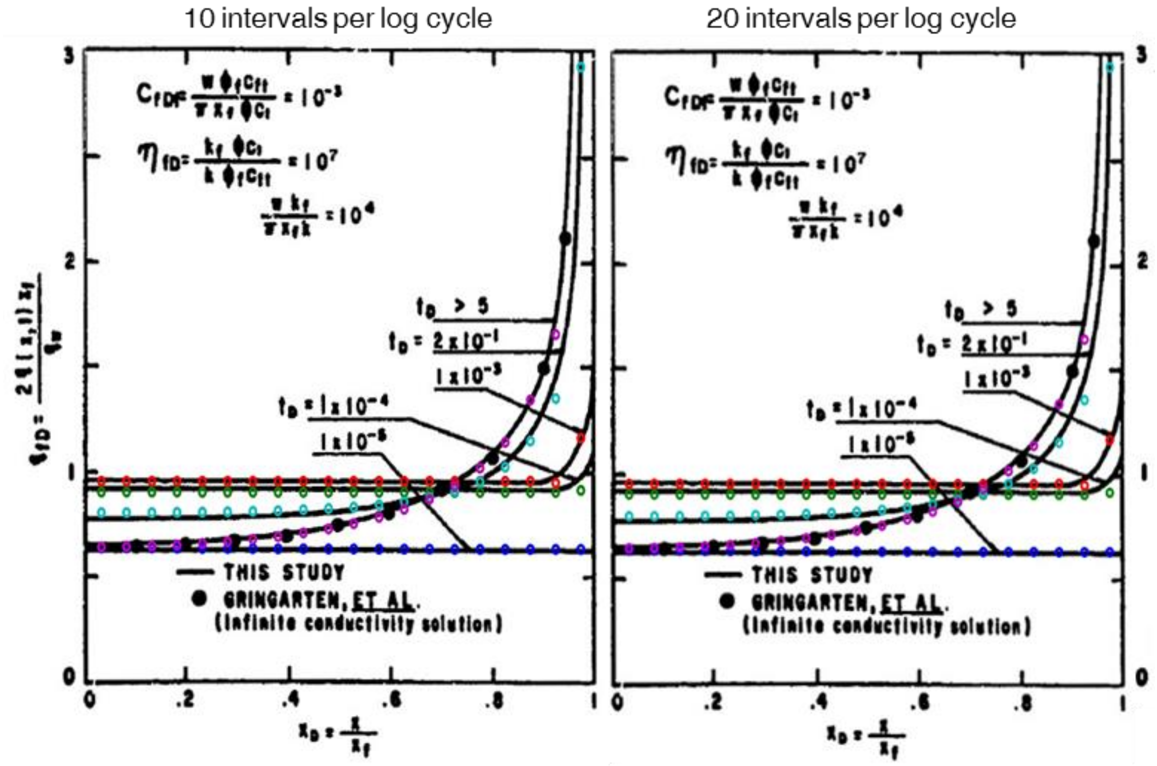

Figure 4-11. Comparison of Cinco-Ley et al.'s (1978) solution for different number of intervals per log cycle (10 vs. 20)

It is important to mention that the results for Cinco-Ley et al.'s (1978) semi-analytical solution for early times ($t_D \leq 1\times10^{-4}$) are affected by the first dimensionless timestep (Δt_{Di}). Figure 4-12 shows two cases: one in which the first dimensionless timestep was 1×10^{-5} and another in which it was 1×10^{-6}. Ten intervals per log cycle were used in both instances. The case with $\Delta t_{Di} = 1\times10^{-5}$ matches Cinco-Ley et al.'s (1978) plot perfectly at $t_D = 1\times10^{-5}$, while the simulation with the initial dimensionless timestep of 1×10^{-6} is off by roughly 15%. The results at later times ($t_D \geq 1\times10^{-4}$) are identical in both cases. From these results, it can be assumed that Cinco-Ley et al. (1978) used an initial dimensionless timestep of 1×10^{-5}, which is not documented in their paper.

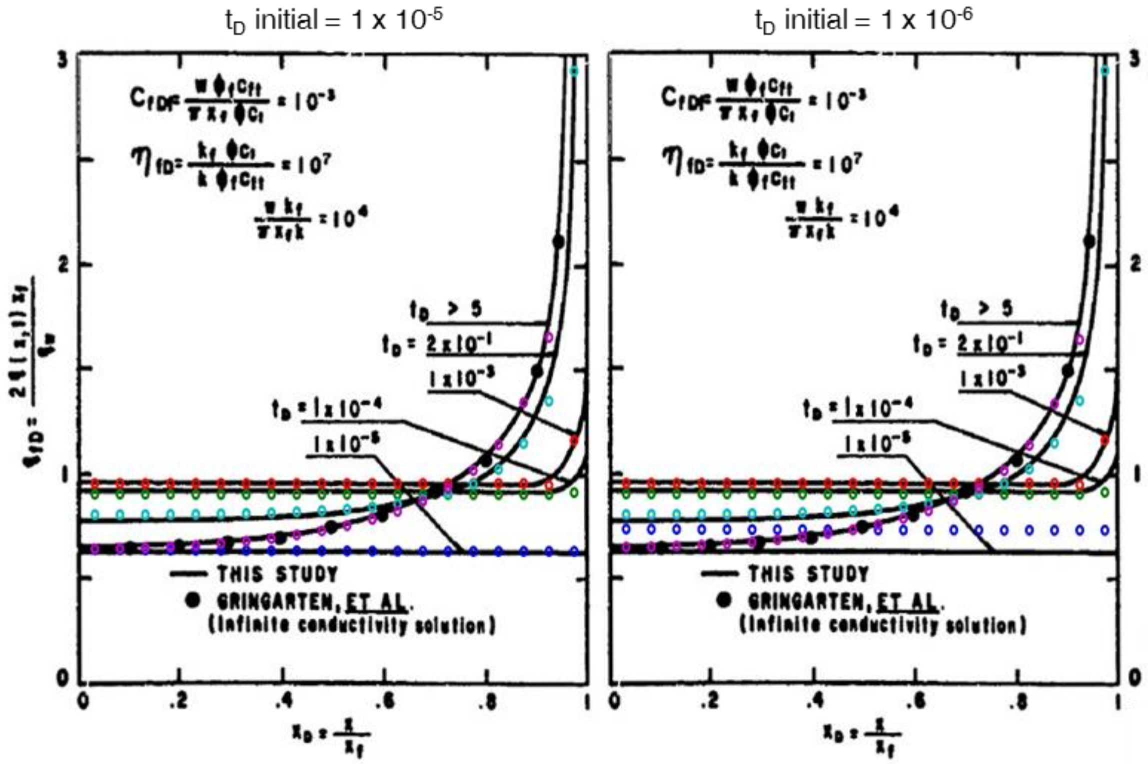
t_D initial = 1 x 10^{-5}

t_D initial = 1 x 10^{-6}

Figure 4-12. Comparison of Cinco-Ley et al.'s (1978) solution for different initial dimensionless times

4.2.2. Full-Domain Finite Difference Modeling

A finite difference numerical reservoir simulator was developed in order to replicate Cinco-Ley et al.'s (1978) semi-analytical solution. In this approach, the fracture is modeled explicitly, as a series of thin high-permeability grid blocks. The domain consists of one quarter of a hydraulically-fractured rectangular reservoir of length 2^*L_x and width 2^*L_y with the assumptions listed for the Cinco-Ley et al. (1978) model in Section 4.1 (Figure 4-13). Figure 4-14 shows the discretization of the domain. The shaded region corresponds to a hydraulic fracture of width w, half-length x_f, and fracture permeability k_f. The reservoir is discretized into N_x blocks in the x-direction and N_y blocks in the y-direction. Meanwhile, the fracture is modeled as an N_{fx} by N_{fy} sector of blocks of constant length and width[5]. The fracture blocks are assigned permeability k_f, while the remaining blocks are assigned matrix permeability k. The domain bisects the hydraulic fracture along its length, which is why only half of the fracture width is modeled. Local refinement is applied around the fracture: the grid blocks get wider in the y-direction and longer in the x-direction as they approach the edge of the reservoir. A constant pressure or constant rate source term is placed along the edge of the fracture (shown in bold in Figure 4-14) in order to simulate production. Neumann (no-flux) boundary conditions are imposed on all other boundaries. The entire system (fracture + matrix) is solved together implicitly as a single domain, moving forward in time from $t_{initial}$ until t_{final}.

---

[5] Length: x_f / N_{fx} ; Width: $w/(2^*N_{fy})$

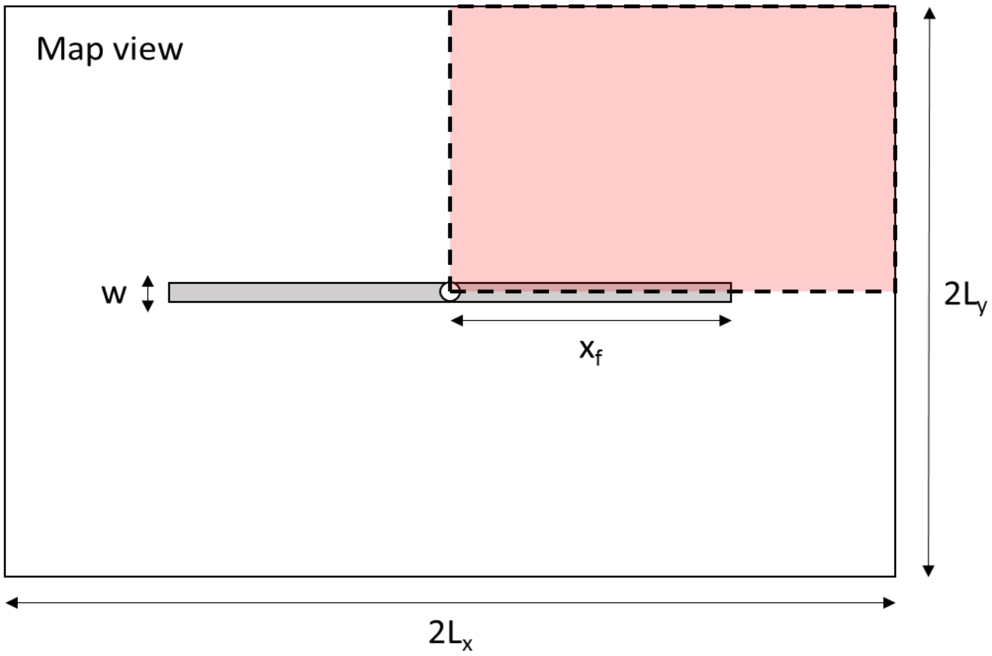

Figure 4-13. Reservoir model domain (shaded in red)

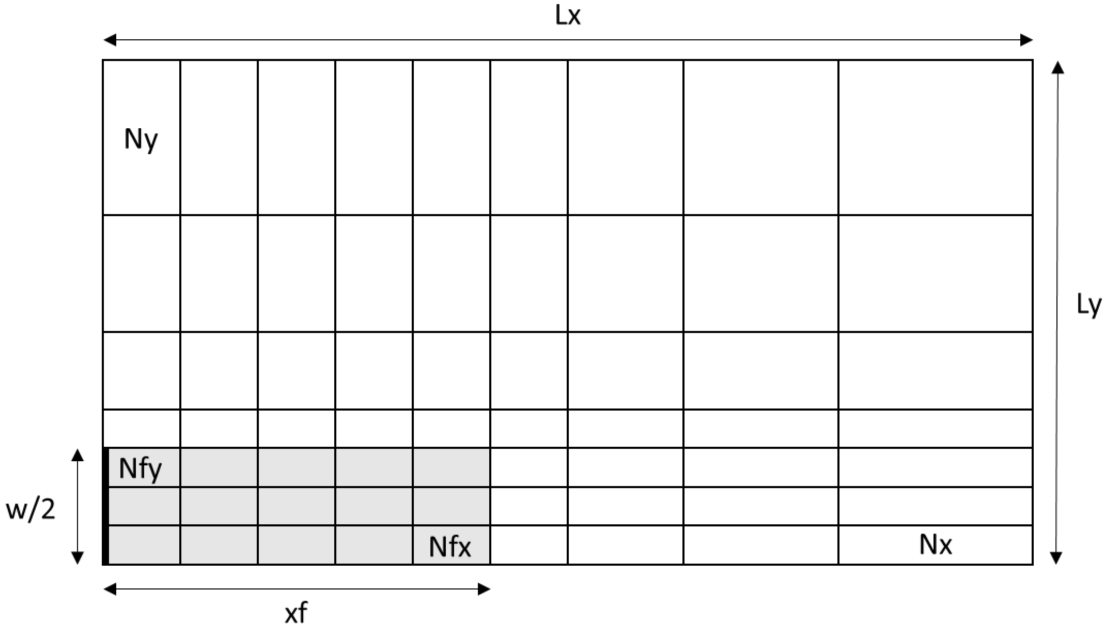

Figure 4-14. Domain discretization for finite difference model

Values for the fracture width (w) and matrix permeability (k) are calculated from the C_{fDf} and n_{fD} inputs. The porosity and total compressibility of the fracture and matrix are set equal to each other in order to clear terms (Eq. 4-19 and 4-20). By doing this, n_{fD} becomes the ratio of fracture to matrix permeability, and C_{fDf} turns into a measure of the fracture's width with respect to its half-length. The fracture width is calculated from C_{fD} using Eq. 4-21, and the matrix permeability is calculated from n_{fD} assuming a fracture permeability of 10,000 mD (Eq. 4-22).

Assuming $c_{\mathrm{tf}} = c_{\mathrm{t}}$ and $\varphi = \varphi_{\mathrm{f}}$:

$$C_{fDf} = \frac{w}{\pi x_f};\ n_{fD} = \frac{k_f}{k} \tag{4-19; 4-20}$$

$$w = \pi C_{fDf} x_f \tag{4-21}$$

$$k = \frac{k_f}{n_{fD}} \tag{4-22}$$

Figure 4-15 shows the stabilized ($t_{\mathrm{D}} \geq 5$) pressure distribution for a case with $C_{\mathrm{fDf}} = 1\times10^{-3}$, $n_{\mathrm{fD}} = 1\times10^{7}$, and $C_{\mathrm{D}} = 1\times10^{4}$. The fracture half-length (x_{f}) was set equal to 1,000 ft., and $L_{\mathrm{x}} = L_{\mathrm{y}} = 5*x_{\mathrm{f}}$ (5,000 ft.). The reservoir was discretized into 50 grid blocks in the x-direction (N_{x}) and 30 in the y-direction (N_{y}); 20 grid blocks were used for the fracture ($N_{\mathrm{fx}} = 20$, $N_{\mathrm{fy}} = 1$). Fracture half-width ($w/2$) was 1.57 ft., matrix permeability was 0.001 mD, and fracture permeability was 10,000 mD. Initial reservoir pressure was 1,000 psi, and a 100-psi constant pressure source term was placed at the wellbore. The gridding scheme can be seen in Figure 4-15, including the local refinement around the fracture. The pressure distribution is as expected: pressure is lowest at the fracture and increases towards the edge of the reservoir. Because this is a highly-conductive fracture ($C_{\mathrm{D}} \geq 300/\pi$), there is a negligible pressure drop along the fracture length. As Figure 4-16 shows, pressure is practically constant inside the fracture, from tip to wellbore. On the other hand, Figure 4-17 shows a low-conductivity fracture with a dimensionless fracture conductivity (C_D) of 1 ($C_{fDf} = 1\times10^{-3}$, $n_{fD} = 1\times10^{3}$). The fracture dimensions were the same as for the highly-conductive model ($x_f = 1{,}000$ ft., $w/2 = 1.57$ ft.), but the matrix permeability was 10,000 times larger (10 mD vs. 0.001 mD). As Figure 4-17 shows, there is a significant pressure drop from fracture tip to wellbore, which is consistent with the finite-conductivity transient behavior shown in Figure 4-8.

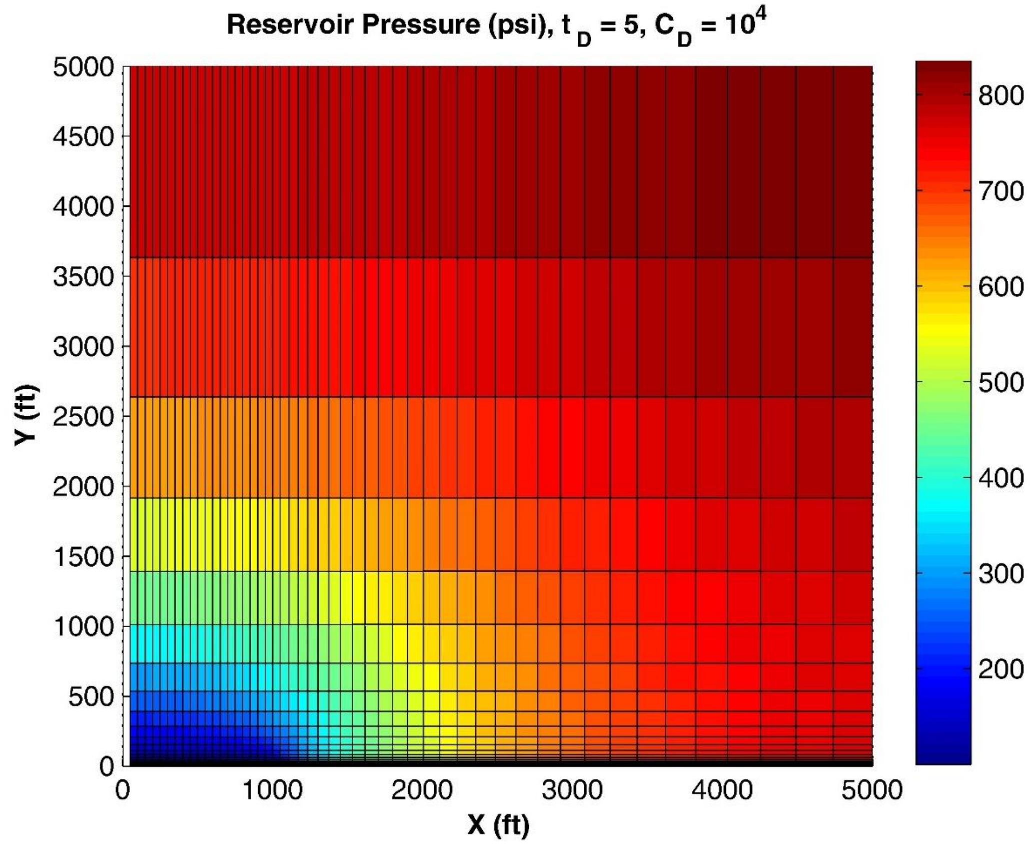

Figure 4-15. Gridding example for full-domain finite difference model

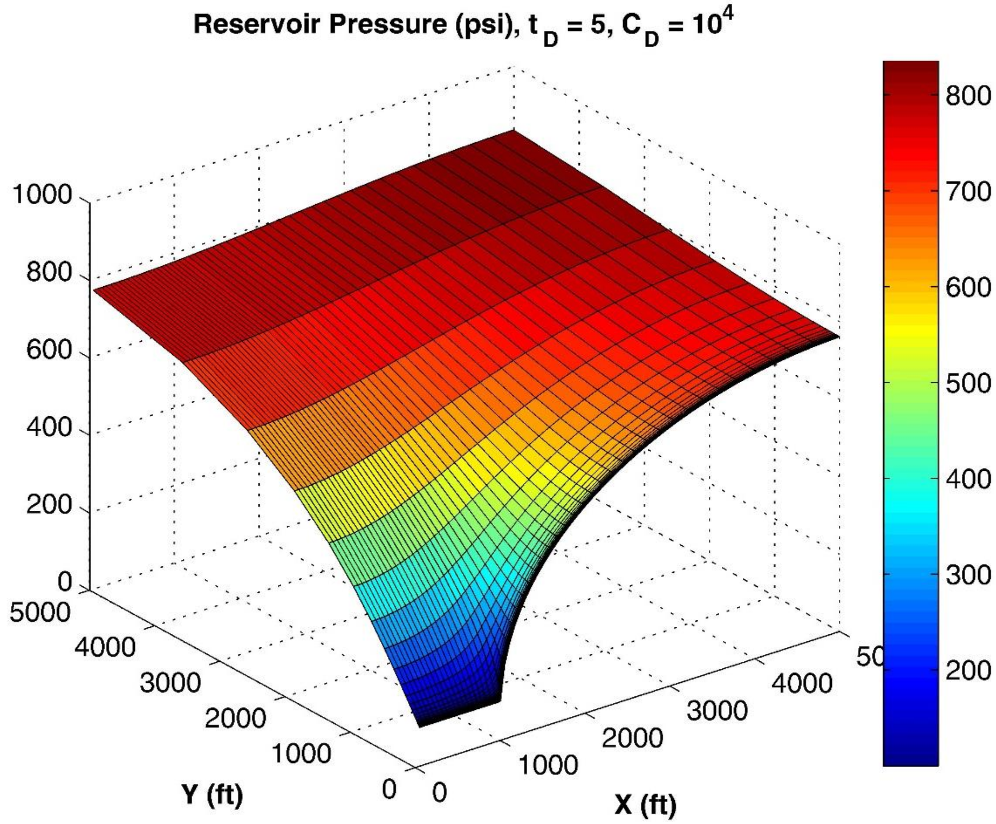

Figure 4-16. Pressure distribution for full-domain finite difference model, high-conductivity fracture

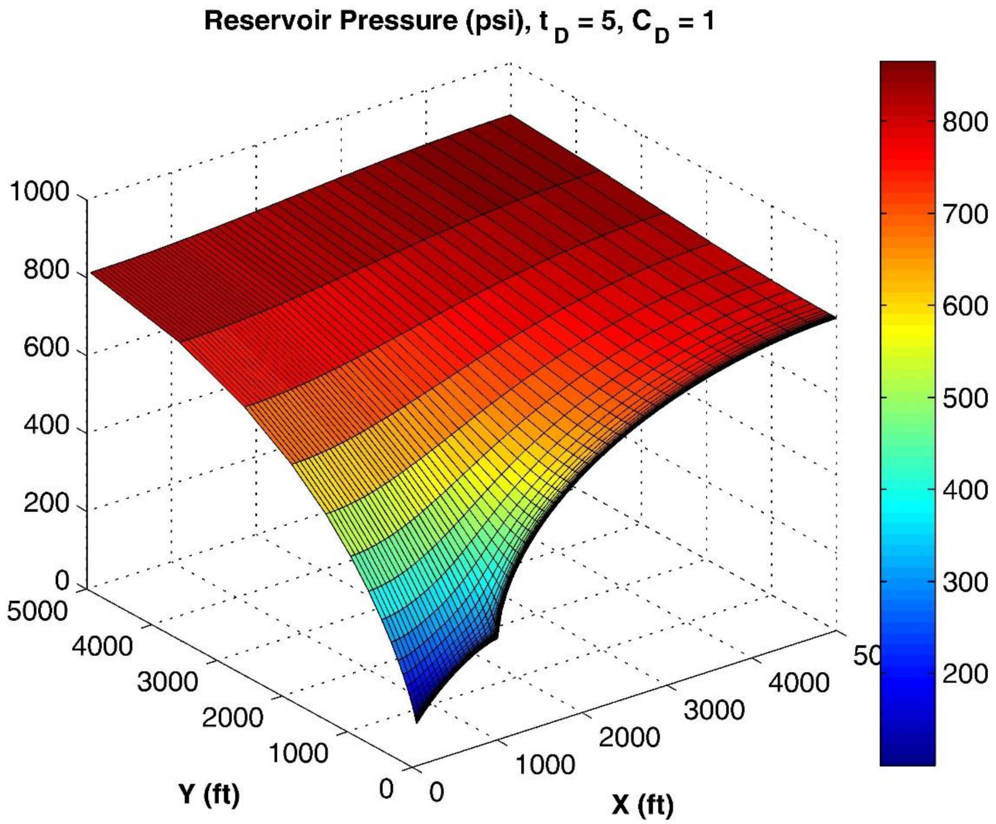

Figure 4-17. Pressure distribution for full-domain finite difference model, low-conductivity fracture

4.2.3. Mortar Coupling

The alternative to finite difference modeling of the full domain involves a domain decomposition technique known as mortar coupling. Mortar coupling allows for the matrix and fracture to be solved independently of each other and then coupled together by imposing continuity conditions (of flux, pressure, concentration, and/or other variables) at the fracture-matrix interface. The fracture-matrix interface (i.e., the mortar space) is discretized into elements called nodes, which construct the interface condition profile (pressure, concentration, etc.) and provide the boundary conditions for both subdomains (Arbogast et al., 2007). The interface condition at the nodes is iterated on, re-solving both subdomains in every iteration until the continuity criteria are met. After continuity is achieved the simulation moves forward in time and the process is repeated. In this study, flux continuity at the interface was imposed as the criterion for convergence. In other words, the total flow rate in or out of the matrix had to be equal (but opposite in sign) to the flow rate in or out of the fracture. Pressure was used as the interface condition – the pressure at the nodes was iterated on until flux continuity at the interface was obtained.

The main advantage of mortar coupling is that it breaks down a large, complex system into smaller, simpler subdomains. Because continuity is satisfied weakly through finite-element basis functions, the subdomains can contain different meshes (finer or coarser gridding), flow mechanisms, physics, or even scales (Sun, 2012). For example, Balhoff et al. (2007) showed that it is possible to couple pore-scale to continuum-scale models (Figure 4-18), and Sun (2012) developed a multi-scale simulator that "enables performing pore-scale simulation directly at the field scale." Mortar coupling's capability of handling various scales and physics is especially useful when dealing with distinctly different regions within the same system. In hydraulically-fractured reservoirs, flow behavior in the high-permeability fracture is significantly different from flow in the tight, ultralow-permeability matrix. From a numerical standpoint, stability is expected to be enhanced by eliminating large permeability contrasts from both subdomains. The high-permeability fracture and the low-permeability matrix are no longer solved together as a single system, but as independent subdomains that are later coupled together.

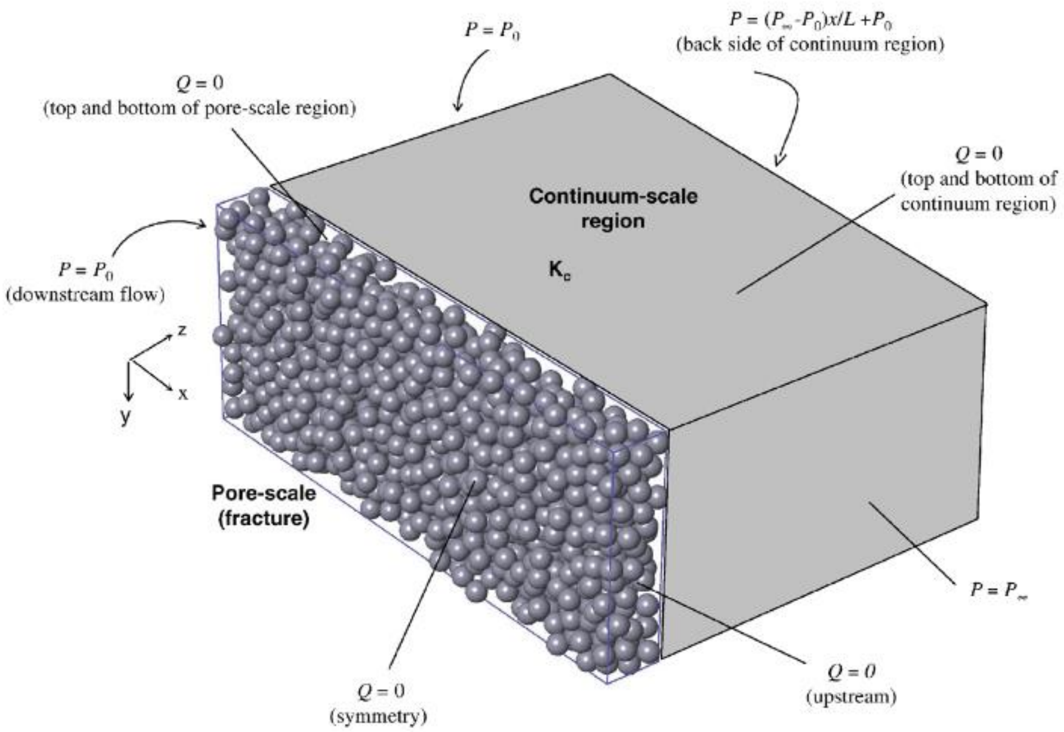

Figure 4-18. Schematic of coupled pore-scale and continuum regions (Balhoff et al., 2007)

A numerical reservoir simulator was built to model the domain in Figure 4-13 using a mortar coupling approach. This is the same system solved by the full-domain finite difference method, but decomposed into two regions: fracture and matrix. Figure 4-19 shows a representation of the two subdomains and the fracture-matrix interface. As in the full-domain finite difference model, the fracture (shaded in grey) is discretized into

$N_{fx} \times N_{fy}$ grid blocks of constant length and width. The matrix side is discretized into $N_x \times N_y$ blocks, and local refining can be applied parallel to the boundary in contact with the fracture. On the matrix side, the number of blocks in contact with the fracture is designated by N_{xf}[6]. In Figure 4-19 the interface (dashed line) has been divided into three nodes, but any number can be used as long as the mortar space is not over-discretized. Dirichlet (constant pressure) boundary conditions are imposed on both subdomains along the fracture-matrix interface. No-flow boundaries are assumed everywhere else, except for a source term on the edge of the fracture to simulate production. The Dirichlet constraints for both subdomains are obtained by projecting the pressure distribution at the interface onto the boundaries; an example can be seen in Figure 4-20. As Figure 4-20 shows, both subdomains can contain different gridding – in this example, the fracture has five grid blocks in contact with the matrix ($N_{fx} = 5$), while the matrix has four grid blocks in contact with the fracture ($N_{xf} = 4$). This is possible with mortar coupling, but not with full-domain models, in which N_{fx} is always equal to N_{xf} because the domain is discretized as a single system. This feature of mortar coupling provides great flexibility in areas of the reservoir that require a high degree of grid refining in order to achieve the desired accuracy.

---

[6] Please notice the difference between N_{fx}, the number of fracture grid blocks in the x-direction, and N_{xf}, the number of matrix grid blocks in contact with the fracture.

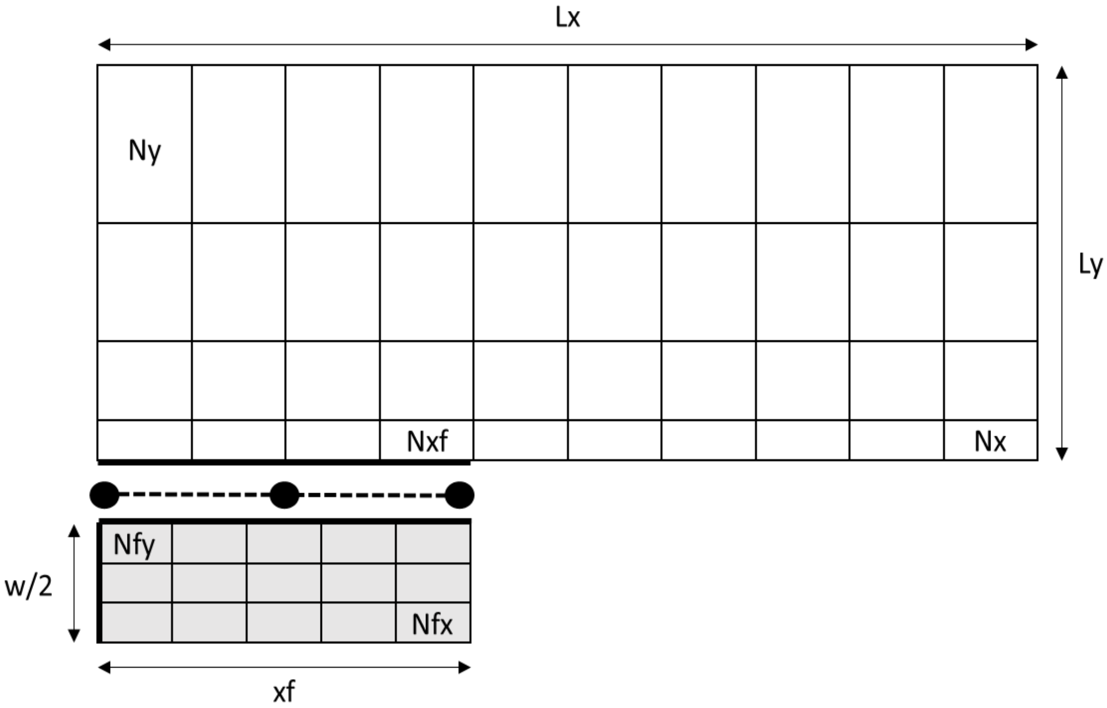

Figure 4-19. Domain discretization for mortar coupling model

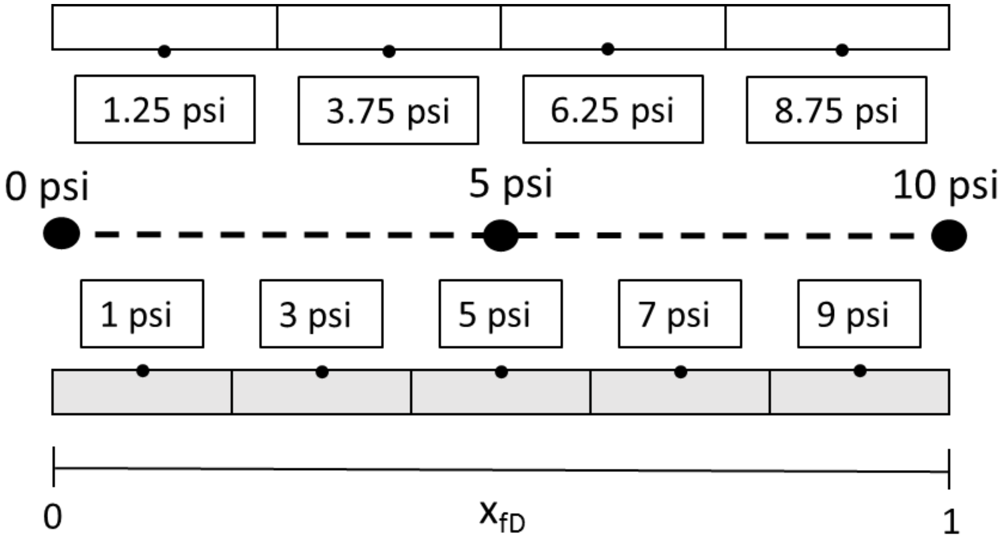

Figure 4-20. Example of interface pressure projection onto the boundaries

The pressure profile in the mortar space is a linear combination of basis functions (Eq. 4-23), where N is the number of nodes, α_i is the pressure at each node, and Φ_i is a linear basis function in the form of Eq. 4-24. Eq. 4-24 describes a "hat" function, which has a value of 1 at one of the nodes and zero at all the others. Figure 4-21 shows an example of a hat function for nodes 1 and 3 (N_1 and N_3) on a four-node mortar space.

$$P = \sum_{i=1}^{N} \alpha_i \Phi_i \tag{4-23}$$

$$\Phi_i(x) = \begin{cases} \dfrac{1}{x_{N_i} - x_{N_{i-1}}} x & \mathit{for}\ x_{N_{i-1}} \le x \le x_{N_i} \\ -\dfrac{1}{x_{N_{i+1}} - x_{N_i}} (x - x_{N_{i+1}}) & \mathit{for}\ x_{N_i} \le x \le x_{N_{i+1}} \\ 0\ \mathit{everywhere\ else} & \end{cases} \text{, where} \tag{4-24}$$

x = dimensionless position ($0 \le x \le 1$) along the fracture-matrix interface, and

x_{Ni} = dimensionless position of node i

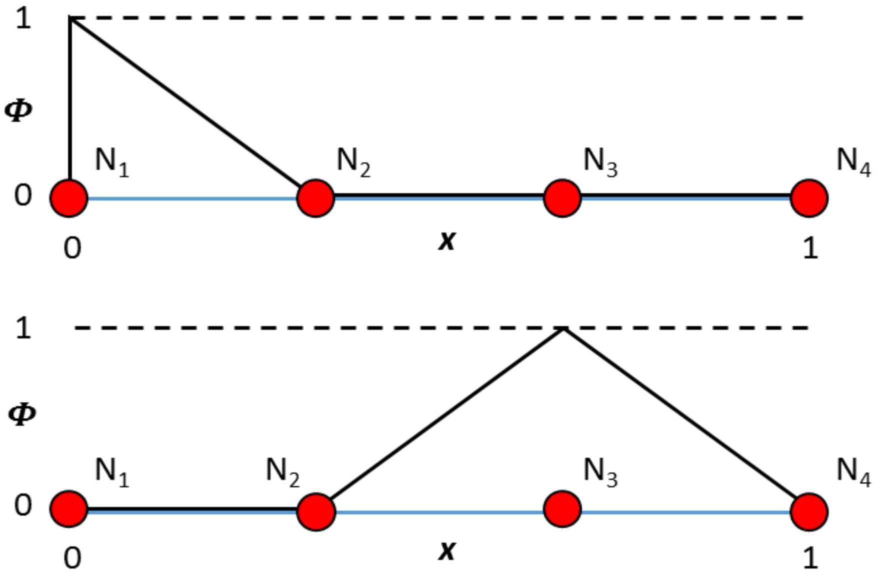

Figure 4-21. Example of "hat" linear basis function

Figure 4-22 shows the pressure distribution on the matrix side at t_D = 5 for a highly-conductive fracture. The fracture, reservoir, and well properties are the same as for the full-domain finite difference case shown in Figure 4-15: x_f =1,000 ft., $L_x = L_y$ = 5,000 ft., $w/2$ = 1.57 ft., k_f = 10,000 mD, k = 0.001 mD, initial reservoir pressure = 1,000 psi, constant production pressure = 100 psi. The matrix side was discretized into 50 blocks in the *x*-direction and 30 in the *y*-direction; 5 blocks were placed in contact with the fracture. Local refinement was applied in the *y*-direction (parallel to the fracture) but not in the *x*-direction. Meanwhile, the fracture was divided into 10 blocks in the *x*-direction (one in the *y*-direction) and four nodes were placed along the interface. The initial reservoir pressure (p_i) was used as the initial guess of the node pressures, α_i, to initialize the simulation.

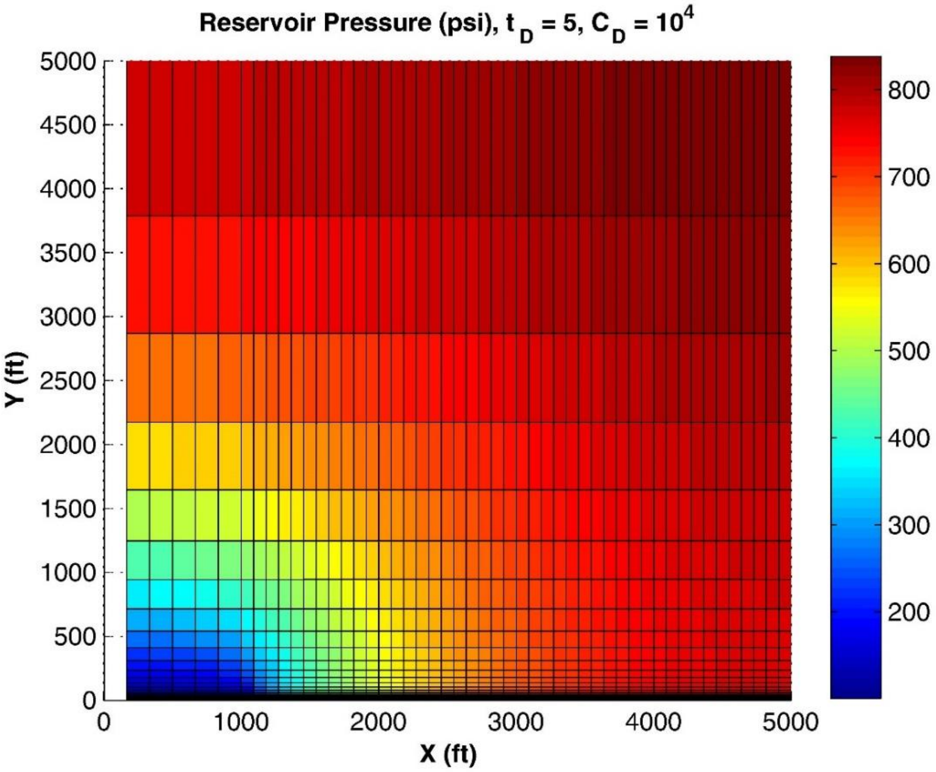

Figure 4-22. Gridding example for mortar coupling model, matrix side

As Figure 4-22 shows, the pressure distribution is almost identical to the full-domain finite difference model, with pressures ranging from 100 to 838 psi (compared to 100 to 835 psi). The model also displays the expected pressure drop behavior along the fracture for low and high-conductivity systems. Figure 4-23 shows the pressure profile of the fracture on the matrix side, the fracture side, and at the interface. Two cases were considered: the highly-conductive system shown in Figure 4-22, and a low-conductivity fracture ($C_D = 1$) like the one in Figure 4-17. As expected, pressure is practically constant along the high-conductivity fracture and a significant pressure drop is observed in the low-conductivity case. The simulation results make numerical sense, as well: both subdomains have smooth pressure distributions, with the matrix and fracture falling nicely along the pressure profile of the interface.

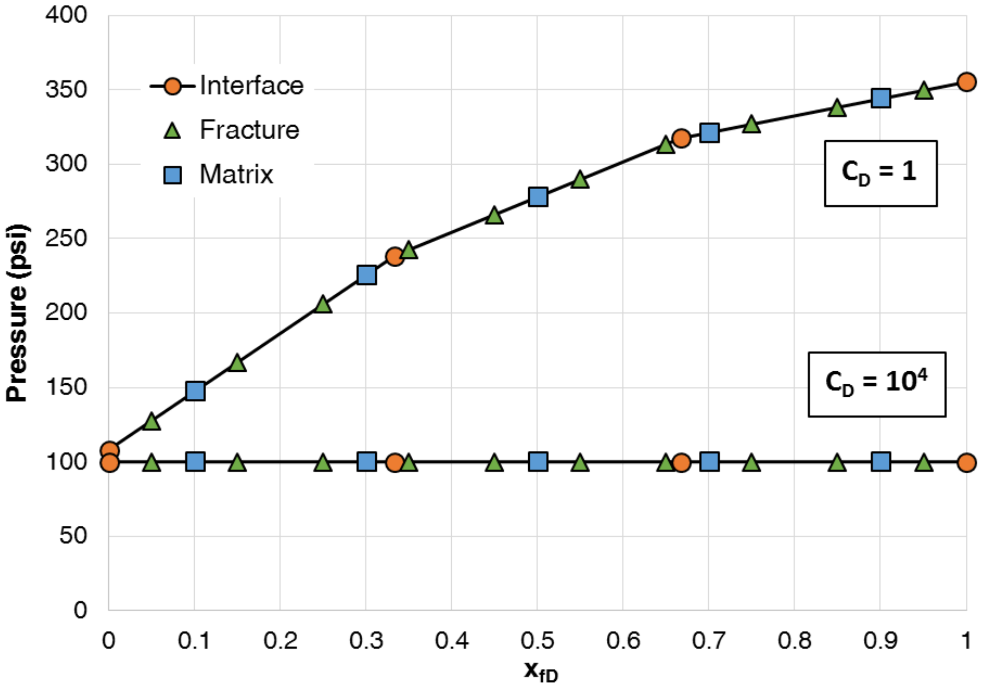

Figure 4-23. Pressure along fracture side, matrix side, and interface for low and high-conductivity fracture at $t_D = 5$.

4.3. COMPARISON OF FULL-DOMAIN FINITE DIFFERENCE AND MORTAR COUPLING RESULTS

The mortar coupling and finite difference results were compared against Cinco-Ley et al.'s (1978) semi-analytical solution. The semi-analytical values were obtained from the Matlab program described in Section 4.2.1, which was validated against the figures from Cinco-Ley et al.'s (1978) paper. The two numerical approaches were used to calculate the flux distribution at several dimensionless times for C_D values of 1×10^4, 1×10^2, 10, and 1, as well as the stabilized flux distribution and dimensionless pressure drop for different dimensionless conductivities. In all cases, C_{fDf} was held constant at 1×10^{-3} and n_{fD} was varied. This was done in order to simulate somewhat realistic fracture dimensions (x_f = 1,000, $w/2$ = 1.57 ft.) while changing the permeability contrast between the fracture and the reservoir. The results are shown in Figures 4-24 through 4-29. In all figures, the semi-analytical values are plotted as solid lines and the numerical results as markers. The semi-analytical data from the Matlab program can be found in Appendix IV. The discretization and simulation parameters for both methods are listed in Table 4-1.

Table 4-1 – Input parameters for numerical reservoir simulators

Parameter	**Value**	**Parameter**	**Value**
N_x	50	L_x	5,000 ft.
N_y	30	L_y	5,000 ft.
N_{xf}*	20	k_f	10,000 mD
N_{fx}	20	Number of nodes*	5
N_{fy}	1	t_D initial	1×10^{-5}
x_f	1,000 ft.	t_D final	10
$w/2$	1.57 ft.	Time intervals per log cycle	10
*Mortar coupling only			

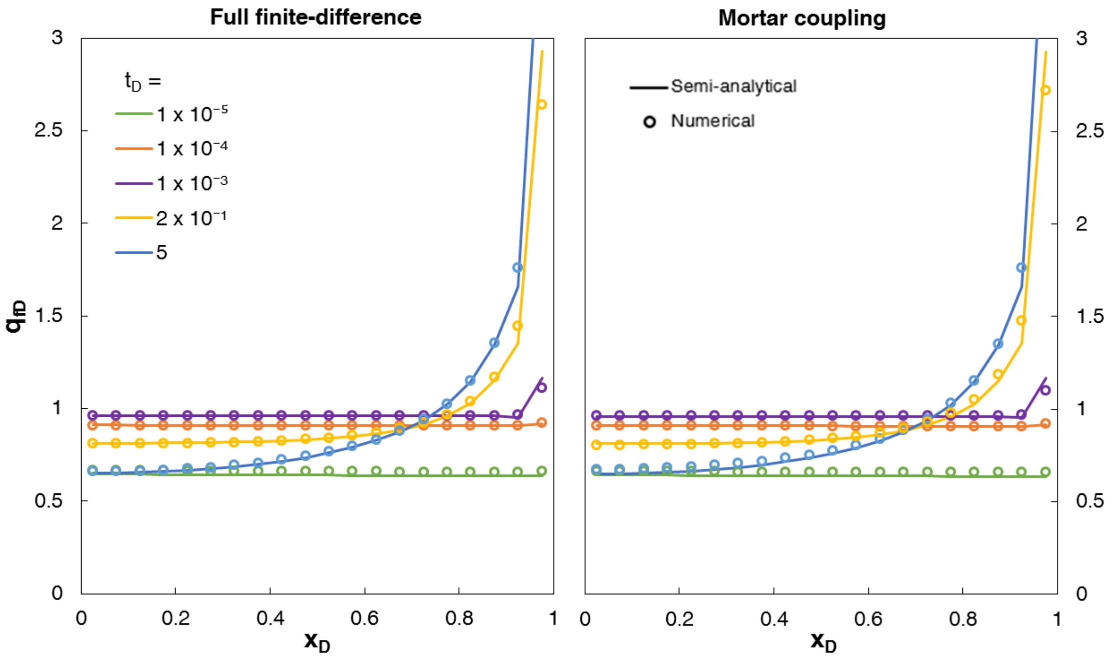

Figure 4-24. Comparison of full-domain F.D. vs. mortar coupling, q_{fD} vs. x_D, $C_D = 1\times10^4$

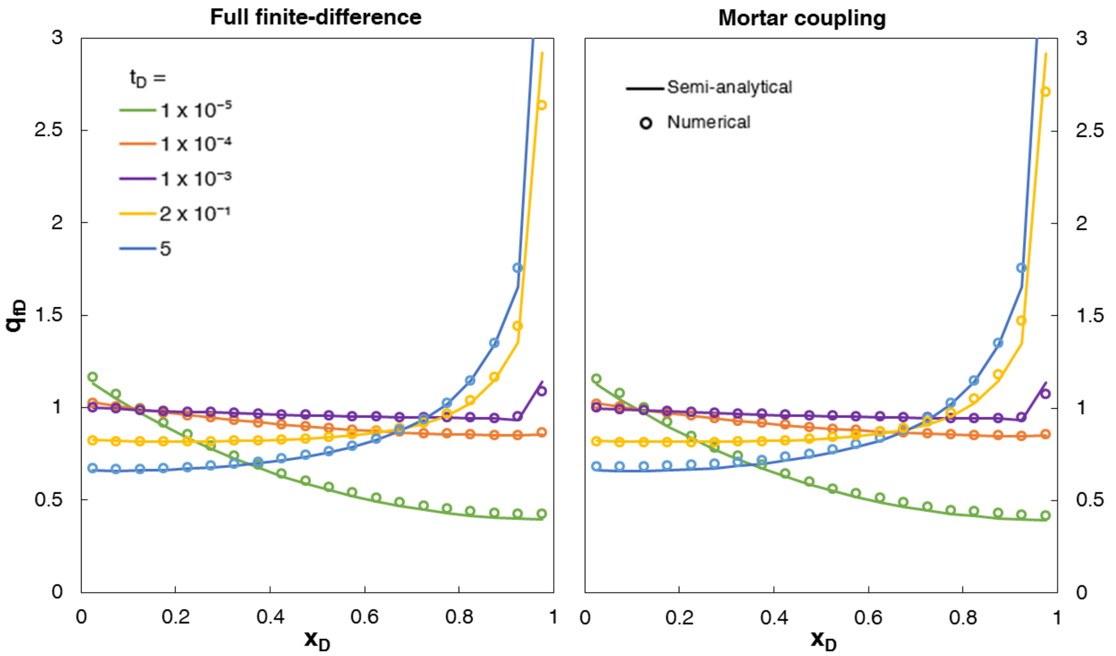

Figure 4-25. Comparison of full-domain F.D. vs. mortar coupling, q_{fD} vs. x_D, $C_D = 1\times10^2$

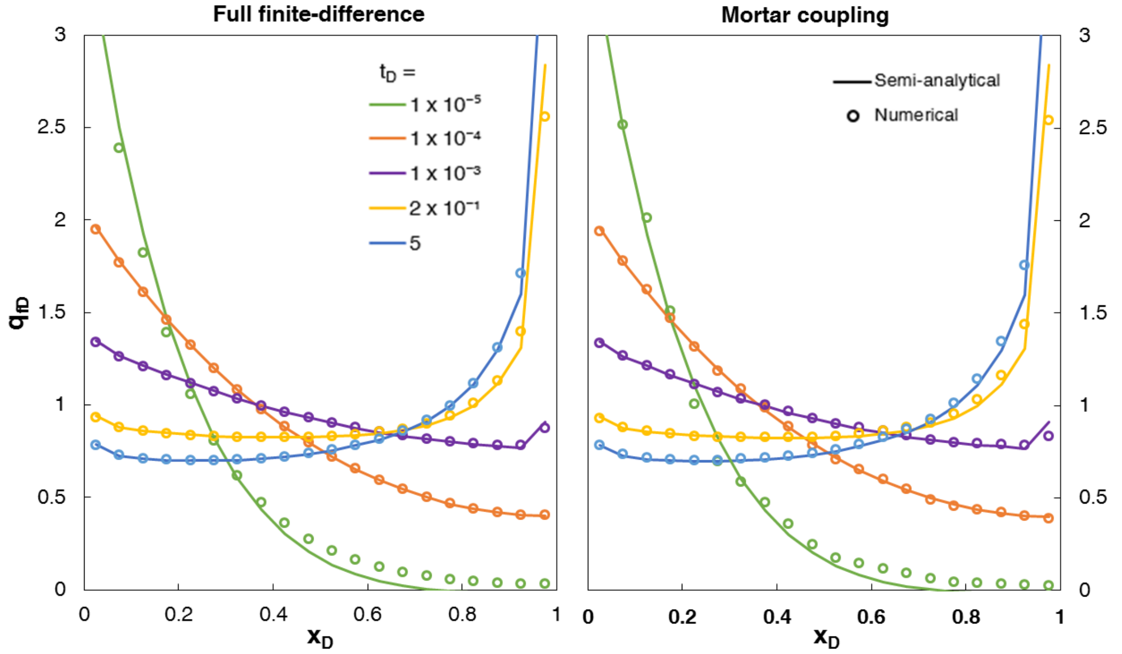

Figure 4-26. Comparison of full-domain F.D. vs. mortar coupling, q_{fD} vs. x_D, $C_D = 10$

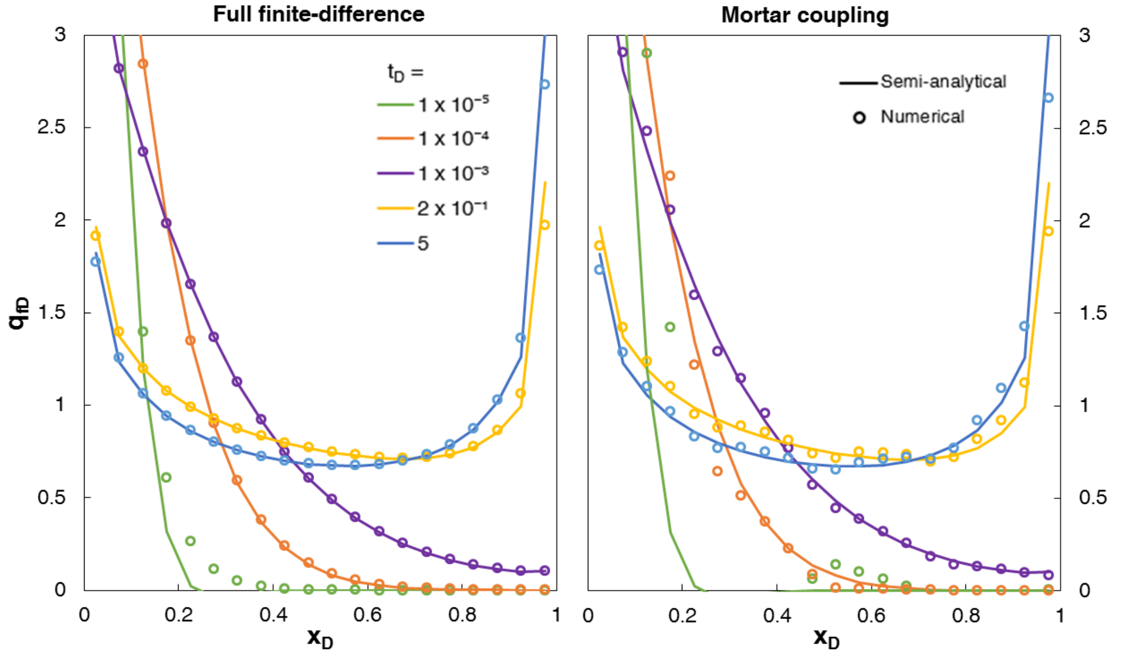

Figure 4-27. Comparison of full-domain F.D. vs. mortar coupling, q_{fD} vs. x_D, $C_D = 1$

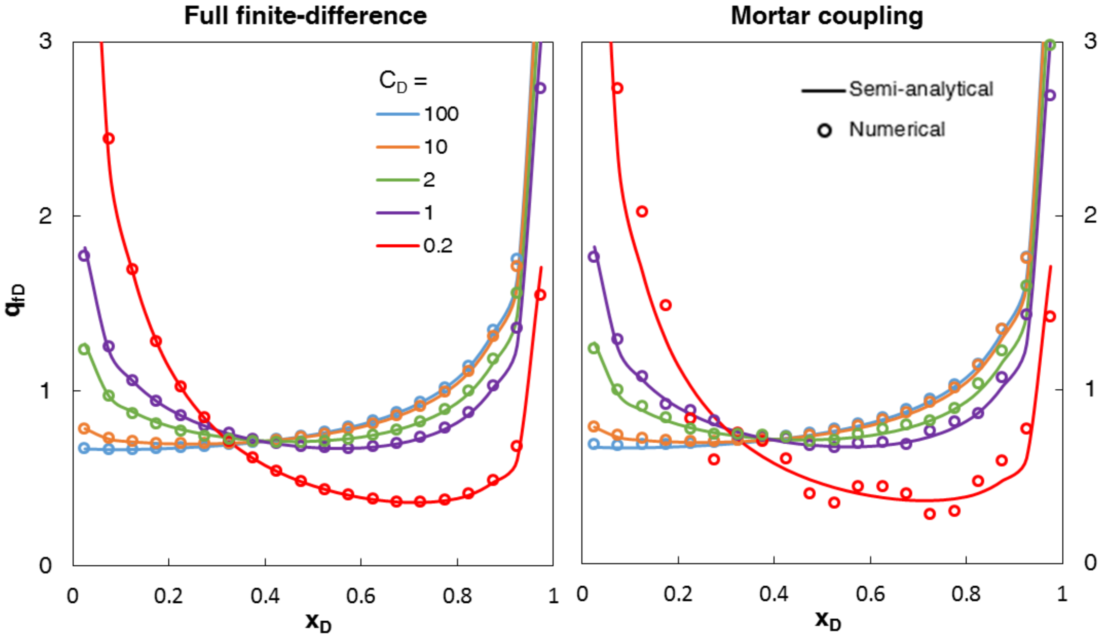

Figure 4-28. Comparison of stabilized flux distribution between full-domain F.D. and mortar coupling models for different fracture conductivities, $t_D = 5$

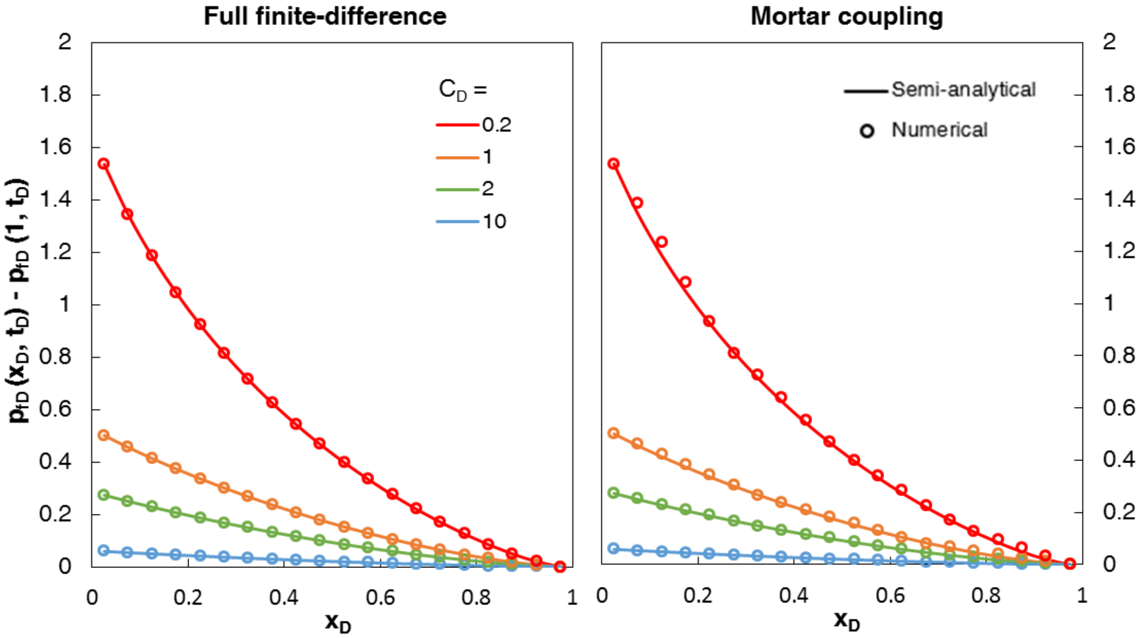

Figure 4-29. Comparison of dimensionless pressure drop along the fracture between full-domain F.D. and mortar coupling models, $t_D = 5$

The full-domain finite difference and mortar coupling models have almost identical results for dimensionless conductivity (C_D) values of 10 or above. They both match the semi-analytical solution almost perfectly, especially at $t_D \geq 1\times10^{-3}$. However, at $C_D \leq 1$ the mortar coupling model displays some numerical issues that are particularly evident in the $C_D = 0.2$ curve of Figure 4-28. While the stabilized pressure drop is still accurate at lower dimensionless conductivities, the flux distribution oscillates along the fracture length. Increasing the number of nodes significantly improves the match to the semi-analytical solution, as shown in Figures 4-30 and 4-31. Figure 4-30 shows the dimensionless flux profile at various dimensionless times for $C_D = 1$, and Figure 4-31 focuses on the $C_D = 0.2$ curve of Figure 4-28. Increasing the number of nodes from 5 to 10 reduces the flux oscillations dramatically, and using 15 nodes almost eliminates them completely. These results agree with Sun (2012), who found that finer discretization of the mortar space (i.e. using more nodes) yields smoother pressure and flux distributions. He attributed the perturbations in the flux profiles to the inability of the linear basis functions to guarantee "the continuity of pressure derivatives at the [mortar] element edge" and concluded that "more advanced basis functions need to be implemented to achieve a smooth profile" (Sun, 2012). A discussion of other numerical issues associated with mortar coupling modeling of hydraulically-fractured reservoirs is presented in Section 4.4.

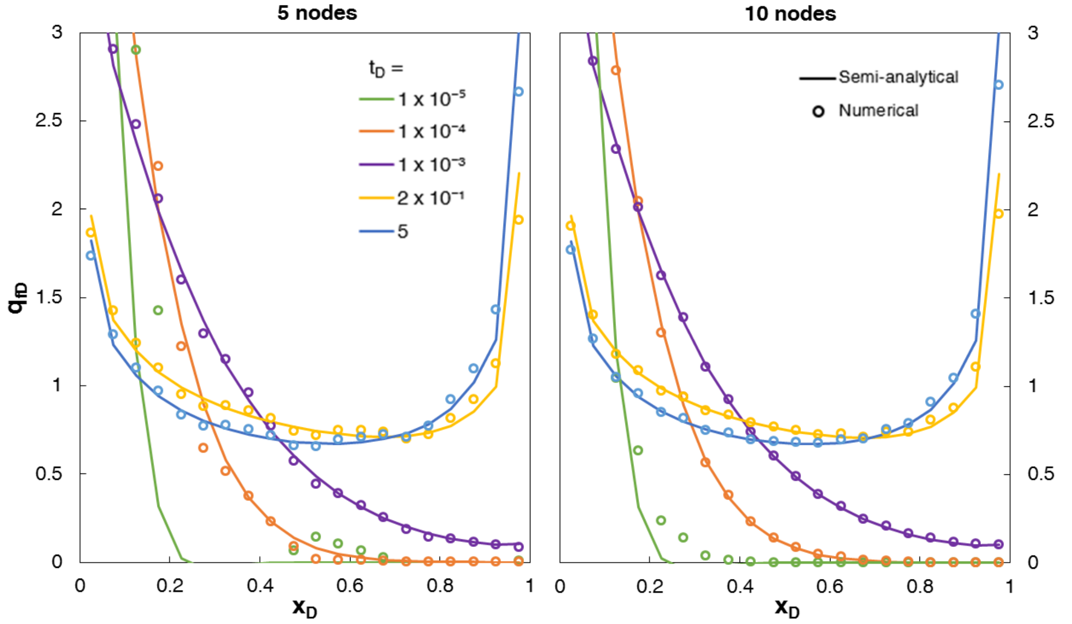

Figure 4-30. Comparison between 5 and 10 nodes for mortar coupling model, q_{fD} vs. x_D, $C_D = 1$

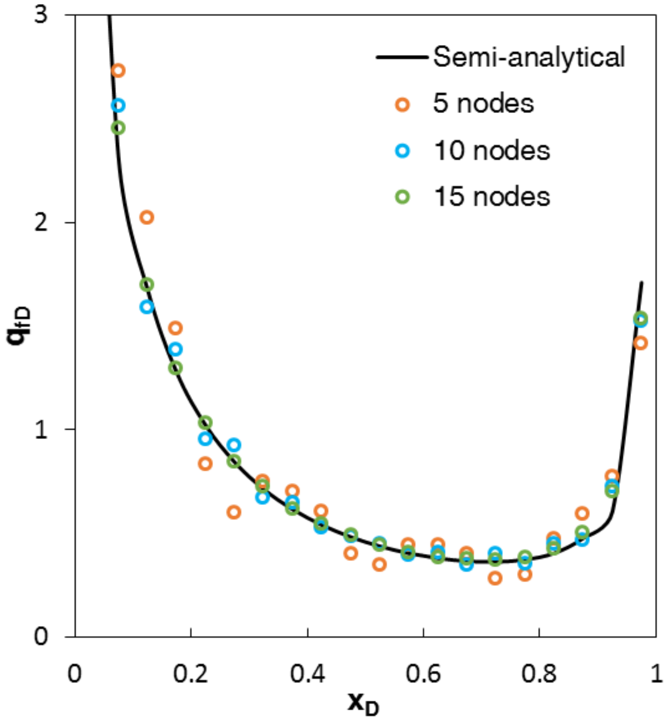

Figure 4-31. Dimensionless flux profile for different number of nodes, $C_D = 0.2$, $t_D = 5$

This study was able to replicate the flux distributions from Cinco-Ley et al.'s (1978) semi-analytical solution at early times ($t_D \leq 1\times10^{-4}$) using mortar coupling for dimensionless conductivity values (C_D) above 10. This is an improvement over Sun (2012), who determined that mortar coupling "quantitatively reproduced the semi-analytical solution, except for the early time flux," which he deemed to be "very sensitive to model configuration (e.g. grid size and time step selection) and truncation errors." His reproduction of Figure 5 in Cinco-Ley et al.'s (1978) paper is shown below in Figure 4-32. Sun (2012) was correct in concluding that the early time flux is extremely sensitive to the simulation's time-stepping scheme. However, Figure 4-24 in this study closely reproduces Cinco-Ley et al.'s (1978) plot even for the earliest dimensionless time ($t_D = 1\times10^{-5}$). As in the Matlab semi-analytical program, the initial timestep proved to be critical when calculating the flux distribution for early times ($t_D \leq 1\times10^{-4}$). Figure 4-33 shows the $C_D = 1\times10^4$ case for $\Delta t_{Di} = 1\times10^{-5}$ and $\Delta t_{Di} = 1\times10^{-6}$. Once again, selecting an initial dimensionless timestep equal to the earliest time of interest ($t_D = 1\times10^{-5}$) results in an almost perfect match. As Figure 4-33 shows, choosing a Δt_{Di} of 1×10^{-6} results in an incorrect dimensionless flux distribution at $\mathrm{t_D} = 1\times10^{-5}$. Selecting the earliest desired time as the initial dimensionless timestep also yields the most accurately results for the full-domain finite difference model. This is contrary to the recommendations by Bennett et al. (1986), who created a finite difference model to study the "influence of vertical variations in fracture conductivity on well performance," and concluded that starting the simulation "one log cycle of dimensionless time before the earliest time of interest" provides the largest degree of accuracy.

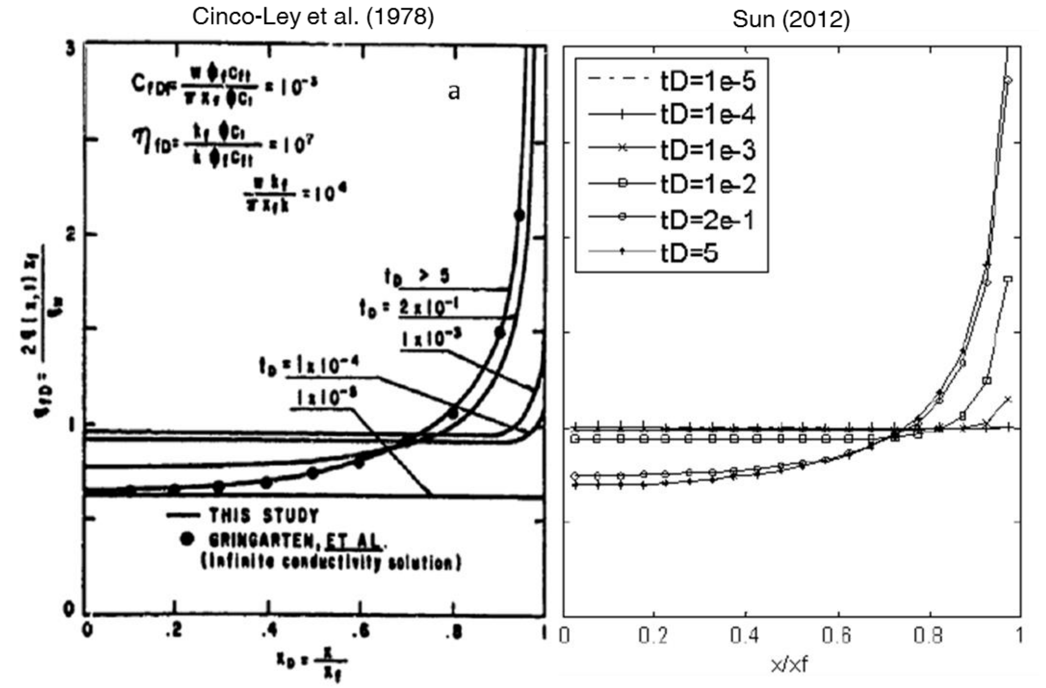
Cinco-Ley et al. (1978)

Sun (2012)

Figure 4-32. Comparison of Sun's (2012) mortar coupling solution to Cinco-Ley et al. (1978), $C_D = 1 \times 10^4$

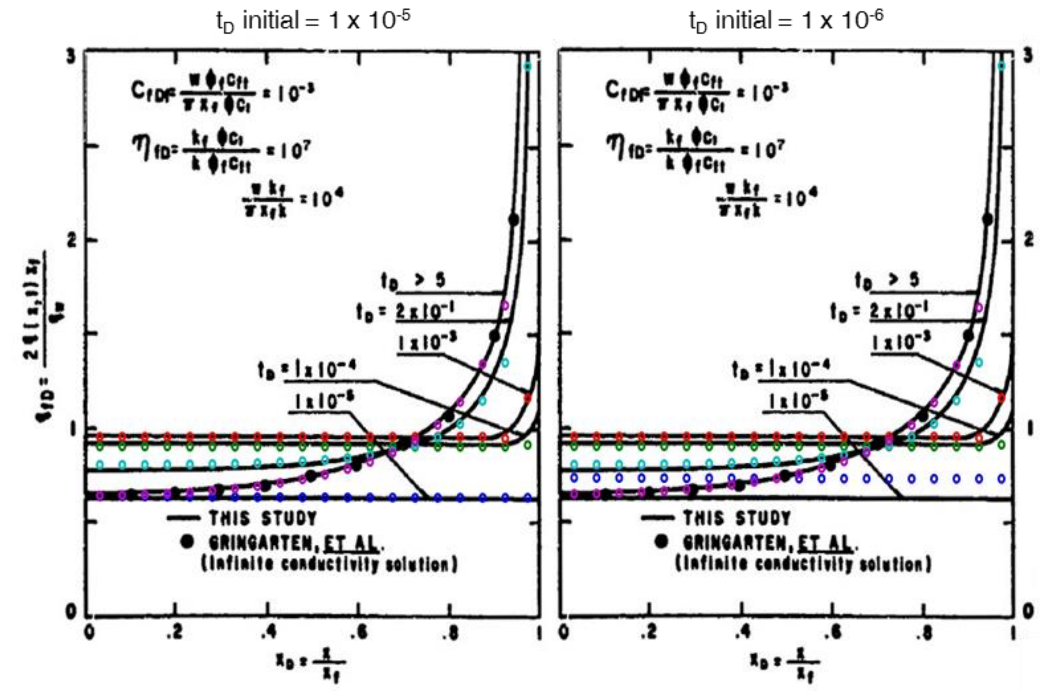
t_D initial = 1 x 10^{-5}

t_D initial = 1 x 10^{-6}

Figure 4-33. Comparison of initial dimensionless timestep for mortar coupling model, $C_D = 1 \times 10^4$

4.4. NUMERICAL ISSUES ASSOCIATED WITH MORTAR COUPLING OF THE CINCO-LEY ET AL. (1978) PROBLEM

The results in Section 4.3 show that mortar coupling accurately models transient pressure behavior for the Cinco-Ley et al. (1978) problem. This is in agreement with Sun (2012), who found that mortar coupling "successfully reproduced the transient flux, semi-steady-state pressure, and semi-steady-state flux entering the fractures." An important detail about Section 4.3's results is that the flux and pressure distributions were extracted from the *reservoir* side of the system, as opposed to the fracture side. Sun (2012) also depicts fluid behavior on the matrix side, as it is flowing towards the interface.

Studying the flux distribution from the *fracture* side of the interface shed light on interesting numerical phenomena. Figure 4-34 shows the flux distribution for a finite-conductivity vertical fracture at $t_D = 5$. The reservoir model has a dimensionless fracture conductivity (C_D) of 1×10^4, with a dimensionless storage capacity (C_{fDf}) of 1×10^{-3} and a dimensionless hydraulic diffusivity (n_{fD}) of 1×10^7. Five nodes were placed on the mortar space, at x_{fD} = 0, 0.25, 0.50, 0.75, and 1. As Figure 4-34 shows, there is a smooth flux profile on the matrix side, which matches the flux distribution at $t_D = 5$ in Figure 4-24. From the fracture side, however, there are spikes in the flux distribution at the location of the nodes. The area under both curves is the same, because the weak condition of convergence (flow into the fracture must be equal to the flow out of the matrix) is met. However, the flow distribution is distinctly different, as it tends to accumulate around the nodes on the fracture side. As Figure 4-25 shows, placing ten nodes on the interface only increases the number of flux spikes. This is in stark contrast with the flux distribution oscillations on the matrix side, which were addressed by increasing the number of nodes on the mortar space.

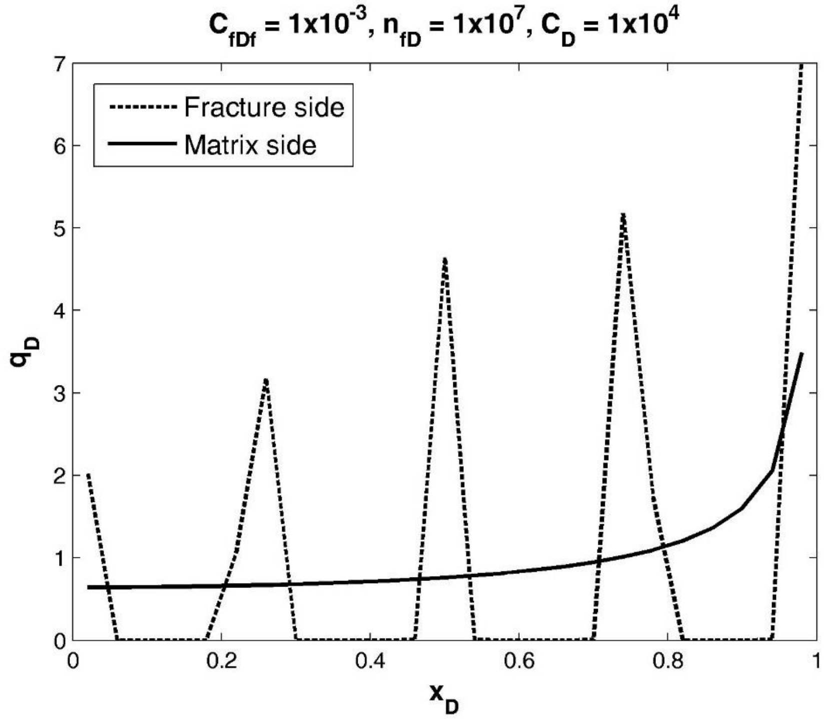

Figure 4-34. Dimensionless flux distribution from the matrix and fracture sides, 5 nodes

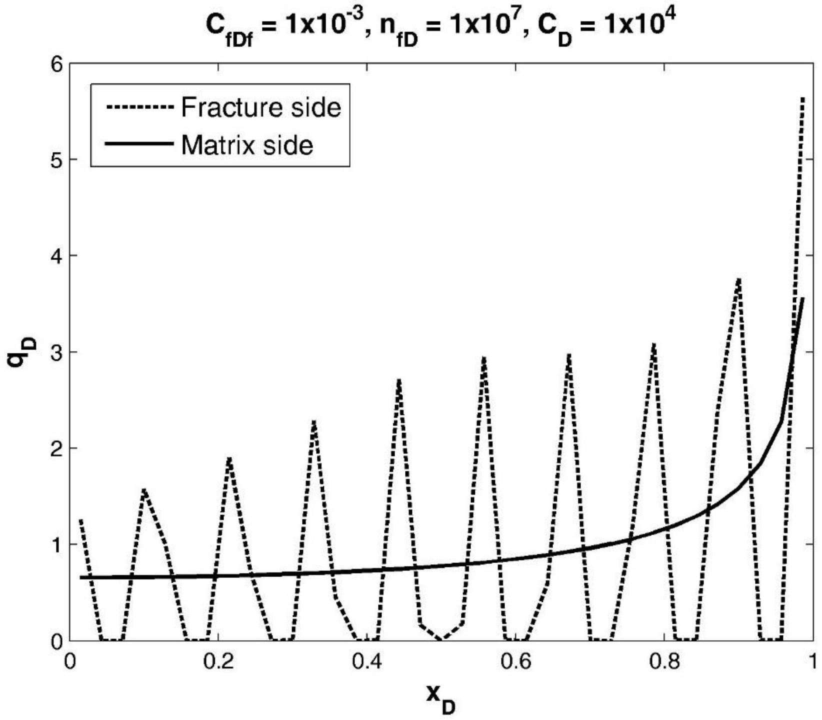

Figure 4-35. Dimensionless flux distribution from the matrix and fracture sides, 10 nodes

In order to determine the origin of these flux spikes, an additional three cases were run (Table 4-2). The dimensionless fracture conductivity was set constant at 1×10^4 while varying the ratio of n_{fD} to C_{fDf} (reducing n_{fD} while increasing C_{fDf}), and the mortar space was discretized into five nodes. In all simulations, the fracture half-length (x_f) was fixed at 1,000 ft. Reservoir length in the *x* and *y* directions was set to 50 times the fracture half-length (50,000 ft.) in order to simulate a truly infinite reservoir. The first case consisted of $n_{fD} = 1\times10^7$ and $C_{fDf} = 1\times10^{-3}$, which is shown above in Figures 4-34 and 4-35.

Table 4-2 – Flux distribution parameters, $C_D = 1\times10^4$

Case	**Figure**	C_{fDf}	n_{fD}	C_D **(**$C_{fDf}\cdot n_{fD}$**)**
1	4-34, 4-35	1×10^{-3}	1×10^7	1×10^4
2	4-36	1×10^{-2}	1×10^6	1×10^4
3	4-37	1×10^{-1}	1×10^5	1×10^4
4	4-38	1×10^0	1×10^4	1×10^4

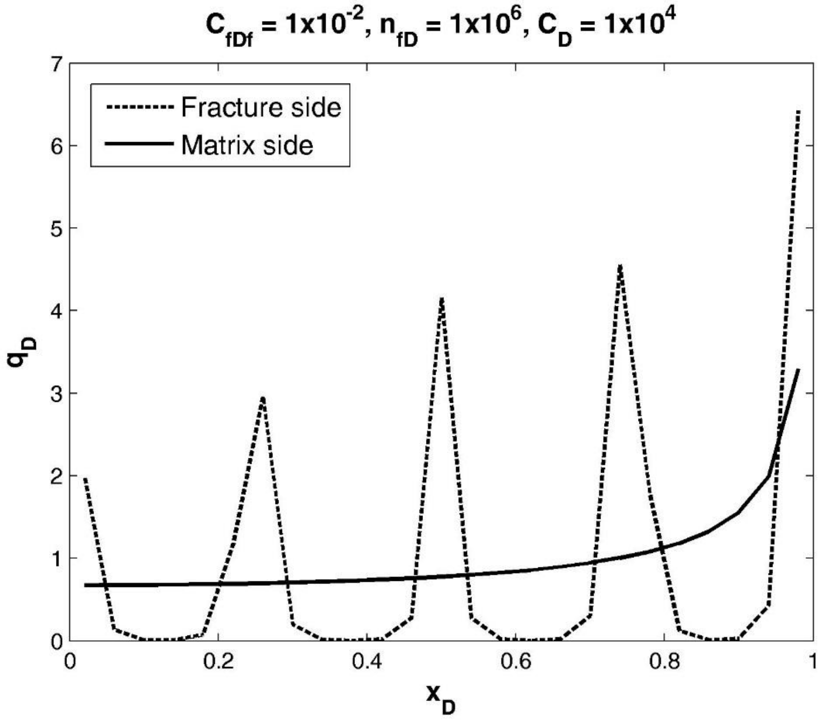

Figure 4-36. Dimensionless flux distribution from the matrix and fracture sides, Case 2

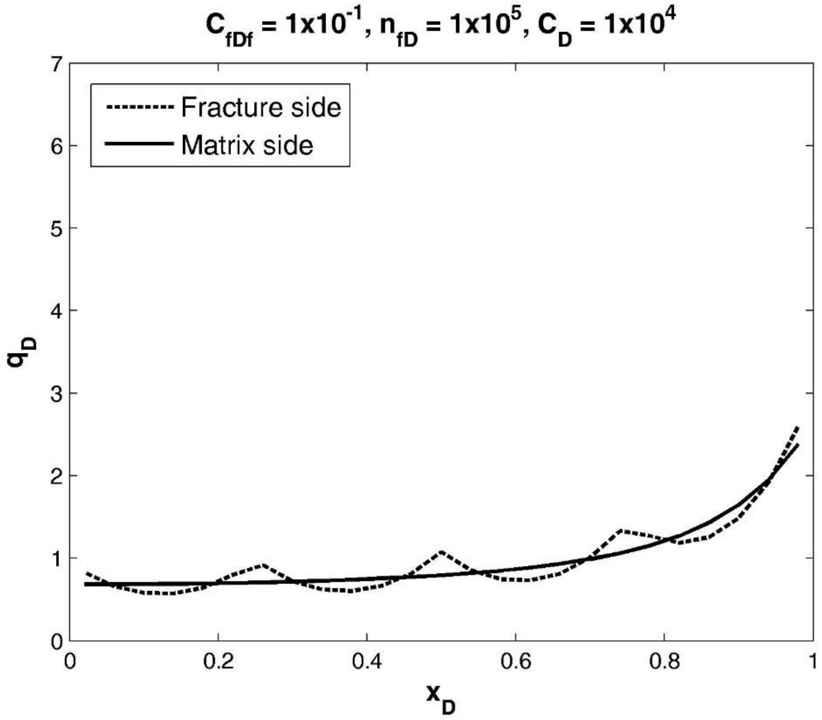

Figure 4-37. Dimensionless flux distribution from the matrix and fracture sides, Case 3

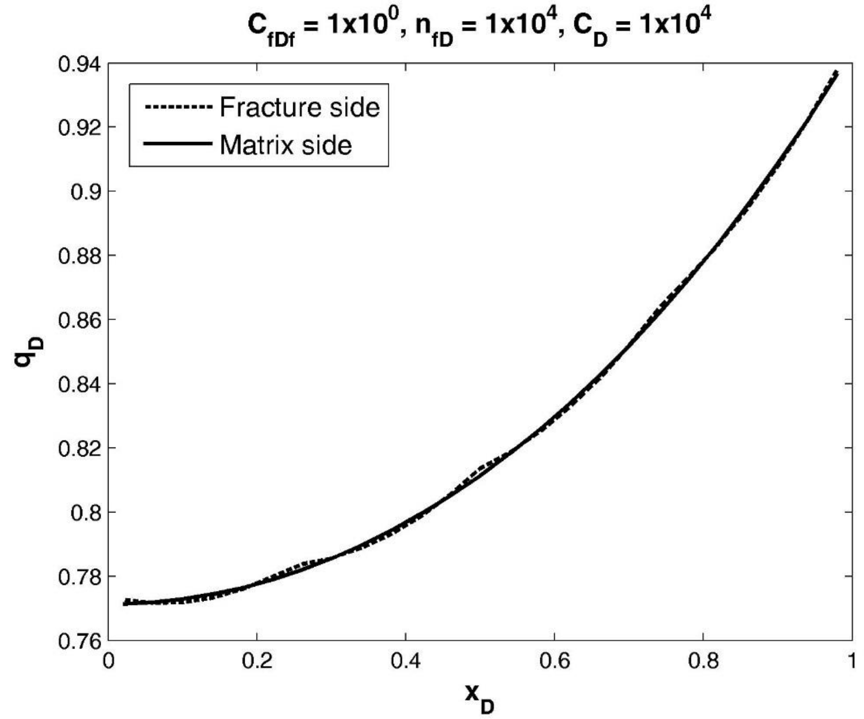

Figure 4-38. Dimensionless flux distribution from the matrix and fracture sides, Case 4

As Figure 4-36 shows, the flux distribution spreads out slightly over the length of the fracture (on the fracture side) when C_{fDf} is increased from 1×10^{-3} to 1×10^{-2} and C_D is maintained constant. Further increasing C_{fDf} and decreasing n_{fD} to 1×10^{-1} and 1×10^5, respectively, significantly smoothens out the flux distribution (Figure 4-37), and setting C_{fDf} to 1 and n_{fD} to 1×10^4 causes the flux peaks to disappear almost entirely (Figure 4-38). The conclusion appears to be that the peaks in flux distribution on the fracture side disappear as the value of C_{fDf} approaches 1. In order to understand if this behavior is also present at lower values of C_D, an additional set of cases was run at a constant dimensionless fracture conductivity of 10 (Table 4-3). As Figures 4-39 through 4-41 show, the dimensionless flux peaks once again disappear as C_{fDf} approaches 1, regardless of the value of n_{fD} and C_D.

Table 4-3 – Flux distribution parameters, $C_D = 10$

Case	**Figure**	C_{fDf}	n_{fD}	$C_D\,(C_{fDf} \cdot n_{fD})$
5	4-39	1×10^{-2}	1×10^{3}	1×10^{1}
6	4-40	1×10^{-1}	1×10^{2}	1×10^{1}
7	4-41	1×10^{0}	1×10^{1}	1×10^{1}

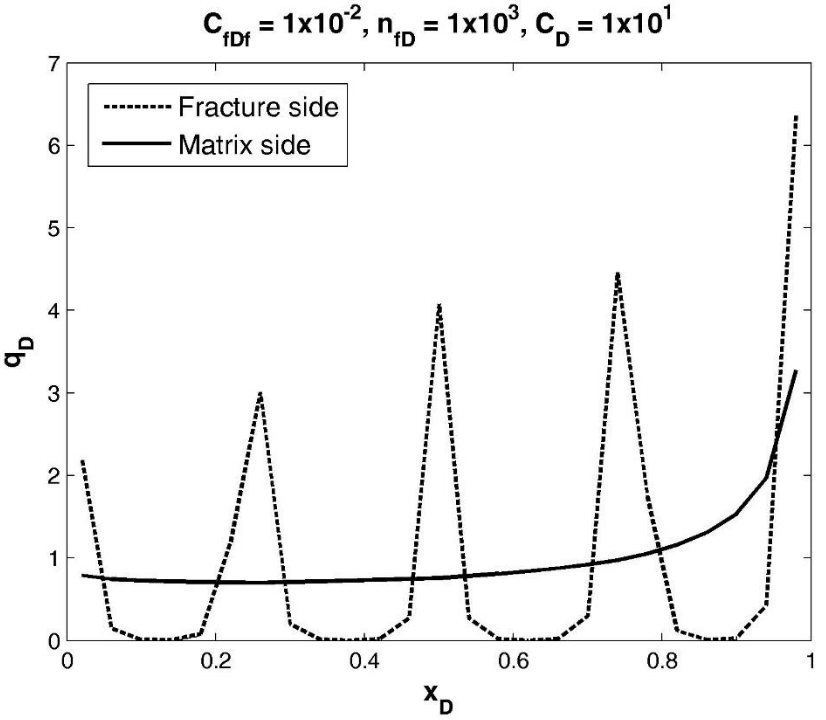

Figure 4-39. Dimensionless flux distribution from the matrix and fracture sides, Case 5

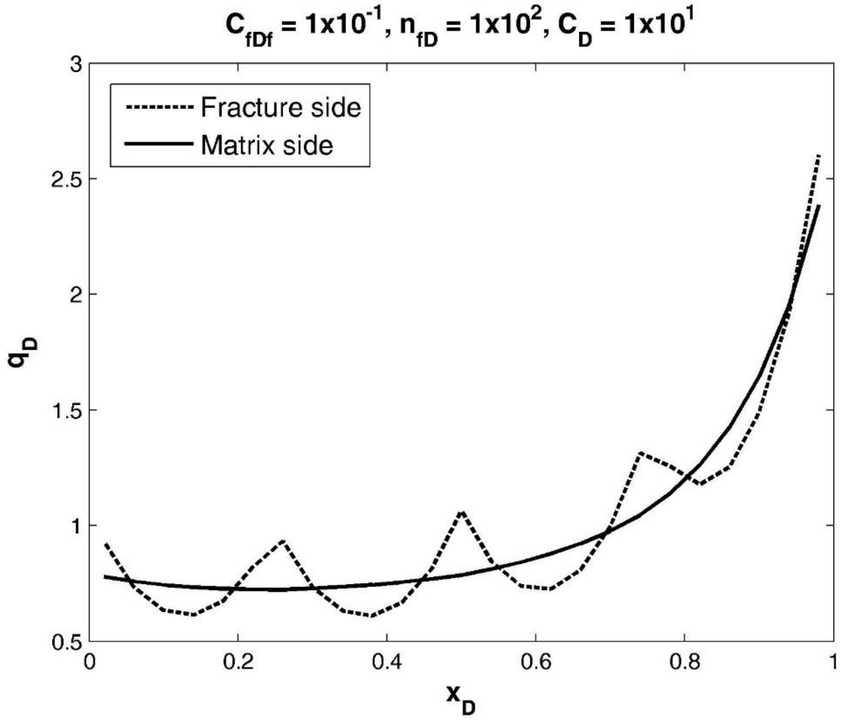

Figure 4-40. Dimensionless flux distribution from the matrix and fracture sides, Case 6

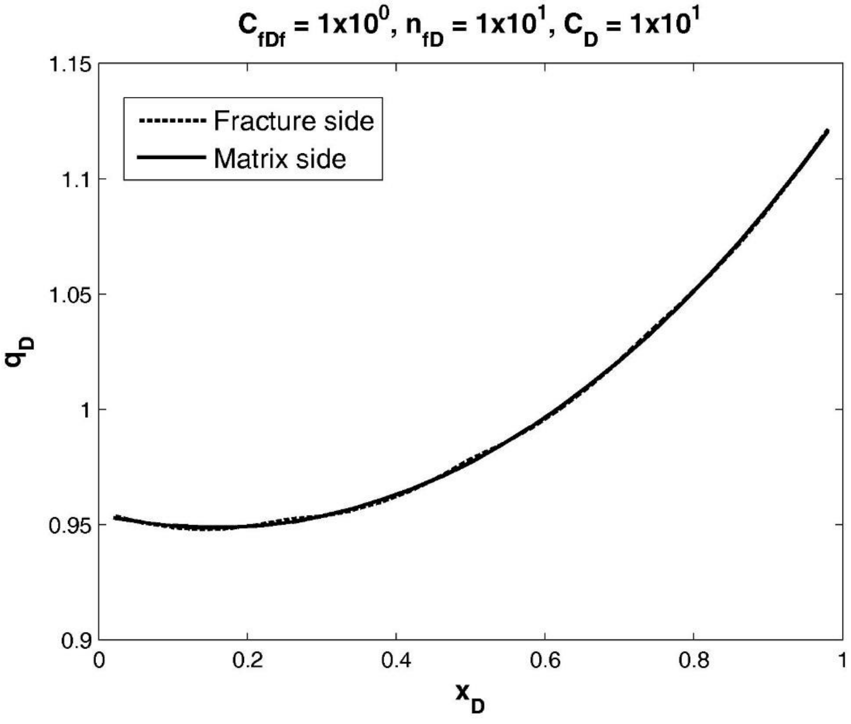

Figure 4-41. Dimensionless flux distribution from the matrix and fracture sides, Case 7

In order to understand the cause of these flux peaks, it is helpful to think of the dimensionless values C_{fDf}, n_{fD}, and C_{D}, in terms of physical properties and dimensions. Table 4-4 shows the calculated values of fracture half-width and matrix permeability for Cases 1 through 7 using Eq. 4-21 and 4-22.

Table 4-4 – Calculated fracture half-width and matrix permeability

Case	C_{fDf}	n_{fD}	C_{D} ($C_{\mathrm{fDf}} \cdot n_{\mathrm{fD}}$)	x_{f} **(ft.)**	$L_{\mathrm{x}}, L_{\mathrm{y}}$ **(ft.)**	$w/2$ **(ft.)**	k_{f} **(mD)**	k **(mD)**
1	1×10^{-3}	1×10^{7}	1×10^{4}	1,000	50,000	1.57	10,000	.001
2	1×10^{-2}	1×10^{6}	1×10^{4}	1,000	50,000	15.7	10,000	0.01
3	1×10^{-1}	1×10^{5}	1×10^{4}	1,000	50,000	157	10,000	0.1
4	1×10^{0}	1×10^{4}	1×10^{4}	1,000	50,000	1,570	10,000	1
5	1×10^{-2}	1×10^{3}	1×10^{1}	1,000	50,000	15.7	10,000	10
6	1×10^{-1}	1×10^{2}	1×10^{1}	1,000	50,000	157	10,000	100
7	1×10^{0}	1×10^{1}	1×10^{1}	1,000	50,000	1,570	10,000	1,000

From Table 4-4, it appears that the peaks in flux distribution on the matrix side are an issue of the fracture's dimensions rather than the contrast in magnitude between k and k_{f}. This conclusion is reached by looking at Cases 4 and 7, which do not have any fluctuations in their flux profiles on either side of the interface. While the fractures in both instances have the same length and width, the permeability in the matrix is 1,000 times larger in Case 7 than in Case 4.

In order to understand the causes of the flux fluctuations, an analysis was performed on Case 4. Local refinement parallel to the fracture was turned off (the width of the grid blocks on the matrix side was simply L_{y} divided by N_{y}) and the number of reservoir grid blocks in the *y*-direction was varied. As Figure 4-42 shows, under-discretizing the matrix subdomain causes the flux peaks to appear where they had previously not existed. As the size of the reservoir grid blocks is reduced by increasing N_y (and their width approaches that of the fracture) the flux profile becomes smooth once again.

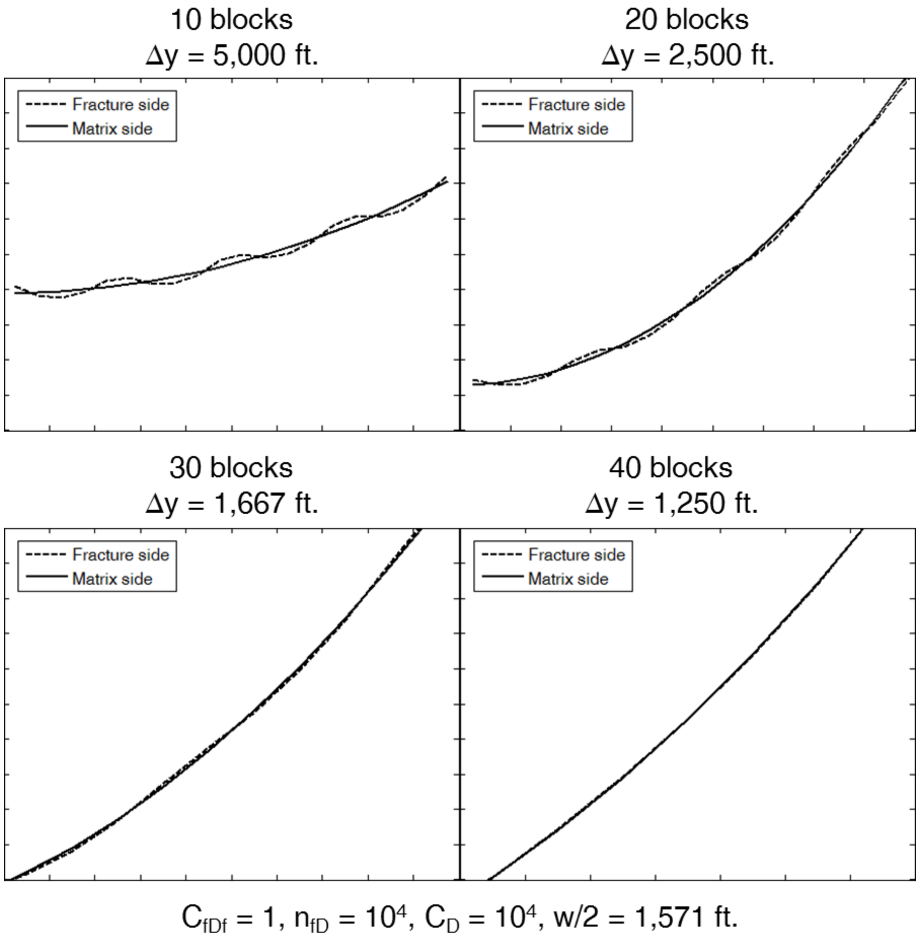

Figure 4-42. Flux profile on the matrix and fracture sides for different values of N_y, $C_{fDf} = 1$, $n_{fD} = 1\times10^4$

The same test was repeated for $C_{fDf} = 1\times10^{-1}$ and $n_{fD} = 1\times10^5$ hoping to find the reservoir block width that would eliminate the flux distribution peaks. Fracture half-width was 157 ft., so it was expected for the profile to smoothen out as Δy in the matrix approached that value (which was the case in Figure 4-42). As Figure 4-43 shows, however, the flux peaks are present regardless of the number of grid blocks used. The perturbations become slightly smoother as Δy approaches $w/2$, but they do not disappear even when Δy is smaller than the fracture half-width. The conclusion is that while the perturbations appear to be dominated by the C_{fDf} term, and possibly related to the discretization of the reservoir subdomain, the true source of the flux peaks is unknown and should be the subject of future research.

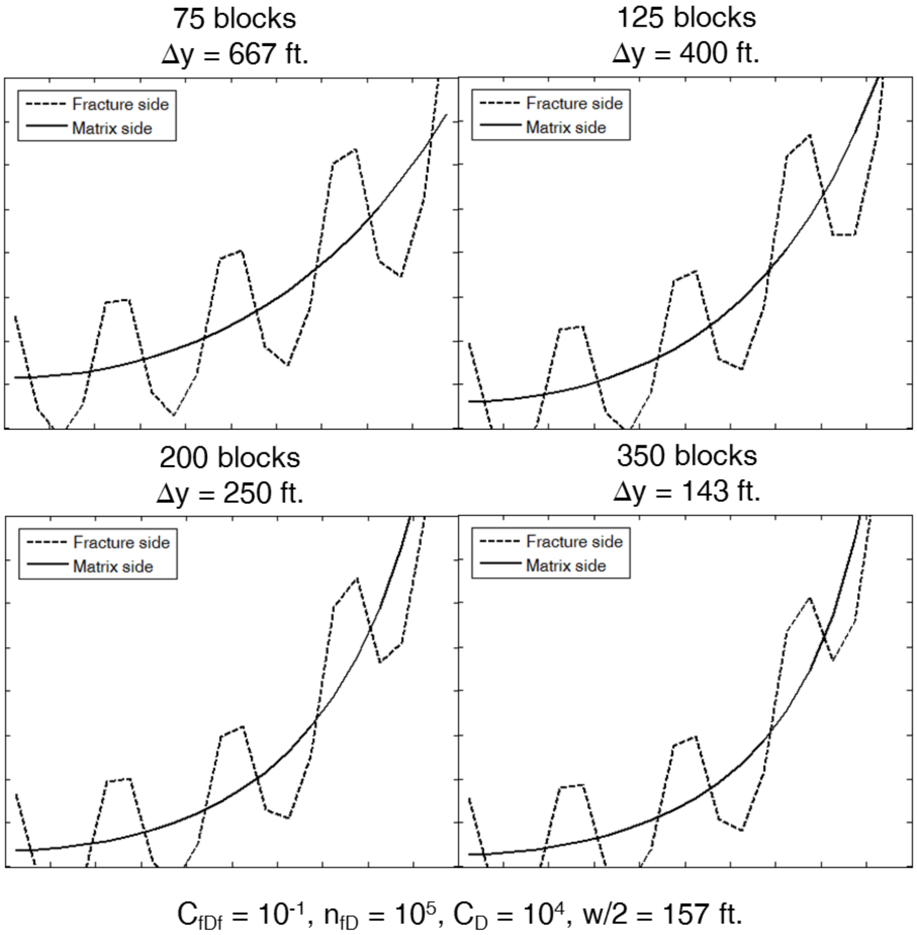

Figure 4-43. Flux profile on the matrix and fracture sides for different values of N_{y}, $C_{\mathrm{fDf}} = 1\times10^{-1}$, $n_{\mathrm{fD}} = 1\times10^{5}$

5. Conclusions and Recommendations

A reservoir model was created to determine the optimum method of maximizing incremental oil recovery in the Bakken Shale by CO_2 Huff-and-Puff. A compositional reservoir simulator was used to study the various design components of the Huff-and-Puff process in order to identify the parameters with the largest impact on production and understand the reservoir's response to cyclical CO_2 injection. A simple economic analysis was run for one and two-fracture configurations, and the effect of domain discretization was studied. Additionally, mortar coupling was explored as an alternative method of solving hydraulically-fractured reservoir models, and compared against the Cinco-Ley et al. (1978) semi-analytical solution for finite-conductivity fractures. A Matlab program of Cinco-Ley et al.'s (1978) semi-analytical solution was created and validated by replicating the figures from their original paper. This program was used to obtain the pressure and flux distributions along the fracture for any value of the dimensionless conductivity (C_{D}), diffusivity (n_{fD}), and storage capacity (C_{fDf}). Two numerical reservoir simulators (full-domain finite difference and mortar-coupled subdomains) were created to solve the Cinco-Ley et al. (1978) problem and their results were compared against each other. Finally, numerical issues associated with mortar coupling of the Cinco-Ley et al. (1978) problem were explored. This chapter presents the conclusions reached in this study and provides recommendations for future research.

5.1. CONCLUSIONS ON CO_2 HUFF-AND-PUFF AND RECOMMENDATIONS FOR FUTURE STUDIES

As discussed in Sections 3.7 and 3.10, incremental recovery factors from CO_2 Huff-and-Puff appear to be insufficient to make the process commercially viable under current economic conditions. However, from a purely technical standpoint, the simulation results show that cyclical CO_2 is effective at improving oil recovery in the Bakken Shale. This project identified clear ways of increasing the effectiveness and efficiency of Huff-and-Puff operations, which can hopefully guide the design of future treatments. The following are the main conclusions reached in this study:

1. Producing below the bubble point is significantly better for recovery than maintaining undersaturated reservoir conditions. As shown in Section 3.3, developing a robust gas drive provides substantial benefits in terms of pressure support that outweigh the reductions in oil relative permeability.

2. Beginning Huff-and-Puff operations too early in the life of the well negatively affects the effectiveness of the treatment. On the other hand, starting CO_2 injection too late does not impact oil recovery but may diminish the project's net present value. Reliable guidelines for identifying the optimum length of the primary depletion period could not be established. However, treatments started after approximately one year obtained the same incremental recovery regardless of the length of the primary depletion period (all other variables kept constant).

3. While there is a non-linear relationship between injection time and incremental oil recovery, there is a strong positive correlation between the injection volume and the incremental recovery factor. This correlation is approximately linear during the early phases of injection, when the reservoir is being re-pressurized. However, once the near-fracture region approaches the bottomhole injection pressure, longer injection periods

have marginal production benefits. Therefore, the optimal injection time must be calibrated in terms of the surface gas rate and estimated reservoir pressure.

4. Shorter soaking times are preferable over longer waiting periods. The simulation results showed no mixing or diffusion benefits from extended shut-in periods, which is in agreement with Chen et al (2013). These results call into question the need for any type of soaking period during Huff-and-Puff operations in the Bakken.

5. Varying the magnitude of the molecular diffusion coefficients changed the quantitative results of the simulations but not the qualitative conclusions drawn from them. As stated in CMG GEM's User's Guide (2012a), molecular diffusion coefficients should be regarded as "adjustable parameters" that need to be tuned to give acceptable results.

6. The relationship between the number of cycles and incremental oil recovery is decidedly non-linear. The first cycle is by far the most effective, and incremental recovery decreases progressively in subsequent cycles as a result of oil depletion in the near-fracture region. Later cycles are also less efficient, as the decline in reservoir pressure results in larger injection drawdowns and greater CO_2 consumption.

7. The conductivity of natural fractures is more important to the Huff-and-Puff process than the permeability of the matrix. Highly-conductive natural fracture networks allow CO_2 to migrate deep into the formation and contact large volumes of reservoir fluids. In the absence of natural pathways CO_2 accumulates in the near-fracture region, coming out of solution once the well is re-opened to production and blocking oil flow into the well.

8. The discretization of the computational domain has a significant effect on the projected recovery factors. When varying the degree of grid refinement in the near-fracture region, it was found that reservoir models with coarser meshes predict larger

incremental recoveries for the same Huff-and-Puff treatment than finely-gridded domains. Coarser discretization of the domain causes the properties of blocks in the near-fracture region to be averaged together, failing to capture the reservoir conditions in enough detail to accurately model primary and incremental recovery. The number of grid blocks in the model is not as important as the degree of refinement implemented around the fracture.

9. A two-fracture configuration is slightly more effective than a single-fracture scheme, but also less efficient. CO_2 injection requirements in the two-fracture model were considerably greater without resulting in proportionally larger incremental recovery factors.

10. CO_2-enriched hydrocarbon gases are a viable alternative to pure CO_2 injection. Re-injecting the separator gas (approximately 50 mol% CO_2, 50 mol% produced gas) outperformed injecting 100% CO_2, confirming findings by Wang et al. (2010) and Hoffman (2012). The gas injection requirements of a Huff-and-Puff cycle can be fulfilled almost entirely by gas production from the previous cycle. These large reutilization rates (> 90%) have the potential to dramatically improve the commercial viability of Huff-and-Puff by significantly reducing CO_2 acquisition costs.

From these conclusions, it is clear that future studies should focus on identifying ways of enhancing the economic viability of the Huff-and-Puff process. This involves reducing incremental recovery costs and increasing incremental recovery factors. The option of re-injecting produced CO_2 + hydrocarbon gases is particularly promising, because it provides slightly better effectiveness than pure CO_2 injection and significantly more efficiency. While this project was conducted with the utmost thoroughness and attention to detail, there is always room for improvement. Recommendations for future work include:

1. Performing history-matching of field production data at the single-stage scale. As Section 3.9 shows, the choice and discretization of the domain has a significant impact on the simulation results. While history-matched reservoir properties might match production data at the field level, they might not downscale to a smaller domain. A source of significant uncertainty in this study was the relative permeability data, which was adapted from Yu et al. (2014). Yu et al. (2014) obtained their relative permeability curves by history-matching field pressure and production data, but did so on a 326-acre model and then downscaled their results to a 10-acre (340 × 1,320 ft.) domain. It is uncertain how accurately these curves and other reservoir parameters translate to a smaller, more refined scale. Future iterations of this project must include validation of the reservoir model by performing history-matching of field production data that has been appropriately allocated to the single-stage domain.

2. Re-running simulations for a Plug-and-Perf completion style. The current computational domain models an open-hole completion, in which the entire face of the reservoir is exposed to the wellbore. While the hydraulic fracture is still the main conduit for fluids in and out of the reservoir, open-hole completions allow for fluid transfer along the entire wellbore length. As Figures 5-1 and 5-2, changing the model's perforation scheme significantly alters the pressure distribution during injection and production, which could affect the reservoir's response to the Huff-and-Puff process.

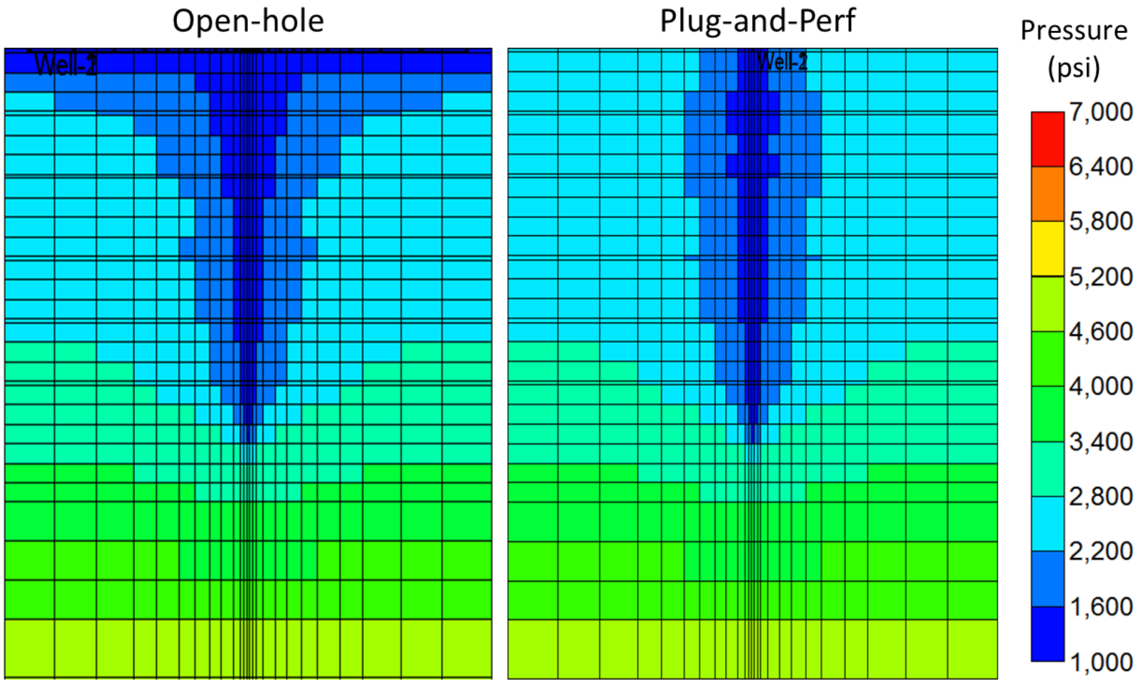

Figure 5-1. Comparison of open-hole and Plug-and-Perf completions during production

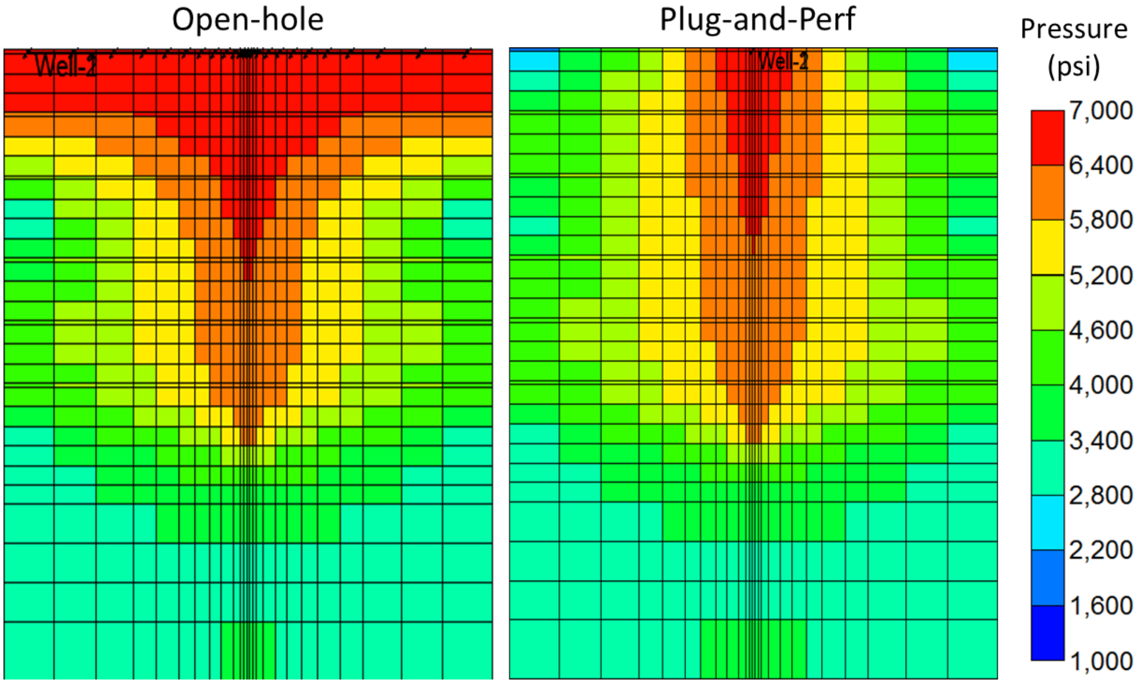

Figure 5-2. Comparison of open-hole and Plug-and-Perf completions during injection

3. Running additional simulations with the two-fracture model, and experimenting with different domain sizes. The two-fracture configuration was shown to be slightly more effective but considerably less efficient than the single-fracture model. Future studies should study other domain sizes and fracture configurations. For example, the domain could be made shorter or longer in the x and y-directions to model different fracture and well-spacing schemes, and the number, half-length, and conductivity of the hydraulic fractures could be varied.

5.2. CONCLUSIONS ON MORTAR COUPLING AND RECOMMENDATIONS FOR FUTURE STUDIES

Mortar coupling was studied as an alternative to full-domain finite difference modeling for solving hydraulically-fractured reservoir systems. While it was able to correctly replicate the Cinco-Ley et al. (1978) semi-analytical solution for single-phase flow into a finite-conductivity fracture, there were instances in which it failed to outperform the full-domain simulator in terms of accuracy and numerical stability. However, mortar coupling could be useful in more complex cases that capitalize on the benefits of decoupling the fracture from the reservoir. The following conclusions have been reached for the mortar coupling portion of this study:

1. The full-domain and mortar coupling models were able to replicate the Cinco-Ley et al. (1978) semi-analytical solution with almost identical degrees of accuracy for dimensionless conductivity (C_D) values of 10 and above, even for early times ($t_D \leq 1\times10^{-4}$).

2. Obtaining accurate results for early times using the full-domain and mortar coupling models is extremely sensitive to the initial dimensionless timestep. The initial dimensionless timestep must be equal to the earliest time of interest.

3. The mortar coupling simulator had problems modeling the stabilized dimensionless flux distribution at $C_D < 1$. Increasing the number of nodes in the mortar space eliminated the oscillations in the flux profile.

4. The peaks in flux distribution on the fracture side of the interface appear to be linked to the dimensionless storage capacity (C_{fDf}) term, and related (to some degree) to the discretization of the reservoir subdomain. The perturbations do not appear to be caused by the permeability contrast between the two subdomains, but rather by the dimensions of the fracture and its width-to-length ratio.

Despite some of the numerical issues on the fracture subdomain, mortar coupling proved to be an accurate method for modeling hydraulically-fractured reservoir models. Future research should focus on demonstrating its applicability to more complex cases than the Cinco-Ley et al. (1978) problem, and on better understanding its numerical capabilities and limitations. Recommendations for future work include:

1. Understanding and addressing the numerical causes of the fluctuations in the fracture-side dimensionless flux distribution. Implementing higher-order basis functions (quadratic, polynomial) could help solve this issue by improving continuity of the pressure derivative at the mortar element edge.

2. Applying mortar coupling to more complicated problems, or to systems that cannot by modeled entirely by full-domain finite difference simulators. For instance, mortar coupling could be used to model single-phase flow in the fracture and two-phase flow in the matrix, or use a black oil model (oil + gas + water) in the fracture and model the reservoir as a compositional system. This is in addition to the multi-scale applications described by Balhoff et al. (2007) and Sun (2012), in which pore-scale models are coupled together with continuum-scale blocks in areas of the reservoir where an extremely high degree of resolution is needed.

Appendix I. Coefficients for Peng-Robinson and Soave-Redlich-Kwong EOS Critical Properties Correlations (from Pedersen et al., 2007)

Table I-1 – Coefficients for critical property correlations, Soave-Redlich-Kwong Equation of State

	1	**2**	**3**	**4**	**5**
c	1.6312×10^{2}	8.6052×10	4.3475×10^{-1}	-1.8774×10^{3}	-
d	-1.3408×10^{-1}	2.5019	2.0846×10^{2}	-3.9872×10^{3}	1.0
e	7.4310×10^{-1}	4.8122×10^{-3}	9.6707×10^{-3}	-3.7194×10^{-6}	-
f	0.4800	1.5740	0.1760	-	-

Table I-2 – Coefficients for critical property correlations, Peng-Robinson Equation of State

	1	**2**	**3**	**4**	**5**
c	7.3404×10	9.7356×10	6.1874×10^{-1}	-2.0593×10^{3}	-
d	7.2846×10^{-2}	2.1881	1.6391×10^{2}	-4.0432×10^{3}	1/4
e	3.7377×10^{-1}	5.4927×10^{-3}	1.1793×10^{-2}	-4.9305×10^{-6}	-
f	0.3746	1.5423	0.2699	-	-

$$T_c = c_1\rho + c_2 \ln M + c_3 M + \frac{c_4}{M} \tag{I-1}$$

$$\ln P_c = d_1 + d_2\rho^{d_5} + \frac{d_3}{M} + \frac{d_4}{M^2} \tag{I-2}$$

$$e_1 + e_2 M + e_3\rho + e_4 M^2 = f_1 + f_2\omega - f_3\omega^2 \tag{I-3}$$

Appendix II. Discretization of Computational Domain

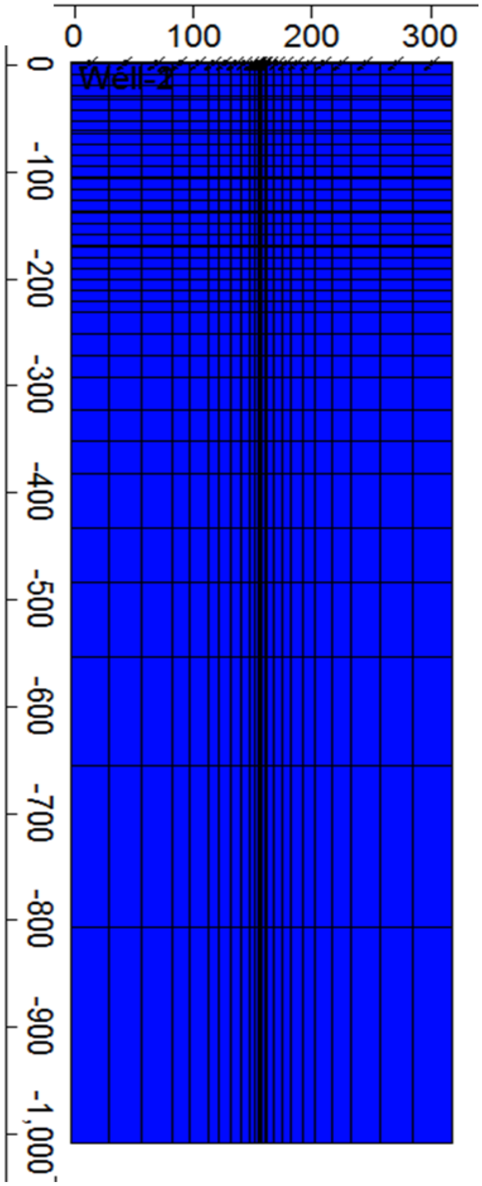

Figure II-1. Discretization of computational domain

25 × 40 × 1
320 ft. × 1000 ft. × 10 ft.

x-direction: 32.5, 27.5, 25, 2×15, 2×10, 2×7.5, 5, 5×2, 5, 2×7.5, 2×10, 2×15, 25, 27.5, 32.5

y-direction: 2, 3×10, 2, 3×10, 2, 4×10, 2, 3×10, 2, 3×10, 2, 3×10, 3×10, 3×20, 3×30, 2×50, 70, 100, 150, 200

Appendix III. Discretization of Two-Fracture Computational Domain

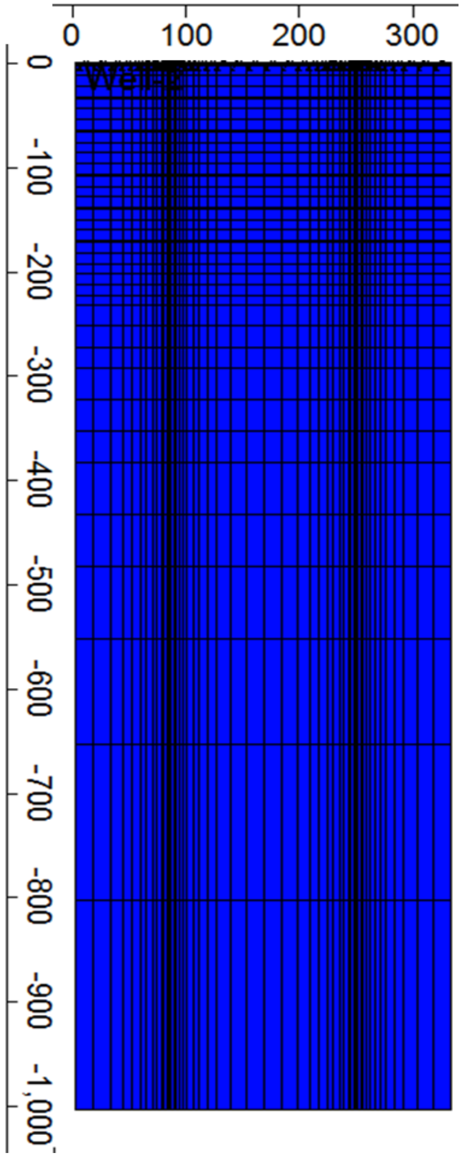

Figure III-1. Discretization of two-fracture computational domain

50 × 40 × 1
320 ft. × 1000 ft. × 10 ft.

x-direction: 15, 13.75, 11.25, 2×7.5, 2×5, 2×3.75, 2.5, 5×2, 2.5, 2×3.75, 2×5, 2×7.5, 11.25, 13.75, 2×15, 13.75, 11.25, 2×7.5, 2×5, 2×3.75, 2.5, 5×2, 2.5, 2×3.75, 2×5, 2×7.5, 11.25, 13.75, 15

y-direction: 2, 3×10, 2, 3×10, 2, 4×10, 2, 3×10, 2, 3×10, 2, 3×10, 3×10, 3×20, 3×30, 2×50, 70, 100, 150, 200

Appendix IV. Cinco-Ley et al. (1978) Semi-Analytical Data from Matlab Program

Table IV-1 – Dimensionless flux for Cinco-Ley et al. (1978) semi-analytical solution, $C_{\mathrm{fDf}} = 1\times10^{-3}$, $n_{\mathrm{fD}} = 1\times10^{7}$, $C_{\mathrm{D}} = 1\times10^{4}$

t_D → x_D ↓	1×10^{-5}	1×10^{-4}	1×10^{-3}	2×10^{-1}	5
0.025	0.6463	0.9108	0.9623	0.8127	0.6501
0.075	0.6455	0.9106	0.9622	0.8128	0.6516
0.125	0.6447	0.9105	0.9622	0.8133	0.6548
0.175	0.6439	0.9103	0.9621	0.8141	0.6597
0.225	0.6432	0.9102	0.9621	0.8153	0.6664
0.275	0.6425	0.9100	0.9620	0.8169	0.6751
0.325	0.6419	0.9099	0.9620	0.8192	0.6860
0.375	0.6413	0.9098	0.9619	0.8222	0.6995
0.425	0.6408	0.9096	0.9619	0.8263	0.7159
0.475	0.6403	0.9095	0.9619	0.8319	0.7361
0.525	0.6399	0.9095	0.9618	0.8396	0.7606
0.575	0.6395	0.9094	0.9618	0.8501	0.7909
0.625	0.6391	0.9093	0.9618	0.8646	0.8286
0.675	0.6388	0.9092	0.9618	0.8851	0.8766
0.725	0.6385	0.9092	0.9618	0.9147	0.9392
0.775	0.6383	0.9091	0.9617	0.9591	1.0245
0.825	0.6381	0.9091	0.9617	1.0290	1.1475
0.875	0.6380	0.9091	0.9622	1.1534	1.3483
0.925	0.6379	0.9090	0.9534	1.3554	1.6599
0.975	0.6379	0.9185	1.1669	2.9305	3.8278

Table IV-2 – Dimensionless flux for Cinco-Ley et al. (1978) semi-analytical solution,
$C_{\mathrm{fDf}} = 1\times10^{-3}$, $n_{\mathrm{fD}} = 1\times10^{5}$, $C_{\mathrm{D}} = 1\times10^{2}$

t_{D} → **x_{D} ↓**	**1×10^{-5}**	**1×10^{-4}**	**1×10^{-3}**	**2×10^{-1}**	**5**
0.025	1.1315	1.0268	1.0012	0.8254	0.6630
0.075	1.0489	1.0083	0.9930	0.8195	0.6585
0.125	0.9726	0.9913	0.9878	0.8181	0.6597
0.175	0.9022	0.9752	0.9828	0.8175	0.6632
0.225	0.8375	0.9601	0.9781	0.8177	0.6689
0.275	0.7781	0.9460	0.9737	0.8185	0.6768
0.325	0.7237	0.9328	0.9696	0.8201	0.6870
0.375	0.6743	0.9205	0.9657	0.8226	0.6999
0.425	0.6294	0.9092	0.9621	0.8262	0.7159
0.475	0.5889	0.8988	0.9589	0.8313	0.7355
0.525	0.5527	0.8894	0.9559	0.8386	0.7597
0.575	0.5205	0.8809	0.9532	0.8487	0.7895
0.625	0.4923	0.8734	0.9508	0.8629	0.8268
0.675	0.4678	0.8668	0.9487	0.8830	0.8744
0.725	0.4471	0.8611	0.9468	0.9123	0.9367
0.775	0.4299	0.8564	0.9453	0.9563	1.0215
0.825	0.4163	0.8527	0.9440	1.0258	1.1441
0.875	0.4061	0.8498	0.9435	1.1496	1.3443
0.925	0.3994	0.8479	0.9343	1.3509	1.6551
0.975	0.3960	0.8547	1.1397	2.9213	3.8184

Table IV-3 – Dimensionless flux for Cinco-Ley et al. (1978) semi-analytical solution, $C_{\mathrm{fDf}} = 1\times10^{-3}$, $n_{\mathrm{fD}} = 1\times10^{4}$, $C_{\mathrm{D}} = 10$

t_D → x_D ↓	**1 × 10⁻⁵**	**1 × 10⁻⁴**	**1 × 10⁻³**	**2 × 10⁻¹**	**5**
0.025	3.2197	1.9607	1.3481	0.9398	0.7858
0.075	2.4999	1.7785	1.2665	0.8792	0.7265
0.125	1.9248	1.6150	1.2149	0.8605	0.7103
0.175	1.4675	1.4639	1.1654	0.8477	0.7015
0.225	1.1060	1.3249	1.1188	0.8389	0.6979
0.275	0.8224	1.1974	1.0752	0.8326	0.6982
0.325	0.6019	1.0812	1.0346	0.8282	0.7020
0.375	0.4321	0.9757	0.9970	0.8255	0.7092
0.425	0.3029	0.8804	0.9623	0.8247	0.7200
0.475	0.2061	0.7950	0.9304	0.8258	0.7349
0.525	0.1347	0.7189	0.9015	0.8294	0.7545
0.575	0.0831	0.6518	0.8755	0.8362	0.7799
0.625	0.0466	0.5933	0.8523	0.8472	0.8128
0.675	0.0215	0.5429	0.8320	0.8643	0.8559
0.725	0.0049	0.5003	0.8145	0.8905	0.9133
0.775	-0.0058	0.4653	0.7998	0.9313	0.9928
0.825	-0.0123	0.4376	0.7879	0.9971	1.1089
0.875	-0.0161	0.4170	0.7791	1.1161	1.3004
0.925	-0.0181	0.4033	0.7666	1.3107	1.5991
0.975	-0.0189	0.3978	0.9104	2.8405	3.6940

Table IV-4 – Dimensionless flux for Cinco-Ley et al. (1978) semi-analytical solution, $C_{\mathrm{fDf}} = 1\times10^{-3}$, $n_{\mathrm{fD}} = 1\times10^{3}$, $C_{\mathrm{D}} = 1$

$t_D \rightarrow$ $x_D \downarrow$	1×10^{-5}	1×10^{-4}	1×10^{-3}	2×10^{-1}	5
0.025	7.9252	5.5833	3.5827	1.9645	1.8222
0.075	3.3076	4.0220	2.8158	1.3730	1.2318
0.125	1.1884	2.8605	2.3794	1.1967	1.0578
0.175	0.3179	1.9870	1.9894	1.0767	0.9414
0.225	0.0247	1.3486	1.6532	0.9912	0.8606
0.275	-0.0375	0.8947	1.3655	0.9258	0.8012
0.325	-0.0296	0.5803	1.1214	0.8737	0.7565
0.375	-0.0130	0.3680	0.9160	0.8313	0.7229
0.425	-0.0033	0.2283	0.7445	0.7964	0.6985
0.475	0.0001	0.1386	0.6024	0.7678	0.6822
0.525	0.0006	0.0822	0.4854	0.7448	0.6734
0.575	0.0003	0.0477	0.3899	0.7273	0.6726
0.625	0.0000	0.0270	0.3125	0.7155	0.6805
0.675	-0.0001	0.0149	0.2506	0.7107	0.6990
0.725	-0.0002	0.0080	0.2015	0.7148	0.7314
0.775	-0.0002	0.0042	0.1635	0.7321	0.7840
0.825	-0.0002	0.0022	0.1348	0.7706	0.8691
0.875	-0.0002	0.0011	0.1142	0.8527	1.0197
0.925	-0.0002	0.0005	0.1004	0.9956	1.2623
0.975	-0.0002	0.0003	0.1028	2.2035	3.0309

Table IV-5 – Stabilized flux distributions for Cinco-Ley et al. (1978) semi-analytical solution, $C_{fDf} = 1\times10^{-3}$, $t_D > 5$

C_D → **x_D ↓**	**100**	**10**	**2**	**1**	**0.2**
0.025	0.6703	0.7858	1.2711	1.8222	4.9771
0.075	0.6657	0.7265	0.9721	1.2318	2.3171
0.125	0.6668	0.7103	0.8825	1.0578	1.6783
0.175	0.6702	0.7015	0.8228	0.9414	1.2780
0.225	0.6756	0.6979	0.7821	0.8606	1.0222
0.275	0.6832	0.6982	0.7532	0.8012	0.8439
0.325	0.6930	0.7020	0.7330	0.7565	0.7139
0.375	0.7055	0.7092	0.7198	0.7229	0.6161
0.425	0.7209	0.7200	0.7128	0.6985	0.5410
0.475	0.7399	0.7349	0.7118	0.6822	0.4829
0.525	0.7633	0.7545	0.7168	0.6734	0.4382
0.575	0.7923	0.7799	0.7287	0.6726	0.4045
0.625	0.8287	0.8128	0.7487	0.6805	0.3807
0.675	0.8750	0.8559	0.7791	0.6990	0.3666
0.725	0.9358	0.9133	0.8238	0.7314	0.3633
0.775	1.0188	0.9928	0.8896	0.7840	0.3739
0.825	1.1390	1.1089	0.9902	0.8691	0.4055
0.875	1.3356	1.3004	1.1613	1.0197	0.4784
0.925	1.6413	1.5991	1.4322	1.2623	0.6062
0.975	3.7768	3.6940	3.3662	3.0309	1.7100

Table IV-6 – Dimensionless pressure drop distribution for Cinco-Ley et al. (1978) semi-analytical solution, $C_{\mathrm{fDf}} = 1\times10^{-3}$, $t_{\mathrm{D}} > 5$

C_{D} →	**10**	**2**	**1**	**0.2**
x_{D} ↓				
0.025	0.0590	0.2735	0.5013	1.5358
0.075	0.0542	0.2500	0.4557	1.3438
0.125	0.0496	0.2278	0.4132	1.1839
0.175	0.0452	0.2066	0.3734	1.0453
0.225	0.0409	0.1865	0.3360	0.9229
0.275	0.0368	0.1674	0.3007	0.8133
0.325	0.0329	0.1492	0.2674	0.7144
0.375	0.0291	0.1319	0.2360	0.6244
0.425	0.0255	0.1155	0.2063	0.5420
0.475	0.0221	0.1000	0.1784	0.4665
0.525	0.0189	0.0854	0.1522	0.3969
0.575	0.0159	0.0717	0.1277	0.3329
0.625	0.0130	0.0589	0.1049	0.2738
0.675	0.0104	0.0470	0.0838	0.2196
0.725	0.0080	0.0361	0.0644	0.1699
0.775	0.0058	0.0262	0.0468	0.1248
0.825	0.0039	0.0175	0.0313	0.0844
0.875	0.0022	0.0100	0.0179	0.0491
0.925	0.0009	0.0040	0.0071	0.0199
0.975	0.0000	0.0000	0.0000	0.0000

References

Adekunle, O. O., & Hoffman, B. T. (2014, April 12). Minimum Miscibility Pressure Studies in the Bakken. Society of Petroleum Engineers. doi:10.2118/169077-MS

Appleton, J., & Rivenbark, M. (2013, January 28). Cemented Versus Open Hole Completions: What is Best for Your Well? Society of Petroleum Engineers. doi:10.2118/163946-MS

Arbogast, T., Pencheva, G., Wheeler, M. F., & Yotov, I. (2007). A Multiscale Mortar Mixed Finite Element Method. *Multiscale Modeling & Simulation*, *6*(1), 319–346. doi:10.1137/060662587

Balhoff, M. T., Thompson, K. E., & Hjortsø, M. (2007). Coupling pore-scale networks to continuum-scale models of porous media. *Computers & Geosciences*, *33*(3), 393–410. doi:10.1016/j.cageo.2006.05.012

Bennett, C., Reynolds, A., Raghavan, R. 1986. Performance of Finite-Conductivity, Vertically Fractured Wells in Single Layer Reservoirs. SPE Formation Evaluation 1(4). DOI 10.2118/11029-PA

BP Statistical Review of World Energy. (2013). Retrieved from British Petroleum website: http://www.bp.com/content/dam/bp/pdf/statistical-review/statistical_review_of_world_energy_2013.pdf

Breit, V. S., Stright, D. H., & Dozzo, J. A. (1992, January 1). Reservoir Characterization of the Bakken Shale From Modeling of Horizontal Well Production Interference Data. Society of Petroleum Engineers. doi:10.2118/24320-MS

Chen, C., Mohanty, K. K., & Balhoff, M. T. (2013, April 10). Effect of Reservoir Heterogeneity on Improved Shale Oil Recovery by CO Huff-n-Puff. Society of Petroleum Engineers. doi:10.2118/164553-MS

Clark, A. J. (2009, January 1). Determination of Recovery Factor in the Bakken Formation, Mountrail County, ND. Society of Petroleum Engineers. doi:10.2118/133719-STU

Computer Modeling Group Ltd. (CMG). (2012a). *User's Guide - GEM: Advanced Compositional and Unconventional Reservoir Simulator*. Calgary, Canada.

Computer Modeling Group Ltd. (CMG). (2012b). *User's Guide - WinProp: Phase Behavior and Fluid Property Program.* Calgary, Canada.

Gamadi, T. D., Sheng, J. J., & Soliman, M. Y. (2013, September 30). An Experimental Study of Cyclic Gas Injection to Improve Shale Oil Recovery. Society of Petroleum Engineers. doi:10.2118/166334-MS

Gringarten, A. C., Ramey, H. J., & Raghavan, R. (1974, August 1). Unsteady-State Pressure Distributions Created by a Well With a Single Infinite-Conductivity Vertical Fracture. Society of Petroleum Engineers. doi:10.2118/4051-PA

Hoffman, B. T. (2012, January 1). Comparison of Various Gases for Enhanced Recovery from Shale Oil Reservoirs. Society of Petroleum Engineers. doi:10.2118/154329-MS

Kurtoglu, B., & Kazemi, H. (2012, January 1). Evaluation of Bakken Performance Using Coreflooding, Well Testing, and Reservoir Simulation. Society of Petroleum Engineers. doi:10.2118/155655-MS

Kurtoglu, B., Sorensen, J. A., Braunberger, J., Smith, S., & Kazemi, H. (2013, August 12). Geologic Characterization of a Bakken Reservoir for Potential CO2 EOR. Society of Petroleum Engineers. doi:10.1190/URTEC2013-186

Li, J., Du, C., & Zhang, X. (2011, January 1). Critical Evaluations of Shale Gas Reservoir Simulation Approaches: Single Porosity and Dual Porosity Modeling. Society of Petroleum Engineers. doi:10.2118/141756-MS

Liu, H., Wang, M. C., Zhou, X., & Zhang, Y. P. (2005, January 1). EOS Simulation for CO Huff-n-Puff Process. Petroleum Society of Canada. doi:10.2118/2005-120

Nicas, J. (2012, May 15). North Dakota Tops Alaska in Oil Output. *The Wall Street Journal*. Retrieved from http://online.wsj.com/news/articles/SB10001424052702304192704577406493478214670

North Dakota Department of Mineral Resources. (n.d.). *North Dakota Drilling and Production Statistics*. Retrieved from https://www.dmr.nd.gov/oilgas/stats/statisticsvw.asp

Palmer, F. S., Landry, R. W., & Bou-Mikael, S. (1986, January 1). Design and Implementation of Immiscible Carbon Dioxide Displacement Projects (CO2 Huff-Puff) in South Louisiana. Society of Petroleum Engineers. doi:10.2118/15497-MS

Pedersen, K. S., Christensen, P. L., & Shaikh, J. A. (2007). *Phase behavior of petroleum reservoir fluids*. Boca Raton: CRC/Taylor & Francis.

Pollastro, R. M., Roberts, L. N., & Cook, T. A. (2010). *Geologic Assessment of Technically Recoverable Oil in the Devonian and Mississippian Bakken Formation*. U.S. Geological Survey.

Shoaib, S., & Hoffman, B. T. (2009, January 1). CO2 Flooding the Elm Coulee Field. Society of Petroleum Engineers. doi:10.2118/123176-MS

Shuler, P. J., Tang, H., Lu, Z., & Tang, Y. (2011, January 1). Chemical Process for Improved Oil Recovery From Bakken Shale. Society of Petroleum Engineers. doi:10.2118/147531-MS

Song, C., & Yang, D. (2013, November 5). Performance Evaluation of CO2 Huff-n-Puff Processes in Tight Oil Formations. Society of Petroleum Engineers. doi:10.2118/167217-MS

Sonnenberg, S. A., & Pramudito, A. (2009). Petroleum geology of the giant Elm Coulee field, Williston Basin. *AAPG Bulletin*. doi:10.1306/05280909006

Sun, T. (2012). *Upscaling and Multiscale Simulation by Bridging Pore Scale and Continuum Scale Models*. (Doctoral dissertation). Austin, TX: The University of Texas at Austin.

Tang, X., Li, G., Wang, R., & Wu, X. (2011, January 1). Innovative In-situ Natural Gas Huff And Puff In Same Well Bore For Cost-Effective Development: A Case Study in Sudan. Society of Petroleum Engineers. doi:10.2118/144836-MS

Tran, T., Sinurat, P. D., & Wattenbarger, B. A. (2011, January 1). Production Characteristics of the Bakken Shale Oil. Society of Petroleum Engineers. doi:10.2118/145684-MS

U.S. Energy Information Administration (EIA). (2012, August 15) *North Dakota crude oil production continues to rise - Today in Energy - U.S. Energy Information Administration (EIA)*. Retrieved from http://www.eia.gov/todayinenergy/detail.cfm?id=7550

U.S. Energy Information Administration (EIA). (2014, June 6). *Increases in U.S. crude oil production come from light, sweet crude from tight formations - Today in Energy - U.S. Energy Information Administration (EIA)*. Retrieved from http://www.eia.gov/todayinenergy/detail.cfm?id=16591

U.S. Geological Survey. (2013). *Assessment of undiscovered oil resources in the Bakken and Three Forks Formations, Williston Basin Province, Montana, North Dakota, and South Dakota, 2013*. Reston, Va.: U.S. Dept. of the Interior, U.S. Geological Survey.

Wang, X., Luo, P., Er, V., & Huang, S.-S. S. (2010, January 1). Assessment of CO2 Flooding Potential for Bakken Formation, Saskatchewan. Society of Petroleum Engineers. doi:10.2118/137728-MS

Wang, D., Seright, R. S., & Zhang, J. (2012, January 1). Wettability Survey in Bakken Shale Using Surfactant Formulation Imbibition. Society of Petroleum Engineers. doi:10.2118/153853-MS

Wenlong, G., Shuhong, W., Jian, Z., Xialin, Z., Jinzhong, L., & Xiao, M. (2008, January 1). Utilizing Natural Gas Huff and Puff to Enhance Production in Heavy Oil Reservoir. Society of Petroleum Engineers. doi:10.2118/117335-MS

Wu, R. S., & Batycky, J. P. (1990, November 1). Evaluation Of Miscibility From Slim Tube Tests. Petroleum Society of Canada. doi:10.2118/90-06-06

Yu, W., Lashgari, H., & Sepehrnoori, K. (2014, April 17). Simulation Study of CO2 Huff-n-Puff Process in Bakken Tight Oil Reservoirs. Society of Petroleum Engineers. doi:10.2118/169575-MS

Zargari, S., & Mohaghegh, S. D. (2010, January 1). Field Development Strategies for Bakken Shale Formation. Society of Petroleum Engineers. doi:10.2118/139032-MS

Vita

Daniel Sánchez Rivera was born and raised in Mexico City. After graduating from the American School Foundation in 2007, he enrolled at the Instituto Tecnológico y de Estudios Superiores de Monterrey (ITESM) Campus Santa Fe for three semesters before transferring to The University of Texas at Austin in January 2009. He obtained a Bachelor of Science degree in Petroleum Engineering in May 2012, graduating with Highest Honors. He attended graduate school at The University of Texas at Austin, where he obtained a Master of Science degree in Petroleum Engineering in August 2014.

Permanent email: danielsanchez@utexas.edu
This thesis was typed by Daniel Sánchez Rivera